Angular correlations between fragments and neutrons in the spontaneous fissions of 252 Cf

Andreina Chietera

Université de Strasbourg

Ecole doctorale de physique et chimie physique
Institut Pluridisciplinaire Hubert Curien
UMR 7178 CNRS/IN2P3

Thèse présentée par
Andreina Chietera
soutenue publiquement le jeudi 22 octobre 2015
discipline: physique
Spécialité: Physique Subatomique

Angular correlations between fragments and neutrons in the spontaneous fission of ^{252}Cf

(Corrélations angulaires entre les fragments et les neutrons dans la fission spontanée du ^{252}Cf)

Thèse dirigée par

Madame L. Stuttgé, Chargée des recherches, IPHC Strasbourg

Rapporteurs :

Madame B. Jurado, Chargée des recherches, CENBG Bordeaux

Monsieur O. Serot, Chercheur-Ingénieur, CEA-Cadarache.

Autres membres du jury :

Monsieur B. Gall, Professeur, Université de Strasbourg

Monsieur F. Gönnenwein, Professeur, Universität Tübingen

Monsieur E. Vardaci, Professeur, Università degli Studi di Napoli Federico II

La follia, come sai, è come la gravità:
basta solo una piccola spinta.

See, madness, as you know, is like gravity:
all it takes is a little push!

La folie, tu ne l'ignores pas, suit les lois de la gravité.
Il n'y a qu'à donner une légère pichenette.

The Dark Knight (2008),
David S. Goyer

Acknowledgements

After an intensive period of three years I flow into this note of thanks: this is the finishing touch on my thesis. It has been a period of intense learning for me, not only in the scientific arena, but also on a personal level. Writing this thesis has had a big impact on me and on my intellectual and personal growth.

The first responsible of that is my advisor, Louise Stuttgé. To her I extend my deepest gratitude. I have been amazingly fortunate to have an advisor with an impressive KARMA, who gave me the freedom to explore on my own, and at the same time the guidance to recover when my steps faltered. She has no idea how much I had appreciated when she sat close to me sometimes just to encourage me, sometimes to help me to understand where my mistakes were hidden. She taught me how to question thoughts and express ideas. Her patience and support helped me overcome many crisis as the fear not to be able to finish my thesis. I can't forget the huge effort that she made to give me the possibility to had a financial support for my Ph.D. and the struggle she made so that I'd the chance to have this opportunity. Thank you for having conducted this battle, for believing in me. I hope I have lived up to her expectations.

I would like to thank C. Roy the IPHC laboratory director. She welcomed me warmly in this laboratory. I never forget the warmth and simplicity of her words when she announced me that I obtained the Ph.D. funding. I still have a trace in my heart and in my e-mail account. Thank you to provide the support and equipment I have needed to produce and complete my thesis.

Many thanks to B. Jurado and O. Serot for accepting to report my Ph.D. thesis, I hope to have the opportunity to discuss with them in the future. Many thankS^3 to the B. Gall as the president of my Ph.D comity. He also guided me into the "monitorat world" , which sometimes appeared incomprehensible to my eyes.

I am also indebted to F. Gönnenweinn, who always has been there to listen and give his advice. I am deeply grateful to him for the long discussions that helped me to sort out the theoretical details of my work and for the numerous lectures on related topics that helped me to improve my knowledge in the fission area. I am also thankful to him for encouraging the use of correct english grammar and consistent notation in my writings and for carefully reading and commenting on countless revisions of this manuscript. I am grateful to E. Verdaci for the patient remarks, comments and questions on my work. Further more I discovered that we have in common not only the passion for physics but also for "la vecchia signora bianco-nera".

I would like to acknowledge the members of the CORA collaboration that with many insightful comments and constructive criticisms at different stages of my research were thought-provoking and helped me to focus my ideas. I am grateful to all members of the collaboration for holding me to a high research standard and enforcing strict validations for each research result and thus teaching me how to do research.

In addition, I would like to thank my tutor C. Fink and M. Vanstalle for their valuable guidance. You definitely provided me with the help and the knowledge to complete successfully my simulation code.

I am also grateful to the the other colleagues at IPHC of the nuclear group and the theoretical one for their various forms of support during my graduate study: D. Curien, F. Didierjean , O. Dorvaux, G. Duchen, F. Le Blanc, F. Nowacki, M. Rousseau and K. Seja. Many thanks for all the discussions we have had together, for the sharing relaxed moments at the coffee room and for having accompanied me in this experience gladdening every single day.

Beyond Nuclear Physics, I would also like to thank N. Liewig for the wisdom of her advice for having listened patiently to my daily whining and laughter shared in our offices. She was always attentive to soften the saddest and difficult moments.

I am also thankful to the IPHC IT technical staff (Cedric, Safia and the rest of the team) at the IPHC who handle and maintain all the electronic devices. I'd like you to know that I learned a lot from you.

Many thanks to all secretaries and to the whole administrative department at IPHC. I am most appreciative of all your hard work with me.

I would also like to thank my family for their wise counsel and sympathetic ear. You are always there for me and none of this would have been possible without your love and your patience. You are a constant source of love, concern, support and strength. We are far but knowing that someone somewhere supports me and believes in my capacities was really encouraging and helpful during these years.

Thanks to Patrick and Sylvie I had the pleasure to know the last year of my thesis, they have aided and encouraged me throughout this endeavor.

I offer my sincerest gratitude to a special person, Fabien, for the care, the attention and the unfailing love that I needed to choose the right direction and successfully complete my thesis. He was always around with discretion to supervise my health and to help me to keep things in perspective.

Finally, there are my friends/colleagues. We were not only able to support each other by deliberating over our problems and findings, but also happily by talking about things other than just our papers. I have to give a special mention for the support given by Regina and Anis: they helped me to stay sane through these difficult years. Their support and care helped me to overcome setbacks and stay focused on my graduate study. I greatly value their friendship and I deeply appreciate their belief in me. I am deeply grateful to Regina who, in this intensive period of three years, taught me the deepest secrets of Geant4 "monster" and followed my professional

growth with patience and with love.

I would like to thank my two splendid “co-bureau” colleagues Houda and Michael (alias Michael Khol -MK). I thank them for having participated with me to the joys and sorrows of this thesis, for having enlivened all my working days, MK with his defiant gags and Houda for the sweetness and the older sister attentions she had towards me.

Thanks to Irene for her smile, her gags and for the “psychological installation” in her office! Many thanks to Mateo because we can discuss about everything in front of a pint of beer.

Though only my name appears on the cover of this dissertation, a great many people have contributed to its production. I owe my gratitude to all those people who have made this dissertation possible and thanks to whom my graduate experience has been one of the most challenging experience of my life.

Contents

List of Figures

List of Tables

Résumé de la thèse

s

Introduction

L' objectif de cette thèse est d'explorer les mécanismes d'émission des neutrons dans le processus de fission. En particulier l'existence de l'anisotropie dynamique dans le centre de masse des fragments de fission et/ou une possible émission de neutrons de scission est investiguée . Dans ce but, une analyse très originale, basée sur une nouvelle stratégie conçue par la collaboration CORA, a été développée.

La thèse débute par une introduction qui situe le sujet de ce travail dans le contexte général de la fission en introduisant les principales notions théoriques concernant la fission et les mécanismes d'émission des neutrons. La nécessité de concevoir une méthode d'analyse appropriée est soulignée. En fait, quand un processus très subtile est étudié, les diverses approximations et/ou les biais expérimentaux peuvent cacher les phénomènes physiques.
Dans le travail présenté ici, un effort important a été nécessaire pour développer une procédure Monte Carlo basée sur un modèle cohérent décrivant la fission spontanée de ^{252}Cf. Parallèlement à ce modèle théorique, le dispositif utilisé pour la détection des neutrons dans l'expérience CORA3 à Strasbourg a été simulé le plus soigneusement possible.
Comme mentionné, quand des effets très faibles doivent être explorés, une connaissance complète du dispositif expérimental est indispensable. La procédure de simulation semble une stratégie adéquate pour contrôler les biais expérimentaux ainsi que pour acquérir une bonne connaissance des mécanismes d'émission de neutrons.

Contexte

En 1962, Henry R. Bowman [1] publiait un travail dans lequel il étudiait les détails de l'émission de neutrons dans la fission spontanée du ^{252}Cf. Cet article fut le précurseur d'une longue série de travaux qui contestaient en partie l'hypothèse à la base de la théorie de l'évaporation des neutrons

1. H. R. Bowman *et al.*, Phys. Rev., 126, 2120 (1962).

de Weisskopf [2] qui déclarait que l'émission était isotrope dans le centre de masse des fragments de fission (CM). Bowman a mis en évidence une émission qu'il a attribuée à des neutrons de scission.

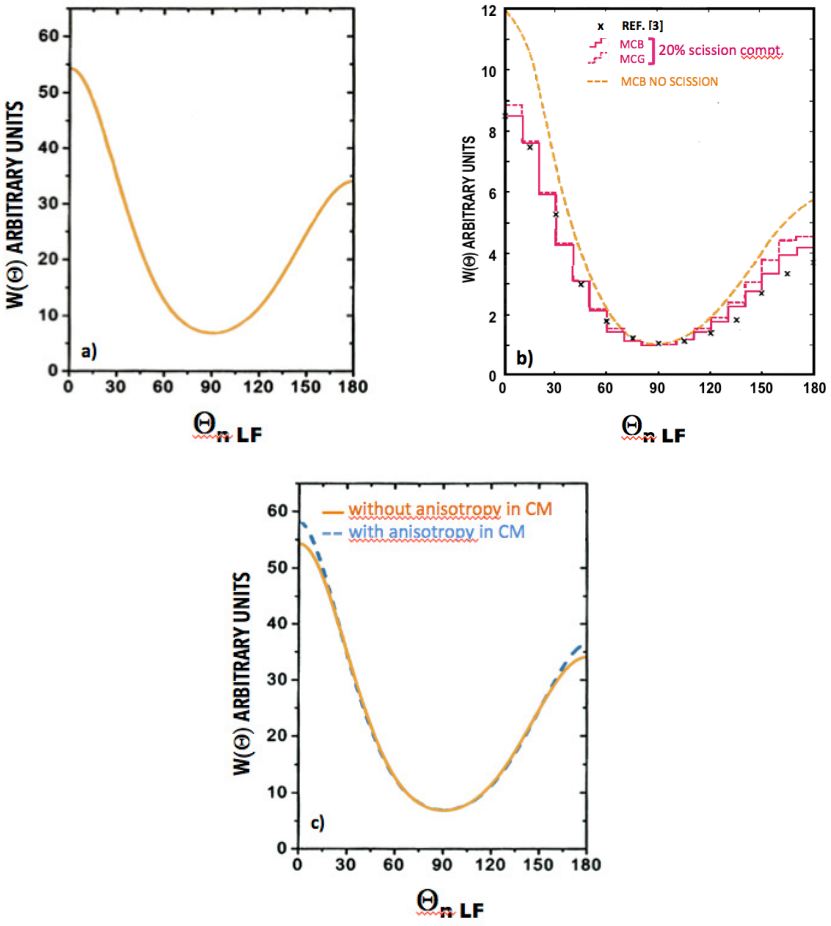

FIGURE 1: Distributions angulaires des neutrons en fonction de l'angle entre la direction d'émission du neutron et celle du fragment léger (LF). Les figures illustrent trois effets influençant ces distributions angulaires : la focalisation cinématique (a), l'effet des neutrons de scission[3] (b, rose) et l'anisotropie dynamique[4] (c, bleu).

BOWMAN affirme que la plus grande partie des neutrons prompts est évaporée lors du processus de fission par les fragments entièrement accélérés (FF), en accord avec la théorie de Weisskopf. Mais il remarque que, lorsqu'on compare les distributions angulaires expérimentales à celle d'une évaporation purement isotrope, des contradictions apparaissent, malgré la prise en compte des effets dus au changement de repère. En effet, BOWMAN montre qu'en raison de la vitesse des fragments de fission (FF), en passant du référentiel du CM à celui du laboratoire, les distributions

2. V. F. Weisskopf, Statistics and Nuclear Reactions, Phys. Rev., 52, 295-303, 1937.

angulaires de neutrons présentent une augmentation à 0° et 180°, un effet appelé *focalisation cinématique* (Fig.1(a)). Cependant la prise en compte de cette focalisation ne permet pas de reproduire complètement les distributions observées expérimentalement.
Pour comprendre l'origine de ces déviations, il a ajouté une contribution aux distributions angulaires de neutrons émis au début du processus de fission (Fig.1(b)), au point de scission [3]. Mais même en ajoutant ces neutrons de scission, il observe un excès de neutrons aux petits angles dans le référentiel du laboratoire autour des fragments lourd et léger. Ceci l'a amené à faire l'hypothèse qu'une anisotropie dynamique (Fig.1(c)) apparaissait aussi dans le CM des deux fragments ; cet effet renforce l'anisotropie cinématique dans le système du laboratoire [4].

Il existe des arguments théoriques et des calculs qui établissent que cette anisotropie existe, mais l'observation expérimentale directe est très difficile, car la contribution due à l'anisotropie dans le CM est très faible. De plus les deux effets agissent en sens contraire, l'émission de scission réduisant la focalisation à 0° et à 180° tandis que l'anisotropie dynamique la rehausse légèrement. Pour montrer l'effet d'anisotropie dynamique, une nouvelle méthode d'analyse [5, 6] a été développée, permettant de s'affranchir de l'effet de l'anisotropie cinématique. Elle est basée sur la mesure de coïncidences triples entre un fragment de fission et deux neutrons émis. L'expérience CORA, présentée dans cette thèse a été effectuée à cette fin.

Le contexte théorique de la problématique concernant l'émission des neutrons est présenté dans un premier chapitre introductif ainsi que la nouvelle approche d'analyse. Cette approche théorique est suivie par un deuxième chapitre présentant l'expérience CORA, la description et l'étalonnage du système de détection ainsi que les résultats expérimentaux obtenus. Le chapitre 3 décrit les simulations mises en place pour gérer les biais expérimentaux du dispositif expérimental et déterminer les paramètres caractérisant les effets recherchés : neutrons de scission et anisotropie dans le CM des FF. L'accord entre simulation et expérience permet de quantifier l'importance relative des deux effets. Les résultats expérimentaux et ceux obtenus par les simulations sont comparés les uns aux autres dans le chapitre 4. Suivent les conclusions du travail de thèse.

Le système de détection

L'expérience CORA a mis en oeuvre les détecteurs CODIS et DEMON.
Le système de détection CODIS permet de détecter les fragments de fission dans un angle solide de 4π. Il est constitué d'une double chambre à ionisation remplie de CF_4 à une pression de 2.64 x 10^4 Pa. Les deux chambres à ionisation sont assemblées sur une cathode segmentée commune constituée de PCB avec des couches doubles de cuivre sur PF_4, matériel époxyde plaqué or

3. C.B. Franklyn *et al.*, Phys. Lett. B, 564 (1978).
4. V. Bunakov *et al.*, Proc. "Int. Sem. ISINN-13" Dubna, Russia, 2005, p.175.
5. F. Gönnenwein *et al.*, Seminar on Fission 6 (2007) 1 (World Scientific).
6. L. Stuttgé *et al.*, Proc. Seminar on Fission VII, Het Pand, Belgium (2010).

et d'épaisseur égale à 1.6 mm. La source ^{252}Cf est placée au centre de cette cathode. Une grille de Frisch est insérée près de chacune des deux anodes de la chambre. La détermination des angles des fragments de fission est réalisée en mesurant les temps de dérive des électrons d'ionisation entre la cathode et les grilles de Frisch, mais aussi à partir de la position déduite des signaux obtenus dans les différents secteurs de la cathode segmentée. Les énergies et les angles polaires, θ et ϕ, des deux fragments de fission peuvent ainsi être déterminés et les masses des fragments peuvent en être déduites.

Le multidétecteur DEMON est composé d'une centaine de cellules cylindriques individuelles de profondeur $L = 20\ cm$ et de diamètre $D = 16\ cm$, chacune contenant 4,4 litres de liquide organique $NE213$ riche en hydrogène ($^1H/^{12}C \sim 1,2$ en moyenne). Dans les expériences CORA seuls 60 modules ont été utilisés et la configuration géométrique de DEMON permettait de couvrir une fraction d'environ 20% de 4π, avec une ouverture angulaire des modules individuels comprise entre $2.2° < \Delta\theta < 5.8°$ dans cette configuration. La configuration géométrique de DEMON a été optimisée dans l'expérience CORA3, configuration quasiment sphérique, ce qui a permis d'accéder non seulement à l'émission dynamique mais en même temps à l'émission de scission. L'énergie des neutrons est déterminée par la technique de temps de vol et la discrimination entre le rayonnement γ et les neutrons est obtenue par l'analyse de la forme des impulsions complétée par une sélection en temps de vol. Les angles d'émission des neutrons sont donnés par les angles centraux de chacune des cellules de DEMON touchées.

Le multidétecteur DEMON dispose d'une acquisition indépendante permettant d'associer l'électronique au standard VXI de DEMON et celle au standard CAMAC et VME de CODIS. L'utilisation de l'électronique VXI présentait l'avantage de pouvoir utiliser un fonctionnement asynchrone : dès qu'une cellule DEMON est touchée, sa voie électronique démarre le codage qui est ensuite validé par un signal venant du trigger principal ou stoppé si aucun signal trigger n'arrive pendant une durée choisie. Ce mode de fonctionnement permet de minimiser le temps mort.

Analyse des données expérimentales

Pour exploiter l'ensemble des données enregistrées, il faut traiter les données brutes codées par le système d'acquisition afin d'accéder aux paramètres physiques nécessaires à notre étude. Pour cela un certain nombre d'étapes sont nécessaires :

1. **la discrimination neutrons-γ**, les scintillateurs de DEMON étant sensibles aux neutrons mais aussi aux rayonnements γ. Seuls les neutrons nous intéressent.
   La séparation neutron-γ se fait en deux étapes. D'abord les spectres bidimensionnels sont construits à partir de l'intégration des impulsions sur deux portes d'intégration appelées Q_{tot} et Q_{lent}. Ensuite, pour améliorer la séparation, une sélection est effectuée sur le spectre monodimensionnel du temps de vol. Q_{tot} représente la charge de l'impulsion intégrée sur la

porte totale. Dans ce cas, la totalité du signal est prise en compte. Par contre, Q_{lent} est la charge intégrée sur la porte lente, retardée de l'ordre de 70 ns par rapport à la porte totale ce qui permet d'intégrer la composante lente du signal. En effet les composantes lentes des neutrons et des γ très différentes, permettent de séparer les deux entités.
À partir de ces spectres bidimensionnels, on détermine par ajustement un polynôme de quatrième degré qui délimite la région peuplée par les neutrons de celle peuplée par les γ. Pour que la particule soit identifiée comme un neutron, elle doit se placer dans la partie au-dessus de ce polynôme, condition donnée par la relation suivante :

$$Q_{ratio} > a_0 + a_1\,Q_{tot} + a_2\,Q_{tot}^2 + a_3\,Q_{tot}^3 + a_4\,Q_{tot}^4 \tag{1}$$

Pour vérifier que la méthode de séparation permet de sélectionner les neutrons de façon satisfaisante et optimiser cette séparation, on utilise l'histogramme monodimensionnel du temps qui fournit le temps de vol de la particule détectée et on vérifie que le pic en temps de vol correspondant aux rayonnements γ ait complètement disparu. En effet, les spectres bidimensionnels ne permettent pas de distinguer les neutrons des γ pour les petites valeurs des Q_{tot}. Il faut donc introduire cette condition supplémentaire pour rejeter ces γ.

En combinant ces deux méthodes, on obtient une discrimination neutrons-γ tout à fait satisfaisante.

2. **détermination de l'énergie des neutrons** obtenue à partir de leur temps de vol déterminé par la distance entre la source d'émission et sa détection dans une cellule de DEMON incluant une méthode d'itération pour tenir compte de la distance d'interaction des neutrons dans le détecteur. La première étape consiste à transformer le temps de vol brut (TAC) exprimé en canaux en grandeur physique, t donné en nanosecondes, pour chaque cellule de DEMON. Pour cela, il faut déterminer, pour chacune des 60 cellules, les coefficients a_i et b_i de la droite d'étalonnage qui s'écrit sous la forme :

$$t_i(ns) = b_i - a_i\,T_i(canaux) \tag{2}$$

La valeur négative de la pente de l'équation est due au fonctionnement asynchrone, qui est utilisé pour réduire le temps mort de l'acquisition.
L'étalonnage des pentes a_i de l'équation 2 a été effectué en utilisant un time-calibrator qui délivre une suite d'impulsions équidistantes en temps. Les coefficients directeurs a_i ont ensuite été déterminés par des régressions linéaires du type :

$$t_i(ns) = a_i\,T_i(canaux). \tag{3}$$

Les cordonnées à l'origine b_i sont déterminées grâce aux rayonnements γ dont le temps de vol est connu puisqu'ils se déplacent à la vitesse de la lumière.

Comme mentionné plus haut, pour calculer l'énergie des neutrons, il faut un autre ingrédient : la profondeur d'interaction d_n^{int} d'un neutron dans un module DEMON. En considérant que la distance de vol d'un neutron est $d_n = D + d_n^{int}$ où D est la distance entre la source et la face d'entrée de la cellule. Pour connaître cette distance d_n^{int} qui dépend de l'énergie du neutron, nous avons développé un algorithme à l'aide du code *MENATE* qui permet de simuler la distance parcourue par un neutron dans un milieu en fonction de son énergie.

$$E_n = \frac{1}{2}\frac{M_n}{c^2}\left(\frac{d_n}{t_n}\right)^2 \tag{4}$$

Cette méthode n'est cependant pas parfaite à cause des nombreuses diffusions des neutrons dans le volume sensible des cellules DEMON.

3. **détermination du seuil en énergie des scintillateurs DEMON** afin de minimiser le bruit électronique et de connaître l'efficacité intrinsèque de détection.
   Fixer un seuil commun à toutes les cellules permet d'avoir une homogénéité dans l'exploitation de l'ensemble des détecteurs DEMON.
   L'énergie seuil a été déterminée à l'aide de sources radioactives γ connues. L'énergie déposée par les différentes sources γ est analysée dans les spectres Q_{tot}. Les cellules DEMON ne permettent pas d'accéder au photopic généralement. C'est donc le front Compton qui nous permet d'effectuer l'étalonnage de l'énergie déposée. Nous avons choisi des sources ^{22}Na et ^{137}Cs dont les caractéristiques sont données dans la table 1.

Source	**E$_\gamma$(keV)**	**Position du front Compton E$_{e^-Compton}$(keVee)**
^{22}Na	511	341
	1274	1062
^{137}Cs	662	477

TABLE 1: Sources radioactives utilisées pour l'étalonnage du seuil de détection des cellules DEMON. Pour chacune d'elles sont données l'énergie des raies γ ainsi que la valeur E$_{e^-Compton}$ du front Compton correspondant.

L'expérience nous donne ainsi accès aux masses, énergies et angles des FF ainsi qu'à l'énergie et aux angles des neutrons associés, événement par événement.

Simulations

Le code de simulation développé dans ce travail est basé sur GEANT4. Il permet de reconstruire le système de détection utilisé dans l'expérience CORA3 et de modéliser la physique des interactions des neutrons dans les cellules de DEMON en se basant sur le code MENATE. Il permet aussi d'ajuster les paramètres caractérisant les neutrons de scission (ω_{sci}) et l'anisotropie dynamique(A$_{\mathrm{nJ}}$).

Le code reproduit un système fissionnant de ^{252}Cf. Les FF qui définissent l'axe de fission sont distribués de manière isotrope dans l'espace 3D. Les paramètres physiques nécessaires pour simuler l'émission des neutrons à partir des fragments du ^{252}Cf sont présentés dans le tableau 2.

Parameters	**LF**	**HF**
v (cm/ns)	1.355	1.022
T (MeV)	0.91	0.93
$< \nu >$	2.056	1.710
σ_ν	0.94	1.07

TABLE 2: Paramètres adoptés dans le code de simulation[7]. LF et HF indiquent respectivement les fragments léger et lourd.

La multiplicité des neutrons, ν, pour chaque fragment est tirée aléatoirement à partir d'une distribution gaussienne à deux dimensions définie avec les grandeurs physiques également indiquées dans le tableau 2 [7] et avec une valeur de corrélation de $\rho = -0,2$. Afin d'extraire les quantités cinématiques relatives aux neutrons dans le système du CM, les énergies des neutrons sont tirées au hasard à partir d'une distribution de type Maxwell :

$$\varphi(\eta) \sim \sqrt{\eta}\, e^{\frac{-\eta}{T}},$$

où T est la température du FF et η représente l'énergie du neutron dans le CM du FF correspondant.
La construction du code permet d'introduire les trois effets cités dans l'introduction à partir de l'émission isotrope de neutrons dans les CM des fragments :

- la focalisation cinématique est obtenue en ajoutant la vitesse des FFs (tableau 2) à la vitesse de chaque neutron.
- l'anisotropie dynamique est introduite en faisant l'hypothèse que les FFs ont un grand moment angulaire, J $\sim 8\hbar$ [8], aligné perpendiculairement à l'axe de fission. Les neutrons évaporés à partir d'un noyau en rotation seront préférentiellement émis dans le plan perpendiculaire à l'axe de fission. Cette anisotropie est paramétrée suivant les prescriptions de I. Guseva[4] par :

  $$W(\theta_{CM_{nJ}}) \sim 1 + A_{nJ} \sin^2 \theta_{CM_{nJ}}, \tag{5}$$

  où $A_{nJ} \neq 0$ est le paramètre d'anisotropie[4] et $\theta_{CM_{nJ}}$ l'angle entre le spin du FF et la direction d'émission du neutron dans le CM.
- la probabilité p_{sci} d'avoir des neutrons de scission est aussi calculée. Dans le cas d'une source de ^{252}Cf on suppose une certaine probabilité d'avoir au maximum un neutron de

7. N.V. Kornilov *et al.*, IAEA 2, 61 (2001).
8. J.B. Wilhelmy *et al.*, Phys. Rev. C, 5, 2041(1972).

scission émis par une source de température de $T_{Cf} = 1.2$ MeV [9], avec une distribution d'énergie de type Weisskopf, $\varphi(E_{sci}) \sim E_{sci}\, e^{\frac{-E_{sci}}{T_{Cf}}}$.

Les paramètres d'entrée dans la simulation qu'on cherche à déterminer par confrontation entre les données expérimentales et la simulation sont :

- A_{nJ} : le paramètre d'anisotropie ;
- p_{sci} : la fraction de neutrons de scission.

Confrontation simulation/expérience et résultats

La stratégie de simuler l'expérience a ainsi permis de comprendre les biais dus au filtre expérimental et de bien maîtriser leur impact sur les observables physiques.
Pour chaque événement de fission, qu'il soit simulé ou expérimental, les observables prises en compte sont :

- l'angle θ_{nLF} entre un neutron et le fragment de fission léger (LF) ;
- l'angle relatif θ_{nn} entre toutes les paires de neutrons émis dans un évènement ;
- la différence entre les angles azimutaux entre tous les couples de neutrons d'un évènement, $\Phi_{12} = \phi_2 - \phi_1$;

Une procédure de minimisation du χ^2 pour les distribution θ_{nn} et θ_{nLF} a été utilisée afin de déterminer le couple (A_{nJ}, p_{sci}) qui donne le meilleur accord entre simulation et expérience. Les résultats obtenus sont comparés aux prévisions théoriques d'I. Guseva [10] avec qui nous collaborons et qui a effectué des calculs dédiés particulièrement au ^{252}Cf. La distribution des différences entre les angles azimutaux Φ_{nn} permet de déterminer le facteur d'anisotropie dynamique de façon indépendante. La méthode utilisée pour cette analyse a été présentée en détail dans le chapitre 1. L'avantage de cette méthode est qu'elle permet de se débarrasser de la focalisation cinématique ainsi que de l'influence des neutrons de scission, pour ainsi obtenir une meilleure évaluation de l'anisotropie. La distribution angulaire des neutrons émis par les fragments de fission dans leur centre de masse a été décrite par l'équation 5. Cette formule mène à la distribution Φ_{nn} exprimée dans la note de bas de page nº 4 :

$$W(\phi_{nn}) = p_0(1 + a_2\, cos^2\phi_{nn}) \tag{6}$$

Les simulations ont permis de développer une bonne stratégie pour s'affranchir du filtre expérimental et reconstruire la distribution avant le filtre expérimental. La validation de cette méthode mise en place à été faite en ajustant la distribution obtenue par les simulations à l'équation 6. A travers l'ajustement il a été possible de déterminer la grandeur a_2 liée au coefficient d'anisotropie A_{nJ} suivant la courbe de la fig. 2 [11]. Si le coefficient a_2 trouvé nous permet de remonter au paramètre

9. A. M. Gagarski, I. Guseva *et al.*, Bulletin of the Russian Academy of Sciences : Physics, 2008, 72 (6), 773-777.
10. I. Guseva, private communication, 2014.
11. I.Guseva, ISINN-23, Dubna 2015.

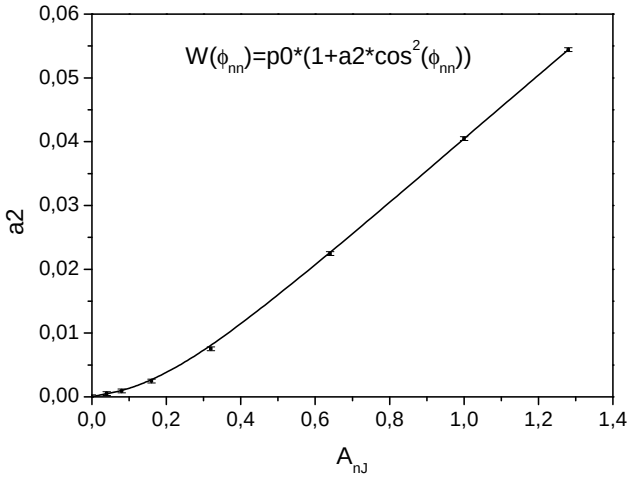

FIGURE 2: Le coefficient a_2 en function du paramètre d'anisotropie A_{nJ}.

A_{nJ} utilisé dans la simulation, la technique développée pour s'affranchir du filtre expérimental peut être appliquée aux données expérimentales. La fonction 6 est donc utilisée pour ajuster la distribution expérimentale et estimer le paramètre d'anisotropie A_{nJ} expérimental.

Conclusions

L'existence de l'anisotropie des neutrons dans le centre de masse des fragments de fission et l'émission de neutrons de scission est un problème irrésolu depuis le travail pionnier de H.R. Bowman en 1962. Beaucoup de travaux, théoriques aussi bien qu'expérimentaux, ont été consacrés à cette question mais ils ont mené à des résultats contradictoires. Toutes les expériences ont été dédiées soit à l'étude de l'anisotropie dynamique soit à l'émission de neutrons de scission. Personne n'a réalisé une expérience permettant la mesure des deux processus dans une même mesure. L'expérience CORA a été initialement conçue par F. Gönnenwein pour explorer l'anisotropie dynamique d'une nouvelle façon qui permet d'éviter l'influence de la focalisation cinématique et des neutrons de scission qui, dans les approches habituelles, cachent le faible effet de l'anisotropie dynamique. L'expérience CORA a été optimisée jusqu'à parvenir à celle de CORA3 qui a permis de mesurer simultanément, pour la première fois, les deux processus. Les distributions θ_{nn}, θ_{nLF} et ϕ_{nn}, étudiées par différents auteurs, ont ainsi pu être mesurées, pour la première fois, simultanément.

Une simulation détaillée a été développée en parallèle à l'analyse des données expérimentales afin d'avoir un bon contrôle sur les nombreux biais expérimentaux. Ces simulations ont montré aussi qu'une caractérisation quantitative des deux processus était accessible avec l'expérience CORA3. Une valeur de A_{nJ}=0.16 pour l'anisotropie dynamique avec une émission de neutrons de scission

ω_{sci}=8 % ont pu être déduits de notre travail.
Ces quantités sont complètement cohérentes avec les prédictions théoriques de I. Guseva.
Le distributions θ_{nn} et θ_{nLF} montrent clairement l'existence de l'émission de neutrons de scission.
L'effet d'anisotropie dans la distribution ϕ_{nn} a une amplitude très faible et est de ce fait très délicate à extraire.

Quelques améliorations des résultats présents peuvent être obtenues. En effet, comme a montré la figure 4.22 du chapitre 4, une augmentation de la statistique ne change pas significativement la valeur du paramètre d'anisotropie mais il diminue les barres d'erreur et l'erreur de l'ajustement. Dans la dernière figure, uniquement la moitié de la statistique expérimentale disponible a été utilisée, par manque de temps. L'expérience CORA3 a duré cinq mois ce qui a permis de collecter de l'ordre de 10^9 coïncidences triples FF-n-n. Une nouvelle expérience avec plus de statistique peut mener à une erreur suffisamment basse pour renforcer la fiabilité de la valeur d'anisotropie que nous avons obtenue.

En prenant en compte toutes ces considérations, nous pouvons considérer que l'expérience CORA3 a fourni des arguments convaincants en faveur de l'existence d'une émission de neutrons de scission ainsi que d'une anisotropie dynamique dans les centres de masse des fragments de fission. De plus, un haut niveau de confiance peut être attribué aux valeurs estimées des contributions de ces deux processus déduites dans ce travail.

Introduction

The aim of this thesis is to explore the neutron emission mechanisms in the fission process. In particular a long standing open question, the existence of a dynamical anisotropy in the centre of mass of the fission fragments and/or a possible scission neutron emission is explored. To this purpose a very original analysis based on a new strategy designed by the CORA collaboration to disentangle the physical phenomenon from other effects has been developed.
Chapter 1 will start with an overview of the theoretical concepts on the fission process and on the neutron emission mechanisms. Also the necessity to conceive an appropriate analysis method is stressed, when a very subtle mechanism is studied as various approximations or/and experimental biases not completely handled can hide the physical phenomenon. In this framework the CORA collaboration proposed a new analysis method and the experimental set up designed to explore the neutron emission mechanism during the fission process.
Chapter 2 is devoted to the description of the experimental devices, CODIS for fission fragments and DEMON for neutrons, and to their working principles.
As mentioned before when very tiny effects have to be explored a careful knowledge of the experimental setup is mandatory. The simulation procedure seems an adequate strategy to investigate how to control the experimental biases and learn more about the neutron emission mechanisms. Chapter 3 describes the simulation code especially developed for the CORA3 experiment. The simulation will allow also to understand the strong points and the weaknesses of the experiment. Only by this simulation exploratory procedure were we able to conceive an adequate analysis strategy.
It is interesting to point out that historically the use of simulations emerged in the 1940's with the study of the fission process. In fact the first computer simulation was performed by the mathematician John Von Neumann to model the process of nuclear detonation during the Manhattan project [1]. As in our case, to complete the tests and the theoretical predictions, a huge computing power to complete calculations in a reasonable amount of time was required. To satisfy this necessity Von Neumann conceived the so called Von Neumann architecture, applied today to the modern computers. Von Neumann is also known in the nuclear explosion simulation framework for his contribution in the development of the pseudo-random numbers algorithm employed in the Monte Carlo method, applied in our simulation code.
In the presented work a huge effort was invested to writing a Monte Carlo procedure based on a

coherent model for the spontaneous fission of ^{252}Cf and to couple it with the devices exploited in the CORA3 experiment.
In chapter 4 the simulation results will be confronted to the experimental observables. The two above mentioned neutron emission mechanisms will be highlighted and their quantitative contribution will be extracted.
A final conclusion will state on the validity of many approaches, experimental as well as theoretical, against or in favour of these two mechanisms. Weak points of the present analysis and of the CORA3 experiment will also be underlined and future possibilities to overcome them will be suggested. Preliminary results have been presented at conferences [2][3].

Chapter 1

Introduction and motivations

Fission of uranium was discovered in 1939 by O. Hahn and F. Strassmann [4] in the neutron induced reaction. Ten years later Fermi observed the first chain reaction of history and constructed the first nuclear reactor, the so called Chicago Pile-1. Despite the remarkable achievements realised since then, after more than 70 years from the fission discovery, many questions remain still open.

1.1 Fission

Historically, the discovery of the neutron in 1932 by J. Chadwick [5] was the starting point for radioactivity studies: this uncharged nuclear particle could easily penetrate the secrets of the atomic nucleus. L. Meitner, O. Hahn and their collaborator F. Strassmann were deeply involved in identifying the products of neutron bombardment of uranium and their decay patterns. It was generally expected that elements with higher atomic numbers than uranium would be produced. Fermi hoped to increase in this way the nuclear chart towards unknown heavy elements. But O. Hahn and F. Strassmann found that they had unexpectedly produced barium, a much lighter element than uranium, which they identified among other products.

L. Meitner and O.R. Frisch worked on calculations based on N. Bohr's droplet model of the nucleus [6] and clearly stated that nuclear fission of uranium had occurred. O.R. Frisch wrote [7, 8]: "*there were strong forces that would resist such a process, just as the surface tension of an ordinary liquid drop resists its division into two smaller ones. But nuclei differ from ordinary drops in one important way: they are electrically charged and this is known to diminish the effect of the surface tension... . The charge of the uranium nucleus... is indeed large enough to destroy the effect of the surface tension almost completely; so the uranium nucleus might indeed be a very wobbly, unstable drop, ready to divide itself at the slightest provocation*", such as the impact of a neutron. It was quickly recognized that barium was a stable isotope resulting from the radioactive decay after neutron bombardment of uranium.

Already in 1939, the first model describing theoretically the fission process was developed by

N. Bohr and J. Wheeler [9]. They claimed that the fissioning nucleus was similar to a deformed liquid drop.

1.1.1 Liquid Drop Model (LDM) and overview on other fission models

The LDM model treats the nucleus as a drop of a homogeneous incompressible fluid uniformly charged. Its justification is founded on the characteristics of the strong interaction: it is short ranged, so occurs mainly between neighbouring nucleons, leading to the phenomenon of saturation. Thanks to this force nuclei are bound due to the overall attractive strong interactions between nucleons with a nearly constant interior nucleon density and a radius proportional to $A^{1/3}$. The analogy of this situation with a liquid droplet results in the LDM for the nuclear binding energies in which the binding energy is expressed by the Weizsacker formula [10] in the following form:

$$E_B(A,Z) = a_V A - a_S A^{2/3} - a_C \frac{Z(Z-1)}{A^{1/3}} - a_A \frac{(A-2Z)^2}{A} + a_P \delta(A,Z) A^{-1/2} \tag{1.1}$$

where the five terms are sketched in fig. 1.1. The four terms on the right-hand side, which

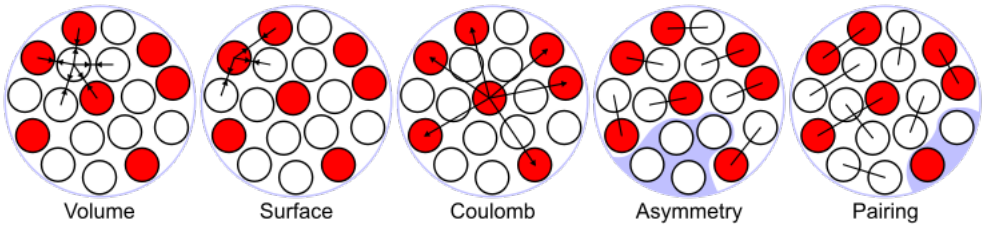

Figure 1.1: Schematic representation of the different terms in the Weizäcker formula.

contributions are presented in fig. 1.2, are referred to as the volume, surface, Coulomb and asymmetry energy terms, respectively. The first term represents the nearest neighbour attractive interaction between nucleons. The second term represents the correction due to the fact that the nucleons on the surface interact only with those in the interior. The third term is due to the Coulomb repulsion between protons. The fourth term called the asymmetry energy arises because protons and neutrons, being distinct types of particles, occupy different quantum states. One can think of two different "pools" of states, one for protons and one for neutrons. If there are significantly more neutrons than protons in a nucleus, some of the neutrons will be higher in energy than the occupied states in the proton pool. The imbalance between the number of protons and neutrons causes in this case a lowering of the binding energy. The last term

represents the pairing interaction. This term captures the effect of spin-coupling. It is given by:

$$\delta(A,Z) = \begin{cases} +\delta_0 & Z,N \text{ even } (A \text{ even}) \\ 0 & A \text{ odd} \\ -\delta_0 & Z,N \text{ odd } (A \text{ even}) \end{cases}$$

where $\delta_0 = \frac{a_P}{A^{1/2}}$ and a_P is the pairing empirical coefficient.
The nuclear force is attractive and of short range. Therefore its contribution to the stability of nuclei is largest if two nucleons can come as close as possible. Due to the Pauli exclusion principle the two nucleons should have opposite spins. This is true for protons and neutrons. Only if both Z and N are even can both protons and neutrons have equal numbers of spin up and spin down. This is an effect similar to the asymmetry term.

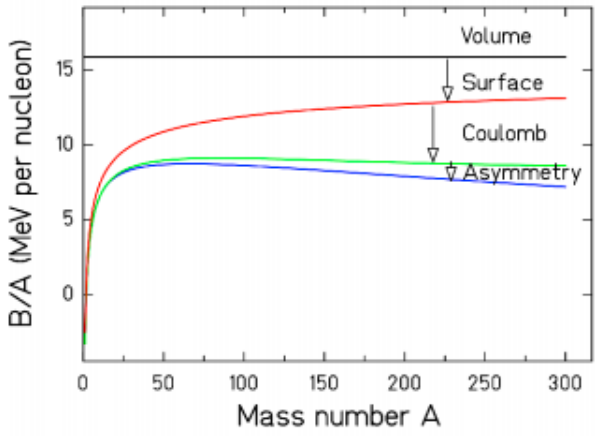

Figure 1.2: The contributions of the different terms to the binding energy per nucleon according to the liquid-drop model. The total binding energy per nucleon (blue line) is maximum around A = 56. Lighter nuclei as well as heavier nuclei are less bound [11].

The empirically deduced values of the liquid-drop constants that reproduce the average trends in the experimental data are given by $a_V = 15.85$ MeV/c^2, $a_S = 18.34$ MeV/c^2, $a_C = 0.71$ MeV/c^2, $a_A = 92.86$ MeV/c^2 and $a_P = 11.46$ MeV/c^2 [12].

The stability of nuclei against deformation depends on the competition between Coulomb repulsion and the surface tension. Since we assume volume conservation in order to reflect the saturate behaviour of the nuclear density, leading to the incompressibility [1], the volume term is not affected by any deformation of the drop. The surface term takes into account the reduction of nuclear binding for the nucleons on the surface of the nucleus. Hence this term is negative

1. The incompressibility is required to reflect the saturation of the nuclear force due to the strong repulsion at very short distances.

in relation to the volume term. The surface term is the smallest for a sphere; any distortion away from a sphere results in a larger contribution of the surface term. The Coulomb term describes the repulsion of the protons; hence if we deform the nucleus this term decreases due to the larger separation of nucleons compared to a sphere. The asymmetry term, as introduced in 1.1, depends only on the nuclear volume and is therefore independent of deformation. The pairing term is neglected here, although pairing should change with deformation, however on much smaller scales than the other terms.

This model has the advantage to express in a very simple way the variation of binding energy as a function of deformation and describes very easily the fission mechanism [9].
To analyze the influence on the energy of the distortion from a spherical shape of the drop to a deformed one [13], the drop radius $\mathcal{R}(\theta)$, depending on the polar angle θ relative to the symmetry axis of the deformation, is developed for small deformations as a function of the parameter $\alpha_\mathbf{l} = (\alpha_0, \alpha_1, \alpha_2, \alpha_3, \alpha_4, ...)$ fixing the shape of the nuclei as

$$\mathcal{R}(\theta) = \mathcal{R}_0\left[1 + \sum_{l=0}^{\infty} \alpha_l P_l(cos\theta)\right] \tag{1.2}$$

where $\mathcal{R}_0 = r_0 A^{1/3}$, $P_l(cos\theta)$ are the Legendre polynomials and l is the multipole parameter. The multipole parameters define different forms of deformation of the nuclear shape.

Let us consider only small, axially symmetric and reflection symmetric [2] deformations. Hence we may approximate the nuclear surface by

$$\mathcal{R}(\theta) = \mathcal{R}_0[1 + \alpha_2 P_2(cos\theta)]$$

The corresponding surface and Coulomb terms for such deformations are given [9, 14, 15] by

$$E_C(\alpha) = \frac{1}{2}\int\int \frac{\rho(\vec{r}_1)\rho(\vec{r}_2)}{|\vec{r}_1 - \vec{r}_2|} dV_1 dV_2 = E_C^{(0)}\left(1 - \frac{1}{5}\alpha^2 - \frac{4}{105}\alpha^3 ....\right)$$
$$E_S(\alpha) = E_S^{(0)} S(\alpha) = E_S^{(0)}\int dS = E_S^{(0)}\left(1 + \frac{2}{5}\alpha^2 - \frac{4}{105}\alpha^3 ....\right)$$

with $E_C^{(0)}$, $E_S^{(0)}$ being the terms for the spherical case. The decrease in the Coulomb term $\Delta E_C = -\frac{1}{5}\alpha^2 E_C^{(0)}$ must be smaller than the increase in the surface energy $\Delta E_S = +\frac{2}{5}\alpha^2 E_S^{(0)}$ for the drop in order to be stable against deformation. The drop will become unstable when the ratio of the changes becomes unity:

$$\frac{|\Delta E_C|}{\Delta E_S} \approx 1 \quad \Longleftrightarrow \quad \frac{E_C}{2E_S} = \chi \approx 1 \tag{1.3}$$

We may define the latter quantity of eq. 1.3 as the fissility parameter χ (see also [9, 14, 15]). For values of χ below unity, the nucleus will be stable against small deformations; for values larger than unity there is no potential barrier to inhibit a spontaneous division of the drop. The

2. In axial symmetry, we define reflection symmetry or mirror symmetry as the symmetry related to an axis perpendicular to the symmetry axis.

LDM predicts that these nuclei are unstable against spontaneous fission. We may now use the terms in eq. 1.1 to estimate the fission probability of a nucleus: the closer its fissibility to unity the higher the probability to fission. If the fissibility is larger than unity the nucleus cannot exist in this LDM and it will instantly separate. According to eq. 1.1, we can write the fissility parameter as

$$\chi = \frac{a_C \frac{Z^2}{A^{1/3}}}{2a_S A^{2/3}} = \frac{a_C}{2a_S}\frac{Z^2}{A} \tag{1.4}$$

A short handed formula is derived in [14] using experimentally fitted values for a_C and a_S,

$$\chi = \frac{Z^2}{50.13A} \tag{1.5}$$

This corresponds to the fact that all nuclei with $\frac{Z^2}{A} \geq 50$ are unstable against spontaneous fission in the liquid drop model.

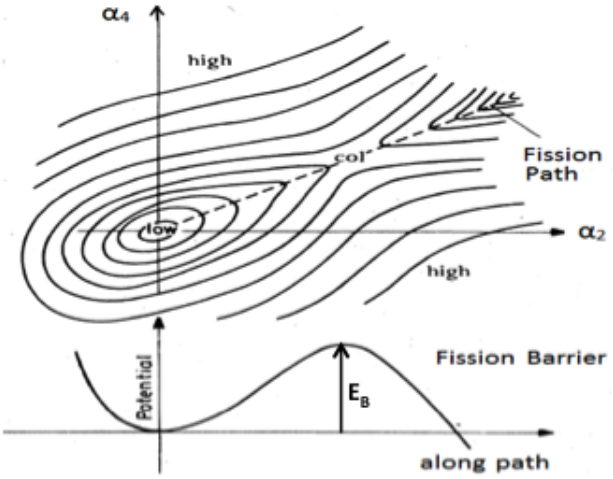

Figure 1.3: The potential energy associated with any arbitrary deformation of the nuclear form may be plotted as a function of the parameters which specify the deformation, thus giving a contour surface which is represented schematically in the top portion of the figure. The pass or saddle point corresponds to the critical deformation of unstable equilibrium (from [9]). At the bottom the fission barrier E_B is plotted.

In their article [9], N. Bohr and J. Wheeler perform the calculation of the deformation energy by developing eq. 1.2 up to the fourth multipole order and considering only the axial and octupolar parameters α_2 and α_4. They then minimise this energy with respect to α_4 for each value of α_2. This allows them to find on the $E_{def}(\alpha_2, \alpha_4)$ landscape displayed on the top of fig.1.3, the equation $\alpha_4 = \alpha_4(\alpha_2)$ of the bottom of the valley that leads to the nucleus separation. The $E_{def}(\alpha_2, \alpha_4(\alpha_2))$ function represents the deformation energy along the bottom of the

valley. N. Bohr and J. Wheeler then show that for fissilities $\chi < 1$, the energy of deformation reaches a maximum at a saddle point in the (α_2, α_4) deformation space. This is illustrated in fig.1.3. The bottom part of the figure shows the fission potential along the bottom valley which leads to fission. The potential E_B appears as a neck or a saddle point in the energy landscape $E_{def}(\alpha_2, \alpha_4)$ plotted on the top of the figure. At this step, the drop is about to be split into two subdrops. The deformation energy along the fission path therefore presents itself as a potential barrier. This is the famous fission barrier. The existence of this barrier, demonstrated for the first time by N. Bohr and J. Wheeler, gives a physical basis to the observation of L. Meitner and O. Frisch in the case of uranium: in its ground state, the nucleus is stable with respect to the different types of deformation. When an extra energy is supplied to the nucleus, by the capture of a neutron for instance, the barrier can be surmounted and nucleus deformation can reach and cross the point where the nucleus splits irretrievably into two fragments.

In the years that followed N. Bohr and J. Wheeler's article, the LDM was significantly further developed. Their calculation was quickly extended to forms of non-axial and asymmetrical left-right drops. Thereafter, and even very recently, the model has been refined in different ways to reflect in particular the diffusivity of the nuclear surface [16] and its curvature [17]. Another very powerful approach to describe the nuclear drop possessing a diffuse surface and very general deformations is the "Yukawa + exponential model" or " Finite Range Liquid Drop Model" (FRLDM) [18] developed in the late 1970's in Los Alamos which later became the "Finite Range Droplet Model" (FRDM) [19] still in use today. However the LDM implies first that the nucleus has in its fundamental state a spherical shape, while most of the nuclei are deformed in their ground state, and second that the separation is in two subdrops of identical mass, whereas most of actinides preferentially fragment into two nuclei of unequal mass. But in fact this shortcomings of the LDM come from the effects related to the shell structure which cannot appear in this approach. Further developments allowed to correct the behaviour of the deformation energy given by the liquid drop by adding microscopic contributions.

A fairly precise way to study the deformation dependence on the nuclear binding energy is to perform self-consistent Hartree-Fock calculations [20] as a function of the deformation. This method takes into account both the macroscopic contributions to the binding energy that are contained in the LDM and the microscopic single-particle contributions. A more simple calculation of the microscopic contribution to the binding energy is to use an independent-particle model, such as the Nilsson one [21]. This model describes successfully the systematics of the nuclear ground state and the shell structure. However, being an independent-particle model, it does not correctly describe the microscopic contribution to the binding energy.

Thus, even today, many fission barrier calculations begin by determining the deformation energy with the LDM technique and the influence of shells are taken into account in a second step. The application of this procedure then requires to have liquid drop type models as realistic as possible: this is the main reason to this surprising effort to develop other models based on the

LDM.

V.M. Strutinsky [22] first suggested in 1968 a method to combine the macroscopic liquid drop contribution to the binding energy with the microscopic contribution of the independent-particle model. Beginning with an independent particle model the total energy is obtained by summing over the energies of the occupied single-particle states

$$\begin{aligned} E(\beta) &= \sum_{i=0}^{Z} \varepsilon_i^p(\beta) + \sum_{i=0}^{N} \varepsilon_i^n(\beta) \\ &= E_p(\beta) + E_n(\beta) \end{aligned}$$

where $\varepsilon_i^p(\beta)$ and $\varepsilon_i^n(\beta)$ are deformation-dependent proton and neutron single-particle energies. From the proton and the neutron contributions to the total energy, V.M. Strutinsky subtracted average energies $\bar{E}_i^p(\beta)$ and $\bar{E}_i^n(\beta)$ calculated using occupations, n_i^p and n_i^n, that average over the proton and neutron shell structure,

$$\bar{E}_i^n(\beta) = \sum_{i=0}^{Z} \varepsilon_i^p(\beta) n_i^p \qquad \bar{E}_i^n(\beta) = \sum_{i=0}^{N} \varepsilon_i^n(\beta) n_i^n \tag{1.6}$$

to obtain the shell correction energies,

$$\delta E_p(Z,\beta) = E_p(\beta) - \bar{E}_i^p(\beta) \qquad \delta E_n(N,\beta) = E_n(\beta) - \bar{E}_i^n(\beta) \tag{1.7}$$

In principle, the shell correction energies include only the fluctuating microscopic contribution to the binding energy. Then V.M. Strutinsky computed the total binding energy as the sum of the liquid drop energy and the shell correction terms,

$$E(N,Z,\beta) = E(N,Z,\beta)_{LDM} + \delta E_n(N,\beta) + \delta E_p(Z,\beta) \tag{1.8}$$

The shell correction method provides a substantial improvement in the description of the fission barrier compared to the liquid drop model :

1. it provides ground state deformations in good agreement with the experimental ones
2. it produces a double-humped barrier in the region of the actinides, which explains the existence of fission isomers as shape isomers-configurations of single nuclear species with very different deformations
3. it yields quantitative agreement with experimental fission barrier heights, usually within 1 to 2 MeV (except for light, neutron-poor actinides)
4. it produces an outer barrier that is slightly lower for asymmetric deformation, explaining the preference for an asymmetric mass division observed experimentally
5. it predicts the existence of stable superheavy elements with a charge between Z=114 and Z=126. Nowadays elements up to Z=118 have been proved to exist with lifetimes of ms.

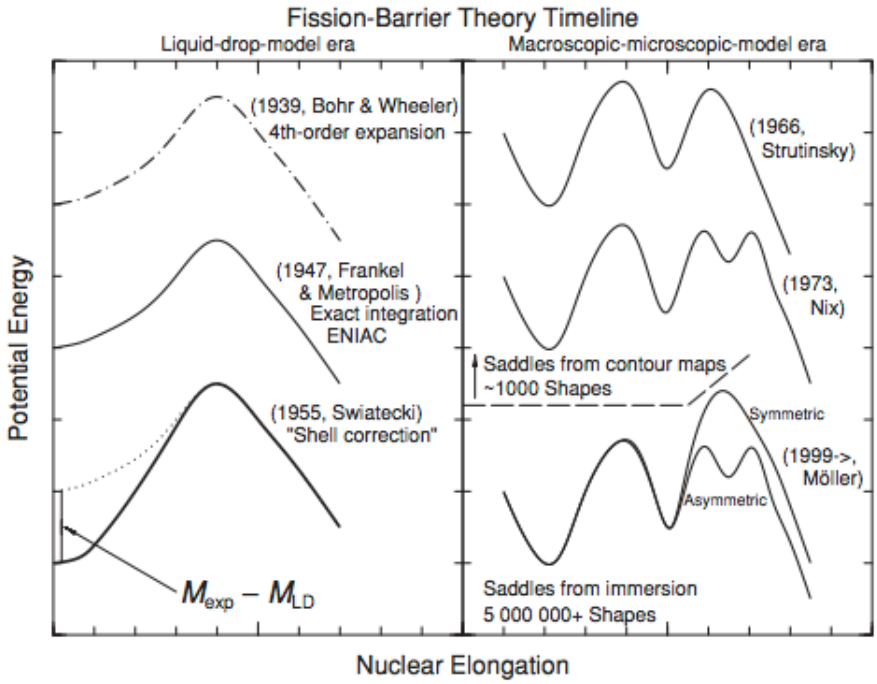

Figure 1.4: Historical development of the fission-barrier theory [23].

The V.M. Strutinsky shell correction method thus provides a quantitative description for most of the characteristics of the fission barrier. A theoretical picture of the history of the fission potential energy is schematically illustrated in fig.1.4 starting from the first model developed by N. Bohr and J. Wheeler that, as explained before, expanded the Coulomb and surface energies to the fourth order in α_4 of Legendre polynomials. In 1947 S. Frankel and N. Metropolis [24] calculated the Coulomb and surface energies of more highly deformed nuclear shapes using numerical integration. In 1955, W.J. Swiatecki [25] suggested that more realistic fission barriers could be obtained by adding a "correction energy" to the LDM barrier. This correction was calculated as the difference between the experimentally observed nuclear ground state mass and the mass given by the LDM. W.J. Swiatecki obtained improved theoretical results for the calculation of the spontaneous fission half lives based on these "modified" LDM barriers. The W.J. Swiatecki observations put the basis for the V.M. Strutinsky [22] shell-correction method. His method and in parallel new experimental results led to realise that the actinide fission barriers are "double-humped": beyond the ground state minimum there are two saddles or maxima in the fission barrier, separated by a fission-isomeric second minimum. Later, P. Möller and R.J. Nix [26] proposed that certain experimental data could best be explained if the outer barrier peak was split into two peaks separated by a shallow third minimum. To obtain a realistic picture of the

potential energy, P. Möller [23] calculated the energy for several millions of different shapes and identified relevant saddle points on the paths from the nuclear ground state to the separated fission fragments.

1.2 Neutron emission in fission

The first point to be investigated in a nuclear disintegration is the available energy. The division of a heavy nucleus into two daughter nuclei of comparable masses is a highly exoenergetic process, thus the sum of the total binding energies of the daughter nuclei is greater than the mother nucleus one. This means that the final products are more bound than the initial one. More bound means that the amount of energy released by the mass rearrangement in binary low energy fission, of the order of 180-240MeV, depending on the fissioning system, is shared between the total kinetic energy TKE* of the primary fission fragments and their excitation energy TXE* in the following way: about 75-85% of the total energy is present as kinetic energy and the remaining one is converted into excitation energy. The latter one is the energy which will be mainly released by neutron and γ emission.
In this scenario, attention has to be put on the role played by neutrons to understand the fission mechanism. Studying low energy fission neutron angular distributions, many features of the fission process can be shown, including the possible existence of neutrons emitted right at the scission point in addition to an isotropic evaporation by the fully accelerated fission fragments following V.F. Weisskopf's theory [27]. Neutron correlations are also a powerful tool to point out a possible anisotropy in the evaporation of the prompt neutrons emitted by the fission fragments. This approach was first developed in 1962 by H.R. Bowman *et al.* in his pioneering work [28]. The aim of his experiment was to study the neutron emission mechanisms in the spontaneous fission of ^{252}Cf, involving measurements in coincidence of neutrons and fission fragments. The main conclusion was that about 90% of neutrons arise from simple isotropic evaporation in the centre of mass (CM) of each fragment. But in the experiment some discrepancies appeared in respect with the isotropic emission as shown in fig. 1.5. In this work the main deviations were found perpendicularly and also along to the fission axis. The analysis on the nature of these discrepancies allowed to assert that most of the systematic deviations from the isotropic emission could be due to a third source at rest in the laboratory, namely the emission of scission neutrons. Fig. 1.5, from H.R. Bowman's cited paper, shows the ratio between the calculated and the experimental data for the neutron yields, the average neutron energies and velocities as a function of the angle in the spontaneous fission of ^{252}Cf. A surplus of neutrons appears at 90° as shown on the left part of fig. 1.5. This feature led H.R. Bowman to assume a scission neutron emission. On the right part of fig. 1.5, the same physical quantities are shown after a subtraction of about 10% applied on the fission neutrons has been performed. After this procedure an excess of neutron appears at 0° and 180°. For H.R. Bowman these features seemed to be the mark of an anisotropic evaporation in the CM of the fission fragments. For these neutrons that

seem to be focused along the fission axis H.R. Bowman ventured the hypothesis of a possible anisotropy in the emission of neutrons by the fragments. But, carefully, because of the very small size of the deviations, he also affirmed that such a phenomenon could be due to non identified inhomogeneities of the detection system.

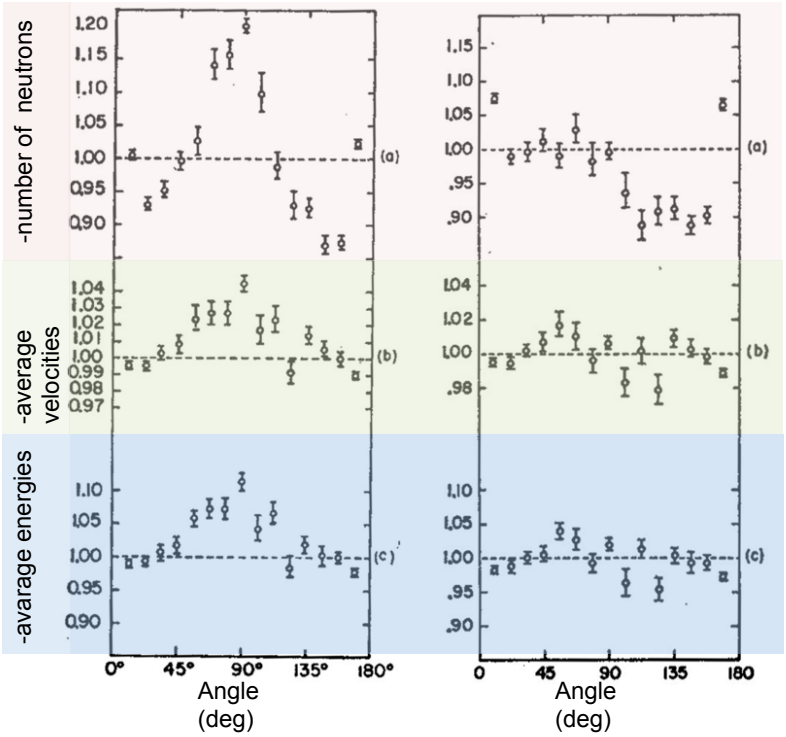

Figure 1.5: Left: Ratio of measured to calculated values for a) numbers of neutrons, b) average velocities and c) average energies as a function of the neutron angles in the laboratory system. The calculated values were obtained by using two sources of neutrons. Right: Same physical quantities after subtraction of about 10% scission neutrons on the fission neutrons. The calculated values were here performed adding a third source with a different temperature. From [28].

1.2.1 Scission neutron models

1.2.1.1 Experimental context

The existing results on scission neutrons are very contradictory. Understanding this point is a central piece to complete the nuclear fission puzzle. Up to now experimental knowledge about the fraction of scission neutrons and their spectrum is scarce and very contradictory. Thus there is a clear need for a more precise picture about this mechanism.

The first evidence of scission neutrons was demonstrated in the already cited work of H.R. Bowman, issued in 1962 [28], who observed an isotropic neutron surplus of about 10% in the lab-

oratory frame. C.B. Franklyn *et al.* [29], in 1978, studied the neutron-fragment (nf) angular correlations of prompt neutrons emitted in the thermal neutron induced fission of ^{235}U in order to see if a similar phenomenon occurred. He performed a simulation with a 20% scission component. But also by adding this huge contribution he noticed that the simulation results were too low in the forward direction and too high at large relative angles between neutrons and the light fragment compared to the experimental data.

Also A.S. Vorobyev, in a work issued thirty years later [30], focused his attention on neutron-

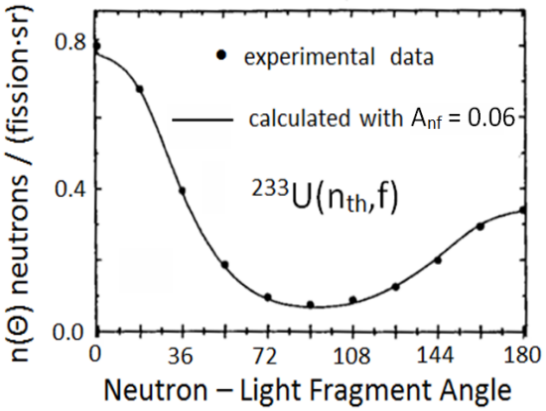

Figure 1.6: Neutron yield as a function of the angle between neutrons and the light fission fragment in the $^{233}U(n_{th}$,f) reaction [30]. The full curve represents a fit obtained with the assumption of a neutron anisotropy (A$_n f$=0.06) and a contribution of scission neutrons of about 5%.

fragment angular correlations in the $^{235}U(n_{th}$,f) reaction, as C.B. Franklyn did. In this recent analysis A.S. Vorobyev assumed also an anisotropic evaporation of the neutrons in the fragment CM systems. The best fit resulting from this work is obtained with 5% of scission neutrons and an anisotropy A$_n f$=0.06, as shown in fig. 1.6.

In other works such as F. Marten's (1989) [31] or C. Budtz-Jørgensen's (1988) [32] experiments, there is no evidence at all for scission neutron emission after the comparison between experiment and theoretical model calculations. But, in a paper dating back to some fifteen years ago, W.V. Kornilov [33] has reanalyzed three independent old experiments on ^{252}Cf(sf) with a more realistic model for the description of the neutron evaporation by the fragments. In all these experiments, the neutron energies and angular distributions relative to the fragment direction were measured. W.V. Kornilov showed that a good agreement exists between these three experiments for a neutron surplus of (30 ± 5)% at about 90° relative to the direction of the moving fragments. These neutrons do not originate from fully accelerated fragments, and would represent about 10% of the total fission neutron yield.

Complementary to studies of neutron-fragment correlation the correlation between two neu-

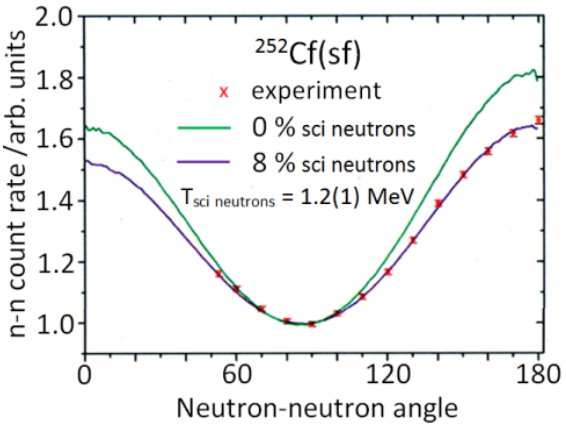

Figure 1.7: Neutron yields as a function of two any neutron relative angles for ^{252}Cf(sf). The data points are given in red. The green curve represents the assumption of no scission neutrons but taking into account neutron anisotropy. In purple the effect of a contribution of scission neutrons of about 8% is shown [34].

trons from a fission event were analyzed.
In 1948 S. DeBenedetti [35] was interested by the investigation of the fission mechanism by means of angular distributions of neutron-neutron coincidences from a source of ^{235}U irradiated with thermal neutrons. Also in this very old work it appeared doubtful that the angular correlations could be explained entirely with the composition of neutron and fragment velocities, without assuming an anisotropy in the emission of neutrons in the fragment's system. In the search for scission neutron emission, A. Gagarski [34] recently analyzed neutron-neutron correlations in the ^{252}Cf(sf) disintegration. Taking also the neutron anisotropy from a theoretical model [36] into account, assuming no scission neutrons at all as shown by the green curve of fig. 1.7 does not reproduce the experimental points. The best agreement was reached for an additional scission neutron contribution of 8% as shown by the purple curve of fig. 1.7.

1.2.1.2 Sudden approximation model

Models, as presented in references [37, 38], predicting the emission of scission neutrons and/or ternary particles stress the importance of the temporal scales for nucleon motion during the fission process. When a cold nucleus undergoes fission, the coupling between the collective evolution (very slow process) and intrinsic motions (fast process) can be either adiabatic, meaning that the nucleons remain in the lowest energy levels, or non-adiabatic when the nucleons are promoted to excited states. In the latter case, the deformation energy accumulated from the saddle to the scission may be converted into intrinsic excitation energy. These mechanisms are mainly governed by the velocity of the collective motion relative to the Fermi velocity.
At the beginning of the descent from saddle to scission, the Coulomb repulsion is almost entirely

compensated by the nuclear attraction. The coupling between the collective and intrinsic motions is therefore weak (quasi-adiabatic): the collective motion is relatively slow and only a few nucleons are excited with increasing deformation of the fissioning nucleus.
Close to scission however this quasi-equilibrium breaks down. The neck between the fragments ruptures and is quickly absorbed by the fragments. The coupling is then non-adiabatic.
In the sudden approximation, an extreme assumption is made: the coupling between the degree of freedom and the rapidly changing interaction potential with the rest of the nucleus is adiabatic until the neck ruptures at a finite radius. The rupture is followed by the sudden absorption of the neck protuberances. At that moment, a transition between two quite different nuclear configurations occurs.

To have an escaping particle at the scission point it is necessary that it is able to acquire the available energy that is released between the fragments. This energy must be stored in a readily convertible form, thus, it is concentrated on very few degrees of freedom.
In the usual picture of fission models most of the energy, appearing as fragment excitation energy,

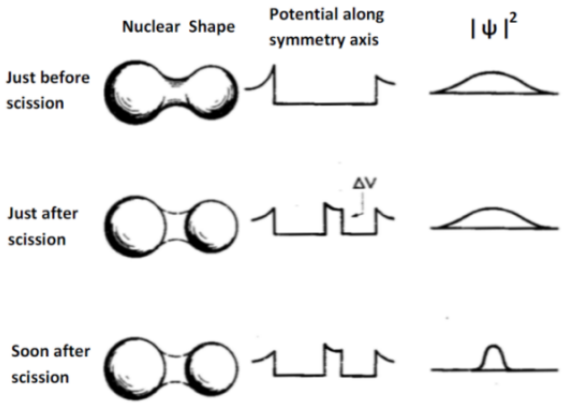

Figure 1.8: Snapshots of the non-adiabatic emission process near scission [37] are shown. The disappearance of the neck results in a rapid change in the potential felt by the neutrons, like a volcano square-well erupting in the potential created by the rest of the nucleus. Part of the neutron wave function is reduced due to the reabsorption by the nuclear matter. The surviving part of the wave function represents a free neutron in the region between the two fragments.

is connected to the distortion energy stored in the collective degrees of freedom at scission (slow motion). In these models, ejecting a third particle is a very rare phenomenon. On the contrary when this excitation energy is related to the degrees of freedom connected to the fragment motion, a third particle can be emitted. The energy transfer to the escaping particle in this elongated fission configuration probably takes place through the sudden snap of the neck after scission. In an extremely short time of about 10^{-22} s, the potential felt by the nucleons located at the scission point suddenly changes as the stubs retract in such a way that those particles can not follow the changes of the potential when the two main fragments start to recede. In this non-

adiabatic process the nucleon wave functions remain unchanged as is shown in fig. 1.8. But soon after scission, the tails of the wave functions inside the fragments are absorbed by the fragments and the neutrons are set free. This sudden release was proposed as an emission mechanism by I. Halpern [37] without a complete mathematical development. A simple schematic mechanism dating back to 1962 of neutron excitation was proposed by R.W. Fuller [39]. He considered the problem of the energy transferred to neutrons as an inverted square-well "volcano" in an infinite square-well containing a Fermi sea of neutrons.

1.2.1.3 Carjan model

The model proposed by N. Carjan is based on the sudden release approximation. The Halpern prescription [37] is developed in a two dimensional model to include realistic nuclear shapes and has been applied to the emission of neutrons during the $^{235}U(n_{th},\mathrm{f})$ reaction. In a first stage, N. Carjan elaborated his model for the symmetric fission [38], a few years later he upgraded his calculation for a more realistic asymmetric fission [40, 41].
To study the characteristics of the scission neutron emission, N. Carjan computed the partial emission probability. This quantity is related to

- the shape evolution of the nuclear surface along the path that leads to fission. A considerable change in the nuclear surface involves an increase of the emission probability.
- the initial position of the neutron. In fact neutrons in initial states with a high probability of presence in the neck are strongly emitted. The probability is very large since they can only expand on final states in the continuum.
- the projection of the angular momentum along the symmetry axis Ω, in the axially symmetric fissioning nucleus case. The deformed potential includes a term expressed as a function of Ω recalling a sort of centrifugal force. This force has the effect to push the neutrons away from the z-axis, far from the neck region.
- bound states near to the fermi level.

Usually it is assumed that the angular distribution of scission neutrons is isotropic. Yet, in view of their initial position in the fissioning nucleus, only neutrons ejected at right angles to the fission axis may have a chance to escape. N. Carjan claims that the reabsorption probability is not negligible. Eigenstates with energies lower than the top of the centrifugal barrier are quasi-bound states and can therefore be considered as still present in the fragments; thus the probability of reabsorption becomes large. N. Carjan states also that with a very low probability also unbound neutrons are present inside the fragments and this component is either reabsorbed or emitted in the direction of the fission axis.
In this first stage of the development of Carjan's model, he stated that for a minimum neck radius of 1.5 fm, 15% of the total amount of neutrons emitted during the symmetric fission of ^{236}U are scission neutrons.

Later in 2010 [38], he improved his model by taking into account the ratio $\frac{A_L}{A_H}$ between the mass of the light (L) and heavy (H) fragments. This new approach is based on the idea that the prompt neutrons contain two components: the scission neutrons and the post-acceleration neutrons. As a result of the upgrade he obtained that 30% of the neutrons emitted are scission neutrons and the energy left to the fragments for the post-acceleration emission is about 50% of the total fragment excitation.

In 2012 [40, 41], N. Carjan computed, in the framework of his sudden approximation model adding a shell model approach, the partition of the excitation energy between the primary fragments at scission. As a result he extracted the temperature at scission as a function of the fragment mass A in the limit of zero reabsorption of the scission neutrons. He found that the ratio $R_T = \frac{T_L}{T_H}$ between the temperature of the light (L) and the heavy (H) fragments is close to 1 for symmetric fission and increases with mass asymmetry.

In a very recent work [42], he finds that up to 100% of the emitted neutrons can be scission neutrons.

1.2.2 Anisotropic neutron emission

As already mentioned before, H.R. Bowman showed in 1962 deviations from a pure isotropic evaporation by the fission fragments in the analysis of spontaneous fission of ^{252}Cf. To bring out the nature of these discrepancies, H.R. Bowman introduced a contribution of 10% of scission neutrons to his calculation. But this third source of neutrons didn't explain all discrepancies observed. The remaining deviations at small angles around the heavy and the light fragments, in H.R. Bowman's opinion, were in favour of an anisotropic emission in the centre of mass of the fission fragments. Because of the weakness of the effect and of the experimental uncertainties H.R. Bowman didn't clarify the nature of this deviation.
Other authors studied these departures from the isotropic hypothesis and the main conclusion was that such deviations originate from the sizable angular momenta J carried by the fission fragments. On average the angular momentum is about $\langle J \rangle \approx 8\hbar$. Intuitively this should lead to an anisotropic neutron emission in the CMs of the fragments. In this scenario neutrons evaporated from such a rotating nucleus will preferentially be emitted in the equatorial plane perpendicular to the angular momentum. For a fixed spin direction, the angular distribution of neutron emission in the CMs is described by :

$$W(\theta_{\mathrm{nJ}}) \propto 1 + A_{\mathrm{nJ}} sin^2\theta_{\mathrm{nJ}} \tag{1.9}$$

where $A_{\mathrm{nJ}} = \frac{W(90°)}{W(0°)} - 1$ is the anisotropic coefficient with respect to neutron and spin directions and θ_{nJ} is the neutron ejection angle with respect to the spin direction J. In fission the spins of fragments are perpendicular to the fission axis. Averaging over all spin orientations perpendicular to the fission axis, an anisotropy for neutrons emerges favoring emission along the fission axis.

This distribution can be written as

$$W(\theta_{\mathrm{nLF}}) \propto 1 + A_{\mathrm{nLF}} cos^2\theta_{\mathrm{nLF}} \tag{1.10}$$

where θ_{nLF} is the angle between neutrons and the light fragment (LF). The anisotropy is $A_{\mathrm{nLF}} = \dfrac{W(0°)}{W(90°)} - 1$.

The theory of anisotropic emission was proposed first by A. Gavron [43] in 1976. He developed a statistical model in which the probability P_{lm} to emit a neutron with a given orbital angular momentum l and its projection m relative to the fragment spin depends on the fragment's level density and on the neutron transmission coefficient. In his model, the evaporation cascade is computed by means of a Monte-Carlo procedure in which the probability P_{lm} is proportional to the sum over all values of final fragment spins J_f. In his calculation the angular momentum J and its projection on the fission axis M are calculated at each stage of the neutron cascade. At the beginning, the initial spin projection on the primary fragment is assumed to be zero ($M = 0$) as a consequence of the hypothesis that the initial fragment's spin is perpendicular to the fission axis. A more recent model was developed by V. Bunakov and I. Guseva in 2006 [36] following

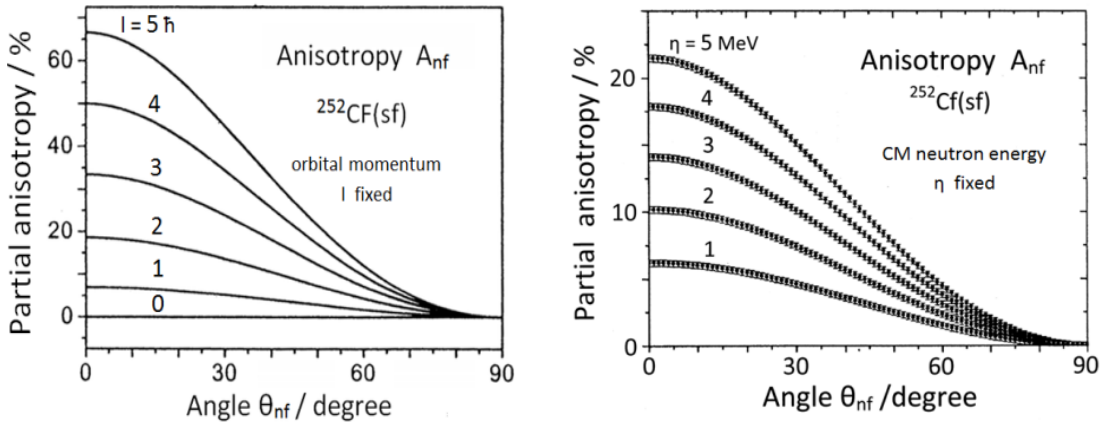

((a)) ((b))

Figure 1.9: (a) Dependence of angular anisotropy in the CMs on the orbital momentum l of evaporated neutrons. (b) Anisotropy coefficient dependence in respect to neutron energy. From [36].

A. Gavron's prescription. As shown in fig. 1.9(a), they demonstrated that the anisotropy depends markedly on the size of the orbital momentum l of the evaporated neutron, the anisotropy increasing with orbital momentum l. As the orbital momentum l is correlated to the neutron energy η, the anisotropy increases also with increasing neutron energy as shown in fig. 1.9(b). V. Bunakov and I. Guseva also showed the influence of the CM neutron energy on the anisotropy A_{nJ} (fig. 1.10(a)). According to this model the anisotropy gets larger as the CM neutron energy η rises. For comparison the η-spectrum is also plotted in fig. 1.10(a). One has to notice that, for

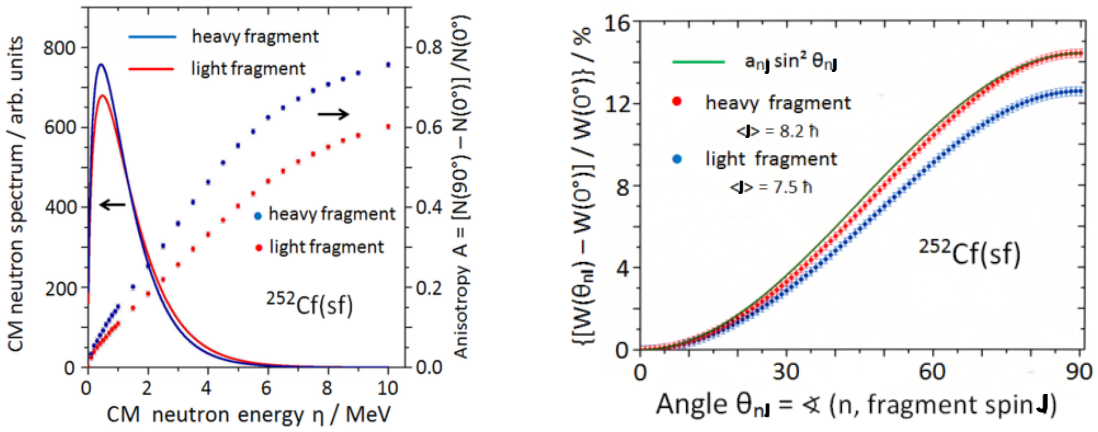

((a)) ((b))

Figure 1.10: (a) Anisotropy coefficient as a function of the CM neutron energy η for the heavy and the light fragments. In the range of η between [0, 2] MeV where the most probable values of neutrons energy are located, the anisotropy coefficient grows linearly with energy and reaches a rather small value of about ~ 0.30 for the heavy fragment. (b) Anisotropy coefficient as a function of the angle between neutrons and the fragment spin is plotted. The anisotropy grows with the growth of the value of the spin J. In fact the greater anisotropic value found for the heavy fragment is accounted to the bigger spin value of the latter one respect to the light fragment. From [36, 44].

the η energies in low energy fission, only rather small anisotropies $W(\theta_{\mathrm{nLF}})$ are to be expected. Finally the angular distribution $W(\theta_{\mathrm{nJ}})$ of neutrons relative to spin in the CM of light and heavy fragments is shown in fig. 1.10(b). Only the angle dependent term $A_{\mathrm{nJ}} sin^2\theta_{\mathrm{nJ}}$ is plotted. The functional form $sin^2\theta_{\mathrm{nJ}}$ is well reproduced. In fig. 1.10(a) and fig. 1.10(b) is also shown the relation between anisotropy A_{nJ} and the fragment spin J, which is different for light and heavy fragments. In fact the anisotropy gets larger for bigger values of the fragment spin J.

1.2.3 Importance of the analysis method

The results regarding the scission neutron emission and the anisotropic evaporation are strongly dependent on how the experiment was performed and on the processing method chosen to analyze the experimental data. To underline the veracity of this statement an example is proposed in the following.

I. Guseva [45] investigated the above mentioned work of C. Budtz-Jørgensen and H. Knitter [32],who deduced the neutron spectrum in the CM system of fission fragments by the determination of all kinematic parameters of the reaction. I. Guseva stressed the choice of the author to proceed in analysing the data with a simplification: neutron emission in the fragment CM

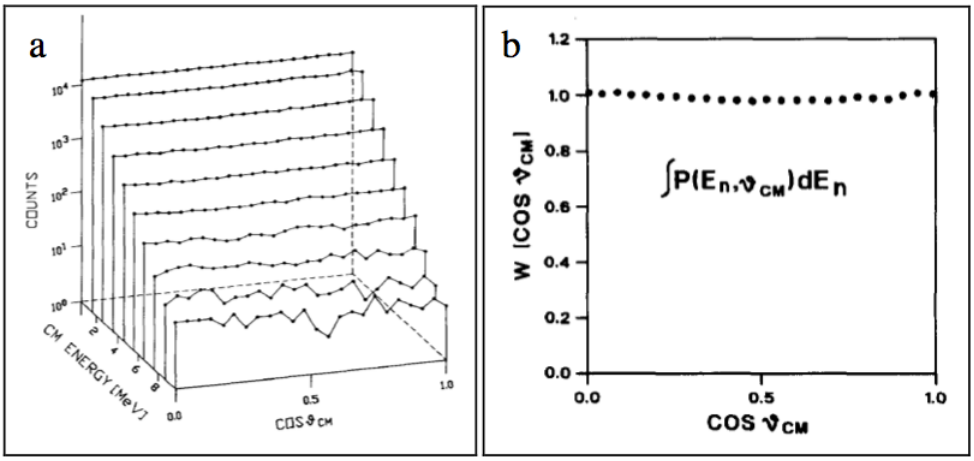

Figure 1.11: (a) Fission neutron angular distribution as a function of the fragment centre of mass and the fission neutron energy; (b) Fission neutron angular distribution in the same frame integrated over all neutron energies.

system is symmetric at about 90°. Thus the analysis could be restricted to the case:

$$0^\circ \leq \theta_{CM} \leq 90^\circ \tag{1.11}$$

where θ_{CM} represents the neutron emission angle relative to the fission axis in the fission fragment CMs. Selecting these events the authors obtained the neutron angular distribution presented in fig. 1.11. This figure shows the energy and angular distributions of neutrons in the fragment CM system using an average fragment mass value. This had to be done because no light and heavy separation was possible in the experiment. However C. Budtz-Jørgensen and H. Knitter came to the conclusion that the major part of the neutrons is emitted isotropically from the fully accelerated fragments and that the influence of a scission component is negligibly small up to 10 MeV neutron energy in the fragment CM system (see fig. 1.11).
Using the C. Budtz-Jørgensen assumption I. Guseva performed a Monte-Carlo calculation to reproduce the above cited method, considering also the contribution of scission neutrons. The central questions of her work were: "What kind of distributions would the authors of this article get in this case? Could they distinguish with the help of their method the scission neutrons from the neutrons emitted by the moving fragments?
She states that a sizable part of scission neutrons close to 90° will have an insufficient velocity to match with eq. 1.11 and will be ignored as shown in fig. 1.12. Curve 2 of the left figure represents all scission neutron events lost in view of the condition 1.11. The answers to I. Guseva's questions are plotted in fig. 1.12. Curve 5 reproduces very nicely the C. Budtz-Jørgensen's plot of fig. 1.11. This result led I. Guseva to assert that the above cited procedure reduces the sensitivity of the analysis to the scission neutrons because C. Budtz-Jørgensen eliminated a significant part of them. Moreover she stated that C. Budtz-Jørgensen's paper underestimates not only the

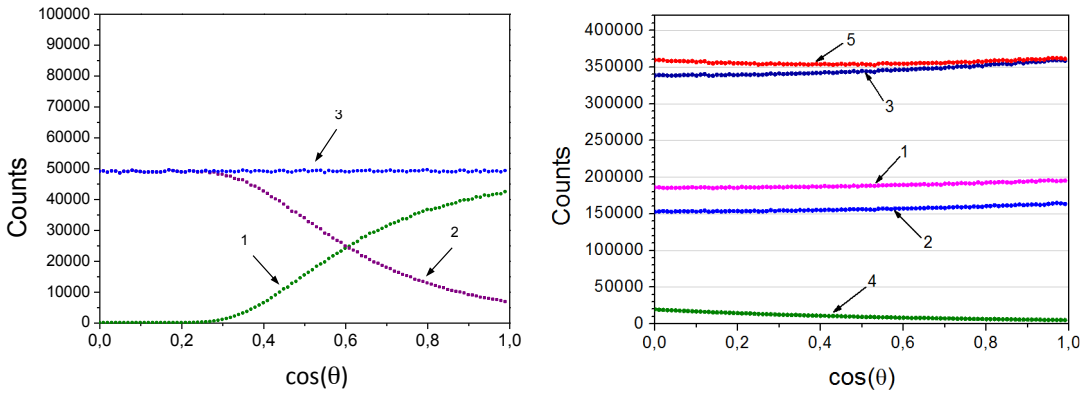

Figure 1.12: Left: Neutron angular yields in the laboratory system - scission neutrons overview: 1: scission component satisfying condition 1.11; 2: scission neutrons which do not match with the condition 1.11; 3: all simulated scission neutrons. Right: Neutron angular yields in the fragment CM: 1,2: neutron emission from forward side of the light and heavy fragments, respectively; 3: sum of the two contributions; 4: scission component satisfying condition 1.11; 5: total amount.

contribution of the scission, but also the anisotropy of the neutron emission in the fragment CM system (curves 1, 2 , 3 of fig. 1.12), because this effect could somehow compensate the scission neutron component (curve 4 of fig. 1.12 b)) .

1.3 A new technique to determine the CM anisotropy

The neutron-neutron and neutron-fragment correlations do not allow to determine unambiguously the relative contributions of scission neutrons and anisotropic neutron evaporation. The CORA collaboration suggested therefore a novel method to determine, in an independent way, the anisotropy of neutrons evaporated in the fragment CM systems [46, 47, 48] . This new method is based on the following considerations. Due to the velocity of the fission fragments (FF), when converting the neutron emission from their CM to the laboratory system, their angular distributions present an enhancement at 0° and 180°, well known as the *kinematical focusing* as appears on fig. 1.13 (a)) for the ^{235}U(n_{th},f) reaction. As shown in fig. 1.13(c), the CM anisotropy reinforces the kinematical anisotropy. The difficulty is to disentangle the real anisotropy from the kinematical focusing as the effect is quite weak. One has to point out that in the calculations presented in fig. 1.13 any contribution by scission neutrons was neglected. The novel approach is based on the measurement of triple or more coincidences between one fission fragment and two or more neutrons. The principle is best explained for very large anisotropies $A_{nJ} \to \infty$. In this extreme case:

- all neutrons are emitted in a plane perpendicular to the fragment spin J;
- it is further taken into account that the spin J is perpendicular to the fission axis.

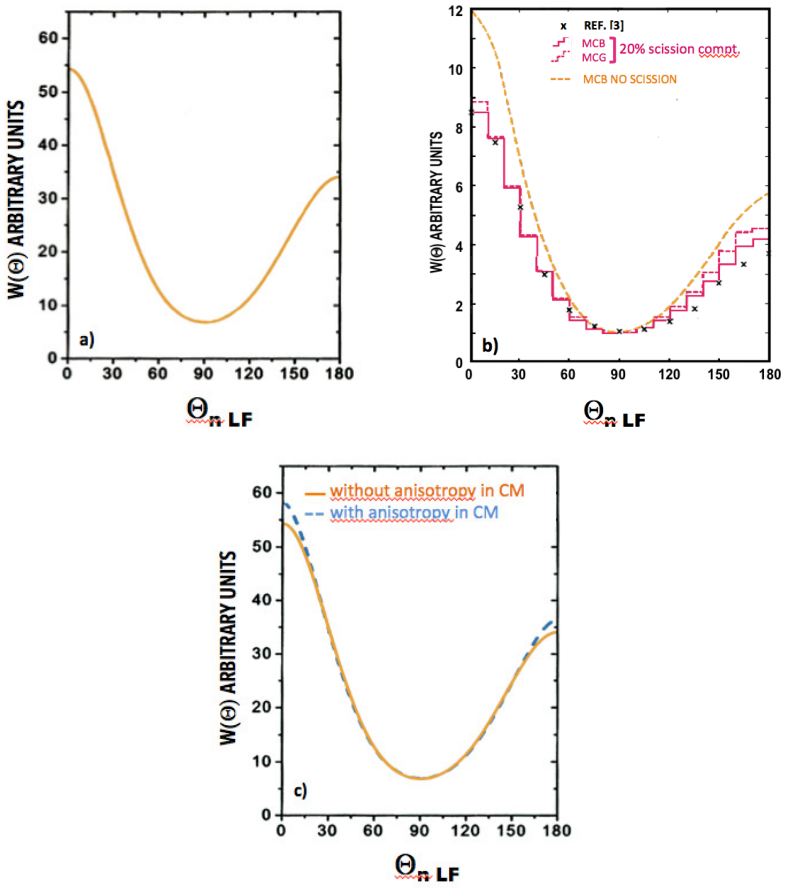

Figure 1.13: Neutron angular distributions as a function of the angle between neutrons and the light fragment (LF). The kinematical focusing (a), the effect of the scission neutrons [29] (b, solid curve) and of the dynamical anisotropy [36] (c, dashed curve) are shown.

As sketched on top of fig. 1.14, for the spin J pointing along the y-axis and projecting the neutrons on a plane perpendicular to the fission axis (the z-axis):

- all neutrons will be aligned along the x-axis;
- these neutron projections follow the spin orientation.

In the experiment the orientation of the fragment spin cannot be fixed, only the fission axis is accessible. As the fragment spins are perpendicular to the fission axis, all fragment spins will lie in a plane perpendicular to the fission axis. In fig. 1.14, this is the (x, y) plane. For any inclination of the spin in the (x, y) plane, the neutrons projected on a line will then follow the inclination of spin. To any spin orientation hence corresponds a neutron projection line. The fragment spins are distributed isotropically in the (x, y) plane. Their orientation in this plane can not be determined. Neutrons emitted from both fission fragments participate and as the

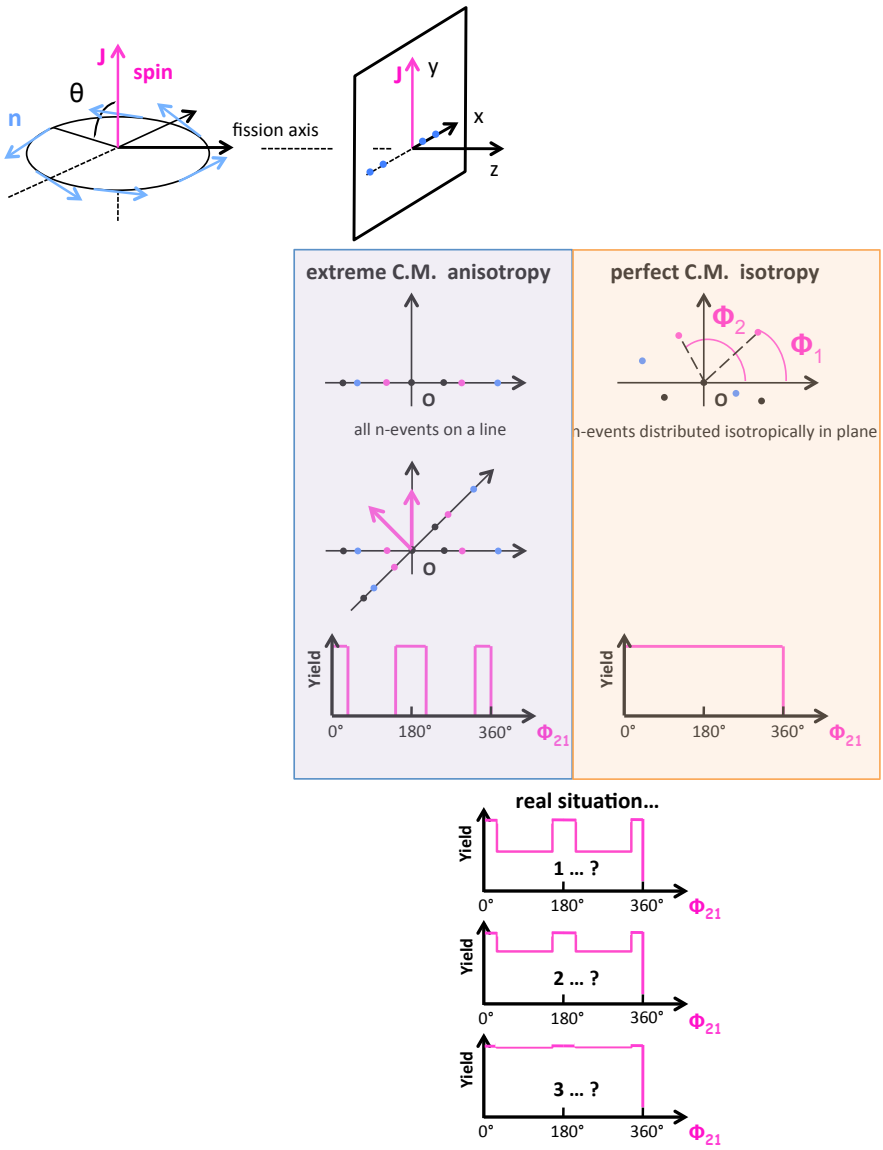

Figure 1.14: Extreme anisotropy in the CMs: all neutrons are emitted in a plane perpendicular to the spin (top). Projection plane (x,y): the projection lines follows the inclination of the spin orientations compared to the random distribution in the perfect isotropy case. Azimuthal angle difference, ϕ_{21}, in both extreme cases. The two extreme cases are detailed in the text.

spins of the complementary fragments are antiparallel all neutrons are emitted in the same plane (x, z).

For each triple (n_1, n_2, FF) or more event the azimuthal angles ϕ_1 and ϕ_2 relative to the x-axis are determined. The crucial parameter is the difference of these two angles:

$$\phi_{21} = \phi_2 - \phi_1 \tag{1.12}$$

Thus in case of extreme anisotropy all the ϕ_{21} angles between two any neutrons are expected to be 0°, 180° or 360° depending on the neutron emission side in respect with the x-axis. Since in ^{252}Cf(sf) the spins of complementary fragments are antiparallel, both fragments contribute to the pattern. In fig. 1.14 this extreme anisotropic case is compared to a perfect isotropic emission case where the neutrons are randomly spread over the (x,y) plane. This case will lead to a flat ϕ_{21} distribution.
The real distribution will be in between these two extreme cases. Our expectation is that the effect is important enough to be extractable as sketched in fig. 1.14 in the very optimistic case 1, or the more probable case 2 of fig. 1.14. The bad situation would be case 3. It has to be stressed that both, the kinematic anisotropy pointed out by H.R. Bowman and the emission pattern of scission neutrons, which is symmetric around the fission axis, will not give rise to anisotropies in the projection plane. Any structure in the distribution of ϕ_{21} is hence uniquely due to the dynamical anisotropy.

1.4 CORA experiment

In the past a great effort has been dedicated to study CM anisotropy for γ emission [49]. Indeed the spin dependence of the CM anisotropy is much more pronounced in this case. Neutron anisotropy is more tricky to determine. Up to now, the existence of scission neutron emission and/or CM anisotropy were deduced either from angular distributions between fragments and neutrons or from angular distributions between two emitted neutrons. But, as shown on fig. 1.16, the two effects appear at the angular region where they reinforce the kinematical focusing. The two effects act the opposite way: anisotropy increases slightly the focusing whereas scission neutron emission decreases it. This renders the identification and the determination of the relative importance of these two contributions very difficult if not impossible.
The CORA experiment which is the subject of this work was initially undertaken to demonstrate the existence of the CMs anisotropy applying the new approach presented above. One has to be aware that the major advantage of this new approach is that it allows to determine the CM anisotropy independently from the scission emission one. We will see in the following chapter that in fact the geometry of the neutron multidetector DEMON adopted in the experiment gives access simultaneously, for the first time, to both the CMs anisotropy and the scission neutron emission.
In fact to reach this purpose three experimental configurations have been tested as shown in fig 1.15. The first experiment was realised with a wall configuration of DEMON. In the second one the DEMON cells were arranged on two curved walls. The more optimized one was centreed with the near-spherical DEMON configuration of fig. 1.15 employed in CORA 3 experiment.
Thus in this work, we will have the opportunity to investigate for the first time, simultaneously three angular distributions: θ_{nLF}, θ_{nn} and ϕ_{21} where

– θ_{nLF} is the relative angle between the light fragment and any neutron emitted in coincidence

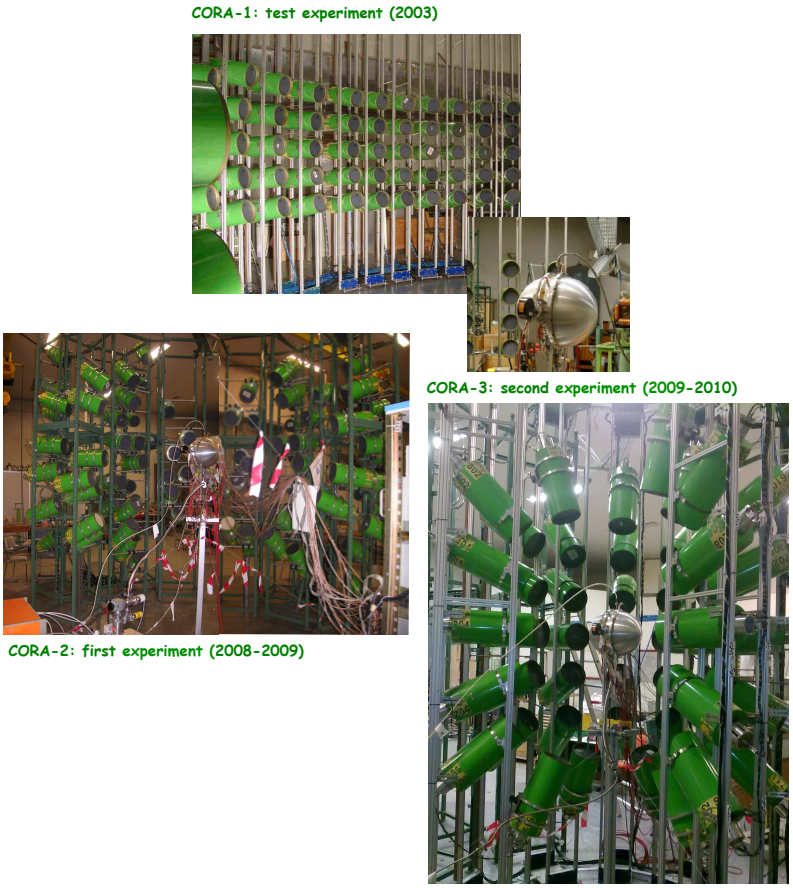

Figure 1.15: The three DEMON configurations are shown. In CORA-1 a wall configuration is used. This experiment represents a preliminary test to demonstrate the existence of the CMs anisotropy; CORA-2: two curved wall arrangements of the detector. The detectors appear shifted respect to each other. This configuration was optimized to avoid the cross talk effect, but the shifted arrangement could have induced neutron scattering on the mechanical supports. To avoid scattering for CORA-3 experiment a near-spherical configuration was preferred.

- θ_{nn} is the relative angle between any two neutrons emitted in a fission event
- ϕ_{21} (called $\phi_{nn|_{LF}}$ from now on) is the azimuthal angle difference between any two neutrons as presented above.

The expected behaviour of the θ_{nLF} distribution is shown in fig. 1.16. The expected behaviour is compared to the pure isotropic case. One can notice that the effects, CM anisotropy and scission neutron emission, affect this distribution mainly around 0° and 180°. Moreover the two effects act in the opposite way: slight increase of the yield for the anisotropy, decrease for the scission emission.

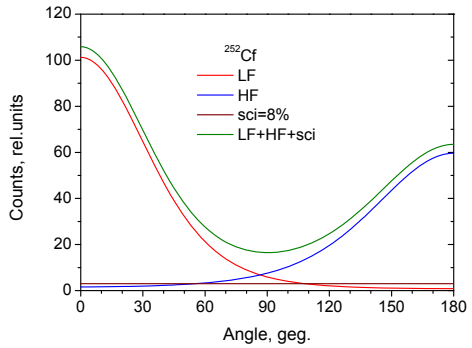

((a))

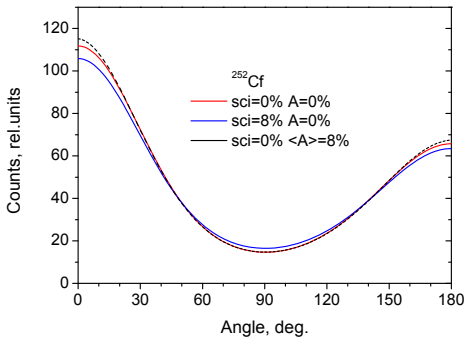

((b))

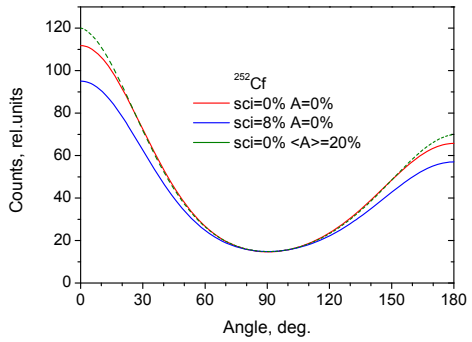

((c))

Figure 1.16: The θ_{nLF} distributions are presented. (a) The brown flat line represents the relative angle between the light fragment (LF) and any scission neutron emitted in coincidence for a scission neutron contribution of 8%; the red curve includes only neutrons emitted from the LF; the blue one only neutrons emitted by the HF. The green curve is the sum of all these contributions. (b) and (c) represent the relative angle between the LF and any neutron emitted in coincidence. The red line represents the isotropic case. A scission neutron component of about 8% is added (blue curve) and also two different anisotropy values are considered respectively equal to $A_{\mathrm{nJ}} = 0.08$ and $A_{\mathrm{nJ}} = 0.20$ (dotted black and green curves). The scission neutron effect is more important on θ_{nLF} in respect to the one ascribed to the anisotropic emission. These two effects appear in the same angular region and act in the opposite sense: the scission neutron component decreases the kinematical focussing whereas the anisotropic emission increases it. From [50].

Chapter 2

Experimental Set-up

One of the main advantages of neutrons as a material probe is their high penetration power which is due to their neutral electrical charge. For the same reason they are very difficult to detect. Mechanisms for detecting neutrons in matter are based on indirect methods. Because of their neutrality they do not interact directly with electrons or electrical charges of nuclei in matter, as gammas do. The process of neutron detection begins when neutrons, interacting with various nuclei, initiate the release of one or more charged particles. The electrical signal produced by the charged particles can then be processed by the detection system. Moreover, in a nuclear reaction neutrons are often the first emitted particles and, besides gammas, sometimes the only ones at low energy. So they reveal the first moments of the history of reactions and offer the best possibility to understand the mechanisms. To investigate the properties of the emitting process one not only has to detect neutrons but for timing purposes also devices are needed providing a fast response. Liquid organic scintillators are generally used in this kind of application because of their fast response and modest cost.

For nuclear modeling the investigation of prompt fission neutron emission in fission is of particular importance for understanding the fission process. But the properties of prompt fission neutrons are not only related to the emission process, they also depend on the properties of the fission fragments emitting neutrons. In view of the fact that both, neutron and fission fragment properties are necessary to study the fission mechanisms we have to detect both, neutrons and fragments.
As a convenient way to study prompt fission neutron emission in spontaneous fission, in the present CORA experiment 60 DEMON cells for detecting neutrons have been mounted, as shown in fig. 2.1, on the surface of a sphere facing a twin back-to-back ionisation chamber at the centre of the sphere called CODIS. In CODIS, two ionisation chambers sharing a common cathode serve to detect the two complementary fission fragments.

Figure 2.1: Experimental set-up: 60 DEMON cells are arranged on the surface of a sphere intercepting neutrons. The CODIS fission chamber is mounted at the centre of the sphere.

2.1 CODIS

Ionisation chambers offer attractive features for detecting fission fragments. First of all, gaseous detection media are generally preferred in the measurement of heavy ionising particles like fission fragments, because of the high ionisation density involved in the slowing down process. At high charge densities electrons and positive ions may recombine and be lost for detection. Another attractive characteristic is that they can be constructed in a large variety of geometries. To allow in the CORA experiment for high fragment-neutron coincidence rates with DEMON, the ionisation chamber CODIS with its large solid angle aperture was chosen. CODIS is a novel type of 4π twin ionisation chamber which, in addition to high efficiency, permits measuring fragment emission angles. With a conventional twin ionisation chamber (IC) only the theta angle between fission axis and chamber axis can be determined. Hence, measuring angular correlations with fission neutrons, only fragments emitted in a small cone around the chamber axis can be used.

2.1.1 Ionisation chamber: general features

Ionisation chambers are based on the production of ions by ionisation when a charged particle passes through a gaseous medium. These devices contain a dedicated gas between two parallel plate electrodes biased with opposite polarities. Incident charged particles produce ionised gas molecules and free electrons along their track of deceleration, named electron-ion pairs. Due to

the presence of an electric field the electrons drift to the positive electrode (anode) while the ions move to the negative electrode (cathode). Ionisation chambers are operated at relatively low voltages between anode and cathode, which results in a collection of only the charges produced in primary ionisations. Compared to proportional chambers with "gas amplification" due to secondary ionisations this type of detector produces a relatively small output signal that corresponds to the number of primary ionisation events. It turns out that the number of produced electrons and ions, to a high degree of accuracy, depends linearly on the energy the particle has lost in the gas volume of the chamber.
This holds true for a wide range of projectile types and velocities. The linear response of a gas-filled ionisation chamber means that there is a fixed mean energy, usually denoted as the W value, required to create one electron-ion pair. The deposited energy E will be proportional to the number of pairs formed n_0 , as in the formula:

$$E = n_0 W \tag{2.1}$$

The W value amounts to about 30 eV for the commonly used counting gases. According to [51] only about 60% of E goes into ionisation, the remaining 40% being consumed by excitation processes and converted into heat. As empirical studies have shown, W is almost independent of the particle's species and energy.

2.1.2 Parallel-plate ionisation chamber

The simplest type of ionisation chamber, the parallel-plate ionisation chamber, consists of two parallel planar electrodes biased with opposite polarities located in the gas atmosphere. Basically two important parameters of a charged particle can be determined in an ionisation chamber:

- the total kinetic energy E , provided the particle is stopped in the chamber;
- the nuclear charge Z, by measuring besides the energy E the energy ΔE the particle has lost on a certain path length Δx.

In an electric field E the positive gas ions and the electrons will move from their point of origin towards the respective electrodes. Their drift velocity v can be found from formula 2.2:

$$v = \mu \frac{E}{p} \tag{2.2}$$

with v the drift velocity, μ the mobility of the particle, E the strength of the electric field and p the gas pressure.

The mean value of the mobility μ of ions in gases lies between 1.0-1.5 $10^4 \frac{m^2\ atm}{V\ s}$. The resulting collection time is of the order of 10 ms. For electrons their smaller mass allows for a higher acceleration between interactions with gas molecules. Therefore their mobility is larger by a factor of 1000. Accordingly their collection time has the order of magnitude of microseconds instead of milliseconds. In most cases the drift velocity increases for higher values of $^E/_P$.

In a parallel-plate ionisation chamber the electrons and ions created through ionisation along the particle track separate by their drift towards the anode and cathode, respectively, where they finally compensate the charges induced on the electrodes. As already outlined, the number of collected charges should be proportional to the energy of the incident radiation. Besides of energy losses in the source material and backing, or in the entrance window in case of external sources, there are some other processes that are affecting proper collection of the charges giving rise to the so called pulse-height defect. The defect is assessed by comparing the pulse height for light and heavy ions of the same energy. The magnitude of the deficit increases with ion mass. In particular for gases with heavy constituents like Ar, Kr etc. the defect becomes sizable. Besides columnar recombination of electrons and positive ions along the particle track of heavily ionising particles, electro-negative gases may trap electrons. In practice, these processes can be minimised by choosing a high enough electric field strength and an as low as possible gas pressure. Furthermore non-ionising collisions between incoming ions and atoms of the counting gas contribute to the electronic pulse height defect.
In a parallel-plate ionisation chamber electronic chains connected to the electrodes see charges being complementary in sign to the charges induced on the electrodes by the formation and drift of both, electrons and ionic charges in the active gas volume. By ionistion positive ionic charges Q^+ and negative electron charges Q^- are created which compensate each other to nil: $Q^+ + Q^- = 0$. In practice the fact is exploited that electron drift times are by a factor of 1000 times faster than those of ions. For this reason the charge signals are measured at a time when all electrons have been collected. This can be achieved by a proper setting of the RC time constants of the order of μs in the electronic amplifier chains connected to the electrodes. For a chamber with the distance between anode and cathode called d and for a point-like ionisation event at a distance x from the cathode, the charge signal Q_A on the anode when all electrons have been removed is:

$$Q_A = Q^- + Q^+\frac{x}{d} = -Q\left(1 - \frac{x}{d}\right) \tag{2.3}$$

with $Q = Q^+ = |Q^-|$. On the cathode the charge Q_C when all electrons have been collected on the anode is:

$$Q_C = Q^+\left(1 - \frac{x}{d}\right) = +Q\left(1 - \frac{x}{d}\right) \tag{2.4}$$

In figs. 2.2 and 2.3 the pulse formation on the anode and the cathode is visualise as a function of time between the start of the ionising event and the time of accumulation of all electrons. In this time window the ions stay virtually stationary. In experiment the point-like charges assumed may be identified as the centres of gravity of charge density along the ion track in the gas.
Both from eqs. 2.3 and 2.4 and figs. 2.2 and 2.3 it is borne out that the charges to be observed on the electrodes at the time when all electrons have been collected depend on the position x of the ions still present in the gas volume. The positions x being in general unknown, the electron signals are not suited for particle spectroscopy. To find the full number n_0 of ion-electron pairs in eq. 2.1, which is proportional to the energy E it lost in the gas, one has to wait until also all ions n_0 have arrived at the cathode where x = 0. However, the long times of several ms involved

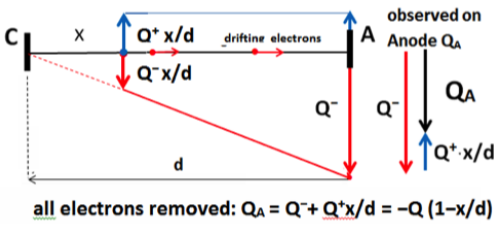

Figure 2.2: Charge signal as a function of time on the anode: from the start when the incoming ion is stopped until all electrons have arrived at the anode. From [52].

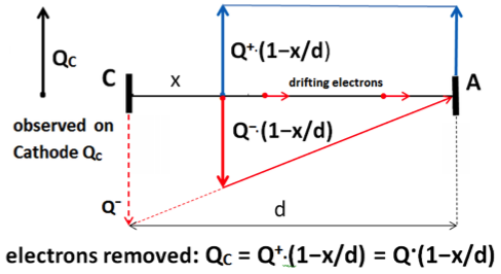

Figure 2.3: Charge signal as a function of time on the cathode: from the start when the incoming ion is stopped until all electrons have arrived at the anode. From [52].

are not convenient for particle spectroscopy.

2.1.3 The Frisch grid

To avoid the difficulties discussed for particle spectroscopy with ionisation chambers it was proposed by O.R. Frisch to install in the chamber a third electrode between anode and cathode. This electrode has to be transparent to charges moving in the chamber. It is in fact a mesh of thin metallic wires called Frisch grid. The grid is held at an intermediate potential between anode and cathode. It is in particular shielding the anode from the influence of the cathode potential. If now the incident radiation is only allowed to enter and produce ionisation in the cathode-grid volume, the anode will not sense any charges as long as all ion-electron pairs are inside the cathode-grid volume. Only once the electrons have traversed the grid the charge influenced on the anode will start to rise. Layout and pulse formation in a gridded ionisation chamber are sketched in fig. 2.4. In this way the slow rise contribution due to the drift of the ions is eliminated and each electron passes through the same grid potential difference and contributes equally to the signal pulse [53]. As a results the pulse amplitude is independent of the position of the original particle interaction and it is simply proportional to the total number of pairs n_0 formed along the track of the incident particle.

In practice however, the shielding of the anode by the grid is never as perfect as assumed in fig. 2.4. Already in 1949 O. Buneman *et al.* [54] calculated the efficiency of grids as a function

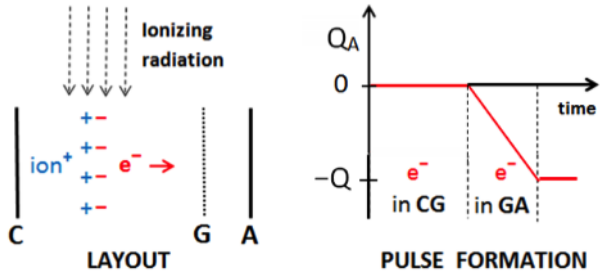

Figure 2.4: Gridded ionisation chamber. In the layout to the left it is emphasised that ionising radiation enters only the cathode-grid volume CG. To the right the formation of the anode pulse is suppressed as long as the electrons are in the CG volume. Only once the electrons traverse the grid the anode pulse starts to rise and reaches its full height $Q_A = -Q$ corresponding to the full number n_0 of electrons created in the ionisation process. From [52].

of the diameters of the wires and the pitch. It was found that typically the inefficiency of grids σ is a few percent. The authors further calculated the bias having to be applied to the grid in order to ensure that no electrons are trapped by the grid. As visualised in fig. 2.5, the formation of the anode pulse taking grid inefficiency σ into account is somewhat more complicated than in the case of an ideal grid with $\sigma = 0$ as in fig. 2.4.

The anode signal Q_A following electron capture is now:

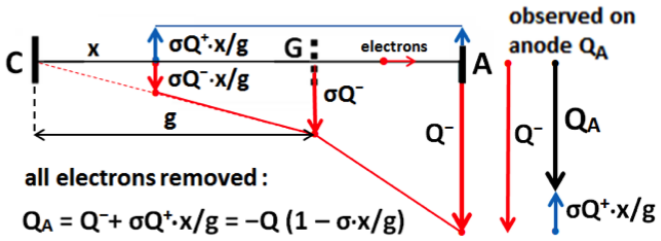

Figure 2.5: Gridded ionisation chamber with grid inefficiency being taken into account. From [52].

$$Q_A = Q^- + \sigma Q^+ \frac{x}{g} = -Q\left(1 - \sigma\frac{x}{g}\right) \tag{2.5}$$

The charge on the anode Q_A still senses the presence of ions in the CG volume but compared to the ungridded chamber in fig. 2.2 and in eq. 2.3 the perturbation by ions is drastically reduced due to the inefficiency factor σ in eq. 2.5 amounting only to a few percents.

2.1.4 Twin ionisation chambers

A convenient way to study spontaneous or neutron-induced fission intercepting in coincidence the two fragments is to use a twin back-to-back ionisation chamber. In a twin ionisation chamber two gridded chambers facing each other are sharing a common cathode. The cathode is made

of conductive material serving as a thin backing for fissile material deposited in the centre. The complementary fragments emitted in spontaneous or neutron induced fission are detected in coincidence in the two chambers. By detecting both fragment energies and applying mass and momentum conservation the masses of the emitted fragments are determined. Studies of thermal neutron induced fission of ^{235}U with twin chambers historically established the proof that in the majority of cases fission is a binary decay process with emergence of two fission fragments of comparable mass. The asymmetry of mass distributions was confirmed as well very early by this technique. An appealing feature of ionisation chambers is their high energy resolution for heavy ions when operated with pure methane as counting gas. Energy resolutions near 100 keV for fission fragments have been a prerequisite for the investigation of true cold fission where the kinetic energy of fragments quantitatively exhausts all available energy. The attractive features of twin ionisation chambers for studying neutron emission from fragments were investigated in detail by C. Budtz-Jørgensen et al. [32]. In particular it was shown that the angle the fragment track is forming with the chamber symmetry axis can be obtained by observing both the anode and the grid signals. This angle can similarly be extracted from observing the drift time of electrons [55]. A more refined method for the determination of fragment angles was proposed recently [56]. There the anode is split into strips and with an additional grid of parallel wires installed in front of the anode with the wires perpendicular to the anode strips the angles of the fragment tracks can be found. The present work is searching for correlations between fission fragments and fission neutrons. As to the fragments they were detected in a specially developed twin ionisation chamber called CODIS. In this chamber the measurement of fragment angles is based on the rather straightforward idea to cut the anode into independent sectors which are read out separately. The chamber is described in detail in the next paragraphs.

2.1.5 CODIS: double ionisation chamber

The CODIS detection system, sketched in fig. 2.6, is a particular type of Frisch gridded 4π twin ionisation chamber which, in addition to high efficiency, permits the localisation of any set of fragment emission angles. The main parameters of its construction and its operation in the CORA project are summarized in table 2.1. The chamber was constructed by a group of the Technical University of Darmstadt and successfully used in a series of ternary fission studies on spontaneous ^{252}Cf and neutron-induced ^{235}U fission [58, 59]. Localisation of arbitrary fragment emission angles in a near 4π geometry permitted arriving at outstanding results on various mutual energy and angular correlations between fission fragments, the rare ternary particles, prompt fission neutrons and γ rays. Needless to say that the chamber again discloses ideal requirements for measuring fragment-neutron correlations in the CORA project with the high statistical accuracy needed.

In ionisation chambers the charges induced on electrodes by an external charge Q in front of the electrodes are measured. In more detail the question is how these induced charges are distributed on the electrodes. It is well known that the distribution of these charges can be found from the

((a))

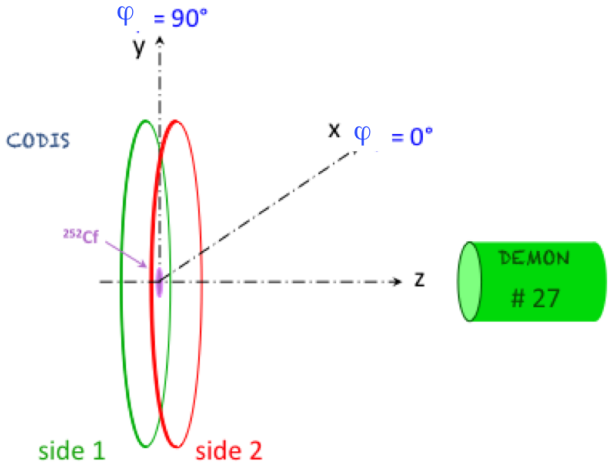

((b))

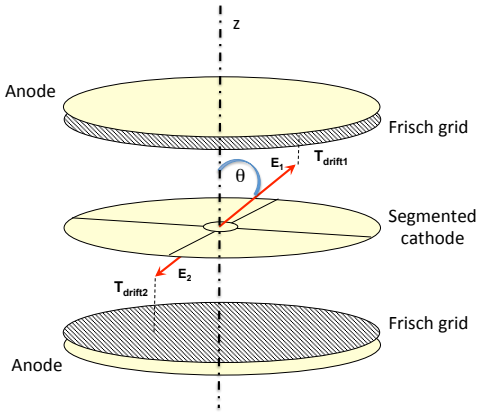

((c))

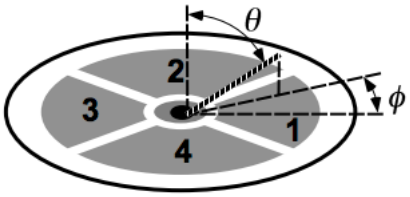

((d))

Figure 2.6: (a) CODIS detection system; (b) DEMON-CORA coupling. The two sides of the chamber are shown. The DEMON 27 is faced to the source side. The backing side corresponds to the side 1. (c) Schematic representation of the fission chamber. (d) Determination of the fission axis from the CODIS cathode signals: the figure shows the first 4 sectors S_i [57].

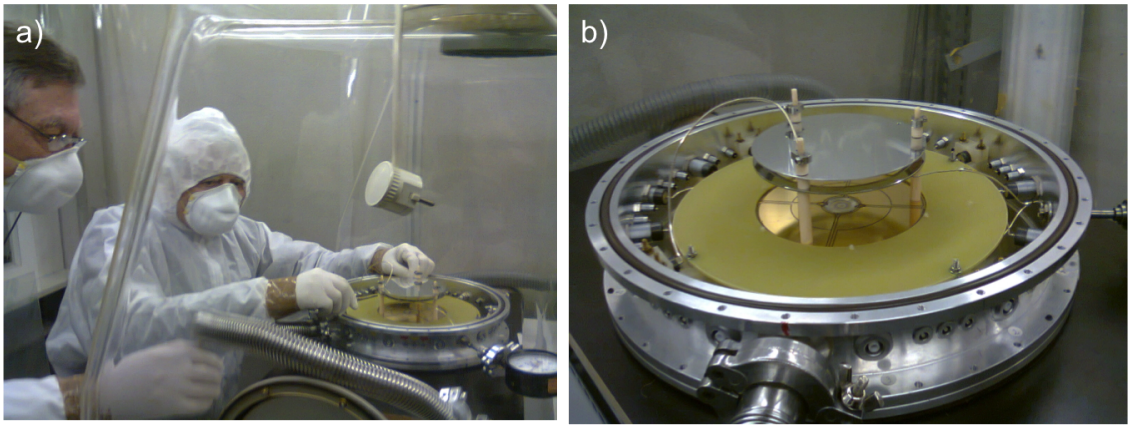

Figure 2.7: (a) Mounting of the ^{252}Cf source at the centre of the cathode; (b) The CODIS central rings and 4 of 8 sectors are shown.

electric field generated by the charge Q as a dipole field with charge Q and mirror charge -Q behind the electrode. The distribution depends on the position of the charge Q in front of the electrodes. It is by no means uniform. The idea behind CODIS is to measure not simply the total induced charge but to sense the distribution of the charge on the electrodes. To this purpose the electrodes have to be segmented. The charges induced on the segments then give the additional information on the position of external charges Q.
In the CODIS chamber the information on emission angles is derived from pulses induced at a split-cathode. It does thus not compromise deduction of the fragment energies from the anode pulses. Both sides of the cathode PCB are subdivided into four electrically isolated quadrants and the two thin ring contacts around the central source which are shortcut by the conducting source holder. While the 8 quadrants are read out individually for deducing fragment angles, the central rings and metallic source get induced signals from both chamber sides for providing the event trigger and start signal for the neutron time of flight. As seen from the photograph of fig. 2.7 b), all quadrants extend to about half the radius of the cathode (38 mm) which corresponds to the cathode - Frisch grid spacing, being larger than the maximum fragment range at operational gas pressure. The outer parts of the quadrants were put together and biased at the cathode potential for attaining electric field homogeneity. Limitation of the active quadrants to the central part of the cathode has only small effect on the fragment signals but reduces considerably the counting efficiency for the about 30 times more frequent ^{252}Cf α particles and thus a distortion of fragment angle registration by α-particle pileup. Reading out the anode signals with fast current sensitive preamplifiers serves the same purpose while for the larger dynamical range of the individual cathode signals a readout by conventional charge sensitive preamplifiers was preferred as the signal to noise ratio is better. Both fragment-fragment and fragment-α particle pileups still lead to a slight distortion of the anode amplitude spectra. In order to clean the experimental data from the pileup events special pileup counters were used in the electronic set-up. For each anode,

the number of events above a corresponding discriminator threshold was counted during the time window needed to integrate the corresponding signal: ≈ 1 μs for the fragment-fragment pileup (integration window in the QDC recording the anode signals) and ≈ 6 μs for the fragment-α pileup (corresponds to the shaping time in the main amplifiers used for measuring the sectored cathode signals). For a most efficient pileup rejection the multiplicity of all pileup counters was requested to be equal to 1.

Vessel: Gas-tight Al cylinder, 330 mm Ø, 170 mm high, with 1 mm thick spherical Al end caps.
IC geometry: Size of all electrodes: 120 mm Ø ionisa Distances: cathode – Frisch grid: 38.0 mm, Frisch grid – anode: 8.0 mm
Electrode material: Cathode: PCB with double-sided copper layers of PF_4 epoxy material, gold-plated: 1.6 mm thick. Anode: Polished Al - plate, 0.5 mm thick
Frisch grid: orthogonally woven CrNi 1.4401 wire mesh - 0.025 mm Ø wires, 0.50 mm pitch
Gas: High-purity CF_4 (tetrafluoromethane) with 2.64 x 10^4 Pa (200 torr) operational pressure, flow controlled.
Electrode bias voltages: Cathode: 1440 V negative, Anode: 960 V positive, Frisch grid: ground.
Electric fields: Cathode – Frisch grid: 378.95 V cm^{-1}or 4.54 10^{-2} V cm^{-1} Pa^{-1}(1.89 V cm^{-1} $torr^{-1}$) Frisch grid – Anode: 1200 V cm^{-1} or 1.44 10^{-2} V $cm^{-1}Pa^{-1}$ (6.00 V cm^{-1} $torr^{-1}$)
Preamplifiers: Anodes 1 and 2: CSTA2, current sensitive for flash-ADC readout, non-inverting, 1G bias resistor. 8 Sector Cathodes and Central Cathode : CSTA2, charge sensitive with 1 pF feedback C for readout with main amplifiers and ADCs, inverting, 1G bias resistor.
Source: ^{252}Cf transfer source of 5 mm Ø deposited onto a 0.00025 mm (222 μg cm^{-2}) thick Ni foil, mounted onto a 26 mm Ø Al support ring and fixed at the centre and mid-thickness of the cathode plate. Activity 0.002 mCi, 2000 fissions/s

Table 2.1: CODIS parameters.

Apart from the sectored cathode, CODIS is designed as a normal twin-IC. The Frisch grid was

made of a orthogonally woven CrNi 1.4401 wire mesh, with 0.025 mm Ø wires and 0.50 mm pitch. According to [51] the grid inefficieny is estimated to be 2%, although available calculations are strictly valid only for a one-dimensional grid and not for a mesh type one as ours. For a best transparency of the grid, the reduced electric field between anode and grid (4.54 10^{-2} V cm^{-1} Pa^{-1}) was chosen larger than 3 times the field between grid and cathode (1.44 10^{-2} V cm^{-1} Pa^{-1}). As for the gas, CF_4 at the low working pressure of 2.64 x 10^4 Pa and the high electric fields minimise trapping and recombination effects and provide fast electron drift velocities of 1 cm/μs before the grid and 14 cm/μs after it [60]. With CF_4, the pulse-height defect for fission fragments was found to be in the order of 5 MeV, for both the light and the heavy groups.

2.1.5.1 Energy and mass measurement

In a gridded ionisation chamber, the anode signals (total collected charges) are basically proportional to the number of electrons produced during deceleration of the fragments and are, thus, only roughly representing their kinetic energies. As already discussed above, there are several effects which make the dependence of the anode signals on fragment kinetic energies more complicated, such as the pulse-height defect and Frisch grid inefficiency. In a twin chamber with an internal source, there is moreover a serious energy loss of the fragments in the source and the backing material. The latter effect leads to a significant decrease of the anode ht for very flat emission angles (signals with long drift times) – see fig. 2.8.

To convert the measured anode charges to real fragment energies from fission the following

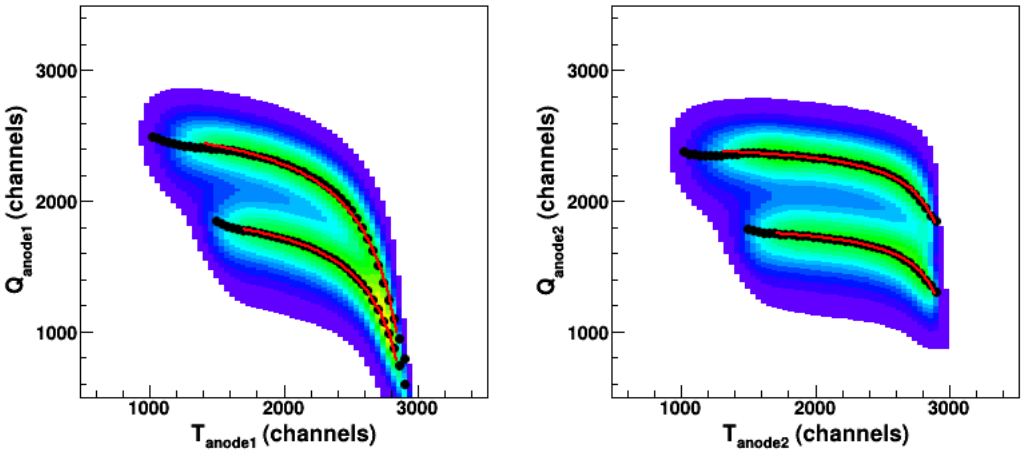

Figure 2.8: Two-dimensional distributions of the anode drift time vs the anode charge. The black points are the mean values of the LF and HF charges for a given drift time slice. The red lines are the fits of the mean charges obtained with formula 2.6.

procedure was applied, based on the known mean fragment post-neutron kinetic energies for

^{252}Cf : $\langle E_{HF}\rangle$=78.7 MeV, $\langle E_{LF}\rangle$=102.5 MeV [61], following the sequence of steps:

1. The groups of light and heavy fragments were separated from each other in the 2D plot of the anode signals measured in both halves of the chamber, such as shown in fig. 2.9.

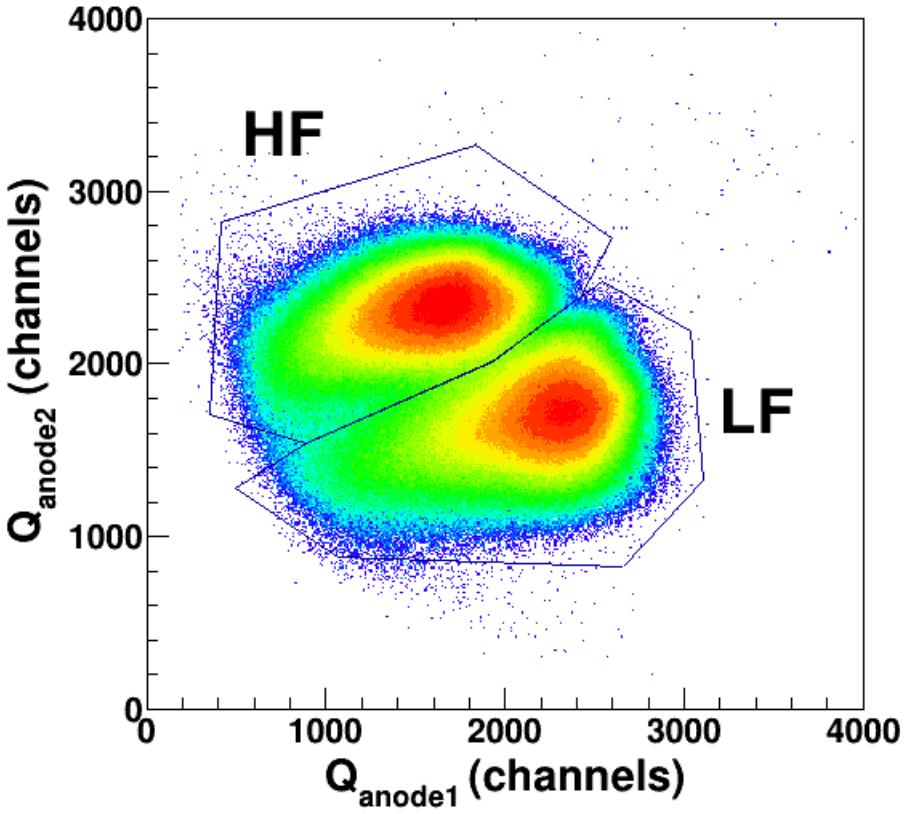

Figure 2.9: Two-dimensional distributions of the anode signals. Contours correspond to the groups of light (LF) or heavy (HF) fragments on the side 1 of the chamber. Data have not yet been corrected for the energy losses in the backing of the source.

2. For each side of the chamber, the anode signals were related to the correlated drift time T, separately for the light and heavy fragment groups.

3. Then, mean values were determined for both, light and heavy fragments, as a function of T, plotted as black dots in fig. 2.8.

4. For each side, the dependence of the mean amplitudes $\langle Q_{LF}(T)\rangle$ and $\langle Q_{HF}(T)\rangle$ on the drift time was fitted by the formula:

$$\langle Q_{LF}(T)\rangle = A_1 + \frac{B_1}{T-C} \tag{2.6}$$

$$\langle Q_{HF}(T)\rangle = A_2 + \frac{B_2}{T-C} \tag{2.7}$$

where the drift time T is in channels, A_1, B_1 are individual parameters for the light fragment, A_2, B_2 individual parameters for the heavy fragment and C is a common parameter for both fragments. The parameter C stands for the maximal drift time, when fragments are emitted at a very flat angle to the cathode plane. Note that both curves, for the light and heavy fragment were fitted simultaneously with one common parameter C.

5. Thus, the mean anode charge of the light or heavy fission fragment on each side was parametrized as a function of the drift time by eq. 2.6, with corresponding coefficients derived from the experimental data.

6. The energy of the fission fragment for each event was derived from the measured anode charge Q and the drift time T of the anode signal by linear interpolation between two drift time dependent mean anode charges $\langle Q_{LF}(T)\rangle$ and $\langle Q_{HF}(T)\rangle$ using the known mean energies of the light and heavy fission fragments as calibration points:

$$E = K(T)\,Q + B(T) \tag{2.8}$$

where $K(T) = \frac{\langle E_{LF}\rangle - \langle E_{HF}\rangle}{\langle Q_{LF}(T)\rangle - \langle Q_{HF}(T)\rangle}$, $B(T) = \frac{\langle E_{HF}\rangle\langle Q_{LF}(T)\rangle - \langle E_{LF}\rangle\langle Q_{HF}(T)\rangle}{\langle Q_{LF}(T)\rangle - \langle Q_{HF}(T)\rangle}$

$$\text{and} \qquad \langle \mathrm{E_{HF}}\rangle = 78.7MeV, \tag{2.9}$$

$$\langle E_{LF}\rangle = 102.5MeV \tag{2.10}$$

The above procedure of the energy calibration with taking into account the drift time dependence of the anode charge signal simultaneously corrects, on average, for all minor effects influencing the linear relation between the initial fragment energy and the measured anode charge. Although this correction is not perfect, it is quite sufficient for the determination of the fragment energies and masses, where no optimisation of energy and mass resolution was required. Fig. 2.10 shows analogous two-dimensional plots with anode energies calibrated and corrected for the drift time dependence according to eqs. 2.6 and 2.9. By measuring the fragment energies and knowing the mass of the parent nucleus it is possible to deduce the mass of the fragments using the mass and the linear momentum conservation. For a fissioning system the momentum of the parent nucleus is zero and the daughters, of masses A_{LF}, A_{HF} and linear momenta p_{LF}, p_{HF} of the light (LF) and the heavy (HF), are emitted on collinear trajectories thus the momentum conservation law is applied as

$$p_{LF} = -p_{HF} \tag{2.11}$$

$$A_{LF}v_{LF} = -A_{HF}v_{HF} \tag{2.12}$$

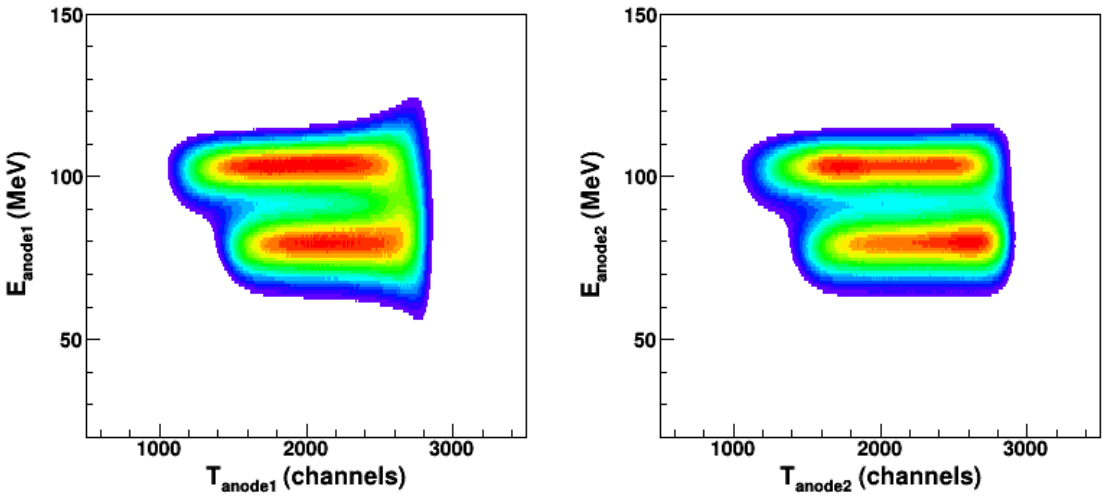

Figure 2.10: Two-dimensional distributions of the anode drift time vs the anode (calibrated) energy.

Knowing that the relationship between the kinetic energy and the velocity is $^1/_2 Av^2$ and solving eq. 2.12 in function of the energy of each fragment the following relation is obtained:

$$A_{LF}\sqrt{\frac{2E_{LF}}{A_{LF}}} = A_{HF}\sqrt{\frac{2E_{HF}}{A_{HF}}} \tag{2.13}$$

From equation 2.13 it follows that the ratio of the provisional fragment masses [1] is inversely proportional to the ratio of the kinetic energies as shown in the following formula:

$$\frac{E_{LF}}{E_{HF}} = \frac{A_{HF}}{A_{LF}} \tag{2.14}$$

Since the sum of the masses of the two daughter nuclei is equal to the parent one, $A_{Cf} = A_{LF} + A_{HF}$ where $A_{Cf} = 252$ is the mass value of ^{252}Cf, it is possible to obtain the following relations:

$$A_{LF} = \frac{A_{Cf}E_{HF}}{E_{LF} + E_{HF}} \tag{2.15}$$

$$A_{HF} = \frac{A_{Cf}E_{LF}}{E_{LF} + E_{HF}} \tag{2.16}$$

Such twin-IC allows to measure simultaneously the masses of both fragments. The resulting energy and mass distributions are shown in figs. 2.11, 2.12 and 2.13.

1. "Provisional masses" are calculated under the assumption that no neutrons at all are evaporated form fragments. The raw data have to be corrected for neutron emission by fragments to obtain pre- or post-neutron-emission mass distributions. This correction is a rather complicated procedure that depends on the experimental arrangements and requires assumptions concerning the neutron multiplicity distribution as a function of fragment mass [62].

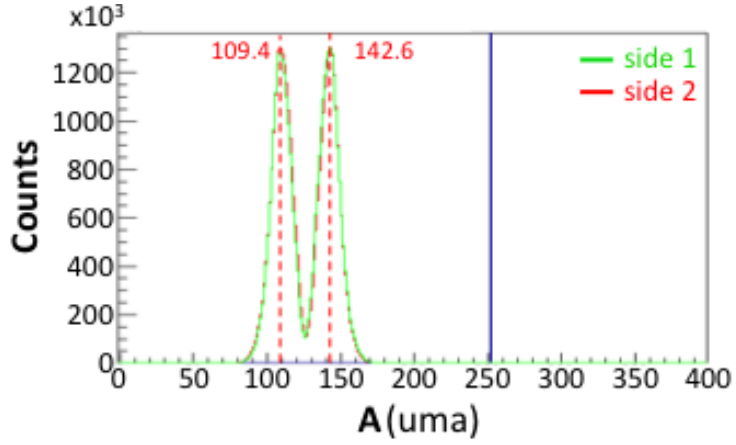

Figure 2.11: In the figure are plotted the mass distributions obtained for the anode 1 signal in green and in red the one computed from the anode 2.

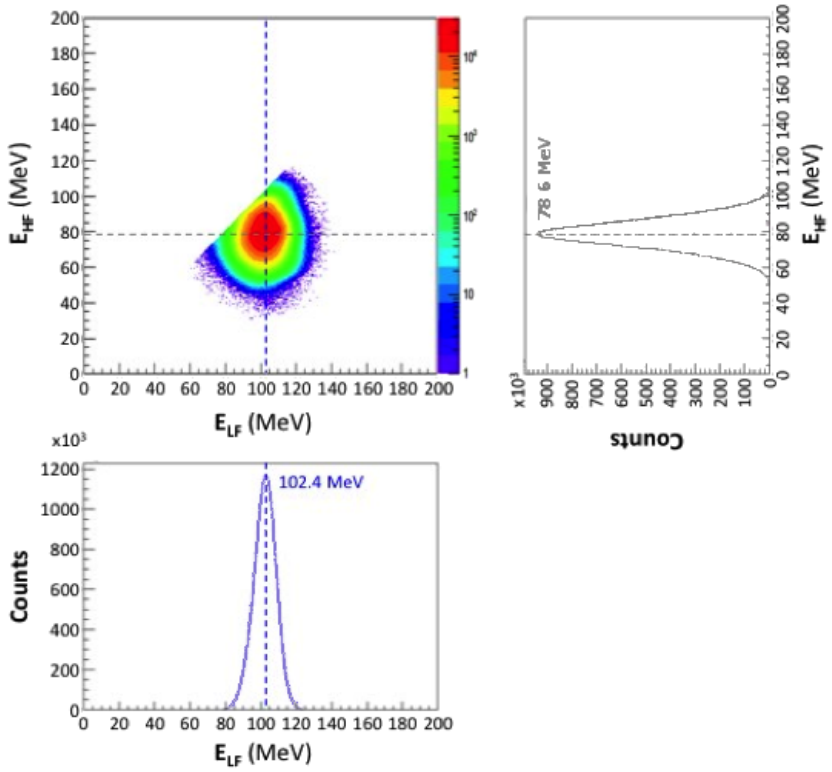

Figure 2.12: The two dimensional histogram represents the energy of the HF versus the energy of the LF. At the right is shown the mass distribution of the HF computed following eq. 2.15, in the bottom part the distribution, calculated as eq. 2.16, of the LF mass.

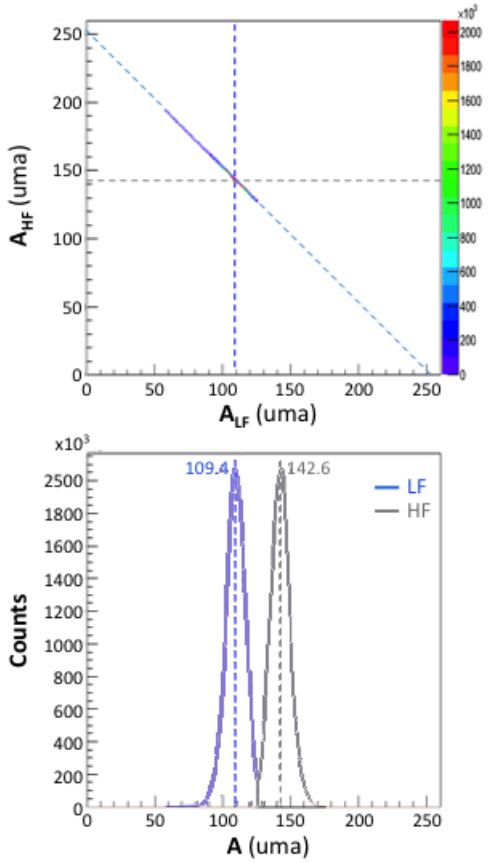

Figure 2.13: The figure shows the resulting masses obtained for the HF and the LF(bottom) and their correlation (top).

2.1.5.2 Determination of the fragment emission angles

The polar angle can be computed from the drift time measurement and by taking into account the distance d between the anode and the cathode following equations:

$$t_{drift} = \frac{\delta}{v_{drift}} \quad \text{where} \quad v_{drift} = 10\frac{cm}{\mu s} \tag{2.17}$$

$$\delta = d - l(E, A) * cos\theta_{FF} \tag{2.18}$$

where l(E,A) is the range of fragments in the CF_4 gas at 2.64 x 10^4 Pa operational pressure. The drift time is measured as the time between the start signal coming from the centre of the cathode and the stop given from the anode.
From equation 2.17 the polar angle can be computed as follows:

$$cos\theta_{FF} = \frac{d - t_{drift}\, v_{drift}}{l(E, A)} \tag{2.19}$$

In practice, the polar angle is not calculated using the drift time velocity, distance and fragment track length but is determined from the drift time by calibrating the end-points of the measured drift time spectra (see fig. 2.14). Formula 2.19 can be written as follows:

$$cos\theta_{FF} = \frac{T_{max} - t_{drift}}{T_{max} - T_{min}} \tag{2.20}$$

where T_{max} and T_{min} are the maximal and minimal drift times for a given fragment; T_{max}

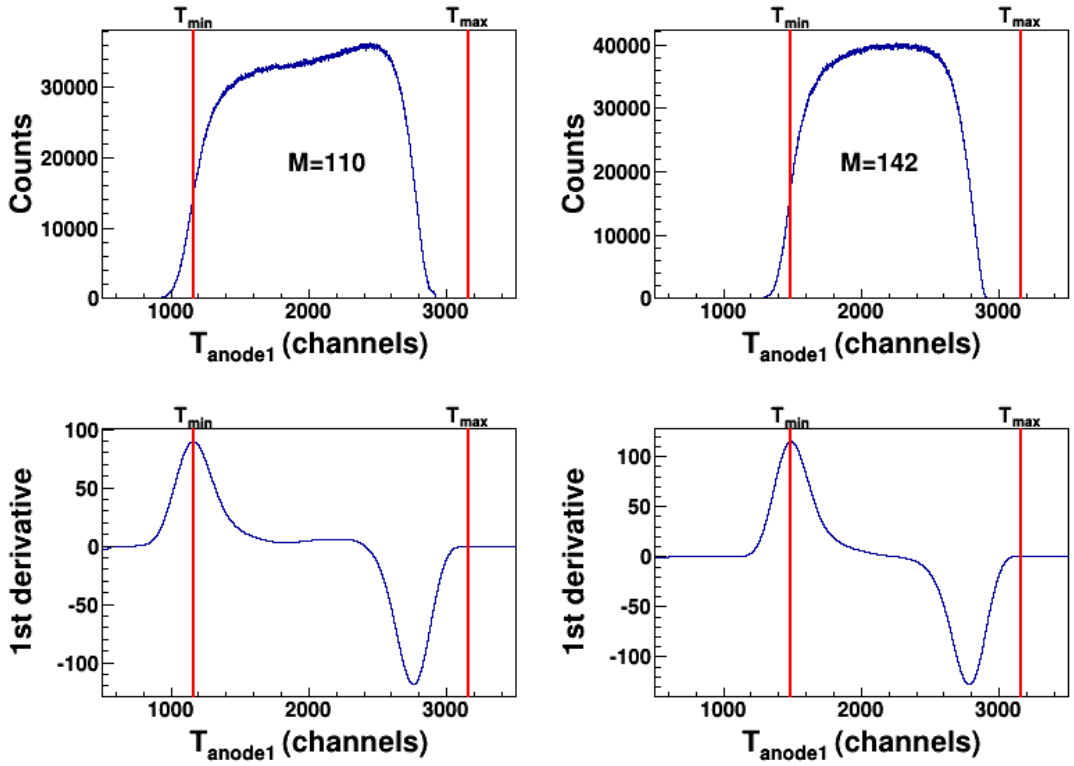

Figure 2.14: Drift time spectra and their 1^{st} derivatives for the most probable provisional masses M_{LF}=110 and M_{HF}=142, side 1 of the chamber. The T_{min} parameter is defined as the position of the maximum in the 1^{st} derivative spectrum.

corresponds to the flat angles ($\theta = 90°$) while T_{min} corresponds to the steep angles ($\theta = 0°$). Obviously, T_{max} is the same for all fission fragments, but T_{min} depends on the length of the fragment track, which, in turn, depends on the fragment mass and energy. The T_{max} parameter was determined for each side of the chamber during the anode energy calibration (it's the parameter C in eq. 2.6). The T_{min} parameter was parameterised as a linear function of the fragment mass only. For simplicity reasons, we didn't consider explicitly the energy dependence of this parameter. However, there is a strong implicit dependence on the fragment energy since the fragment masses and energies are strongly correlated.

The position of the minimum of the drift time was determined from the maximum of the

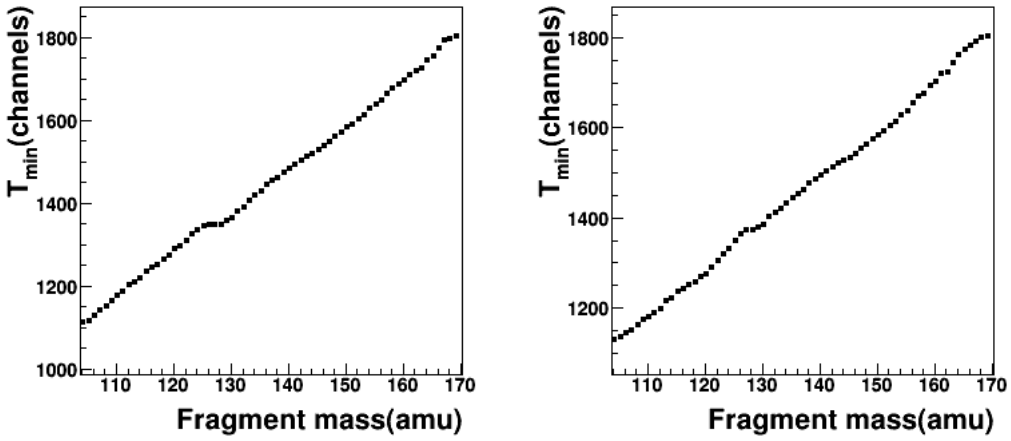

Figure 2.15: The dependence of the T_{min} parameter on the fragment mass for side 1 of the chamber (left) and side 2 (right).

1^{st} derivative spectrum for each fragment mass in steps of 1 amu and then fitted by a linear function. The examples of the drift time spectra and their 1^{st} derivatives for masses 110 and 142 are shown in fig. 2.14. The dependence of the T_{min} parameter on the fragment mass is shown in fig. 2.15. Fig. 2.16 shows the θ_{FF} distribution for each side of the chamber.
For very flat fragment angles the experimentally determined fragment parameters become too much distorted due to scattering and absorption of the fragments in the target and in the backing. So a condition $|cos\theta_{FF}| > 0.4$ was imposed on all analysed events. This corresponds to an angular coverage of $0.6 \cdot 4\pi$. The azimuthal angle of the fragment emission φ_{FF} could be determined using the unique feature of the CODIS chamber sectored cathode. The principle of the angle determination with the cathode is sketched in fig. 2.17. The output signals of each sector S_i (i=1, ...,8) depend on the orientation of the fission axis, i.e. θ and ϕ angles, and on the fragment kinetic energy. In order to determine the azimuthal angle we define variables $q_{i,j}$

$$q_{i,j} = \frac{S_i}{S_i + S_j} \tag{2.21}$$

for sectors i and j lying on the same side of the cathode, but opposite to each other. To demonstrate the method of the determination of the φ angle the distributions of events on a two-dimensional plot $q_{1,3}$ vs $q_{2,4}$ for several cuts in θ (determined from the drift time) are shown in fig. 2.18 (left). We define the polar coordinate system for these plots with the centre at $q_{1,3}$= 0.5, $q_{2,4}$ = 0.5 (see fig. 2.17). The coordinate R in this coordinate system is related with the polar emission angle θ of the fragment, while the coordinate ϕ with the azimuthal angle φ. The distributions of the ϕ angle for the same cuts in θ are plotted in fig. 2.18 (centre). They demonstrate characteristic oscillations with a period of $\pi/2$ which amplitude increases for larger θ angles and which are related with the geometry of the sectors and the process of the charge collection. To

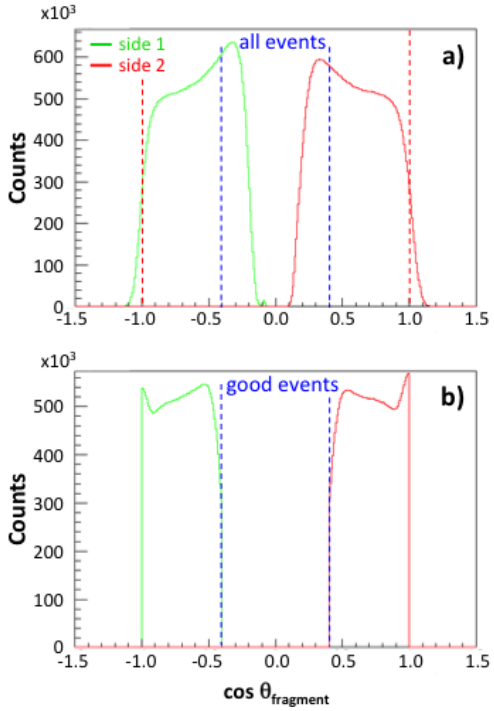

Figure 2.16: In the figures are shown the θ distributions corresponding to side 1 and side 2. In the upper part the distribution by taking into account all events is shown. In the bottom part a selection $|cos\theta_{FF}| > 0.4$, called good events, is made and also the correction on $|cos\theta_{FF}| > 1$ is applied. Since the polar angle is computed from eq. 2.20 also a correction on events that have $|cos\theta_{FF}| > 1$, shown in the top figure, is needed. These events are simply spread on allowed value of cosine respectively around -1 and 1.

find the relation between the angle ϕ and the real azimuthal angle φ we use the fact that the fission fragments are emitted isotropically, so the distributions of events as a function of the azimuthal angle φ should be flat. If the distribution of the ϕ angle is approximated with a function F(ϕ), then the relation between the φ and ϕ angles can be derived from equation:

$$1 \cdot d\varphi = F(\phi)d\phi \tag{2.22}$$

Solving this equation gives:

$$\varphi(\phi) = \int F(\phi)d\phi \tag{2.23}$$

Considering the $\pi/2$ symmetry of the sectored cathode, F(ϕ), can be chosen in a form

$$F(\phi) = a(1 + b\,cos4\phi) \tag{2.24}$$

where a is just a normalisation coefficient and b is the amplitude of the oscillations due to the 4-sector structure of the cathode. In this case the φ angle is defined from 2.24 as

$$\varphi(\phi) = \phi + \frac{b}{4}sin4\phi + \varphi_0 \tag{2.25}$$

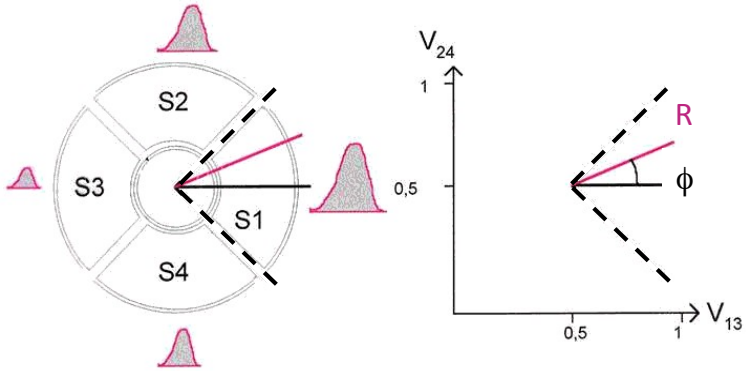

Figure 2.17: Schematic representation of the upper part of the segmented cathode. An interaction in sector S1 is shown. The signals obtained from this interaction are sketched with the relative proportions in the left part. In the right part is represented a typical matrix for the parameters $q_{1,3}$ and $q_{2,4}$. Each fission event is a point in such a plane. The projection of the trace is $R = \sqrt{(q_{i,j} - 0.5)^2 + (q_{i+1,j+1} - 0.5)^2}$ and the angle is $\phi = arctan\left(\frac{q_{i,j}}{q_{i+1,j+1}}\right)$.

The constant φ_0 is determined from the orientation of the cathode plane (in which the ϕ angle is defined) relative to the laboratory coordinate system (in which the ϕ angle is defined). In our case $\varphi_0 = 135^\circ$ as the zero ϕ angle was in the middle of sector 1 of the cathode, and the zero φ angle (direction of the x axis, see fig. 2.6(b)) is between sectors 3 and 4. The coefficient b in 2.24 and 2.25 depends mainly on the polar emission angle θ, but also slightly on the length of the track of the fragment, thus, on the fragment mass and energy. For simplicity reasons, the coefficient b was determined separately for the light and heavy fragment groups by fitting the distributions of the ϕ angle for different values of cosθ in steps of 0.05. The dependence on the cosθ was then interpolated by a 3^{rd} order polynomial (see fig. 2.19). Only events with $|cos\theta_{FF}| < 0.4$ were used.

Having determined the polar and azimuthal emission angles (from eqs. 2.20 and 2.25, respectively) we can construct the two fission fragment emission vectors separately for each side of the chamber, light and heavy fragments being determined from the condition $M_{LF} < M_{HF}$:

$$\vec{V}_{LF} = \begin{bmatrix} sin\theta_{LF}cos\varphi_{LF} \\ sin\theta_{LF}sin\varphi_{LF} \\ cos\theta_{LF} \end{bmatrix} \quad \vec{V}_{HF} = \begin{bmatrix} sin\theta_{HF}cos\varphi_{HF} \\ sin\theta_{HF}sin\varphi_{HF} \\ cos\theta_{HF} \end{bmatrix}$$

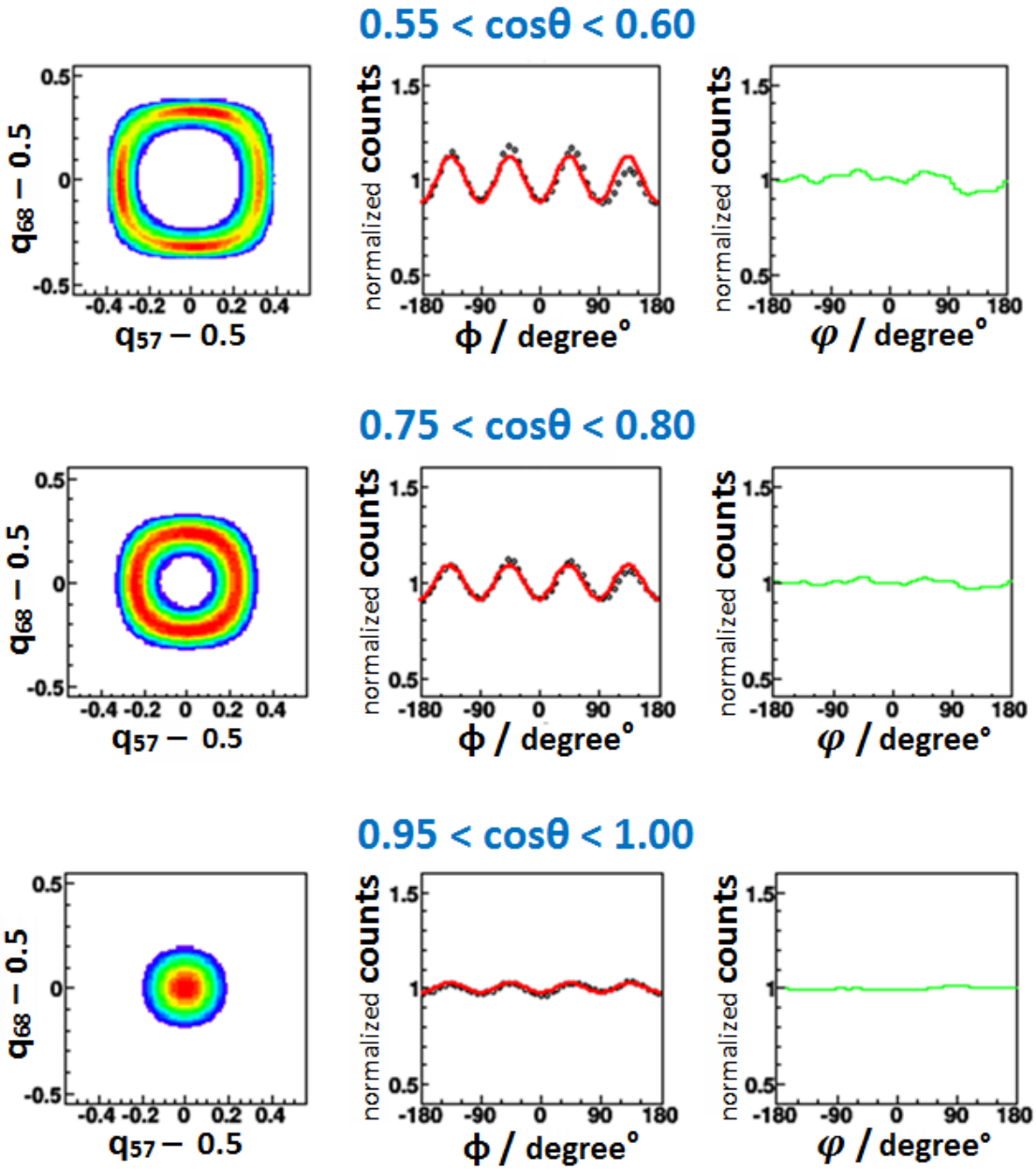

Figure 2.18: Determination of the azimuthal angle φ. Left: two-dimensional plots $q_{1,3}$ vs $q_{2,4}$ for different cuts in $\cos\theta$. Centre: fit of the angle using formula 2.24. Right: the resulting φ angle, determined using formula 2.25.

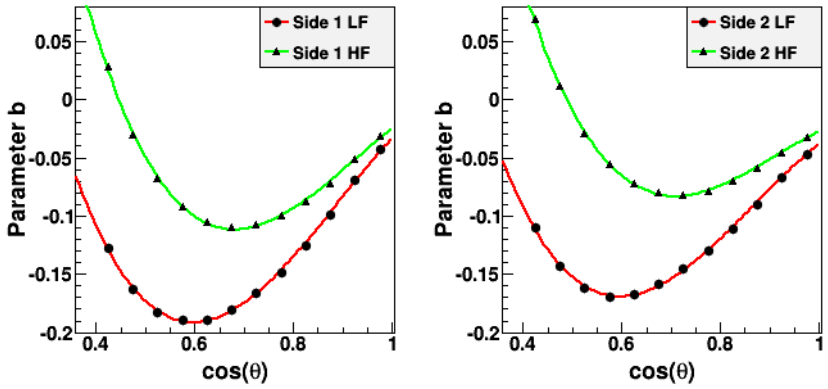

Figure 2.19: Dependence of the fitting parameter b in eqs. 2.24 and 2.25 on $\cos\theta_{FF}$ ($\cos\theta$ in the figure) for the two sides of the chamber and for LF and HF fragment groups.

The fission axis is then determined as a unit vector, average between the two independent fragment vectors using the relation (see fig. 2.20 c)):

$$\vec{V}_{FAXIS} = \vec{V}_{LF} - \vec{V}_{HF} \tag{2.26}$$

Fig. 2.20 shows the distribution of angles between two fission fragments from the same event, as

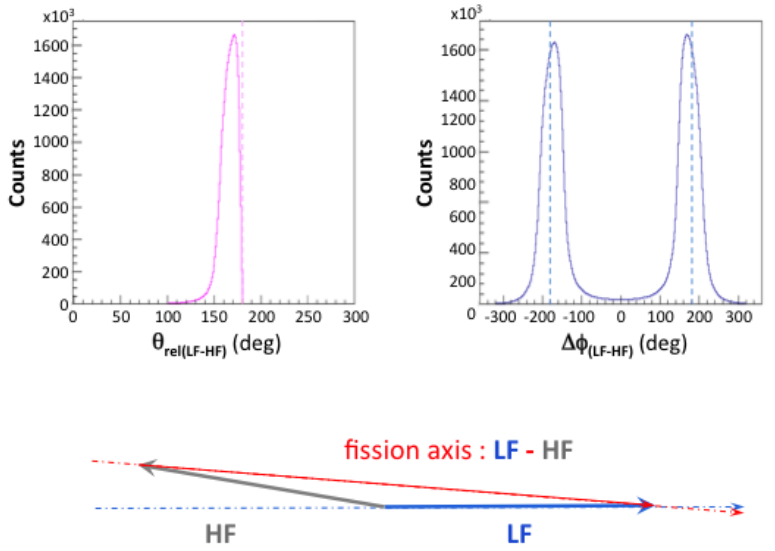

Figure 2.20: (a) Distribution of relative polar angles between two fission fragments from the same event (black curve) and between one fission fragment and the fission axis (red curve). (b) $\Delta\varphi$ distribution between LF and HF from the same event. (c) Scheme of the determination of the fission axis.

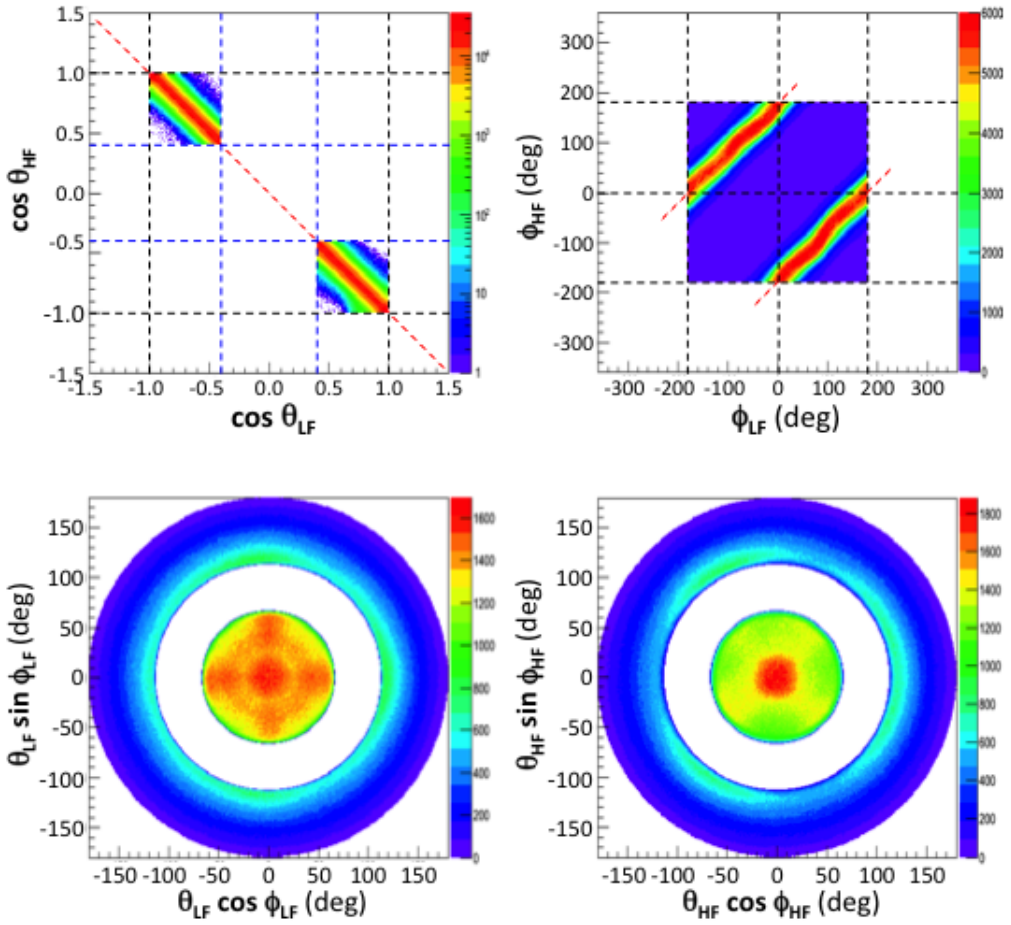

Figure 2.21: In the upper part of the figure correlation matrices respectively in the planes $\cos\theta_{HF}$ vs $\cos\theta_{LF}$ and ϕ_{HF} vs ϕ_{HF} are shown. The left figure shows that θ_{HF} and θ_{LF} are anticorrelated. From the second matrix of correlation on the right it is easy to deduce that the difference between the angles ϕ_{HF} and ϕ_{LF} is spread around 180° as expected. The bottom part shows that LF (left) and HF (right) are emitted isotropically in the 4π space. The uncovered region is due to the source position.

well as the relative polar angles between the fission axis and one of the fragments, all plots made with a condition $|cos\theta_{FF}| > 0.4$. The width of the latter distribution is about 10°, which gives us an estimation of the overall angular resolution of the CODIS chamber with the simplified data analysis procedure, described above. This angular resolution is smaller than the minimal opening angle of the DEMON detectors, estimated for the most distant ones as 12°.

The resulting spatial distribution of the fission fragments are presented in fig. 2.21. The non uniform spots which appear in the bottom spectra are due to the remaining $\pi/2$ oscillations discussed in fig. 2.18. These oscillations are also visible in the $\phi_{LF} - \phi_{HF}$ correlation (top-right). In this work, for the ϕ_{nn} correlations, we select only those events for which the fission fragments

are emitted along the chamber axis, the z-axis. Thus for neutron-fragment correlations only fission fragments with $\theta_{FAXIS} < 5^{\circ}$ are taken into account.
The CODIS calibration has been performed by members of the CORA collaboration.

2.1.6 Sources

The ^{252}Cf source used in the CORA experiment was produced by the **Federal Atomic Energy Agency of Russian Federation V.G KHLOPIN RADIUM INSTITUTE**. The source characteristics are specified in tables 2.2 and 2.3. Californium, the sixth transuranium element to be discovered, was produced by Thompson, Street, Ghioirso, and Seaborg in 1950 by bombarding microgram quantities of ^{242}Cm with 35 MeV helium ions in the Berkeley 60-inch cyclotron.

Californium-252 source	
Activity	0.002 mCi, 2000 f/s
Dimensions:	diameter 25 mm thickness of the Ni film 0.00025 mm active spot diameter 5mm
Mass	0.0037 μg

Table 2.2: Californium source characteristics given by the supplier.

The radioisotope Californium-252 which has a half-life of 2.645 years is routinely encapsulated into compact, portable, intense neutron sources. It is a very strong neutron emitter, which makes it extremely radioactive. It undergoes alpha decay 96.9% of the time to form curium-248 while the remaining 3.1 % of decays are spontaneous fission. One microgram (μg) of californium-252 emits 2.3 million neutrons per second, an average of 3.7 neutrons per spontaneous fission. Most of the other isotopes of californium decay to isotopes of curium (atomic number 96) via alpha decay. The neutron energy spectrum is similar to a fission reactor, with a most probable energy

Isotopes	Abundance
^{249}Cf	15.03%
^{250}Cf	15.80%
^{251}Cf	15.03%
^{252}Cf	61.21%

Table 2.3: The californium isotopic composition at 18/12/2003.

of 0.7 MeV and an average energy of 2.1 MeV. Portable ^{252}Cf neutron sources can provide an ideal non-reactor source of neutrons for lower-flux applications.
The positioning of the source in the CODIS chamber is shown in fig.2.7.

2.2 DEMON

DEMON is the acronym for MOdular Neutron DEtector (DEtecteur MOdulaire de Neutrons). The multidetector DEMON, issued from a french-belgian collaboration and operational since 1994, constitutes an ideal tool to study nuclear reactions in a wide domain of energies ranging from 0.7 MeV up to 1 GeV. It has been used at many nuclear facilities around the world (CYCLONE-LNL, GANIL, VIVTRON, U400/U400M-Dubna, SATURNE-Saclay, TSL-Uppsala, KVI-Groningen, SARA-Grenoble, TAM, JYFL, LNS-Catania, etc...), using a part or the complete set of detectors, to investigate various fields of nuclear physics. Contrary to neutron walls which usually give access only to the multiplicity of the emitted neutrons, DEMON has been conceived to measure angular and energy distributions of the neutrons with a high efficiency and a good energy resolution deduced from the time of flight as well as a large geometrical acceptance. It gives thus access also to the neutron multiplicity. Its modularity allows to adapt the geometrical configuration to the specific needs of the experiments as shown on fig. 2.22. Also the flight distance can be adapted to optimise the geometrical acceptance whilst preserving the required energy resolution. This device includes 100 cylindrical units containing NE213 liquid

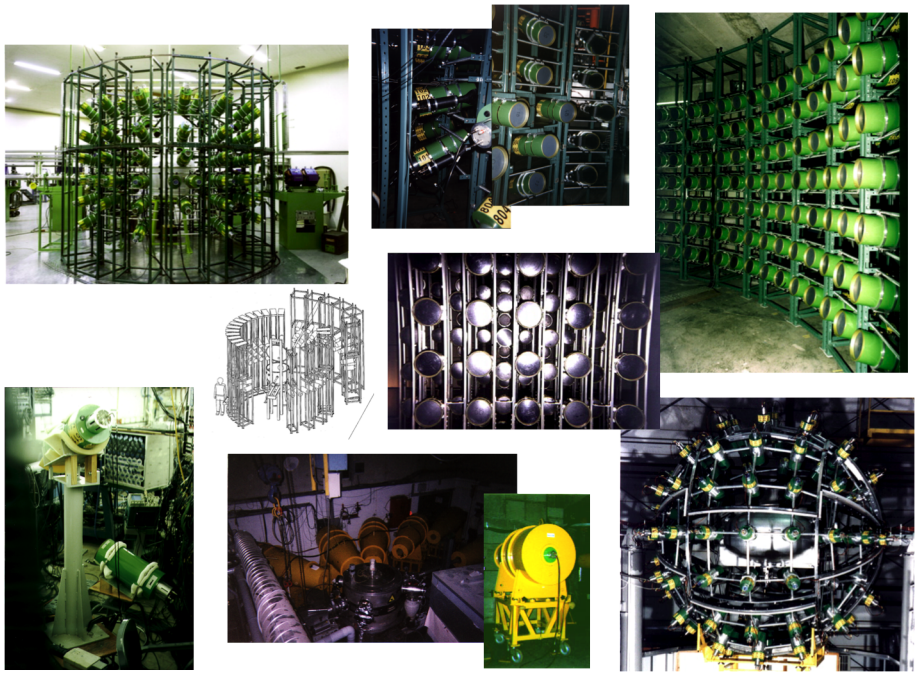

Figure 2.22: Different geometrical configurations used for various experiments performed with the neutron multidetector DEMON.

organic scintillator of diameter 16 cm and 20 cm deep.
DEMON is sensitive to γ-rays and light charged particles as well as to neutrons as shown in fig. 2.23. To reject γ-rays a pulse shape discrimination is applied. This method is based on the

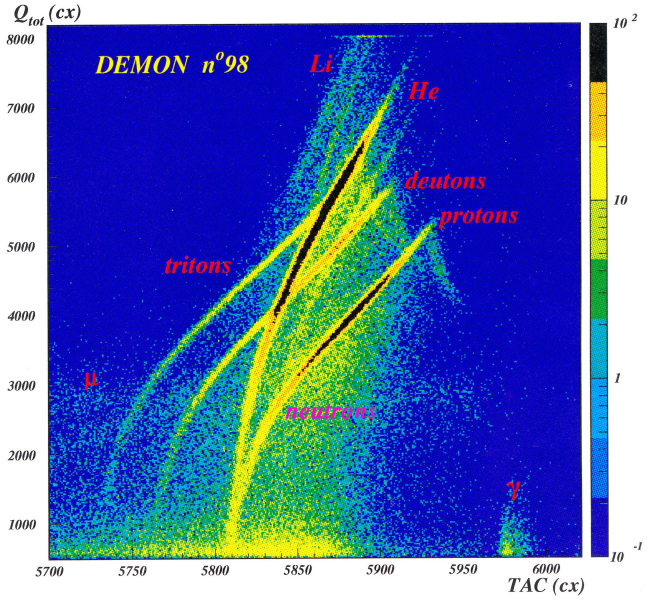

Figure 2.23: Total charge versus time of flight obtained with a DEMON cell which detects γ, neutrons as well light charged particles. From J. Pluta *et al.*, Interferometry experiment E286, GANIL 1998 [63].

time dependence of the scintillator light decay which makes possible to identify particles that have different energy losses but produce the same amount of light in the scintillator.
Also light charged particles can either be measured as in the experiment of fig. 2.23 or rejected. To disentangle an incident neutron from a charged particle, often a proton, DEMON disposes

Figure 2.24: SYREP detectors: thin plastic scintillators placed in front of the DEMON cells and designed to reject light charged particles at high energy.

on 45 additional detectors designated by the acronym “SYREP” for ”SYstème de REjection des Protons” (proton rejection system). These detectors, shown in fig. 2.24, are thin NE102 plastic

scintillators of octagonal shape with a thickness of 3 mm. These detectors were not needed in the low energy CORA experiments. The mean intrinsic efficiency of each cell is of the order of 70% at 5 MeV and approximates 30% at 50 MeV for an energy threshold of 200 keVee [64]. The time resolution determined with the γ peak, is about 1.3 ns. Neutron-γ discrimination remains excellent for low detection thresholds. It is optimised by a time of flight separation.

2.2.1 Detection principle

Fast neutrons interact in scintillators mainly through elastic scattering with the nuclei present, mostly hydrogen and carbon. Most of the useful scintillator light comes from recoiling hydrogen nuclei (protons). This occurs because a neutron can transfer 100% of its energy in an elastic scattering interaction to a recoiling proton but only 28% to a recoiling ^{12}C nucleus. The kinetic energy of the recoiling protons is absorbed by the scintillator and is ultimately converted into visible blue light. The light is collected in a photomultiplier tube optically coupled to the scintillator and converted to an electronic pulse which magnitude is related to the kinetic energy of the recoiling protons.

Fig. 2.25 shows the different interaction processes which occur in a NE213 liquid scintillator as a function of the neutron incident energy. In the energy range our work is dealing with, E_n <10 MeV, one can see that almost exclusively elastic scattering on ^{1}H and ^{12}C takes places. At about 5 MeV, inelastic scattering on ^{12}C appears which leads to a γ-ray emission. These γ's appear as γ's in the discrimination spectrum but they have the time of flight of the corresponding neutron. These γ's are rejected in our analysis. The γ-rays can interact in the detector and

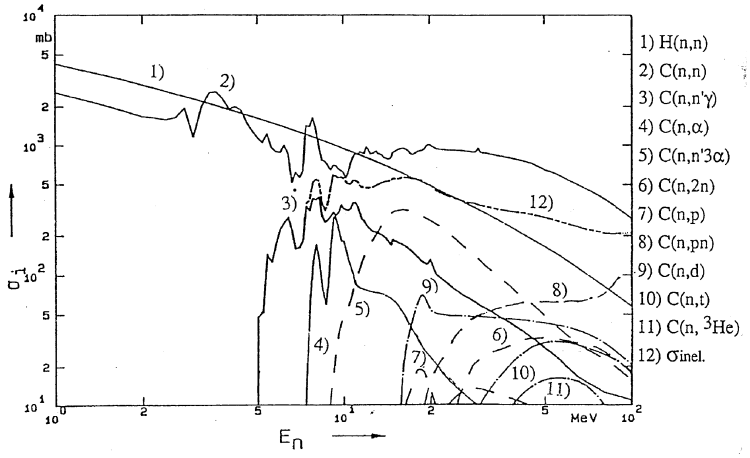

Figure 2.25: Cross sections of the reactions induced by neutrons between 1 and 100 MeV on hydrogen and carbon. From [65].

transfer energy to the scintillator electrons by Compton scattering or by photoelectric effect at very low energy. Compton scattering can take place in the detector yielding to a high energy

electron that in turn produces a column of ionisations as it traverses the volume of the cell.

2.2.1.1 Mechanisms for fast neutron detection: kinematic approach

The reference systems in which a reaction can be studied is the laboratory frame or that of the centre of mass. In the latter system, the centre of mass (CM) of the particles which interact is at rest and the total momentum is zero. Fig. 2.26 schematises the two reference systems and shows the coordinates of the neutron and the nucleus, a proton or a carbon, in each system. The

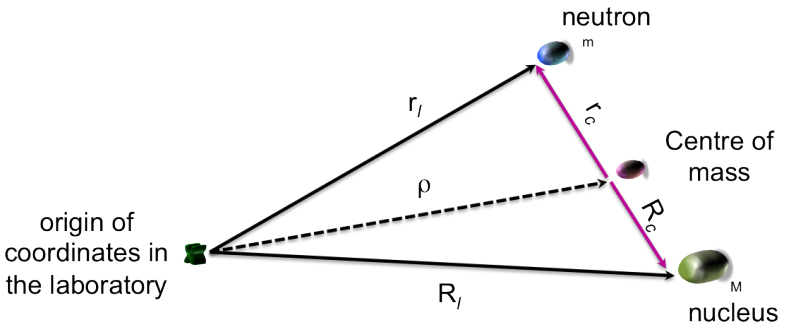

Figure 2.26: Coordinate systems

different coordinates are expressed as follows:

$$\begin{array}{lll} \vec{\rho} = \dfrac{m\vec{r}_l + M\vec{R}_l}{m+M} & \vec{v}_0 = \dfrac{m\vec{v}_l + M\vec{V}_l}{m+M} & \vec{v}_0 = \dfrac{m}{m+M}\vec{v}_l \approx \dfrac{1}{1+A}\vec{v}_l \\ \vec{r}_c = \vec{r}_l - \vec{\rho} & \vec{v}_c = \vec{v}_l - \vec{v}_0 \xrightarrow{\vec{V}_l=0} & \vec{v}_c \approx \vec{v}_l - \dfrac{1}{1+A}\vec{v}_l = \dfrac{A}{1+A}\vec{v}_l \\ \vec{R}_c = \vec{R}_l - \vec{\rho} & \vec{V}_c = \vec{V}_l - \vec{v}_0 & \vec{V}_c = -\vec{v}_0 \approx -\dfrac{1}{1+A}\vec{v}_l \end{array}$$

If the nucleus is at rest in the laboratory frame ($\vec{V}_l = 0$), the total kinetic energy in the laboratory and in the CM will respectively be:

$$\xrightarrow{lab} E_l = \frac{1}{2}mv_l^2 \qquad \xrightarrow{CM} E_c = \frac{1}{2}mv_c^2 + \frac{1}{2}MV_c^2 \approx \frac{1}{2}\frac{mM}{m+M}\vec{v}_l^2 = \frac{M}{m+M}E_l$$

The kinetic energy in the CM is lower than that in the laboratory. In an elastic collision, in addition to the conservation of total energy, there is also the kinetic energy conservation. Therefore we apply simultaneously:

1. the conservation of kinetic energy;
2. the conservation of linear momentum.

In fig. 2.27 we see the scheme of the impact seen from the laboratory and the centre of mass (CM). In the CM system the magnitude of the neutron and the nucleus velocities before and after the

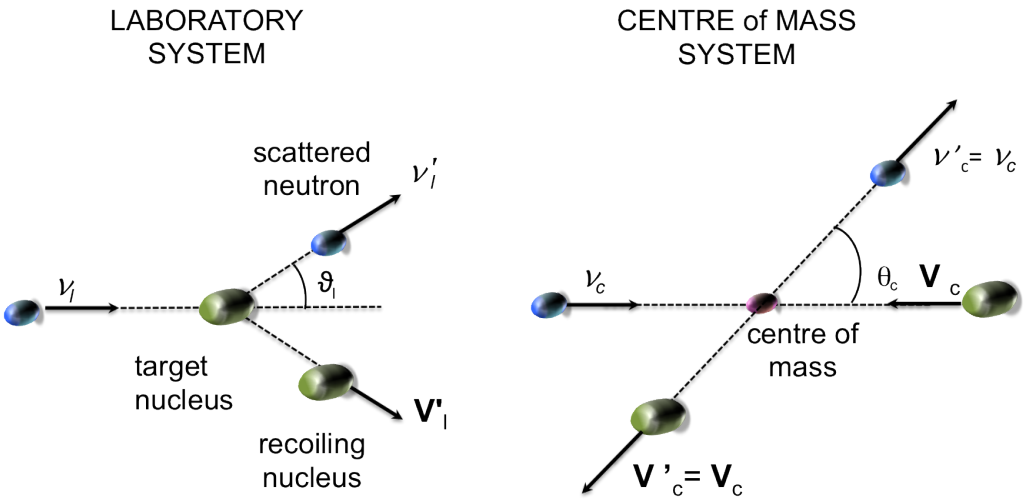

Figure 2.27: Kinematic representation in the laboratory system and in the CM.

collision remain unchanged, only their directions change, i.e:

$$v_c = v'_c$$
$$V_c = V'_c$$

The relation between the scattering angles of the neutron in the CM and in the laboratory, drawn in fig.2.28, starting from the diagram of the velocity vectors after the collision, is computed:

$$\vec{v}'_l = \vec{v}'_c + \vec{v}_0 \qquad\qquad v'_l \sin\theta_l = v'_c \sin\theta_c$$
$$v'_l \cos\theta_l = v'_c \cos\theta_c + v_0$$

The ratio gives:

$$\tan\theta_l = \frac{v'_c \sin\theta_c}{v_0 + v'_c \cos\theta_c}$$

In the case of the nucleus at rest in the laboratory, this formula is simplified by taking into

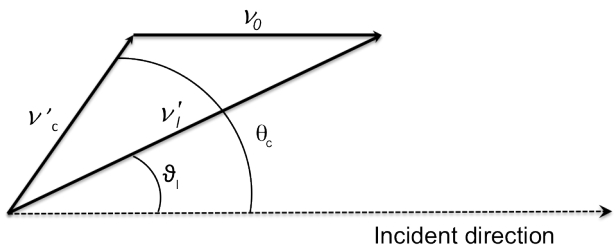

Figure 2.28: Diagram of the velocities after the collision: the neutron scattering angles in the CM and in the laboratory frame are sketched.

account the relations valid in the elastic scattering that allow to express $\vec{v}_0$ and $\vec{v}_c^{'}$ in terms of $\vec{v}_l$:

$$\vec{v}_c^{'} = \vec{v}_c = \frac{A}{1+A}\vec{v}_l \qquad \text{and} \qquad \tilde{\mathrm{v}}_0 = \frac{1}{1+\mathrm{A}}\tilde{\mathrm{v}}_1 \tag{2.27}$$

The following relation between the angles in the two system references, independent of the velocity, is obtained:

$$\tan\theta_l = \frac{\sin\theta_c}{\cos\theta_c + \frac{1}{A}}$$

and from further geometrical considerations this formula is computed as

$$\cos\theta_l = \frac{1 + A\sin\theta_c}{\sqrt{A^2 + 2A\cos\theta_c + 1}} \tag{2.28}$$

The relation in the laboratory frame between the kinetic energies E_l and E_l' of the neutron before and after the collision is computed starting from the cosine rule in the triangle $v_c' v_0 v_l'$ applied to the corner $v_c' v_0$:

$$\vec{v}_l^{'2} = \vec{v}_c^{'2} + \vec{v}_0^2 + 2\vec{v}_c^{'}\vec{v}_0\cos\theta_c \tag{2.29}$$

Taking into account the relations 2.27 and 2.28 the energy E_l' is computed as

$$v_l^{'2} = v_l^2\frac{A^2 + 2A\cos\theta_c + 1}{(1 + A\sin\theta_c)^2} \longrightarrow E_l' = E_l\frac{A^2 + 2A\cos\theta_c + 1}{(1 + A\sin\theta_c)^2} \Rightarrow \frac{E_l'}{E_l} = \frac{A^2 + 2A\cos\theta_c + 1}{(1 + A\sin\theta_c)^2} \tag{2.30}$$

and introducing the parameter $\alpha = \left(\frac{A-1}{A+1}\right)^2$ related to the mass A of the nucleus target, the neutron kinetic energy in the laboratory after the collision is given by

$$E_l' = \frac{1}{2}E_l[(1+\alpha) + (1-\alpha)\cos\theta_c] \tag{2.31}$$

from which one can derive the maximum and minimum energy. Thus the neutron after the collision appears in the CM with an energy range between $[\alpha E_l; E_l]$. αE_l corresponds to the minimum neutron energy and occurs when $\theta_c = \pi$, i.e when the neutron is scattered backwards. Otherwise the emerging neutron energy equal to E_l occurs for ahead scattering, when $\theta_c = 0$. In this case the neutron emerges with the same energy as the incident one. The α parameter is actually the ratio between the neutron minimum energy after the impact and its incident energy:

$$\alpha = \frac{E_{lmin}'}{E_l} \tag{2.32}$$

The energy of the scattered neutron depends on the emission angle in the CM. If the emission is isotropic in the CM it can be easily obtained. If we denote by $P(E \to E')$ the probability that a neutron of incident energy E leads to an energy E', it can be written as:

$$P(E \to E') = \frac{1}{E(1-\alpha)} \qquad if \qquad \alpha E < E' < E$$
$$P(E \to E') = 0 \qquad if \qquad E' < \alpha E$$

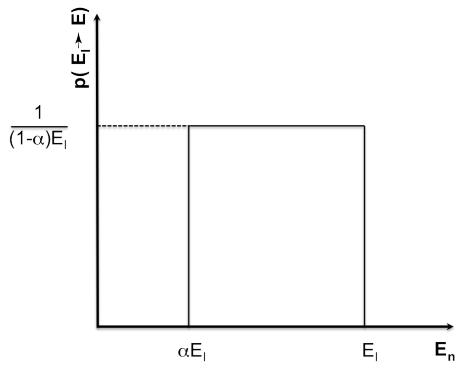

Figure 2.29: Probability of a neutron to have a given energy E_n between the minimum αE_l and the maximum E_l.

Thus, in the elastic and isotropic scattering in the CM after a single impact, the neutron can be scattered with equal probability at any energy E_n in the range $\alpha E < E' < E$, as shown in fig.2.29. Therefore, the average energy of the scattered neutron is:

$$\bar{E}' = \int_E^{\alpha E} E' P(E \to E')\, dE' = \frac{1}{E(1-\alpha)} \frac{1}{2} [E^2 - \alpha^2 E^2] = \frac{1}{2} E(1+\alpha) \tag{2.33}$$

From this formula we can calculate the average energy lost by the neutron as the difference between the energy of the incident neutron and the scattered one:

$$\bar{E}_{loss} = E - \bar{E}' = E - \frac{1}{2} E(1+\alpha) = \frac{1}{2} E(1-\alpha) \tag{2.34}$$

As we see the neutron looses its maximum energy on light nuclei and fewer and fewer as the mass of the target nucleus increases as shown in table 2.4 . On hydrogen neutrons lose an average of half of their energy in a single impact, while only 11% on oxygen and even less on uranium (approximatively 1%). This is the reason why the slowing down of neutrons is entrusted to hydrogenated materials (water, paraffin, polyethylene, ...) and in general materials with low mass number A as boron and carbon (graphite). Starting from expression 2.28 that binds the

nuclei	A	α	E_{loss}
H	1	0	0.5E
D	2	0.111	0.445E
C	12	0.716	0.143E
O	16	0.779	0.111E
Fe	56	0.931	0.0345E
U	238	0.981	0.0095E

Table 2.4: Neutron energy losses on different nuclei of mass A together with the α parameter.

scattering angles in the laboratory and in the CM we can calculate the average scattering angle

in the laboratory. In the case of an isotropic scattering in the CM , the laboratory scattering angle is simply:

$$\langle \cos\theta_l \rangle = \frac{1}{2}\int_{-1}^{1} {}_E \frac{1 + A\sin\theta_c}{\sqrt{A^2 + 2A\cos\theta_c + 1}}\, d(\cos\theta_c) = \frac{2}{3A} \tag{2.35}$$

Thus, the average value of the $\cos\theta_l$ in the laboratory is simply connected to the mass of the target nucleus. The smaller the mass of the nucleus A, the smaller the scattering angle: for $A = 1, \langle\theta_l\rangle = 48°$ and if $A = 238, \langle\theta_l\rangle = 89.8°$. When $A \to \infty$, $\langle\theta_l\rangle \to \frac{\pi}{2}$.

As a special case of neutron-nucleus scattering, we can consider the neutron-proton scattering. In this case the same relations obtained previously for a neutron-nucleus impact are valid with now A = 1. The previous relations become:

$$\begin{aligned}
\xrightarrow{lab} \quad & \vec{v}_0 = \frac{m}{m+M}\vec{v}_l \approx \frac{1}{1+A}\vec{v}_l = \frac{1}{2}\vec{v}_l \\
\xrightarrow{CM} \quad & \vec{v}_c \approx \vec{v}_l - \frac{1}{1+A}\vec{v}_l = \frac{A}{1+A}\vec{v}_l \approx \frac{1}{2}\vec{v}_l \\
& \vec{V}_c = -\vec{v}_0 \approx -\frac{1}{1+A}\vec{v}_l \approx -\frac{1}{2}\vec{v}_l
\end{aligned}$$

Regarding the relation between the scattering angles in the CM and in laboratory they become the following:

$$\tan\theta_l = \frac{\sin\theta_c}{\cos\theta_c + \frac{1}{A}} = \frac{\sin\theta_c}{\cos\theta_c + 1} = \tan\frac{\theta_c}{2}$$

Thus:

$$\theta_l = \frac{\theta_c}{2}$$

θ_c varies between 0 and π whereas θ_l varies between 0 and $\frac{\pi}{2}$: there is no backscattering of the neutron in the laboratory in the case of elastic scattering with a proton. Thus neutrons always go forward in respect with the incidence direction.

All the kinematic relations developed above intervene in the simulation code presented in chapter 3. In particular they were useful to test the output of GEANT 4 and to understand in detail the behaviour of the simulation and experimental observables.

2.2.1.2 Pulse shape discrimination

The mechanism by which a fraction of the kinetic energy of the recoiling particles is transformed into visible light in an organic scintillator is very complex. However, a few features can be simply stated. The major components of the scintillator light decay in times of the order of a few nanoseconds. This means that in principle, organic scintillators can operate at very high counting rates. However, there is a weaker component of the radiation for many scintillators that corresponds to delayed fluorescence. Consequently, the total light output can be represented as the sum of the two exponential decays referred to as the fast and slow components of the scintillation. The slow component has a characteristic decay time in the range of a few hundred nanoseconds. The fraction of the total light observed in this weaker slow component is

a function of the type of particle inducing the radiation.
This mechanism will be presented more in detail in Appendix A dedicated to a R&D on a new material for neutron detection carried out in parallel with the CORA experiment.

2.2.2 Electronics and data acquisition

DEMON's electronics is based on the VXI standard. This electronics, novel and very powerful when DEMON was built, allowed to tune in a very convenient way by computing at once the different parameters of all the sixty individual electronic channels. As this electronics has now become obsolete with the advent of the digital systems, there is no need to detail its operation mode which can be found in reference [66]. Instead a digital FASTER module developed at the LPC of Caen and used for the above mentioned R&D will be presented in Appendix B.
DEMON has an independent acquisition system which allowed to combine the VXI electronics of DEMON and the CAMAC and VME one of CODIS. To avoid the registration of γ background, the usual operation of DEMON needs a master trigger. The trigger module specially designed for DEMON allows to select simultaneously different kind of events which will be registered. In the CORA experiment, four trigger conditions were used:

- a coincidence of at least one CODIS signal validated outside and two DEMON signals; a DEMON signal can come from a neutron or a γ. This condition constituted the main trigger of the experiment
- a coincidence of two CODIS signals corresponding to the two fission fragments, sampled by an important reduction factor (down scaling)
- any DEMON channel. This trigger was used for the DEMON calibration and switched of during the real runs
- a pulse generator to check the stability of the CODIS electronics, operated with a low counting rate not to increase the dead time.

To minimise the dead time DEMON works in an asynchronous mode. This means that any individual DEMON signal starts its own time encoder. If the trigger validates the event, the encoding of the corresponding DEMON parameters is pursued; otherwise the electronics is reset. A common stop is delivered by the trigger signal after a given delay.realis

2.2.2.1 Electronics and data acquisition

Each VXI channel of DEMON encodes three quantities related to an outcoming anode signal of an individual DEMON cell:

- TAC: a TDC (time-to-digital converter) allows to encode on 8K channels a time range of about 800 ns
- Q_{tot}: the anode signal of a DEMON cell is integrated over its entire length by a QDC (charge-to-digital converter) on a tunable gate set to about 350 ns and encoded on 8K

– Q_{slow}: the slow component of the anode signal is also integrated with a delay of about 70 ns after the total charge. The gate is stopped at the same time as the Q_{tot}'s one. It is also encoded on 8K.

The integration principle and the parameters adopted are presented on the left part of fig. 2.30. As the slow component of a neutron is very different from a γ one, for a similar total charge, the Q_{tot}-Q_{slow} correlation allows to discriminate the γ's from the neutrons as shown on the right part of fig. 2.30.

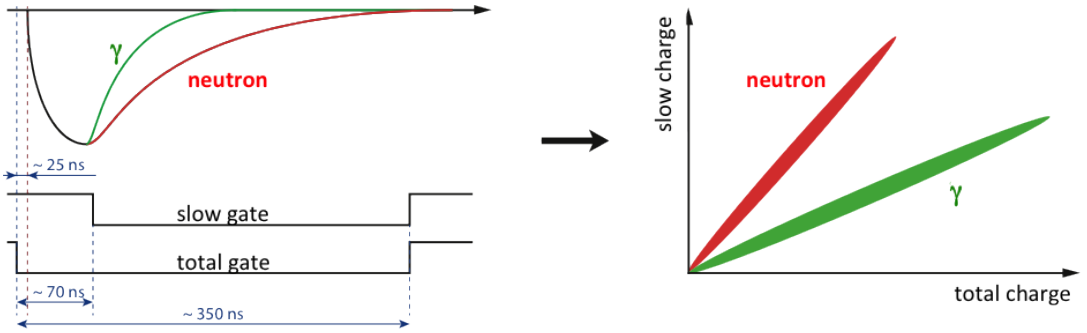

Figure 2.30: Diagram of the outcoming signals of a discriminating scintillator which indicates the different slow components of a γ-ray and a neutron together with the integration gates of the signals (left part) and the resulting correlation between the two integrated charges, Q_{slow} vs Q_{tot}, which exhibits the neutron-γ discrimination (right part).

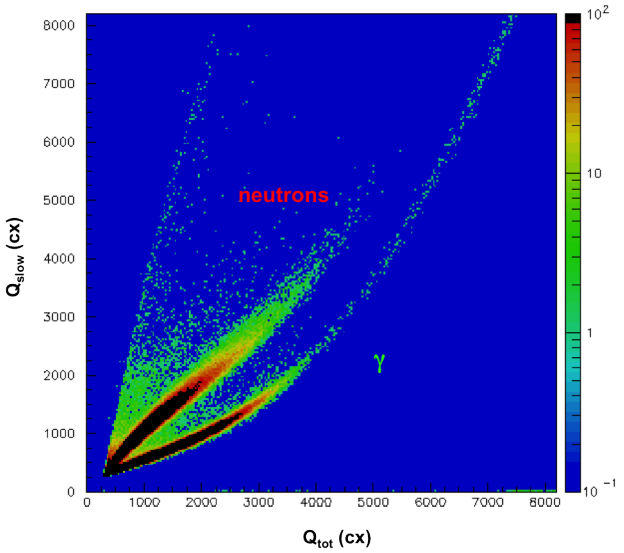

Figure 2.31: Q_{slow} versus Q_{tot} two-dimensional spectrum of an individual DEMON cell in the CORA3 experiment.

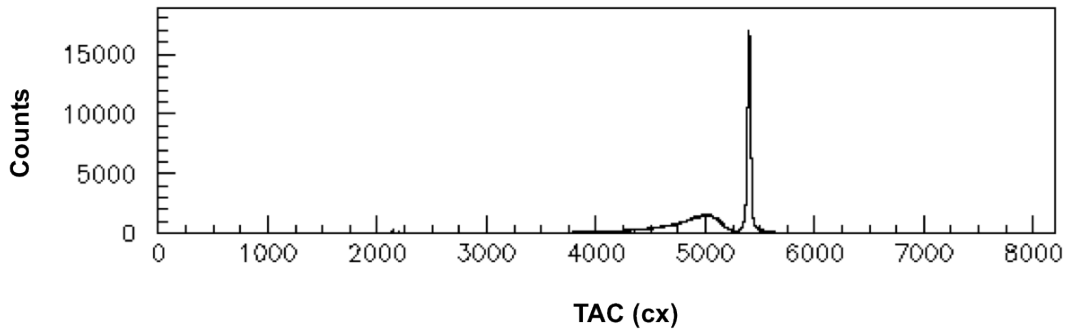

Figure 2.32: TAC signal: raw time of flight spectrum of a DEMON cell. The asynchronous mode implies that the γs have higher TAC values than the neutrons.

Fig. 2.31 shows a measured Q_{slow} - Q_{tot} spectra of an individual detector in the CORA experiment.
Fig. 2.32 shows a raw TDC spectrum of an individual DEMON cell. As DEMON works in an asynchronous way, the γs have a higher TAC value than the neutrons.

2.2.2.2 DEMON calibration

To exploit all the registered data, a number of calibrations are required in order to transform the raw encoded data into physical parameters. The different stages of this operation are:

1. **neutron-γ discrimination.** As mentioned the scintillators made of organic liquid are sensitive not only to the charged particles and neutrons but also to γ radiation. For the purpose of this thesis only the information carried by neutrons are important. The DEMON detectors are placed in the air and the charged particles, possibly issued from the fission reaction, have a low energy and do not reach the DEMON detectors in the geometrical configuration used. Conversely, γ radiation is detected and must be separated from neutrons.
   Instead of using the Q_{slow} - Q_{tot} correlation to discriminate the neutrons from the γ's, we preferred to use the correlation Q_{tot}-Q_{ratio}, where Q_{ratio} is the ratio between Q_{slow} and Q_{tot} after substraction of the pedestal of each charge:

$$Q_{ratio} = \frac{Q_{slow} - Q_{slow_{pedestal}}}{Q_{tot} - Q_{tot_{pedestal}}} \tag{2.36}$$

   The left part of fig. 2.33 shows a typical spectrum of this correlation. One can observe two well separated branches: the top one corresponds to the neutrons and the bottom one to the γs. For each of the sixty channels, a fourth degree polynomial is adjusted as shown by the red curve from graphically chosen (Q_{tot} - Q_{ratio}) couples. This polynomial defines the region populated by neutrons. The particles identified as neutrons are plotted in the right part of fig. 2.33.

The polynomial is obtained starting from the coordinates (Q_{tot}, Q_{ratio}) shown in fig. 2.33,

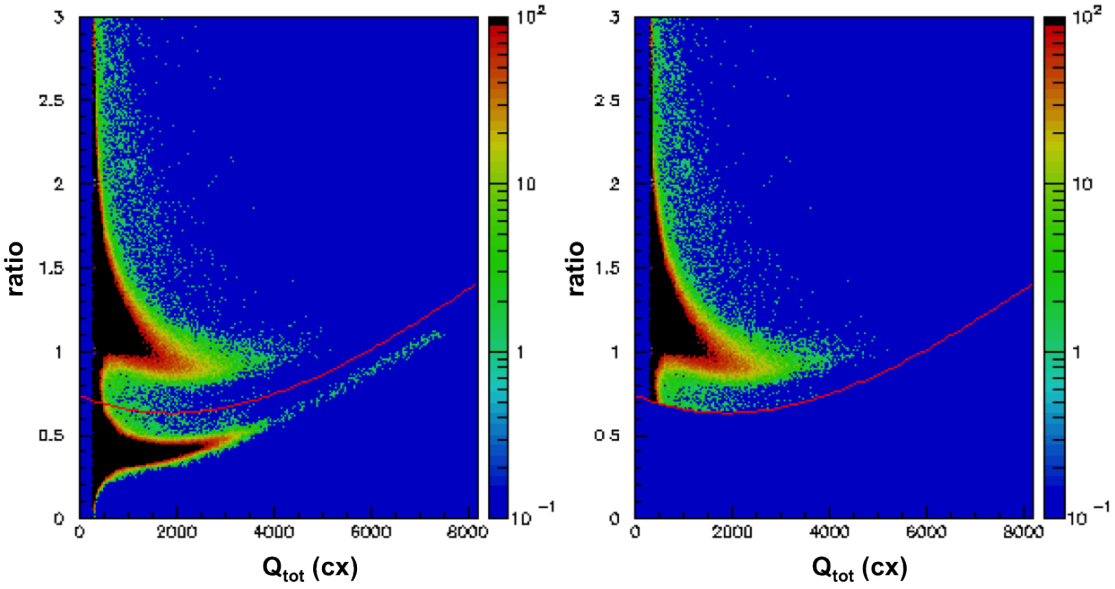

Figure 2.33: Left: Two dimensional plots showing the ratio between the slow and the total components subtracted each by its pedestal versus the total charge Q_{tot} for a typical DEMON cell. In red the polynomial obtained with the Vandermonde technique [67]. Right: Selection of the neutrons in this representation.

in the following way:

- suppose that the interpolation polynomial is of the form:

$$p(x) = a_n x^n + a_{n-1} x^{n-1} + \cdots + a_2 x^2 + a_1 x + a_0. \tag{2.37}$$

- $p(x)$ interpolates the data points $p(x_i) = y_i$ for all i $\in \{0, 1, \ldots, n\}$. If we substitute these coordinates in eq. 2.37, we get a system of linear equations in function of the coefficients a_k. The system in a matrix-vector form reads:

$$\begin{bmatrix} x_0^n & x_0^{n-1} & x_0^{n-2} & \ldots & x_0 & 1 \\ x_1^n & x_1^{n-1} & x_1^{n-2} & \ldots & x_1 & 1 \\ \vdots & \vdots & \vdots & & \vdots & \vdots \\ x_n^n & x_n^{n-1} & x_n^{n-2} & \ldots & x_n & 1 \end{bmatrix} \begin{bmatrix} a_n \\ a_{n-1} \\ \vdots \\ a_0 \end{bmatrix} = \begin{bmatrix} y_0 \\ y_1 \\ \vdots \\ y_n \end{bmatrix}$$

  where (x_i, y_i) corresponds to the coordinates (Q_{tot_i}, Q_{ratio_i}) chosen on fig. 2.33. We have to solve this system for a_k to construct the interpolant $p(x)$. The matrix on the left is commonly referred to as a Vandermonde matrix. The obtained polynomial is:

$$Q_{ratio} = a_0 + a_1\, Q_{tot} + a_2\, Q_{tot}^2 + a_3\, Q_{tot}^3 + a_4\, Q_{tot}^4 \tag{2.38}$$

To verify that the separation method adopted to select the neutrons works well and to optimise this separation, especially for small charges where it is not possible to distinguish

between neutrons and γ's and corresponding mainly to low energy neutrons, an additional cut is applied on the TAC spectrum. Fig. 2.34 shows the TAC histogram, in black and blue respectively, before and after the charge discrimination is performed. The remaining γ's of the blue curve are taken off by a cut in the TAC spectrum as shown by the red line. The final neutron spectrum is shown in red. Combining these two methods, a satisfying discrimination between neutrons and γs is obtained.

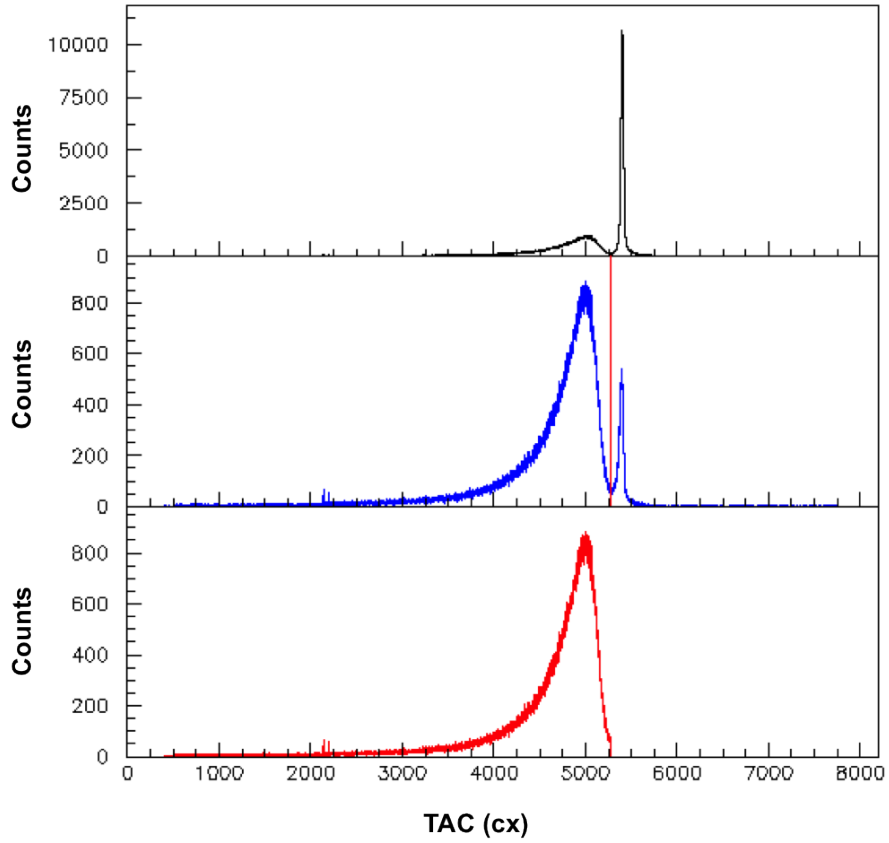

Figure 2.34: TAC spectra of an individual cell for all events (black), after the charge discrimination (blue) and after the TAC separation indicated by the red line (red).

2. **Time calibration.**
   The TAC parameter provides also the time of flight of the neutrons from which the neutron energy is deduced. For each cell, we must transform the raw time, the TAC "T" parameter expressed in channels, in a physical quantity "t" given in nanoseconds. The calibration curve is written in the following form:

$$t_i(ns) = b_i - a_i\, T_i(channels) \tag{2.39}$$

   where the calibration parameters a_i and b_i of the curve are computed for each of the

sixty cells. The negative value of the slope in the equation is due to the asynchronous acquisition mode. This procedure reverses the time scale. The adjustment of the time of flight is performed in two steps. First the TDC slope calibration is evaluated. The slopes a_i were calibrated with a time calibrator and determined with linear regressions as $t_i(ns) = a_i\, T_i(channels)$. The linearity over the entire range of the TDC has been verified. After, the intercepts b_i were evaluated using the γ peaks. The γ times of flight are known as they move at the light velocity and the flight distances have been deduced from a precise measurement of the coordinates of each cell relative to the ^{252}Cf source central point.

3. **Neutron energy determination.**
The energy of the neutrons is obtained by their time of flight. To calculate the neutron energy, we need another ingredient. The interaction depth d_n^{int} of a neutron in a DEMON module has to be considered as the DEMON cells have a depth of 20 cm and the flight distances are quite short, ranging from 60 to 95 cm. Thus we have to consider that the flight distance of a neutron is $d_n = D + d_n^{int}$ where D is the distance between the source and the input face of the cell. To computed the interaction distance d_n^{int}, we have developed an iterative algorithm based on *MENATE* [68]. The *MENATE* simulation calculates the neutron interaction distance in a DEMON cell as a function of its energy:

$$E_n = \frac{1}{2}\frac{M_n}{c^2}\left(\frac{d_n}{t_n}\right)^2 \tag{2.40}$$

The fundamental steps of the algorithm are:

- at the beginning of the procedure an interaction distance $d_n^{int,0}$ is defined arbitrary;
- knowing the neutron time of flight t_n, the energy E_n^0 is computed from eq. 2.40;
- a new interaction distance $d_n^{int,1} \neq d_n^{int,0}$ is evaluated as the distance matching with the *Menate* simulation energy E_n^0;
- starting from $d_n^{int,1}$, E_n^1 is computed. This new value is compared to the energy E_n^0 assigned to the previous distance $d_n^{int,0}$ predicted by *MENATE*.

The iterative process stops when the energies E_n^{k+1} and E_n^k are close enough ($\delta < 1\%$). When the convergence is realised, the estimated neutron energy is $E_n = E_n^k$ and the interaction distance $d_n^{int} = d_n^{int,k}$. Fig.2.35 shows the neutron energy spectra for the sixty DEMON cells. They have been grouped following the vertical columns of the geometrical mounting indicated on the top of the figure. One can notice that the different groups of six detectors corresponding to each column have coherent behaviours: a maximum counting rate for the central row and equivalent ones for symmetric layers, except for detector 12 which has been removed from the analysis. However, the method used for the neutron energy determination is an approximation because of the scattering of the neutrons inside the sensitive volume of the DEMON cells. Therefore, the distance d_n^{int} does not correspond to the real distance traveled by the neutron during the time t_n. Therefore we investigated the possibility to adapt the *backtracing* method developed by P. Désesquelles [69, 70], still

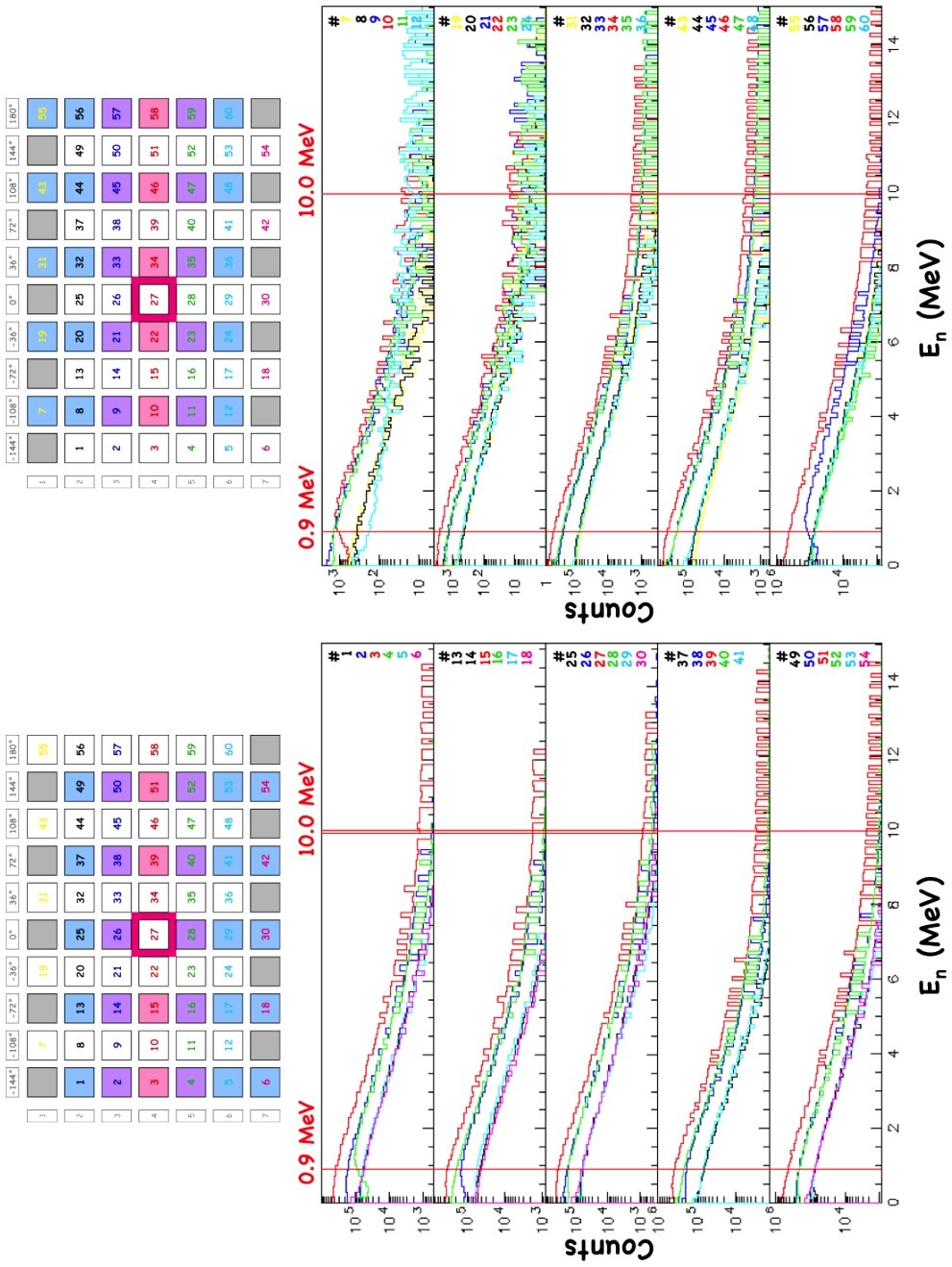

Figure 2.35: Energy spectra of the sixty DEMON cells grouped by columns as indicated on the top of the figure. Similar columns are presented in the two figures. The vertical lines show the common limits of the neutron energies taken into account: a threshold of 0.9 MeV and an upper limit of 10 MeV.

based on the *MENATE* code, to compute in a more accurate way the neutron energy spectrum.

Neutron energy determination with the backtracing method: The kinetic energy of a neutron is determined experimentally by measuring its time of flight and flight distance from the source to the detector. However, this determination is vitiated by errors since the exact location of the interaction of the neutron within the detector is unknown. Moreover, more than one interaction may be necessary for the deposited energy to reach the detector threshold. As mentioned before one method consists to determine the interaction distance d_n^{int}. A more precise estimator of the neutron energy is given by the *backtracing* [69, 70] procedures.

Very generally the backtracing approach searches for a solution to a problem among all available options. It does so by assuming that the solutions are represented by the vectors $(v_1, ..., v_i)$ where every element must be selected in an ordered set of possible candidates for the position i. When invoked, the algorithm starts with an arbitrary vector. At each stage it extends the partial vector with a new value. When reaching a partial vector $(v_1, ..., v_i)$ which can't represent a partial solution, the algorithm backtracks by removing the trailing value from the vector and then proceeds by trying to extend the vector with alternative values.

The backtracking builds a tree of solutions where every vertex is a partial solution and the branch goes from a vertex x to another vertex y. The vertex y is created extending the partial solution of the vertex x. The leaves of the tree are the solutions. In our particular case it consists in the determination of the energy distribution of the neutrons emitted by a source, knowing the detected time of flight distribution $P_{\rm det}(t)$ and the response function of the detector $P_{\rm sim}(t|E)$. The method is based on the inverse problem and is given by equation:

$$P_{\rm det}(t) = \sum_E P_{\rm sim}(t|E)\, P_{\rm sou}(E) \tag{2.41}$$

where $P_{\rm sou}(E)$ is the source distribution.

The estimator of the neutron energy $\bar{E}(t)$ is obtained by inversion of the simulated detector response function $P_{\rm sim}(t|E)$, and it reads:

$$\bar{E}(t) = \frac{\sum_E E\, P_{\rm sim}(t|E)\ P_{\rm sou}(E)}{\sum_E P_{\rm sim}(t|E)\, P_{\rm sou}(E)} \tag{2.42}$$

To compute $\bar{E}(t)$ an iterative method is applied. If k is the iteration number:

$$P_k(t) = \sum_E P_{\rm sim}(t|E)\, P_k(E) \tag{2.43}$$

$$P_{k+1}(E) = \sum_t P_k(E|t)\, P_{\rm det}(t) \tag{2.44}$$

$$= \sum_t \frac{P_{\rm sim}(t|E)\, P_k(E)\, P_{\rm det}(t)}{P_k(t)}$$

where $P_{\rm sim}(t|E)$ and $P_{\rm det}(t)$ are given by the simulation and the experiment respectively. Their normalisations are the following:

$$\sum_t P_{\rm sim}(t|E) = \varepsilon(E) \quad (2.45)$$

$$\sum_t P_{\rm det}(t) = \sum_E \varepsilon(E)\, P_{\rm sou}(E) \quad (2.46)$$

where $\varepsilon(E)$ is the detection efficiency and $P_{\rm sou}(E)$ is the energy distribution of the source we want to determine and which normalisation is:

$$\sum_E P_{\rm sou}(E) = 1 \quad (2.47)$$

The initial distribution of the backtracing $P_0(E)$ can be chosen arbitrarily as mentioned before. Usually, the iterations start with a flat distribution. One has to check that the $P_k(t)$ distribution converges towards $P_{\rm det}(t)$ using, for example, the Kullback-Leibler coefficient:

$$KL_k = \sum_t P_{\rm det}(t)\, \log\left(\frac{P_k(t)}{P_{\rm det}(t)}\right) \quad (2.48)$$

which must tend towards zero.

The iterative procedure is stopped when $\Delta KL(k) = KL_k - KL_{k+1}$ is less than a limit fixed by the user.

The details of this approach and its influence on the neutron energy spectra have given rise to a publication which has been submitted and accepted by Nuclear Instruments and Methods [71].

It has been shown that this method is more precise, especially for high neutron energies. But in our case, to optimise the algorithm development and computing times and given that the energy of the neutrons were not really used in our analysis, we decided to apply the more simpler method presented previously.

4. **Common energy threshold determination.**

The energy threshold of each individual DEMON cell has to be determined in order to set a common neutron threshold. This is necessary to take into account the intrinsic efficiency of DEMON. The experimental threshold has to be known also for the simulations presented in chapter 3. The threshold energy is determined by using known radioactive γ sources: ^{22}Na and ^{137}Cs. DEMON detectors do not provide distinctive photopeaks of the type that are normally used for γ spectroscopy, but only the Compton edge is recognized for these sources. The emitted light depends on the energy of the detected particle and on its charge Z. The light output produced in an organic scintillator is greater for an electron E_{e-} than for a recoiling proton E_p. The energy required to have 1 MeVee of light is by definition generated by an electron of energy equal to 1 MeV [2]. The empirical relation between the

2. Because of the dependence of the light yield of the organic scintillators on the particle type, a specific nomenclature is used to describe the *absolute* light yield. The term *MeV equivalent electron* or *MeVee* is introduced to place the light yield on the electron absolute basis. From [53].

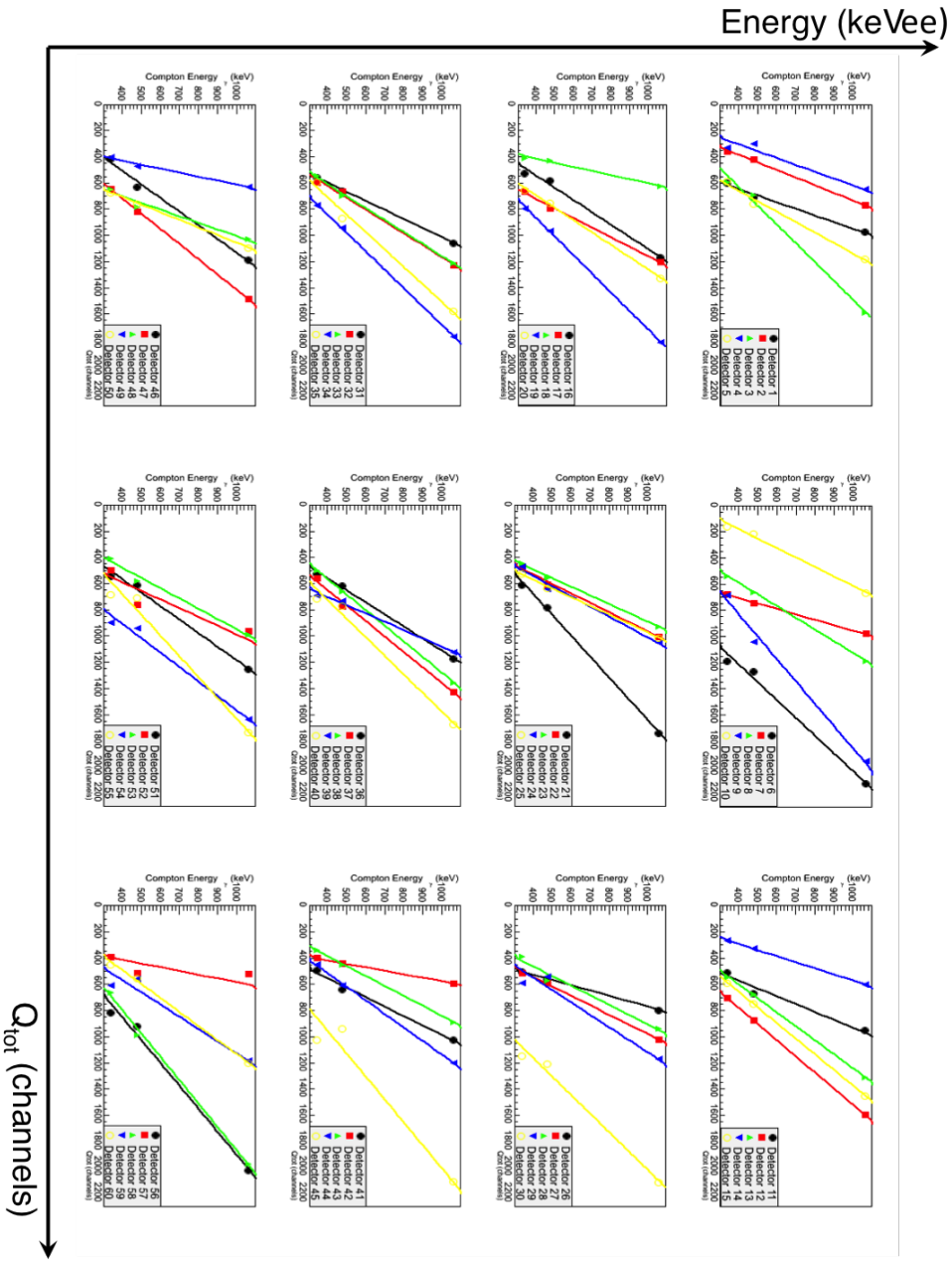

Figure 2.36: The deposited energy calibration fit for the 60 DEMON cells is shown.

energy of the recoiling proton (or incident neutron) and a Compton electron (or incident γ) is given by

$$E_p = 0.14505 + 0.017068.E_{e-}^{0.73267} \tag{2.49}$$

The energies of the Compton edges of those sources, given in tab. 2.5 allowed to obtain the

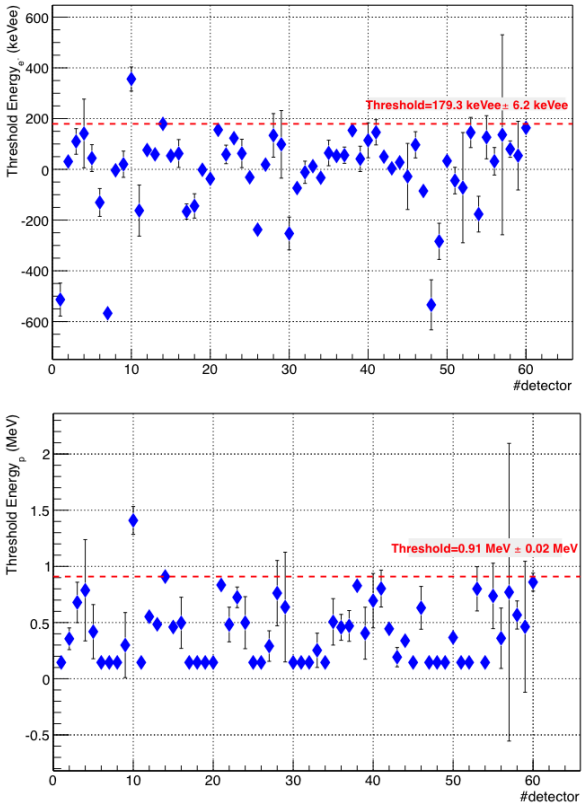

Figure 2.37: Energy thresholds of the sixty individual cells given by the total charge Q_{tot} in keVee (top) and transformed into neutron energy (bottom).

energy calibration in keVee of the total charge Q_{tot} for each cell. They were taken at 60% of the maximum of the Compton bump. A linear fit is applied on the three γ values and gives the relation between Q_{tot} (channels) and Q_{tot} (keVee).

Fig.2.36 shows the calibration curves obtained for the different cells. One can notice that the responses of the sixty cells are very different.

The common threshold is then determined as shown in fig. 2.37. It is given by detector 14 which has a threshold of 179.2 keVee corresponding, as shown on the bottom figure, to a neutron energy threshold of 0.9 MeV. Detector 10 which had a very high threshold was excluded from the analysis.

The energy threshold set on the total charges Q_{tot} and corresponding to the interaction threshold inside the DEMON cells is completed by an energy threshold set on the neutron energy deduced from the time of flight and set to the same value, 0.9 MeV. To consider the same energy range for each cell an upper common limit has also been set at 10 MeV.

Source	E_γ(keV)	Compton edge $E_{e^-Compton}$(keVee)
^{22}Na	511	341
	1274	1062
^{137}Cs	662	477

Table 2.5: Radioactive γ sources used for the calibration of the detection threshold of DEMON. For each of them are given the energy of the γ photopeak and the energy $E_{e^-Compton}$ corresponding to the Compton edge.

These two limits are indicated by the red lines on fig.2.35.

5. **Neutron angle determination.**
   The neutron angles are given by the central angles of each DEMON cell. The central position of each DEMON cell has been measured with a high precision. The central distances and the θ and ϕ angles have been deduced from the (x,y,z) measured coordinates relative to the central point of the ^{252}Cf source. Fig. 2.38 shows the neutron angles in a $\theta cos\phi$ - $\theta sin\phi$ plot which gives a pseudo-projection of the DEMON sphere on a vertical plane.

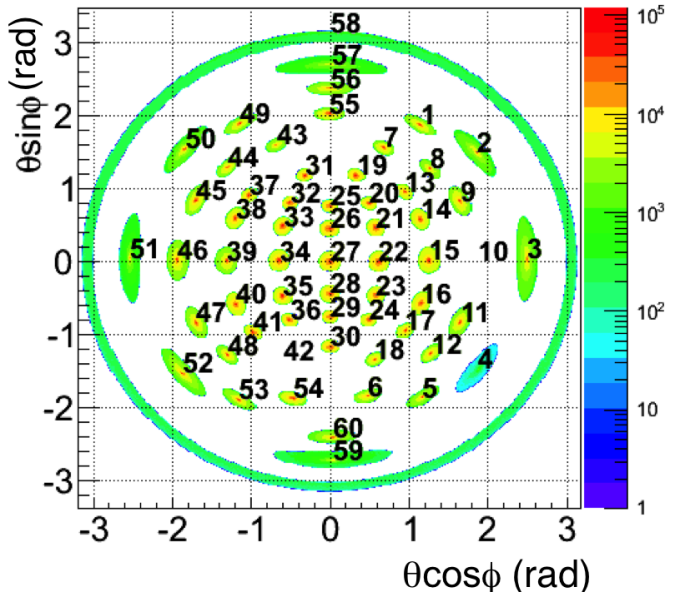

Figure 2.38: DEMON angular coverage in the $\theta cos\phi$ - $\theta sin\phi$ plane. From this representation emerges the coverage edge of each DEMON cell. The z-axis presents the experimental neutron yield hitting a cell. The number of the VXI identifying each DEMON cell is indicated.

.

Chapter 3

Simulations

As the CORA experiment is a multiple parameter experiment, considering DEMON as well as CODIS, it is very complex. Moreover the physical effects we are looking for are very weak. Thus careful and detailed simulations are mandatory.
To study the neutron emission a general-purpose and extensible software to accurately simulate neutron distributions emitted in the spontaneous fission of ^{252}Cf has been developed. The Monte Carlo simulation is based on a simple evaporation model with the possibility to introduce the two mechanisms we are interested in, namely scission neutron emission and/or dynamical anisotropy in the CM of the two FFs.
These simulations have the purpose to study all the effects of the experimental filter:

- geometrical acceptance
- pileup
- DEMON detection threshold
- intrinsic detection efficiency of the DEMON detectors
- neutron cross talk
- central DEMON angles influence

Taking into account all these effects, the different distributions θ_{nn}, ϕ_{nn} and θ_{nLF} are simulated with the possibility to play with the parameters which quantify the contribution of scission emission and/or dynamical anisotropy. In this way it is possible to simulate different cases:

- pure isotropy
- introducing scission and/or anisotropy as predicted by theory [36] but also with various relative importance, including unrealistic high values.

This will allow to get a good feeling of the behaviour of these two mechanisms. The results of these simulations will then be confronted in the next chapter with the experimental distributions presented in chapter 2.

3.1 Introduction

The development of a simulation toolkit based on GEANT4 [72, 73], ROOT [74] and MENATE$_R$ has been adopted as a strategy to investigate the emission of the neutrons by the fission fragments. The GEANT4 code allows to define the CORA neutron detector configuration and to trace the neutrons. Once the neutrons emission along the fission process has been defined, GEANT4 produces complete further kinematical and dynamical information on the emitted neutrons, such as time, position, energy, momentum, etc. To track then the neutrons inside the detectors, the MENATE$_R$ code has been integrated into GEANT4. MENATE$_R$ is based on MENATE, a code initially developed by P. Désesquelles [68] in FORTRAN language and adapted for C++ by B. Roeder [75]. This code is especially well adapted to describe the neutron interactions in the DEMON detectors as it considers with high precision all the reaction cross sections in NE213 material. It allows to estimate with a high accuracy the intrinsic efficiency of the DEMON detectors.

All these ingredients are interlinked within the GEANT4 libraries and used in conjunction with a specific Monte Carlo transport code and provides an event-by-event list of neutrons for the ^{252}Cf fission process.
This code is data-driven as it incorporates also experimentally measured parameters at low energy fission obtained from literature and which were necessary to develop the simulation.

3.2 General features of the simulation toolkit

In each simulation a number of events were generated constituted of a fission axis, defined by the polar and azimuthal angles isotropically distributed and covering a 4π solid angle, two fission fragments, labeled as light (LF) and heavy (HF) and a number of emitted neutrons having specific angular distributions with respect to the fission axis.

Fission axis

To define the fission axis a random point on the surface of a unit sphere is picked. To that purpose two random variables u and v are chosen in the (0,1) interval. Then the fission axis plane is defined following the equations:

$$\phi = 2u\pi \qquad [0, 2\pi) \tag{3.1}$$

$$cos\theta = (2v - 1) \qquad [-1, 1] \tag{3.2}$$

Since the area element $d\Omega$ is defined as:

$$\begin{aligned} d\Omega &= sin\theta d\theta d\phi \\ &= d(cos\theta)d\phi, \end{aligned}$$

where Ω is the solid angle, these two quantities have to be used instead of simply θ and ϕ. By selecting the spherical coordinates θ and ϕ from uniform distributions ϕ in $[0, 2\pi)$ and θ in $[0, \pi]$, points picked will be "bunched" near the poles.

Fission fragments

Following the standard convention, the light fragment has the fission axis direction and consequently the heavy one has the same orientation but with the opposite sign. With these pre-

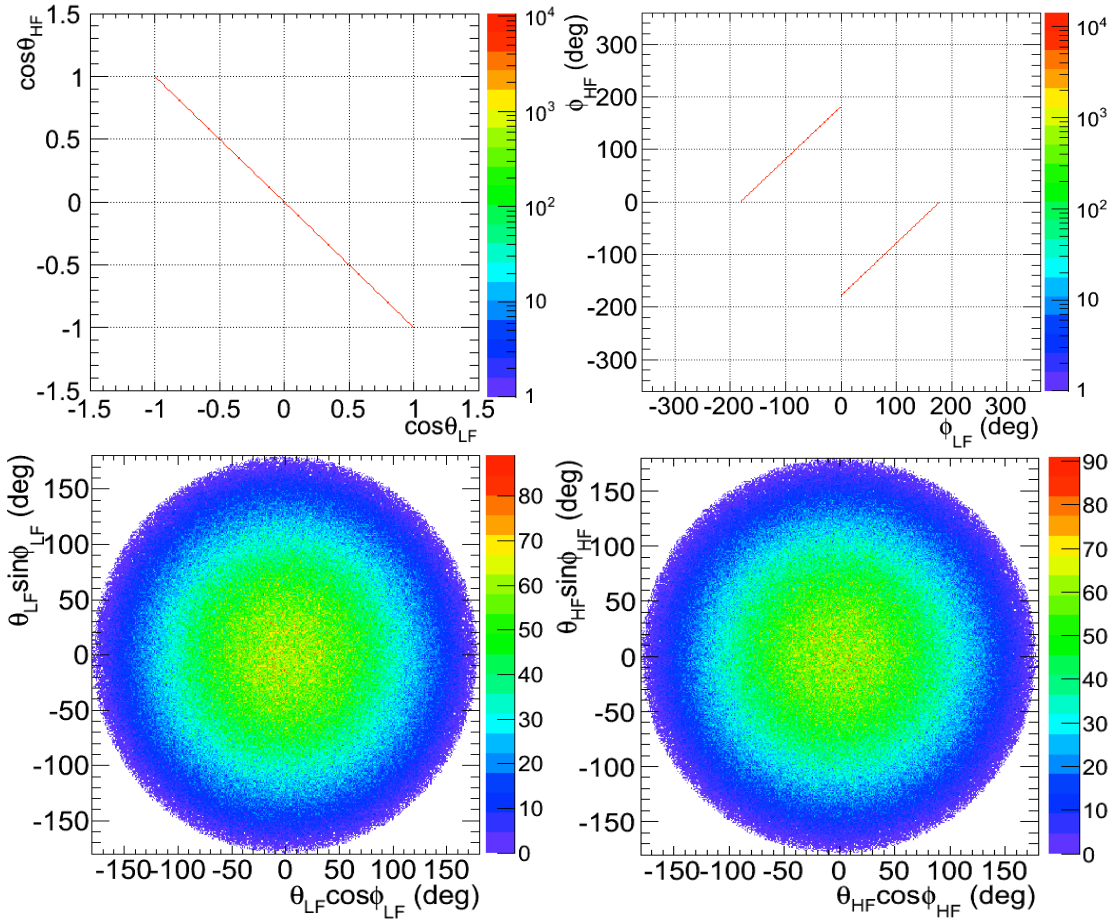

Figure 3.1: In the upper part of the figure the simulated correlation matrixes respectively in the $cos\theta_{HF}$ vs $cos\theta_{LF}$ and ϕ_{HF} vs ϕ_{LF} planes are shown. The histograms show the correctness of the simulations. The left figure shows that θ_{HF} and θ_{LF} are perfectly anticorrelated. From the second matrix of correlation on the right it is easy to deduce that the difference between the angles ϕ_{HF} and ϕ_{LF} is equal to 180° as expected. The bottom part shows that both the simulated LF (left) and HF (right) are emitted isotropically in the 4π space. One can notice also that these matrixes are coherent with the corresponding experimental ones presented in fig. 2.21 of chapter 2.

scriptions, the fragment velocity vectors are set with the magnitude obtained from literature averaged values. All the parameters characterizing the two fission fragments of ^{252}Cf are given in table 3.1. The simulated spatial fragment distributions and their main features are sketched

Parameter	LF	HF
v (cm/ns)	1.355	1.022
T (MeV)	0.91	0.93
$< \nu >$	2.056	1.710
σ	0.94	1.07

Table 3.1: In the table are shown the fission fragment parameters adopted in the simulation code.

in fig. 3.1.
In the simulation code, fission fragments are virtual particles, they were not traced by GEANT4, they are only used to set the initial conditions for the neutron emission. The FFs velocity vectors are necessary to compute the neutron angular distributions transformation from the FFs CM to the laboratory frame and also to study the neutron-fragment correlation.
Another necessary quantity is the fission fragment spin. It is assumed that each FF has a spin J, which is strictly perpendicular to the fragment flight direction and isotropically distributed in the perpendicular plane to the fission axis.

Neutron emission

The neutron multiplicity for each fission event is randomly taken from a gaussian distribution. The mean values of the multiplicity for each fragment and their standard deviation is given in table 3.2. To respect the realistic total multiplicity of ^{252}Cf these two distributions have to be correlated as will be described later. In this way a total number of neutrons per fission event is computed by adding the multiplicity randomly sampled of each FF.

	Initial		corrected		final
	A	ν	A_c	ν_c	ν_{cc}
LF	1	2.06	0.975	2.00	2.05
HF	1	1.71	0.935	1.60	1.72
total (^{252}Cf)		3.76		3.61	3.76

Table 3.2: The table indicates the initial areas A and the mean values of the multiplicity gaussian distributions, the corrected ones as explained in the text for both the light and the heavy fragments. The final mean multiplicities are also indicated as well as the resulting total multiplicity at the different steps of the procedure.

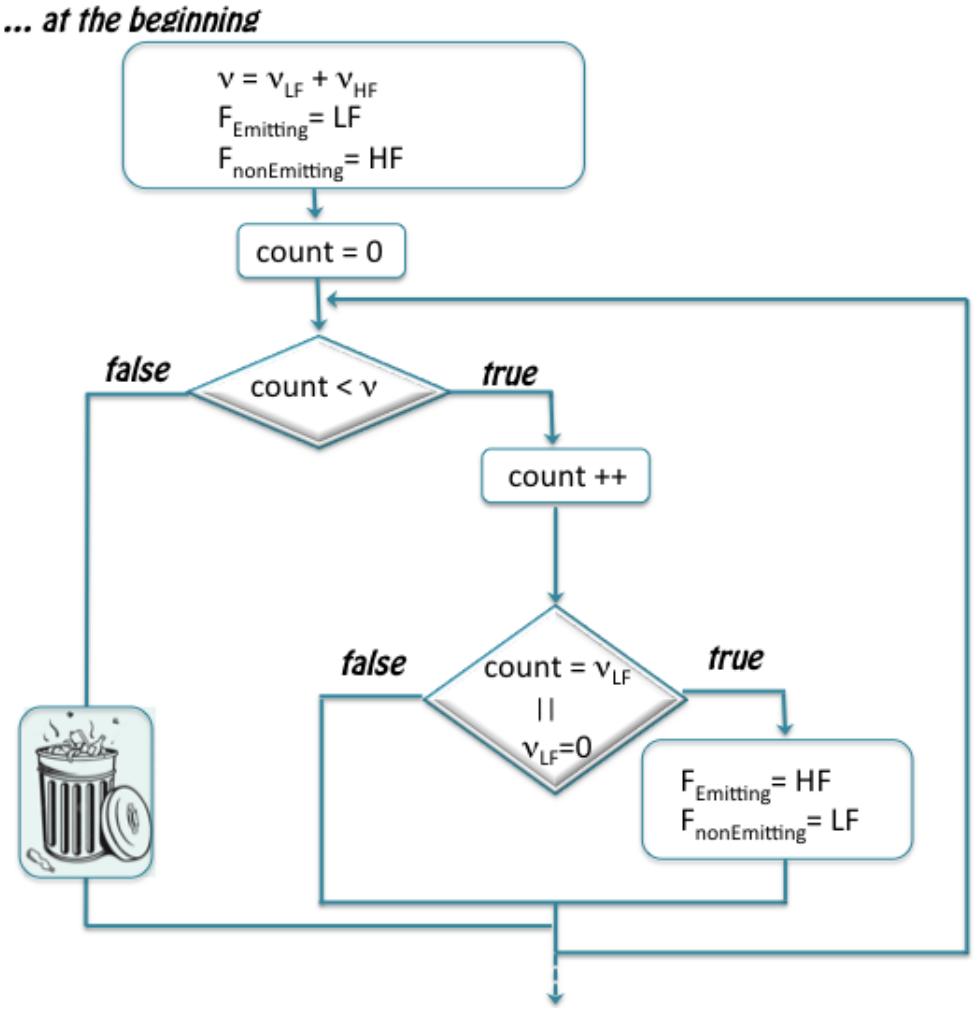

Figure 3.2: Flowchart representation of the algorithm adopted to simulate the neutron cascade emission. The emitting FF, LF or HF, is assigned to every prompt neutron.

After that the cascade emission is simulated. This procedure is sketched in fig. 3.2. The first step consists to define an emitting fragment; as a consequence its complementary fragment is set to a"non-emitting" status. This design allows to store together with each neutron, the properties of its source such as the position, the type, etc... . The emitting fragment evaporates neutrons until its assigned multiplicity is reached. When this happens the remaining neutrons are issued from the complementary fragment, which changes its status to the"emitting" label. The evaporation process stops when the total multiplicity is reached. Each neutron is emitted according to a specific polar angular distribution with respect to the FF spin J in the CM system as expressed by formula 1.9. The coefficient A_{nJ} of formula 1.9 can be set to zero in the case one wants to consider an isotropic emission. The azimuthal ϕ_{nJ} angle is generated randomly in the $[0°, 360°]$

range in the fragment CM frame also with respect to the spin axis.
The transformation from the CM to the laboratory system requires also to set the neutron velocities which are defined by the neutron energies generated according to a Maxwell distribution. This procedure will be discussed in more details later.

Up to now we considered only neutrons evaporated by the fully accelerated FFs. The possibility to emit scission neutrons has now to be introduced. In the simulation code a certain fraction ω_{sci} of the total multiplicity is set. Unlike prompt neutrons, this component is emitted isotropically in the laboratory and no coordinate system transformation is needed. In the simulation the scission neutron source is set to the ^{252}Cf source which is placed at the origin of the laboratory coordinate system.

All these ingredients characterize the neutron emission and constitute the primary vertexes required by GEANT4 to trace the neutrons and by MENATE$_R$ to take into account the interaction in the detectors. Each DEMON detector is represented by a cylinder 16 cm in diameter, 20 cm in length and constituted exclusively of NE213 liquid scintillator. The sixty detectors are placed according to the real experimental geometry. Vacuum is considered instead of air. This approximation has little influence on the results. No other materials constituting the detectors as glass and steel were considered. Neither were the structures supporting the detectors.

3.3 Simulation details

3.3.1 Neutron multiplicity distributions

As already mentioned the number of neutrons per fission event is randomly sampled for each fission fragment. Based on the J. Terrell's [76] assumptions, the probability $P(\nu)$ to observe ν neutrons emitted by a fission fragment can be approximated by a Gaussian-like distribution. Thus the probability density integral is:

$$\sum_{n=0}^{\nu} P(\nu) = \frac{1}{\sqrt{2\pi}} \int_{-\infty}^{\nu-\bar{\nu}+\frac{1}{2}+b} e^{-\frac{t^2}{2}}\, \mathrm{d}t \quad \text{where} \quad t = \frac{\nu-\bar{\nu}}{\sigma}. \tag{3.3}$$

where $\bar{\nu}$ is the average number of emitted neutrons, σ the width of the distribution and b a small correction factor ($b < 0.01$) which ensures that the discrete probability distribution has the correct average.
Following this prescription in the simulation the number of emitted neutrons per fission is randomly chosen by a two-dimensional gaussian distribution P($\boldsymbol{\nu}$), as presented in fig. 3.3, knowing the individual mean multiplicity of each FF and the empirically defined covariance as follows:

$$P(\boldsymbol{\nu}) = \frac{1}{2\pi\sqrt{|\Sigma|}}\, e^{\frac{1}{2}(\boldsymbol{\nu}-\bar{\boldsymbol{\nu}})^T \Sigma^{-1} (\boldsymbol{\nu}-\bar{\boldsymbol{\nu}})} \tag{3.4}$$

where $\bar{\boldsymbol{\nu}}$ is the two-dimensional vector of the mean values $\bar{\nu}_{\mathrm{LF}}$ and $\bar{\nu}_{\mathrm{HF}}$ of the random variables ν_{LF} and ν_{HF}:

$$\bar{\boldsymbol{\nu}} = \begin{bmatrix} \bar{\nu}_{\mathrm{LF}} \\ \\ \bar{\nu}_{\mathrm{HF}} \end{bmatrix}$$

and Σ is the covariance matrix:

$$\Sigma = \begin{bmatrix} \sigma^2_{\mathrm{LF}} & \sigma_{\mathrm{LF\ HF}} \\ \\ \sigma_{\mathrm{LF\ HF}} & \sigma^2_{\mathrm{HF}} \end{bmatrix}$$

where σ^2_{LF} and σ^2_{HF} are the variances of the random variables ν_{LF} and ν_{HF} and $\sigma_{\mathrm{LF\ HF}}$ is the covariance of ν_{LF} and ν_{HF} defined by the following equation:

$$2\sigma_{\mathrm{LF\ HF}} = \sigma^2_{\mathrm{Cf}} - \sigma^2_{\mathrm{LF}} - \sigma^2_{\mathrm{HF}} \tag{3.5}$$

where σ^2_{Cf} is the ^{252}Cf multiplicity distribution variance.The correlation coefficient of the variables ν_{LF} and ν_{HF} is defined as

$$\rho = \frac{\sigma_{\mathrm{LF\ HF}}}{\sigma_{\mathrm{LF}}\,\sigma_{\mathrm{HF}}} \tag{3.6}$$

Experimentally an appreciable anticorrelation has been highlighted in various works: when the light fragment neutron multiplicity increases the heavy one decreases. Vorobyev [77, 78] measured a covariance value of about -0.21 in the spontaneous fission of ^{252}Cf. J. R. Nix and W. J. Swiatecki [79] pointed out that this anticorrelation comes from the asymmetric distribution of the excitation energy between the two fragments.
The simulation code generates the multiplicities ν_{LF} and ν_{HF} for the light and heavy fragments as shown in fig. 3.3.
To generate randomly the latter quantities, the "NORMCO" procedure was coded. NORMCO [80] is a method to transform two random variables into a pair of bivariate normal numbers with a prescribed covariance matrix.

As the mean multiplicities $\bar{\nu}_{\mathrm{LF}}$ and $\bar{\nu}_{\mathrm{HF}}$ for ^{252}Cf are quite low, the probability to sample negative numbers of neutrons is not negligible. This situation would even be worse in the case of ^{235}U for which the total multiplicity is smaller. To generate neutrons, the simulation code requires only positive values. A rough solution would be to truncate negative values. But this would lead to a bad total multiplicity with a too high mean value.
To accurately reproduce the ^{252}Cf neutron multiplicity distribution minor modifications have been applied to the gaussian of formula 3.4. First, to avoid negative multiplicities, the negative tail of the gaussians is truncated. After, a new corrected gaussian area $\mathrm{A_c}$ is computed as

$$A_c = \frac{1}{\sqrt{2\pi}} \int_0^{\infty} e^{-\frac{t^2}{2}}\,\mathrm{d}t \quad \text{where} \quad t = \frac{\nu - \bar{\nu}}{\sigma} \tag{3.7}$$

The corrected centroid $\bar{\nu}_c$ is computed in the following manner:

$$\frac{\bar{\nu}}{A} = \frac{\bar{\nu}_c}{A_c} \tag{3.8}$$

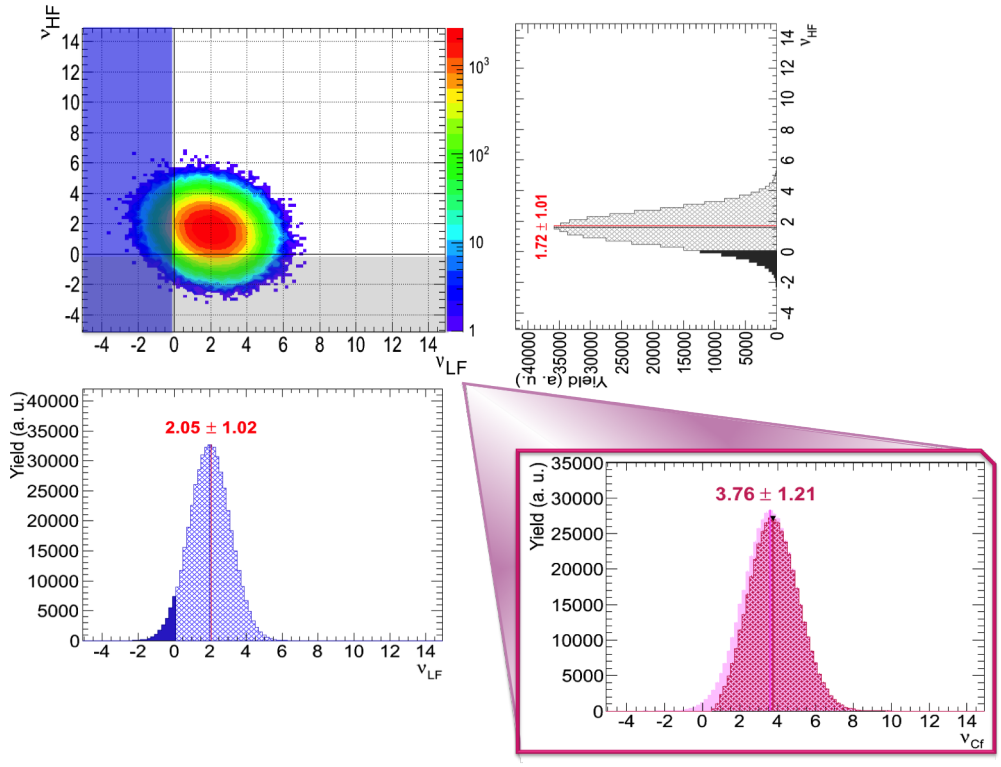

Figure 3.3: The upper left figure shows the matrix correlation between ν_{LF} and ν_{HF}. The projections are obtained applying the NORMCO procedure with the corrected average multiplicity as illustrated in formula 3.8. The projections are still normal distributed and the average multiplicities and their standard deviations are respectively for the light and heavy fragments: [$\bar{\nu}_{\mathrm{LF}}$ =2.05, σ_{LF} = 1.02] and [$\bar{\nu}_{\mathrm{HF}}$ =1.72 ,σ_{HF} = 1.01], whereas the correlation factor is equal to $\rho = -2.14$. The pink distributions shows the resulting distribution before and after the corrections explained in the text.

where A is the the integral of the probability density $p_T(t)$:

$$A = \int_{-\infty}^{+\infty} p_T(t)\,\mathrm{d}t = 1 \quad \text{where} \quad p_T(t) = \frac{1}{\sqrt{2\pi}} e^{-\frac{t^2}{2}}. \tag{3.9}$$

This procedure leads to new values $\bar{\nu}_c$ for both fragments, which are given in table 3.2. Fig. 3.3 shows the correlations between these corrected quantities. One can notice in table 3.2 that the corrected mean values are lower than the true multiplicities. Also, as can be seen on the projections of fig. 3.3 the distributions still present some negative values. But thanks to this procedure, cutting now the negative values, the resulting mean values of the remaining distributions, $\bar{\nu}_c$, will be close to the true mean multiplicities as shown in table 3.2.

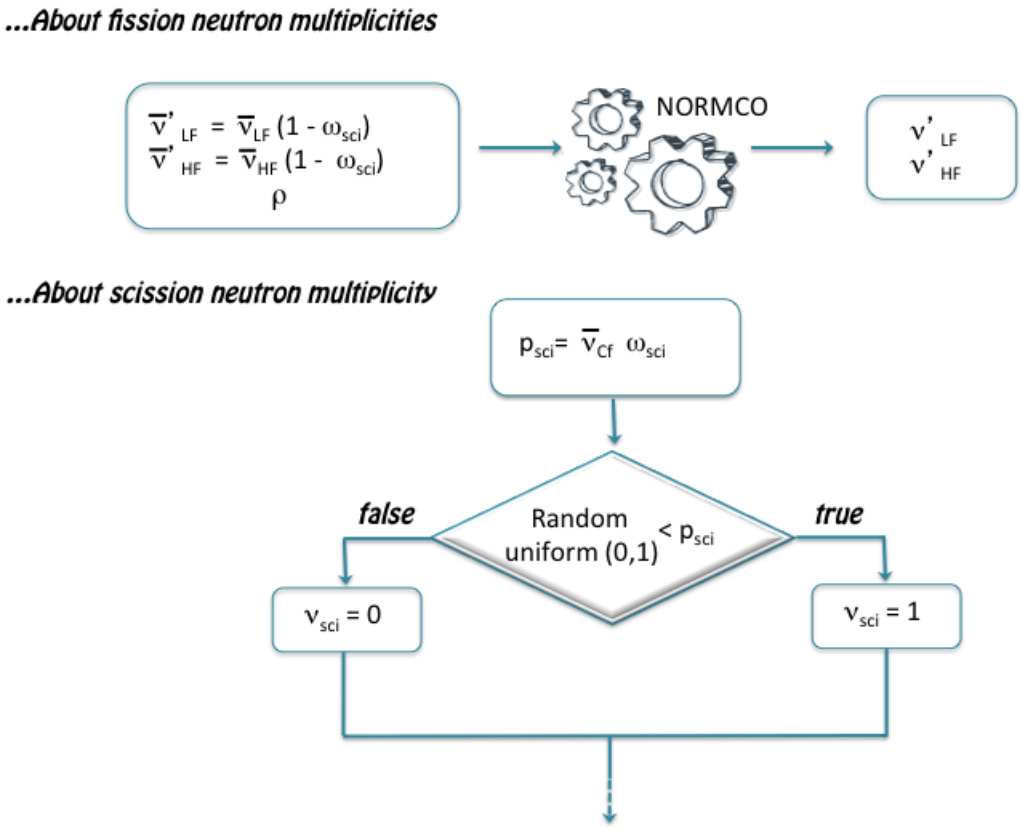

Figure 3.4: Flowchart including scission neutron emission. In the upper part $\bar{\nu}_{\mathrm{LF}}$ and $\bar{\nu}_{\mathrm{HF}}$ are recomputed to be proportionally reduced by the frequency of scission neutron emission ω_{sci}. After, the NORMCO method is applied to the reduced multiplicities $\bar{\nu}'_{\mathrm{LF}}$ and $\bar{\nu}'_{\mathrm{HF}}$. In the bottom part, the workflow describing the scission neutron emission shows the probability $\mathrm{p_{sci}}$ to emit a scission neutron. The decision is sketched in the diamond, representing the parametrization of the random generator with $\mathrm{p_{sci}}$.

Scission neutron emission

Up to this step only prompt neutrons emitted by the FFs have been considered. As mentioned previously, in the simulation code scission neutron emission is also implemented. This is done in the following way. If we consider a certain occurrence ω_{sci} to have a scission emission, this means that the scission neutron multiplicity $\bar{\nu}_{\mathrm{sci}}$ is expressed as

$$\bar{\nu}_{\mathrm{sci}} = \bar{\nu}_{\mathrm{tot}}\,\omega_{\mathrm{sci}} \tag{3.10}$$

The latter formula means that the average fission neutron multiplicity $\bar{\nu}_{\mathrm{tot}} = \bar{\nu}_{\mathrm{Cf}}$ should be proportionally reduced by ω_{sci}. Thus after adding $\bar{\nu}_{\mathrm{sci}}$ scission neutrons the total mean multiplicity, $\bar{\nu}_{\mathrm{Cf}}$ ~3.76 n/fission, will be:

$$\bar{\nu}_{\mathrm{tot}} = \bar{\nu}'_{\mathrm{LF}} + \bar{\nu}'_{\mathrm{HF}} + \bar{\nu}_{\mathrm{sci}} \tag{3.11}$$

To fulfill this constraint the reduction will be propagated on each fragment proportionally as it is presented in the upper part of the flowchart of fig. 3.4.

For example if we take $\omega_{\rm sci} = 0.08$, as considered in different works, 92% neutrons will be fission neutrons and 8% will be scission neutrons. In the simulation only integer number of scission neutrons can be generated. In this example this number can be 0 or at maximum 1. Thus a scission neutron will not be emitted at each event. In the ^{252}Cf fission, 3.76 neutrons/fission at average are emitted. Among them $p_{\rm sci} = 3.76 \cdot 0.08 = 0.30$ neutrons/fission, will be scission neutrons. Thus about every third event will contain a scission neutron. The $p_{\rm sci}$ parameter is used to parametrise a random sampling on a uniform distribution ranging from 0 to 1. In other words following the flowchart of fig. 3.4, if this random number is smaller than $p_{\rm sci}$, one scission neutron will be emitted and $\nu_{\rm sci}$=1; otherwise $\nu_{\rm sci}$=0. The workflow adopted in the simulation code in case of scission neutron emission is sketched in fig. 3.4.

This small probability $p_{\rm sci}$ =0.30% in the case of $\omega_{\rm sci} = 0.08$ is justified by the fact that the emission of neutrons from the neck before fission is a quite improbable process. The main argument that supports this assertion is based on the time scales. For an excitation energy of a system of about $\approx$ 10 MeV the evaporation of a neutron takes $\approx 10^{-18}$s. This time is much longer than the time involved in the descent from the saddle to scission which is about $\approx 10^{-20}$s.

In chapter 4 different values $\omega_{\rm sci}$ will be introduced in the simulation and confronted with the experimental results.

3.3.2 Neutron energy distributions

The CM neutron distribution is represented, following K. J. Lecouteur and D. W. Lang's prescription [82] by:

$$\varphi(\eta) \sim \frac{\eta^{\lambda}}{T_{eff}^{\lambda+1}}\, e^{\frac{-\eta}{T_{eff}}}, \tag{3.12}$$

where $T_{\rm eff} \approx T_{\rm FF}$ and $T_{\rm FF}$ is the daughter nucleus temperature and η the neutron energy in the fragment CM. In the specific case of one neutron emission in the CM of the moving fragment $\lambda = 1$ as was derived by V. F. Weisskopf [27] in 1937. For a cascade emission K. J. Lecouteur and D. W. Lang in 1959 established that $\lambda \approx {}^1/_2$.
In this work the cascade emission of fission neutrons is simulated in this way. Thus the neutron CM energy of the cascade emitted by a fully accelerated fragment at a given temperature $T_{\rm FF}$ is sampled over a Maxwell distribution as

$$\varphi(\eta) \sim \sqrt{\eta}\, e^{\frac{-\eta}{T}} \tag{3.13}$$

Fission neutrons are emitted in the frames of the fully accelerated fission fragments thus the transformation of the CM spectrum to the laboratory frame is done by taking into account the

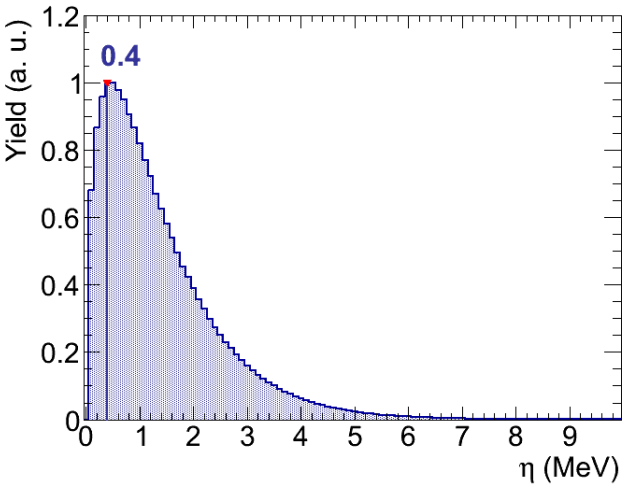

((a))

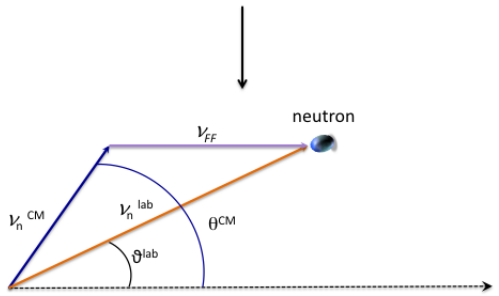

((b))

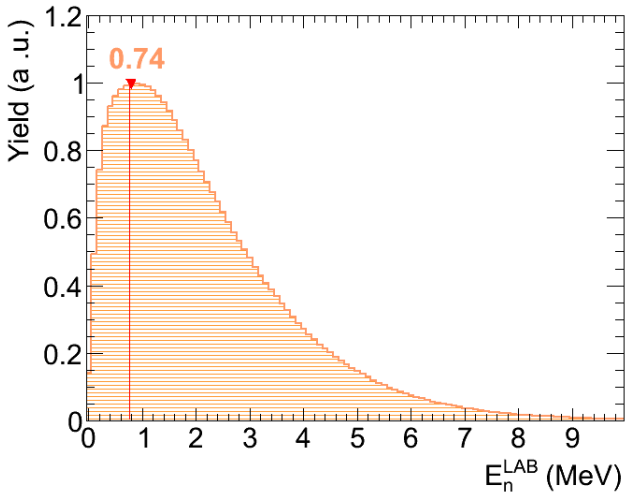

((c))

Figure 3.5: Neutron energy distributions in the CM of FFs and in the laboratory system are shown. a) presents the Maxwell energy distribution of fission neutrons in the CM. The maximum yield energy $\eta_{max} \approx 0.4$ MeV. b) Schematic description of the coordinate system transformation. The transformation from the FF CMs to the laboratory system by adding the velocity of the fission fragments to the velocity of each neutron will lead to a kinematical focusing along the fission axis as well as to an enlargement of the energy spectrum. c) The plot shows the neutron energy distribution transformed in the laboratory frame. The distribution appears larger then the CM one and the maximum yield energy E_{max}^{Lab} shifted to ≈ 0.74 MeV, which is very close to the value usually assigned to the maximum yield energy in literature is $E_{max}^{lab} = 0.71$ MeV [81].

average velocity v_{FF} of FFs as follows

$$v'^2_{FF} = v^2_{FF} + v^2_{cm} + 2v^2_{lab}v^2_{FF}\cos\theta_{lab}, \tag{3.14}$$

as sketched in fig. 3.5(b). The energy $\eta = \frac{1}{2}mv^2_{cm}$ spectrum in the CM of a neutron of mass m and velocity v_{cm} of fig. 3.5(a) is transformed into the laboratory spectrum of fig. 3.5(c).
To move from the CM system to the laboratory frame the assumption that the fission fragments average velocities v_{FF} are unchanged by the neutron emission is used. This approximation is reasonable as was pointed out first by W. E. Stein [83] and after by J. Terrel [84]. J. Terrel computed the velocity v'^2_{FF} obtained by adding to the initial fragment velocity v_{FF} the recoil velocity $\frac{m}{M^*}v_{cm}$ due to the neutron emission with a CM velocity v_{cm} at angle θ_{cm} by a fragment of mass M^*:

$$v'^2_{FF} = v^2_{FF} + \left(\frac{m}{M^*}v_{cm}\right)^2 - \left(2\frac{m}{M^*}v_{cm}\,v_{FF}\right)\cos\theta_{cm} \tag{3.15}$$

Averaging along the neutron cascade the latter equation, the following expressions are obtained:

$$\langle v'^2_{FF}\rangle = v^2_{FF} + \left(\frac{m}{M^*}\right)^2\langle v^2_{cm}\rangle \tag{3.16}$$

and

$$\langle v'_{FF}\rangle = v_{FF}\left[1 + \frac{1}{3}\left(\frac{m}{M^*\,v_{FF}}\right)^2\langle v^2_{cm}\rangle - ...\right] \tag{3.17}$$

Since v'_{FF} and v^2_{cm} are of the same order of magnitude, $\langle v'_{FF}\rangle$ differs only of about 0.01% from the average initial fragment velocity v_{FF}.

Scission neutrons

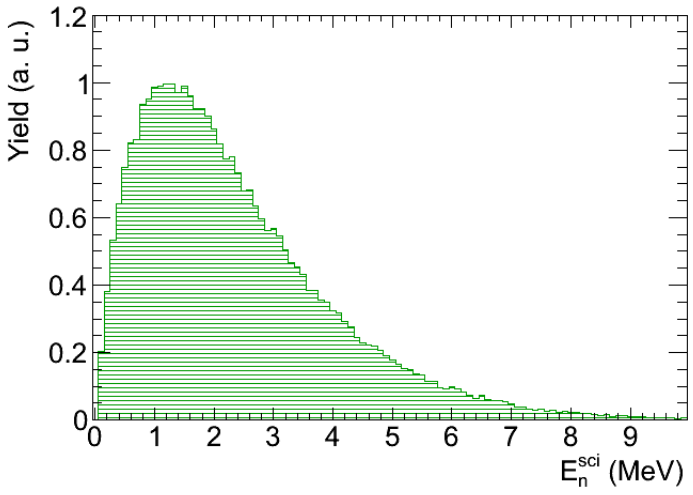

Figure 3.6: Scission neutron energy distribution.

To add the scission neutron component it is assumed [28] that they are emitted by a stationary source in the laboratory frame. As mentioned in section 3.3.1 simulation provides at maximum one scission neutron with a certain fraction ω_{sci}. Thus scission neutron energies are sampled from a Weisskopf evaporation [85] distribution as already mentioned above, of the form:

$$\varphi(\mathrm{E_{sci}}) \sim \mathrm{E_{sci}}\, \mathrm{e}^{\frac{-\mathrm{E_{sci}}}{\mathrm{T_{sci}}}} \tag{3.18}$$

where $\mathrm{T_{sci}}$ is the temperature of the nucleus at the scission point. Fig.3.6 shows the obtained scission neutron energy distribution.

3.3.3 Parameters used in the simulation

The inputs used to simulate the fission neutrons from the spontaneous fission of ^{252}Cf are, as already mentioned, the FF average velocity $\mathrm{v_{FF}}$ and temperature $\mathrm{T_{FF}}$, the average neutron multiplicity $\bar{\nu}$ and its standard deviation σ of each fragment, sketched in table 3.1.

Neutron multiplicity features of fission fragments

We have used the average number of emitted neutrons, the standard deviation and the correlation values to infer the number of neutrons emitted per fission event. These data are defined experimentally in Vorobyev's work [78] on fission neutron emission in the spontaneous fission of ^{252}Cf. The correlation value used is $\rho = -0.21$.

Average fragments velocities

The average fragment velocities weighted with the real neutron multiplicity $\mathrm{v_{FF}}$ [86], are used to assess the neutron emission in the laboratory frame. The fragment velocity generally found in literature $\mathrm{v_{LF}}$=1.367(6) cm/ns and $\mathrm{v_{HF}}$=1.034(4) cm/ns as given in [61] are deduced from $< E_{FF}/M_{FF} >$ where E_{FF} and M_{FF} are the final kinetic energy and mass of the final FFs after evaporation. These values are averaged over all possible neutron multiplicities, including zero. The trigger used in the CORA experiment considers only events with neutron multiplicities higher or equal to one.

The velocities in table 3.1, proposed by Vorobyev, take into account these considerations.

Fragment and fissioning system temperatures

The fission fragment temperatures are taken from N. V. Kornilov who measured mean neutron energies of fission fragments. The mean neutron energy according to formula 3.12 is:

$$\langle \eta \rangle = (1 + \lambda)\mathrm{T} \tag{3.19}$$

Thus it is easy to deduce the temperature T for each fragment.

In our simulation the temperature of the two fission fragments are slightly different in contrast with those of most of fission models which assume that the total excitation energy TXE is shared between the two fragments according to equal final temperatures. However only the intrinsic excitation energy available at scission is shared between the fragments

according to statistical equilibrium. The other form of energy such as deformation and collective energies is dissipated into intrinsic excitation energy after scission, when the fragments are no longer in contact [87].
The temperature $T_{sci} = (1.2 \pm 0.1)$ MeV used to compute the scission neutron energy distribution is a fit result on neutron-neutron correlations with seven different energy thresholds performed by Gagarsky et al [34]. This temperature is close to that employed in Pringle's work [88], $T_{sci} = 1.3$ MeV to obtain neutron-neutron correlations.

3.3.4 Anisotropy function

Up to this point only scission emission has been introduced in the simulation. Let's now consider the dynamical anisotropy in the CM of FFs.
The anisotropy is well parameterized by formula 1.9. Starting from this equation the following function is obtained expressing the cosine dependence:

$$W(x) = 1 + A_{nJ}\,(1 - x^2), \qquad \text{with } x = \cos\theta_{nJ} \tag{3.20}$$

where θ_{nJ} is the neutron polar angle relative to the spin axis. Setting A_{nJ} to a non-zero value the anisotropy emission is obtained.
Following formula 3.20, a random number between -1 and +1 is attributed to $cos\theta_{nJ}$. The isotropic case is easily reproduced by setting $A_{nJ} = 0$. The formula 3.20 is reduced to equation 3.2 of the isotropic emission.

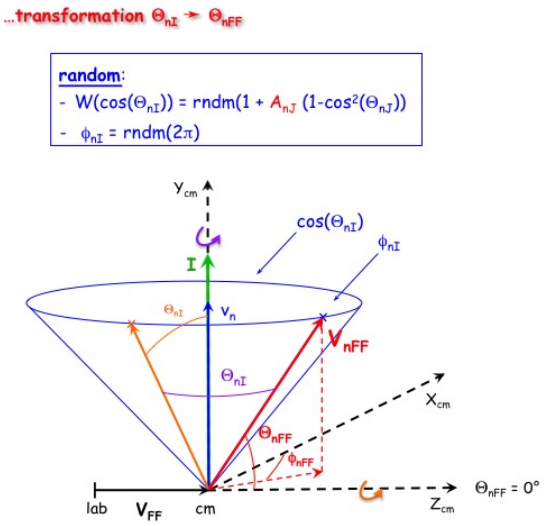

Figure 3.7: Transformation of neutron CM angles relative to the FF spin J into the angles relative to the fission axis FF.

The azimuthal ϕ_{nJ} angle is simply generated randomly in the $[0°, 360°]$ range. These emission angles are expressed relative to the spin axis and have to be transformed into the fragment CM frames where the z-axis coincides with the fission axis. This transformation is sketched in fig. 3.7. As shown in the figure, a first rotation of θ_{nJ} is performed around the fission axis, followed by another one of ϕ_{nJ} around the spin J. These rotations will lead to the spherical coordinates θ_{nFF} and ϕ_{nFF} relative to the CM frame.

To complete the simulation the anisotropy is added to the code according to formula 1.9 as shown in fig. 1.16. The anisotropy effect appears to be very weak, in the neutron-neutron relative angular distribution, as one can observe in fig. 1.16. This observable is thus not the most suitable to investigate the dynamical anisotropy.

3.3.5 Some computing features

To run GEANT4 the user must provide three classes: the PrimaryGeneratorAction, the PhysicsList and the DetectorConstruction as sketched in fig. 3.8.

PrimaryGeneratorAction

For spontaneous fission a special PrimaryGeneratorAction is coded. When GEANT4 needs to generate particles, it calls the method PrimaryGeneratorAction::GeneratePrimaries. The latter method calls in turn the SpontFiss::GeneratePrimaryVertex method. The class SpontFiss generates spontaneous fission neutrons. The latter class sets the primary vertex to the ^{252}Cf position, putting it at the origin of the coordinate system in the laboratory frame. In this method, also the neutrons are added to the stack of primary particles. They are defined as G4DynamicParticle, setting in the prototype class the definition of the particles (neutrons), their emission momentum and their energy. If a scission neutron is emitted its trackID is by default equal to 1 and its source is set to ^{252}Cf. In this case for fission neutrons the trackID will start with a value greater than 1 and their information stored together with the emitting fragment properties. The SpontFiss class is a class derived from SingleSource to construct the process used to generate the emitted particles and their emission features.

In the standard operation of GEANT4 an event corresponds to an individual emitted particle. In our case an event corresponds to the spontaneous fission with several emitted neutrons. Thus the SingleParticle class is designed to extend the G4ParticleGun class to that functionality. It is used by the General Particle source class and it is derived from G4VPrimaryGenerator. Its class establishes the primary vertex.

DetectorConstruction

The DEMON geometry is set with simple placements (G4PVPlacement) and a rotation matrix. The detectors are defined as *sensitive*. The hit is filled with the track information such as position, momentum, energy, particle type of the track, etc... . In this way every hit is stored in a hits collection. They are also defined as *touchable*. This functionality for a given volume provides a unique identification of each DEMON cell. Each detector, which

is recognized by its experimental VXI ID, is defined as a geometrical entity which has a unique placement in the detector description.

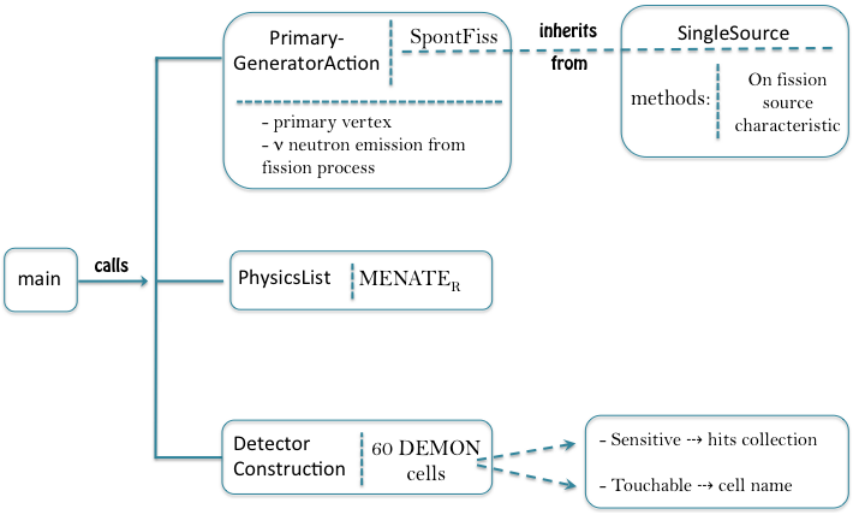

Figure 3.8: Workflow representation of the computing algorithm.

To have information about neutrons that don't interact inside the DEMON cells also the stepping action is coded, which allows to follow step by step the complete track induced by the neutron.

3.4 Simulated distributions

As presented in the previous chapters we are interested mainly in three distributions: θ_{nn}, θ_{nLF} and ϕ_{nn}. Before, all the simulated primary observables, neutron energy and angles, presented in fig. 3.9 have been compared to the experimental ones of figs. 2.35 and 2.38. to check the coherence of our simulation.
The $\cos\theta_{nn}$ distribution where θ_{nn} is the relative angle between two any neutrons and it is computed as the scalar product of their unitary velocity vector by applying the ROOT function *Angle()*.
In the same way the $\cos\theta_{nLF}$ is computed as the relative angle between each emitted neutron and the LF fragment. Also in this case the ROOT function *Angle()* is applied.

The innovative point we are looking for in our work is the distribution of the ϕ_{nn} angle between two neutrons in the plane perpendicular to the fission axis as presented in chapter 1 and above.

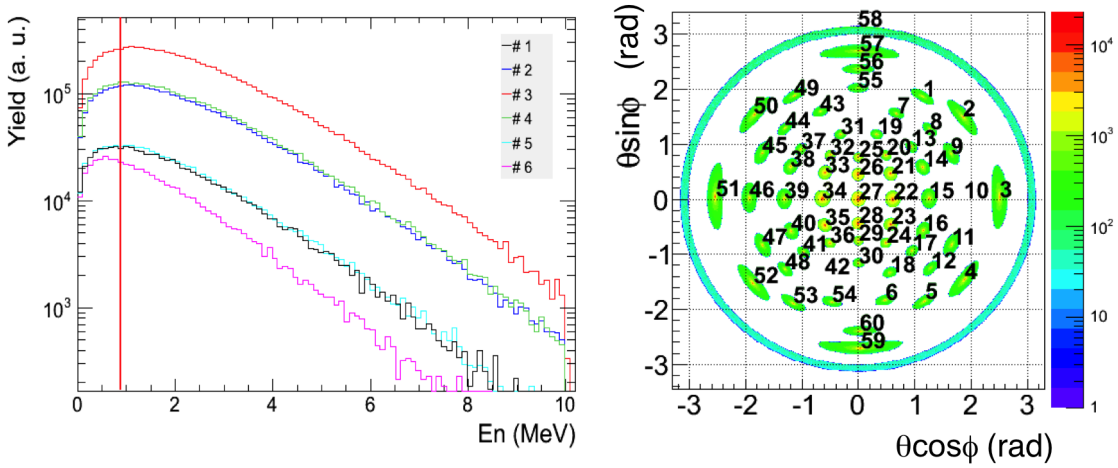

Figure 3.9: Left: The simulated energy spectra of the first 6 DEMON cells placed on the column placed at $\theta = 144°$ for illustration. The red line stands for the common energy threshold. Right: DEMON angular coverage in the $\theta sin\phi$ vs $\theta cos\phi$ plane. The z-axis represents the neutron yield hitting a cell. Also the number of the VXI identifying a DEMON cell is indicated.

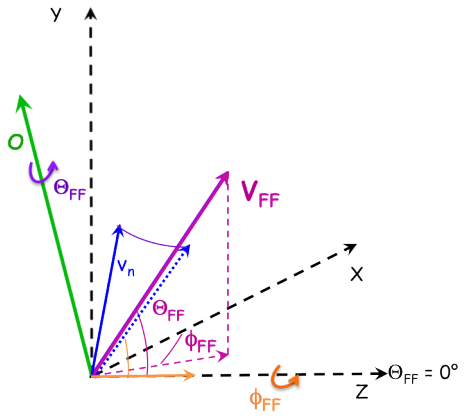

Figure 3.10: The two rotations of the neutron vector v_n are sketched. These rotations are necessary to project all the fission axes with the associated neutrons on a single axis, the Z-axis in the laboratory.

For each fission event the fission axis is rotated in order to coincide with the fixed laboratory Z-axis. For that two rotations are necessary. First, we define the vector O perpendicular to the (fission axis, Z-axis) plane as sketched in fig 3.10. Then a first rotation of the angle θ_{FF} is performed around this axis. A second rotation of the azimuthal angle ϕ_{FF} of the resulting vector is performed around the Z-axis. The same operations are applied to all coincident neutrons.

After that, the ROOT function *DeltaPhi()* calculates the difference ϕ_{nn} angle between two any neutrons.
These three distributions are presented in fig. 3.11.

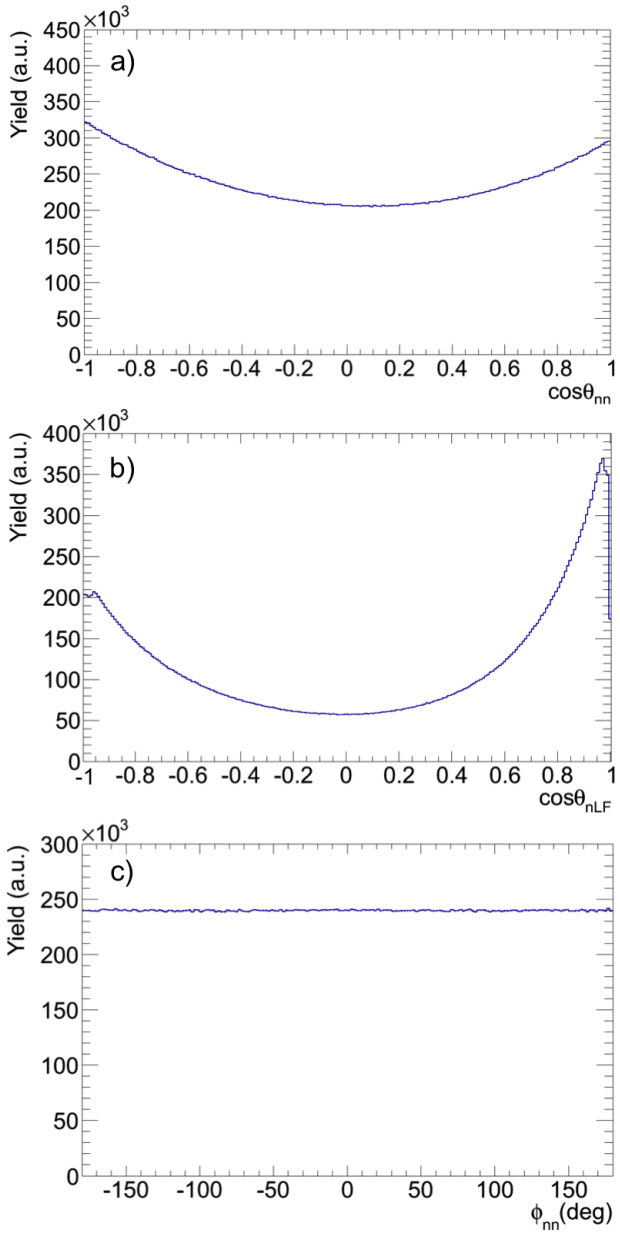

Figure 3.11: Initial simulated distributions without any scission nor anisotropy.

3.5 Effect of the experimental set-up

The effect of the experimental biases on the cosθ_{nn}, ϕ_{nn} and cosθ_{nLF} simulated neutron distributions are studied.

Geometrical acceptance

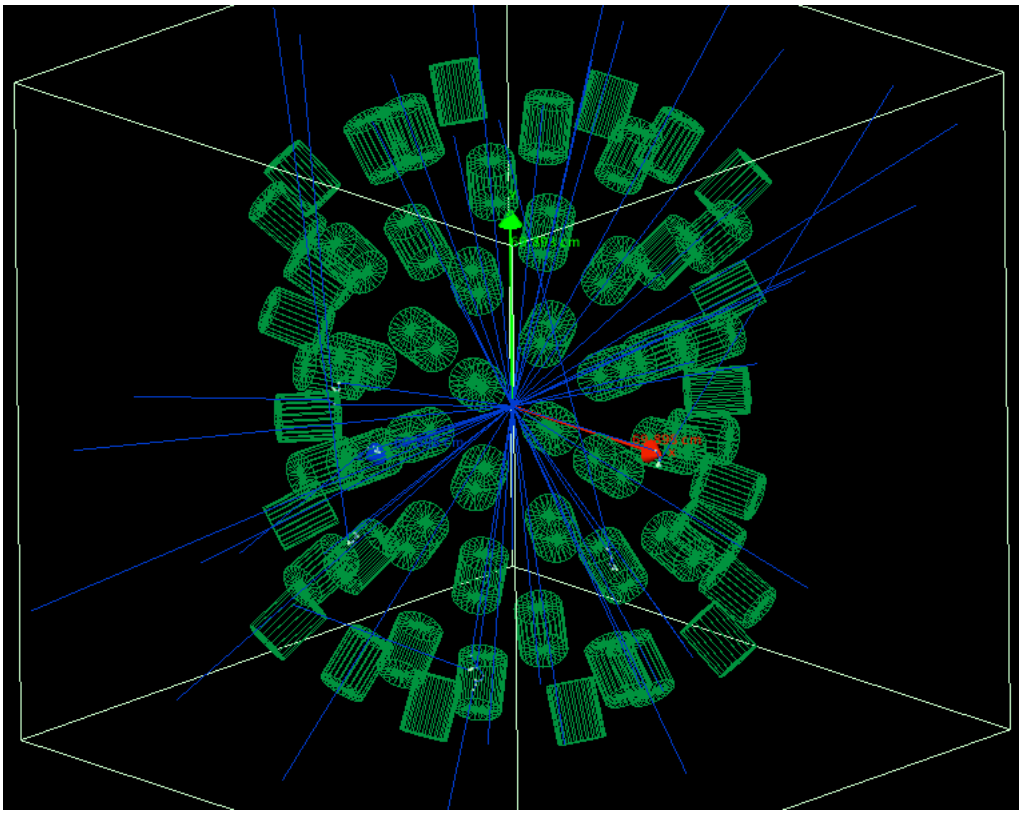

Figure 3.12: Simulated DEMON geometrical configuration adopted in the CORA experiment.

First the impact of the DEMON geometrical acceptance on the three distributions is analysed. Fig. 3.13 compares the distributions before (black curves) and after(yellow curves) taking into account the geometrical acceptance. Testing the geometrical acceptance means that a neutron is able to reach a detector. The DEMON configuration adopted in the CORA experiment covers a solid angle of about 16,4% of 4π as presented in fig 3.12. At this stage, for the cosθ_{nLF} distribution where only coincidences between one neutron and the light fragment are computed, the count loss is about 15.9%. A more significant loss of counts is observed for the cosθ_{nn} and ϕ_{nn} distributions, due to two neutron coincidences. Only about 2.7% of the initially simulated counts remain. It is also observed that passing through the DEMON geometrical configuration, the filtered neutron angular distributions are transformed in shape by the geometrical acceptance

effect (yellow filled curves) as appears well on the right part of fig. 3.13. Only the cosθ_{nLF} curve remains practically unchanged. This is due to the fact that at this point CODIS is assumed to have a 4π acceptance.

Pileup

In the experiment pileup events have to be taken into account especially as the DEMON distances are quite small this effect may be not negligible. In the experiment two different neutrons interacting in the same DEMON cell are treated as one. In the simulation analysis the same procedure is followed. The simulation code allows to identify pileup events. Thus the analysis of the simulated data can be performed in the same way. The blue filled curves of fig. 3.14 represent the (a) cosθ_{nn}, (b) *cos*θ_{nLF} and (c) ϕ_{nn} filtered distributions after the pileup treatment, and they are compared with the previous distributions (yellow curves) where only the geometrical acceptance was considered. As expected in the cosθ_{nn} and ϕ_{nn} distributions the pileup is mainly concentrated at θ_{nn} and ϕ_{nn} close to zero. The widths correspond to the angular apertures of the DEMON cells. For the cosθ_{nLF} distribution the pileup is sprinkled along the full range.
The number of counts after the pileup treatment is 99.2% for cosθ_{nLF} and 97.6% for the two others. These differences are mainly due to the following reason. In the cosθ_{nLF} distribution only one correlation is added for each pileup event whereas in the two other distributions the situation is more complicated and more correlations are added for one pileup event. These additional correlations can be analytically estimated.

In statistics the number of neutron pair correlations are called *simple combinations*. Combinatorics look at the number of possibilities to pick k objects from a set of ν in which the order of the components doesn't matter and without repetition. In neutron-neutron correlations the number of picked objects is k=2 and the combination of 2 elements on 2 neutron strings picked from a set of ν emitted neutrons is formulated in the following manner:

$$C_{\nu,k} = \frac{\nu!}{k!(\nu-k)!} \tag{3.21}$$

If a *pileup* neutron is "added" to the set of ν neutrons the combination becomes:

$$C_{\nu',k} = \frac{\nu'!}{k!(\nu'-k)!} \qquad \text{where} \quad \nu' = \nu + 1 \tag{3.22}$$

Rewriting the latter equation as a function of ν and taking k=2 the formula becomes:

$$C_{\nu',k_{|2}} = \frac{(\nu+1)\nu!}{2(\nu-1)!} \tag{3.23}$$

The number of pairs added by taking into account one neutron more to the neutron-neutron correlation distributions is:

$$n_p = \frac{(\nu+1)!}{2(\nu-1)!} - \frac{\nu!}{2(\nu-2)!} = \nu \tag{3.24}$$

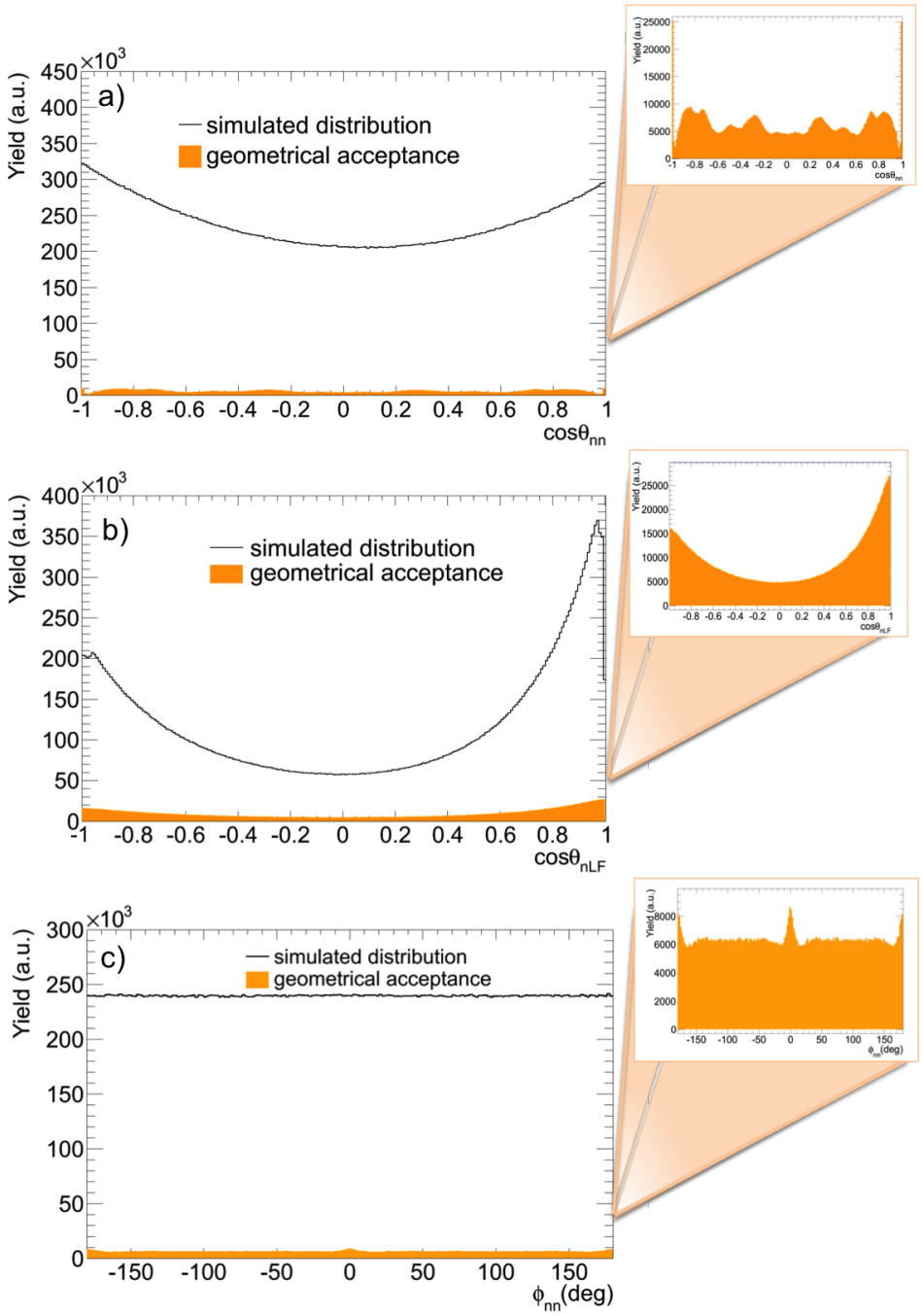

Figure 3.13: Left: Effect of the geometrical acceptance on the (a) $\cos\theta_{nn}$, (b) $\cos\theta_{nLF}$ and (c) ϕ_{nn} initial neutron distributions (black curves). The filtered neutron angular distribution are represented in yellow filled curves. Shape differences induced by the geometrical filter appear in the inserts.

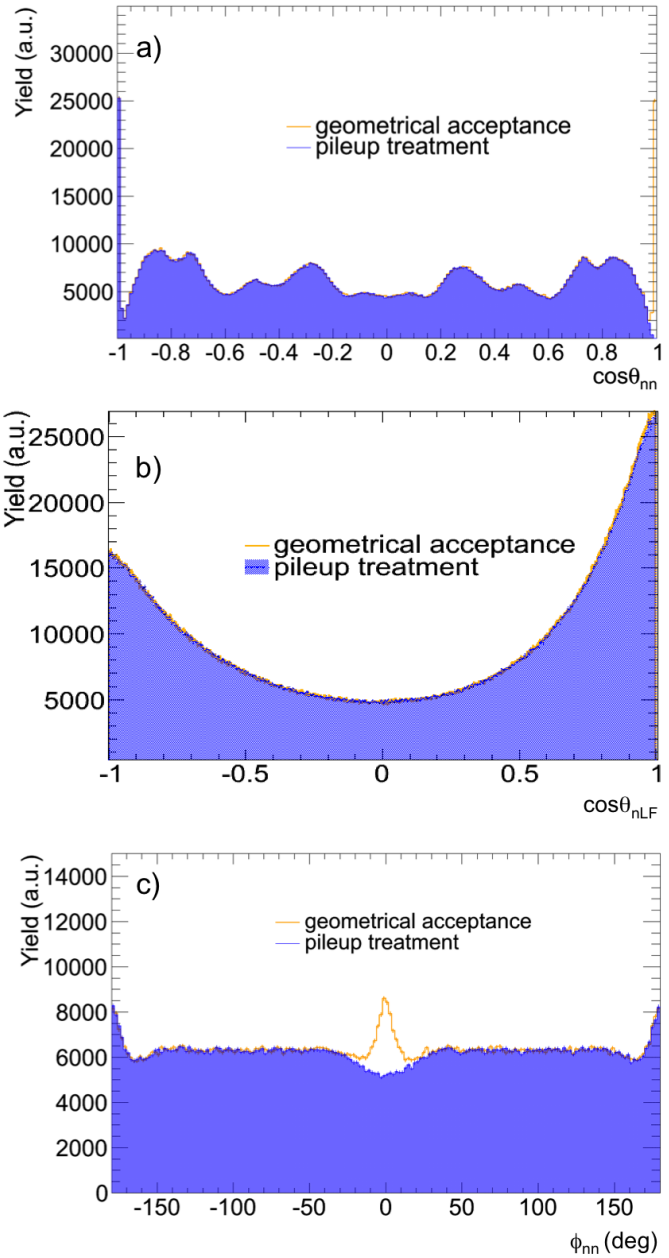

Figure 3.14: The simulation code allows to recognize the pileup effect.The blue filled curves represent the cosθ_{nn} (a), $cos\theta_{nLF}$ (b) ϕ_{nn} (c) filtered distributions after the pileup treatment and are compared with the previous distributions (yellow curves) where only the geometrical acceptance was considered. As expected in the cosθ_{nn} and ϕ_{nn} distributions, the pileup is mainly concentrated at θ_{nn} and ϕ_{nn} close to zero, the widths corresponding to the angular apertures of the DEMON cells. For the cosθ_{nLF} distribution, the pileup is sprinkled along the full range.

Energy threshold

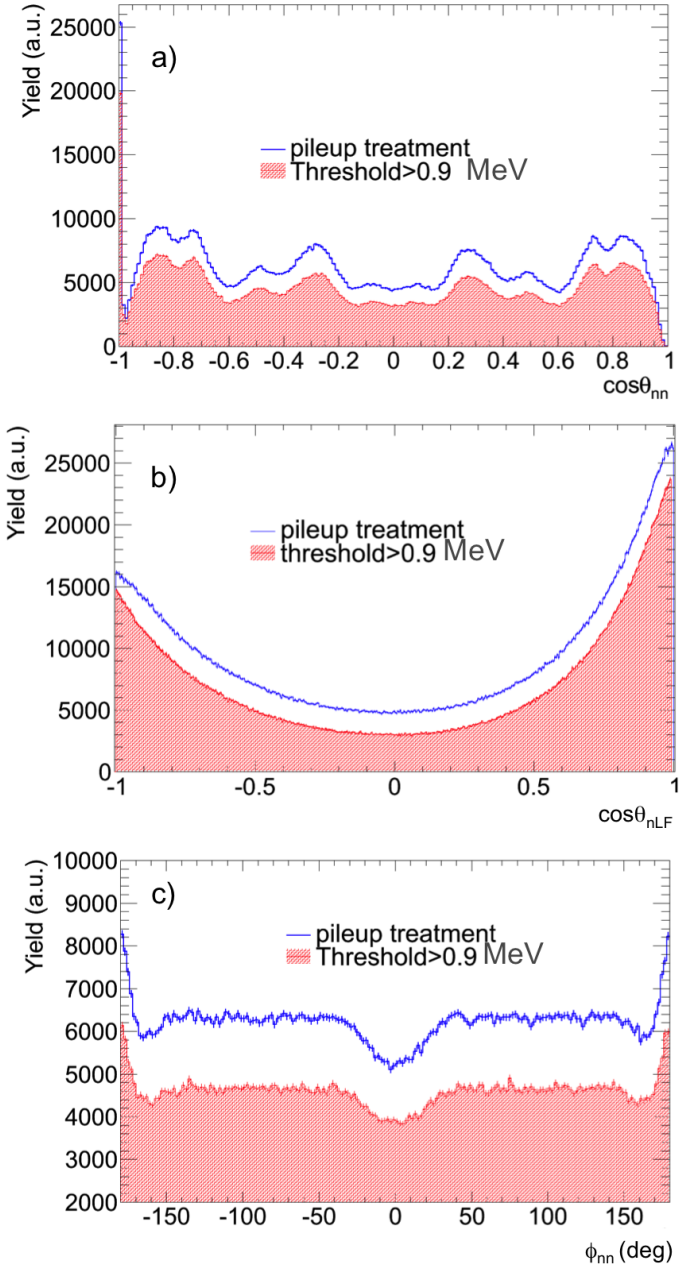

Figure 3.15: In the experiment the neutron energy threshold is fixed at $E_n = 0.9$ MeV. In the simulation analysis the same threshold value is taken thus all incoming neutrons with an energy smaller then this cut off are erased. A significant loss of counts is observed (red filled curves) along the range for all (a) cosθ_{nn}, (b) cosθ_{nLF} and (c) ϕ_{nn} distributions. The cut off has almost no influence on the distribution shapes.

The detection of a neutron is performed in two steps. First a neutron transfers all or part of its kinetic energy to the charged particles in the detector material which produce the detection signal. The neutron must have an incoming energy high enough so that its energy loss during these interactions reaches at least the energy threshold. In order to avoid the generation of useless neutrons we set the cut off of the incoming neutron energies at 0.9 MeV which corresponds to the experimental threshold. Applying this condition the number of events remaining is about 73.8% in the cosθ_{nn} and ϕ_{nn} distributions and 76.5% in the cosθ_{nLF} one as shown in fig. 3.15. These values are in agreement with the neutron energy spectrum of figure fig. 3.5(c). In fact the mean energy value of the distribution in fig. 3.5(c) is E_n^{lab}= 2.13 MeV and the cut off energy value E_n^{th}= 0.9 MeV represents ≈ 30% of the counts of the neutron energy spectrum.
As for the geometrical acceptance effect, the difference between the neutron-neutron (n-n) and neutron-light fragment (n-LF) correlations, which is here of about 2.7%, is due to the greater probability to detect one neutron compared to two in the same fission event.

Intrinsic efficiency

The previous condition on the incoming energy of the neutron, E_n >0.9 MeV, is not enough to insure its detection. It has in addition to transfer enough energy to the detection material. At this point the simulation has to take into account the interaction processes of the neutrons

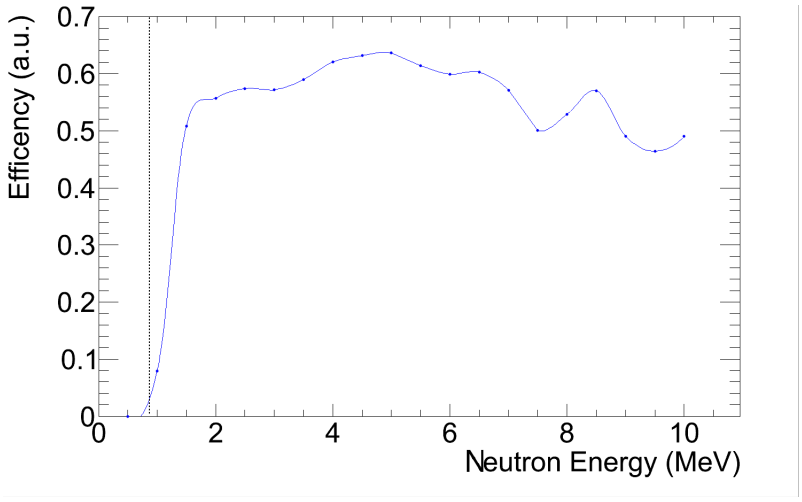

Figure 3.16: Simulated intrinsic efficiency of a DEMON cell.

in a liquid scintillator containing xylene as DEMON is consisted of, which is performed by MENATE$_R$. Fig. 3.16 shows the resulting intrinsic efficiency of a DEMON cell.

The effect of the intrinsic efficiency is shown in fig. 3.17. By taking into account this condition a significant loss of counts is observed: about 57% for cosθ_{nLF}, in agreement with the DEMON

efficiency presented in fig. 3.16 and 20% for the neutron-neutron correlations $\cos\theta_{nn}$ and ϕ_{nn}.

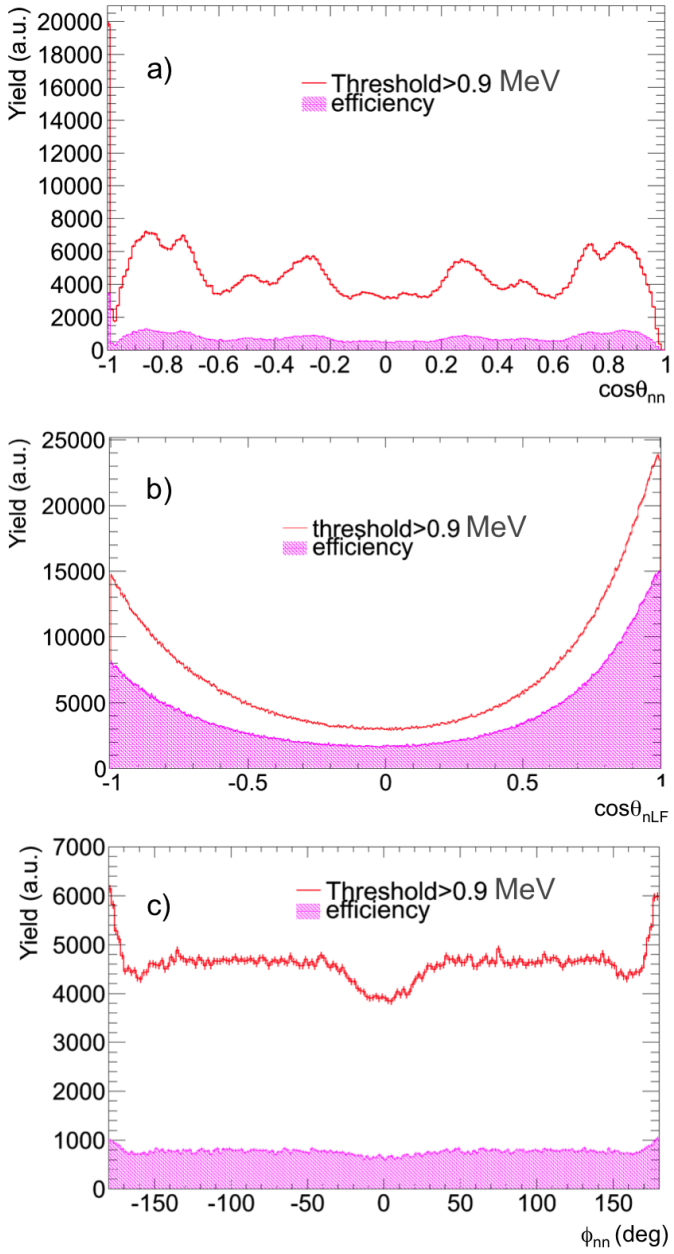

Figure 3.17: The influence of the energy threshold on the incoming neutrons (red curves) and the efficiency effect (pink filled curves) are compared. Including the detectors efficiency, the counting rates decrease considerably, mostly for the neutron-neutron distributions (a) $\cos\theta_{nn}$ and (c) ϕ_{nn}. For the (b) $\cos\theta_{nLF}$ distribution the loss of counts is of about 57% in agreement with the DEMON efficiency.

Cross talk

Another important experimental bias that affects the $\cos\theta_{nn}$, $\cos\theta_{nLF}$ and ϕ_{nn} distributions is the cross talk: instead of one neutron signal the detection system detects two or even more neutrons. It occurs when a neutron interacts in a DEMON volume and is scattered into another cell, most probably in a neighbouring one as sketched in fig. 3.18.

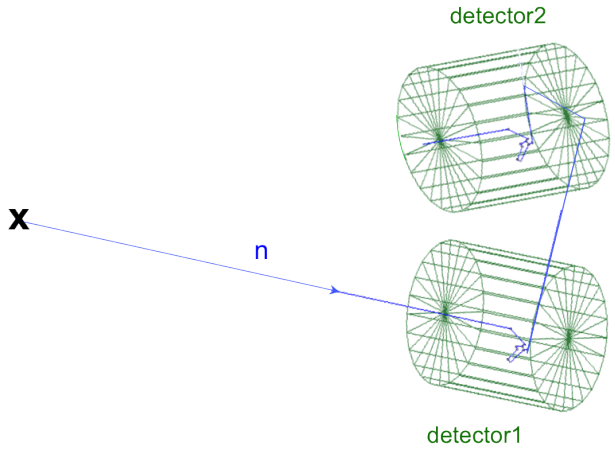

Figure 3.18: Schematic representation of the cross talk. A neutron entering a first detector is scattered into another detector: an additional fake signal is obtained.

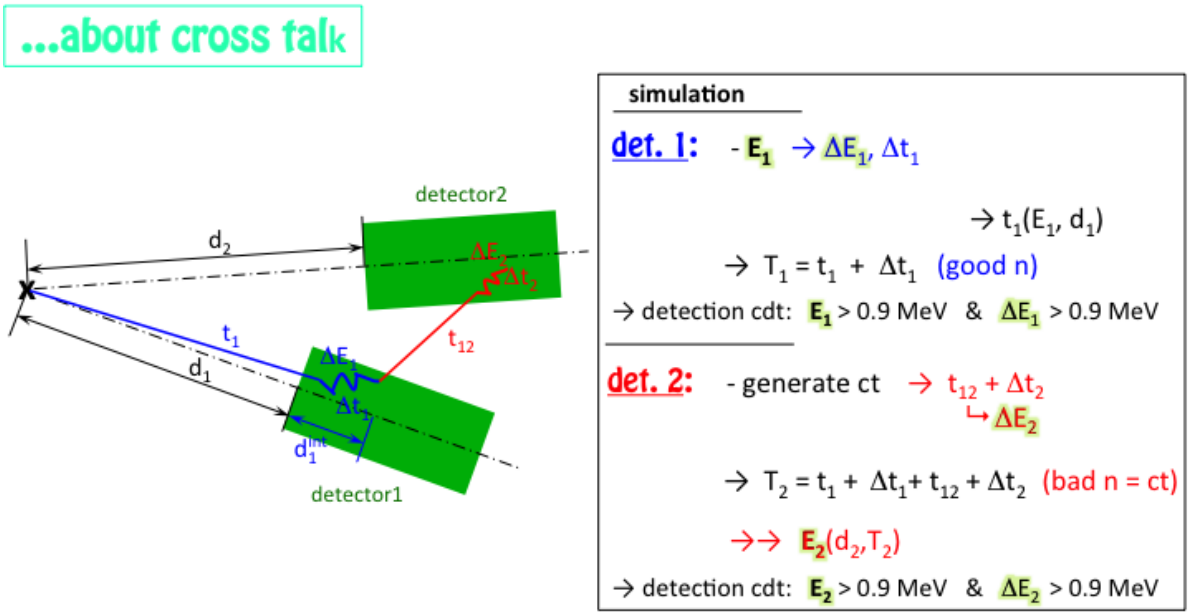

Figure 3.19: Schematic overview of the cross talk treatment procedure

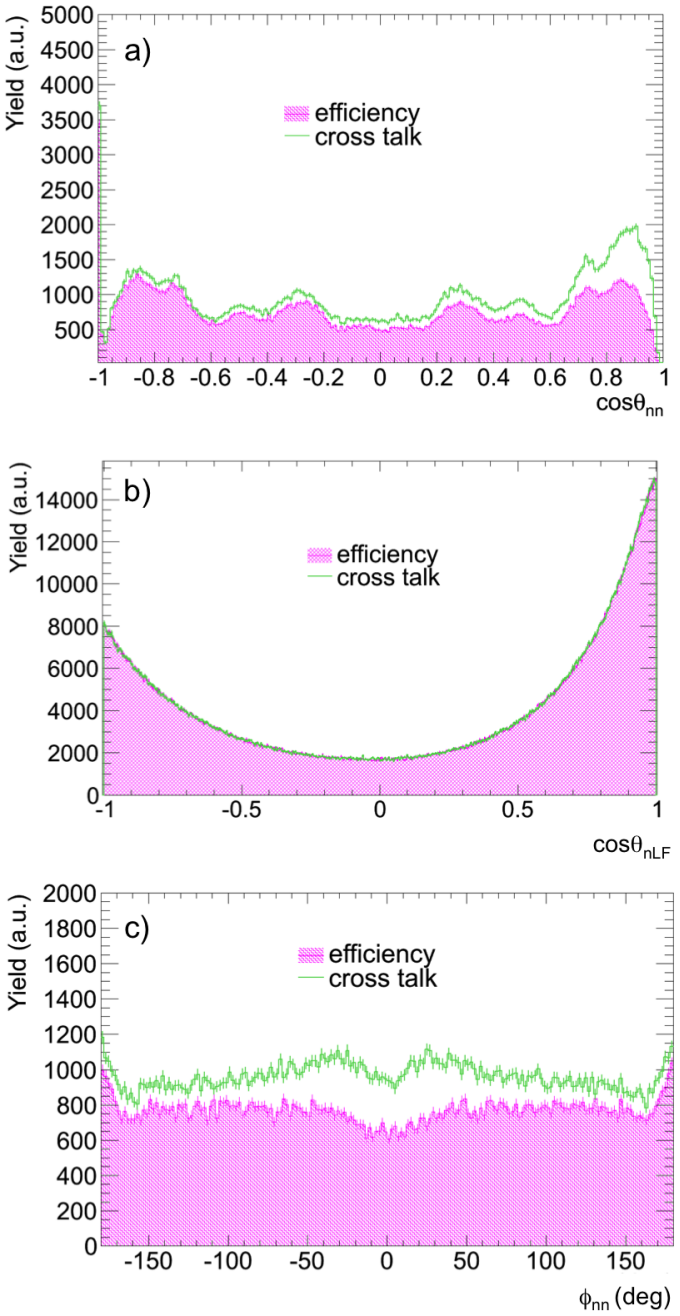

Figure 3.20: The simulation allows to estimate the effect of cross talk on the studied distributions (a) cosθ_{nn}, (b) cosθ_{nLF} and (c) ϕ_{nn}. The main influence of the cross talk in (a) *cos*θ_{nn}, (c) ϕ_{nn} distributions is at small angles, as seen for pileup. For the cosθ_{nLF} distribution the cross talk is rather sprinkled along the full range.

It may happen that the energy loss of the neutron in the first detector is not high enough to induce a signal and only the second detector delivers a signal. In this case only one neutron will be detected but with wrong angular and time of flight informations.
To estimate the cross talk two conditions are applied:

- a condition on the deposited energy by the scattered neutron in the cross talk detector ΔE_2 >0.9 MeV as sketched in fig. 3.19 is applied.
- the total time T_2 deduced from the different times of flight at each interaction step are evaluated in order to define the corresponding energy E_2, with the condition E_2 >0.9 MeV to be in agreement with the experimental analysis.

The cross talk effect involves generally neighbouring detectors because a neutron scattering on hydrogenate material produces small deviation angles. For this reason the neutron-neutron angular distributions $cos\theta_{nn}$ and ϕ_{nn} are mainly affected by this effect at small relative angles as shown in fig. 3.20.
As can be seen in fig. 3.20 the cross talk increases artificially the number of counts contrarily to the previews effects: an increase of about 24% for neutron-neutron correlations and only 0.5% for neutron-fragment correlations. The cross talk doesn't impact the shape of the neutron-fragment correlation.
The same arguments stressed out for the pileup effect explain the differences in percentages between neutron-neutron and neutron-fragment correlations. The cross talk as the pileup has no great influence on the neutron-fragment correlation because it induces just one additional entry in case of a cross talk event.

DEMON central angles

The neutron angles are identified by the central angles of the DEMON cells. The structures generated taking into account the DEMON central angles are sketched in fig 3.21 which shows the distributions when this condition is applied. In the $\cos\theta_{nn}$ distribution the broad structures observed when real angles are considered (green curve) become narrow structures when they are reduced to the central angles. The ϕ_{nn} distribution is less affected from this central angles effect, same wide structures appear with an increase around 0°. In the experiment each detected neutron is identified as the detector central position that it reaches. From the geometrical configuration $\Delta\theta$ between two neighbouring detectors are between $4.5° < \Delta\theta < 12°$. This renders the $\cos\theta_{nn}$ distribution (purple filled curve) quite discontinuous with a lot of narrow structures. Conversely the (b) $\cos\theta_{nLF}$ distribution shape seems very slightly affected by taking the central DEMON angles.

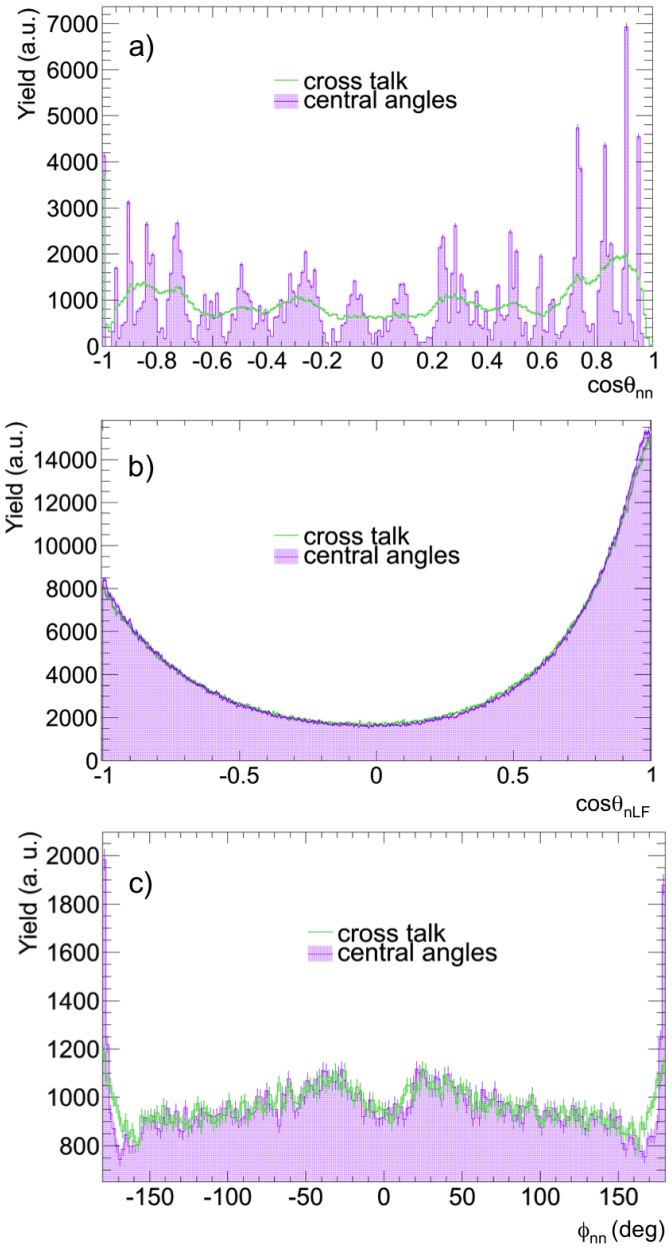

Figure 3.21: In the experiment every detected neutron is identified as the detector central position that it reaches. (a): $\Delta\theta$ between two neighbouring detectors on are between $4.5° < \Delta\theta < 12°$. This makes the $\cos\theta_{nn}$ distribution (purple filled curve) quite discontinuous with a lot of narrow structures. The (c) ϕ_{nn} distribution seems to be less affected by this central angles effect, wide structures appear. Conversely the (b) $\cos\theta_{nLF}$ distribution shape seems slightly affected by taking the central DEMON angles.

3.6 Final remarks

The simulation allows to have the total mastery of the possible effects that can disguise the characteristics of the emission of neutrons in the process of fission. Only armed with the knowledge of each element of the experimental filter it is possible to elaborate a strategy for the study of such weak mechanisms.
After having acquired such knowledge on each part of the experiment and, as far as possible, employed the same analysis procedure as that adopted in the experiment for the simulated data, we can validate the model presented in this chapter by comparing the obtained simulated results with the experimental ones.

Chapter 4

Simulation results and confrontation with the experiment

Computer simulations allow to understand the response of the studied distributions for different pairs (A_{nJ}, ω_{sci}) introduced as input in the code. Fig. 4.1 presents the studied distributions for different sets of (A_{nJ}, ω_{sci}) couples. The different simulations are performed with the same number of fission events for different cases. An unrealistically high anisotropy parameter, A_{nJ}=0.8 and no scission leads to the the red curves. On the opposite an unrealistically high scission neutron occurrence, ω_{sci}=20% and no anisotropy gives the black curves. The purpose is to identify where the scission neutron emission and the dynamical anisotropy affect the distributions and to estimate their relative importance in respect with the pure isotropic case shown in green curves. As we observe in the figure, the black curves with a large percentage of scission neutrons are lowered compared to the other cases. This occurs because every time that a scission neutron is emitted there is less excitation energy (TXE) to emit fission neutrons from fragments. The anisotropy affects slightly the $\cos\theta_{nn}$ and $\cos\theta_{nLF}$ distributions compared to the effect given by the scission neutron emission. By contrast, in the $\phi_{nn|_{LF}}$ distribution, the anisotropy induces clear oscillations that the other curves don't exhibit.

The experimental filter, which takes into account the DEMON geometrical acceptance, the pileup treatment, the threshold energy, the intrinsic efficiency, the cross talk and the DEMON central angles, is applied and the simulations are confronted to the experiment. The confrontation is performed separately for each of the three distributions and a different adapted strategy is designed to analyze each case.

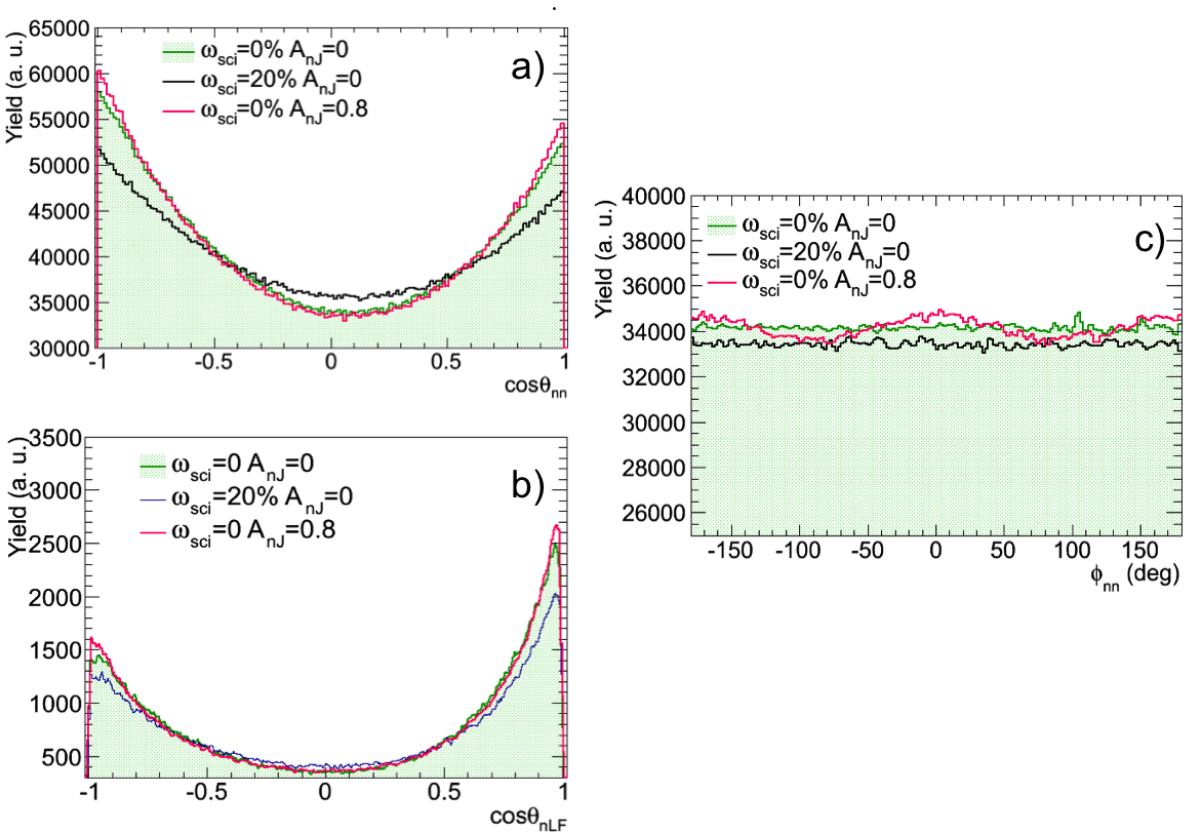

Figure 4.1: Simulated distributions before the experimental filter effect. The scission neutron has a huge influence on the $\cos\theta_{nn}$ distribution, whereas the anisotropy effect remarkably affects the $\phi_{nn|_{LF}}$ distribution as the oscillations shown in the last plot reveal by the red curve.

4.1 $\cos\theta_{nn}$ distribution

For the $\cos\theta_{nn}$ distribution, a χ^2 probability distribution test is used to determine the pair (A_{nJ}, ω_{sci}) which gives the best agreement between simulation and experiment. The following lines describe the mathematical procedure employed for the experiment-simulation confrontation.

4.1.1 Using χ^2 to test hypotheses regarding statistical distributions

The χ^2 test is used most commonly to test the nature of a statistical distribution from which some random sample is drawn. Contrarily to the classical case where the observed experimental data are compared to a known analytically behaviour, in our case, the observables correspond to the simulated data and the experimental distribution represents the expected values. Thus the experiment becomes the"theory" and the simulations play the role of the "measurement". The purpose is thus to find the set of parameters which leads to the best agreement between the simulated and the experimental distributions.

This kind of application has been described by R. D. Evans in reference [89], where this χ^2 test was first formulated. The data can be classified into k classes or bins, with probabilities $p_1, p_2, ..., p_k$ of falling into each class. If all the data are accounted for, $\sum_{i=1}^{k} p_i = 1$.
Now suppose we take the data by classifying them: we count the number of observations falling into each of the k classes: n_1 in the first class, n_2 in the second and so on up to n_k in the k^{th} class. We suppose there are a total of N observations, so $\sum_{i=1}^{k} n_i = N$. It can be shown by non-trivial methods that the quantity:

$$\frac{(n_1 - Np_1)^2}{Np_1} + \frac{(n_2 - Np_2)^2}{Np_2} + ... + \frac{(n_k - Np_k)^2}{Np_k} = \sum_{i=1}^{k} \frac{(n_i - Np_i)^2}{Np_i} \tag{4.1}$$

corresponds approximately to the χ^2 distribution with $d = k - r$ degrees of freedom, where r is the number of constraints or relations used to estimate the p_i from the data. The constraint number r will always be at least 1, since at least $\sum_{i=1}^{k} n_i = \sum_{i=1}^{k} Np_i = N$.
If $\mu_i = Np_i$ is the mean or expected value of n_i, the form of χ^2 given by equation 4.1 corresponds to sum, over all classes, the squares of the deviations of the observed n_i from their mean values divided by their mean values.

The χ^2 is an indicator of the accord between the observed n_i and their averages μ_i. If the model coincides perfectly with the observation, $\chi^2 = 0$. This happens very rarely. But to get a good agreement each single term of the sum presented in equation 4.1 has to be not greater than 1, thus for n terms $\chi^2 \lesssim k$ where k is the total number of classes. If $\chi^2 \lesssim k$ we don't have a reason to doubt that the simulated data are in agreement with the experiment. But if $\chi^2 \gg k$ we must suspect that the simulations aren't governed by the same distribution as the experimental one.

At first glance, $\chi^2 \lesssim k$ gives us a feeling about the correctness of our hypothesis. For a more quantitative measure of the agreement let's introduce the χ^2 probability distribution.

The χ^2 distribution and the χ^2 probability distribution

The quantity χ^2 defined in equation 4.1 has a probability distribution given by

$$f(\chi^2) = \frac{1}{2^{d/2}\Gamma\left(d/2\right)} e^{-\chi^2/2} (\chi^2)^{d/2 - 1} \tag{4.2}$$

This is known as the χ^2 distribution with d, degrees of freedom, which is a positive integer [1]. $f(\chi^2)d(\chi^2)$ is the probability that a particular value of χ^2 falls between χ^2 and $\chi^2 + d(\chi^2)$. The χ^2 distributions computed for different degrees of freedom d is shown in the left part of fig. 4.2. We expect that a single measured value of χ^2 will have a probability α to be greater than $\chi^2_{d,\alpha}$,

1. $\Gamma(p)$ is the "Gamma function" defined by $\Gamma(p+1) = \int_0^\infty x^p e^{-x}\, dx$. It is a generalization of the factorial function to non-integer values of p. If p is an integer, $\Gamma(p+1) = p!$. In general $\Gamma(p+1) = p\Gamma(p)$ and $\Gamma\left(1/2\right) = \sqrt{\pi}$.

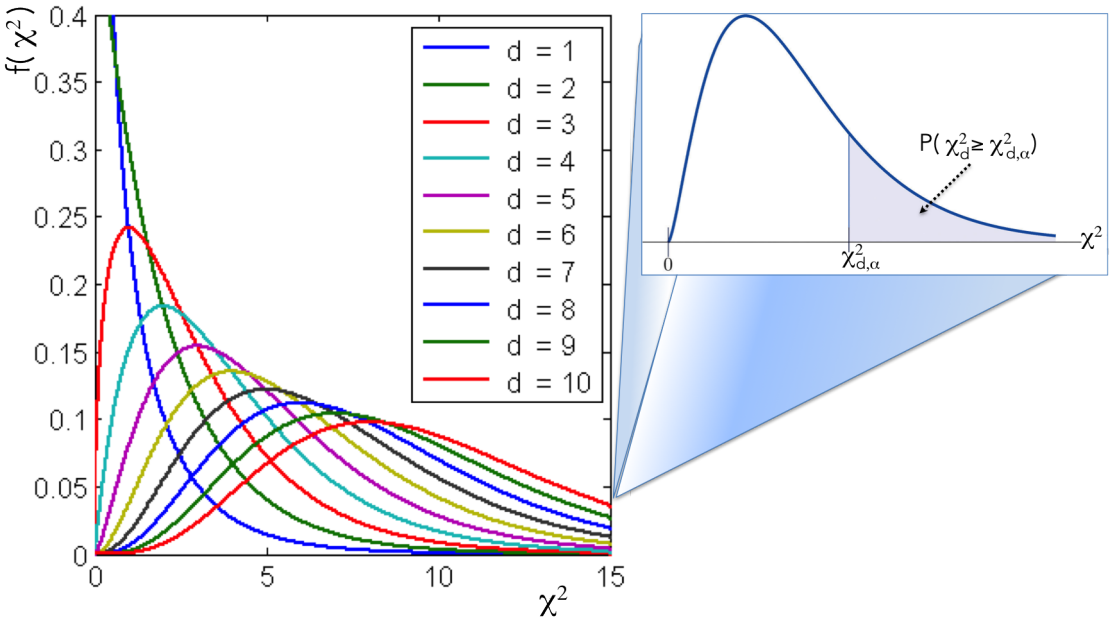

Figure 4.2: χ^2 distributions for d = 2, 4, ... , 10. In the blue frame is sketched the probability of χ^2, for a specific value of d, to be greater than a certain $\chi^2_{d,\alpha}$ critical value.

where $\chi^2_{d,\alpha}$ is defined by

$$P(\chi^2_d \geq \chi_{d,\alpha}) = \int_{\chi^2_{d,\alpha}}^{\infty} f(\chi^2)\,\mathrm{d}\chi^2 = \alpha \tag{4.3}$$

This definition is illustrated by the inset in fig. 4.2.
The χ^2 test works in the following way

1. We hypothesize that our simulated data are appropriately described by our experimental data or set of $\mu_i = Np_i$. In other words, we are going to test if the simulated data are a representative sample of the experimental data distribution.
2. From our data sample we calculate a sample value of $\chi^2_{d,o}$, along with d number of degrees of freedom and so determine $\tilde{\chi}^2_{d,o}$, the $\chi^2_{d,o}$ normalized to d for our data sample, defined by:
$$\tilde{\chi}^2_{d,o} = \frac{\chi^2_{d,o}}{d} \tag{4.4}$$
3. Assuming that the simulation data follow the experimental distribution with the ROOT function *Chi2test()*, we compute the corresponding value of $P(\tilde{\chi}^2_d \geq \tilde{\chi}^2_{d,o})$ to have a $\tilde{\chi}^2_d$ value greater or at least equal to the observed $\tilde{\chi}^2_{d,o}$. If this probability is close to one the $\tilde{\chi}^2_{d,o}$ is admissible and we have no reason to reject the hypothesis.
4. To give strictness to the test, we set a limit to define what is unreasonable and what is not, thus we choose a value of the significance level α (a common value is 0.05%, or 5%...). We

then compare $P(\tilde{\chi}^2_d \geq \tilde{\chi}^2_{d,o})$ with our significance level α computed as formula 4.3 and we may conclude:

- that the model represented by the $\mu_i = Np_i$ is a valid one if $P(\tilde{\chi}^2_d \geq \tilde{\chi}^2_{d,o}) > \alpha$. A statistically improbable excursion of χ^2 may occur if the simulated data are drawn from the experimental ones. This will happen with a probability equal to α, thus we will have $100\cdot(1\text{-}\alpha)\%$ confident in rejecting our model;
- contrarily if $P(\tilde{\chi}^2_d \geq \tilde{\chi}^2_{d,o}) < \alpha$ our model is so poorly chosen that an unacceptably large value of χ^2 has resulted.

This procedure is used to establish a quantitative measure of the agreement between simulation and experiment. To estimate if the $\tilde{\chi}^2_{d,o}$ is enough bigger than 1 to reject the initial hypothesis it is necessary to establish the limit between agreement and disagreement.

Note that this reasoning breaks down if there is a possibility that the data are not normally distributed. The probability $P(\tilde{\chi}^2_d \geq \tilde{\chi}^2_{d,o})$ estimation relies on the assumption that the observed numbers n_i are continuous variables that are normally distributed around their mean values $\mu_i = Np_i$. In our case n_i is a discrete variable, distributed according to a Poisson distribution. Assuming that the numbers involved in our problem are big enough, the discrete character isn't important since the Poisson distribution is well approximated by a gaussian function. For this reason the number of the k classes is chosen to have at least $\mu_i = 5$ counts per bin [2].
For these reasons equation 4.1 presents mean values $\mu_i = Np_i$ according to Poisson distributions. This approach makes sense in situations, as ours, involving counting rates where the counted numbers are distributed according to a Poisson distribution, for which the mean value is equal to the variance: $\mu_i = \sigma_i^2$. To employ the probabilities $P(\tilde{\chi}^2_d \geq \tilde{\chi}^2_{d,o})$ computed by ROOT [92] these conditions have to be fulfilled.

4.1.2 Application of the χ^2 test to $\cos\theta_{nn}$ distribution

Considering the DEMON central angles, as already explained in chapter 3, very narrow structures appear. This feature prevents from using the χ^2 test for the model-experiment comparison because the model is hidden in the angular resolution details: any small discrepancy of $\cos\theta_{nn}$ between the simulated structures (blue curve) of fig. 4.3 and the experimental ones (cyan curve) has a very important contribution to the χ^2 summation of formula 4.1, even if the simulation reproduces very well the experimental bumps. To make use of the χ^2 test one has to get rid of the effect of the experimental filter. This is performed in two steps:

1. smear the neutron coordinates over the entrance surface of each DEMON cell instead of taking the central angle.

2. The exact value of the Poisson $P_\mu(n)$, applying the condition for the *continuity*, is approximated to the area over the curve $G_{X,\sigma}(n)$ in the range $[n\text{-}{}^1/_2,\ n\text{+}{}^1/_2]$. It is demonstrated that this approximation is satisfactory for $\mu_i \geq 5$ [90, 91].

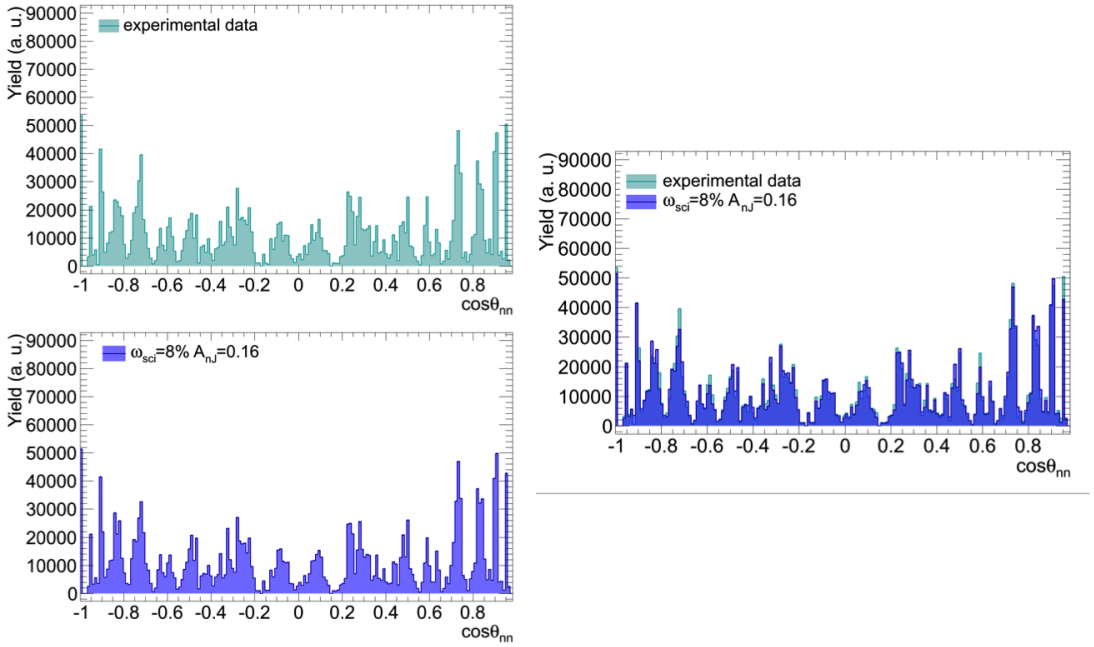

Figure 4.3: Comparison between the experimental $\cos\theta_{nn}$ in cyan and the simulated one in blue, for a pair of parameters A_{nJ}=0.16 and ω_{sci}=8%. The simulated bumps coincide very well with the experimental structures as appears on the right figure.

The *smear* function, written in the insert below, returns the smeared neutron vector $\boldsymbol{N}$ on the entrance side of a DEMON cell. The prototype of the function has in input the coordinate vector $\boldsymbol{DEMON}$ identifying a cell:

```
TVector3 smear(TVector3 DEMON)
{
        TVector3 uDEMON =  DEMON.Unit();
        float mR = gRandom->Uniform(0, 80);
        // DEMON Radii = 80 mm
        uR = uDEMON.Orthogonal().Unit();
        TVector3 R = uR *mR;

        float thetaND = TMath::ATan2(R.Mag(), DEMON.Mag());
        // thetaND is the angle between the new neutron vector N and DEMON
        float phiN = gRandom->Uniform() * TMath::TwoPi();
        float mN= TMath::Sqrt(DEMON.Mag() * DEMON.Mag() + R.Mag() * R.Mag());

        TVector3 N = mN*uDEMON;
        //  at the beginning N is set toward the DEMON vector
        N.Rotate(thetaND, uR);
        N.Rotate(phiN, uDEMON);
        return N;
}
```

Fig 4.4 shows the $\cos\theta_{nn}$ distributions after this procedure is applied both on the experimental and simulated data. The narrow structures have disappeared but broad structures

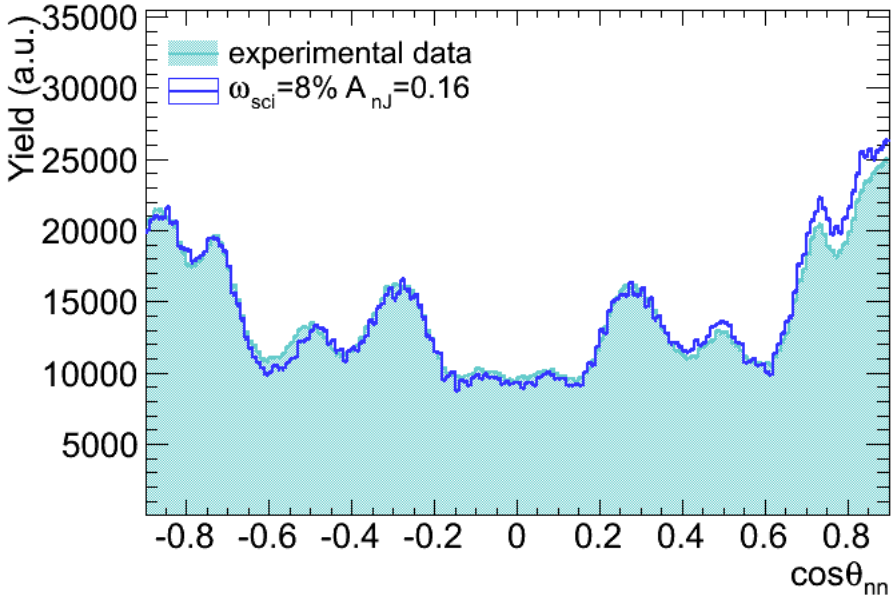

Figure 4.4: Smeared filtered $\cos\theta_{nn}$ distributions: the experimental one, $F_{exp}(\cos\theta_{nn})$, is the cyan filled curve and the simulated one, $F_{sim}(\cos\theta_{nn})$, for a pair of parameters A_{nJ}=0.16 and ω_{sci}=8%, is in blue. The experimental bumps coincide very well with the simulated structures.

remain.

2. determine the correlation distribution $I(\cos\theta_{nn})$ as if the neutrons were detected from a perfect 4π detector. To avoid the structures induced by the detectors configuration a simple idea is applied:

   if the efficiency (intrinsic and geometrical) is the ratio between the observed correlations and the theoretical ones expected in the spontaneous fission, the initial distribution without the effect of the filter is simply obtained by dividing the observed counting rate by the efficiency, as explained mathematically by the following equation:

$$I(\cos\theta_{nn}) = \frac{F(\cos\theta_{nn})}{R(\cos\theta_{nn})} \tag{4.5}$$

   where $I(\cos\theta_{nn})$ is the initial distribution, $F(\cos\theta_{nn})$ the smeared filtered distribution and $R(\cos\theta_{nn})$ the smeared detector response distribution.This procedure implies to divide the distribution of the detected neutron coincidences by the detector response. As these two distributions represent experimental counting rates, the Poisson statistics can be applied to the individual distributions. But what about the ratio $I(\cos\theta_{nn})$? Are its bin contents still distributed like Poisson distributions?
   In principle the ratio between two Poisson distributions isn't a Poisson distribution and the bin contents of the ratio are distributed in a more complicated way; for example a ratio

distribution could be a Cauchy distribution. Often the ratio distributions are heavy-tailed and it may be difficult to work with such distributions and develop an associated statistical test. So the prerequisites to apply the chi square method, mentioned before, may not be totally fulfilled.

Nevertheless we can choose a specific interval of the detector response distribution characterized by small oscillation amplitudes, as shown in the inserts of fig. 4.5. In this way the poissonian nature of the smeared neutron-neutron distribution remains unchanged when divided by a distribution roughly constant.
In addition we can arrange our distributions to fulfil the "at least 5 counts per bin" criterion by adapting the binning of the distribution.

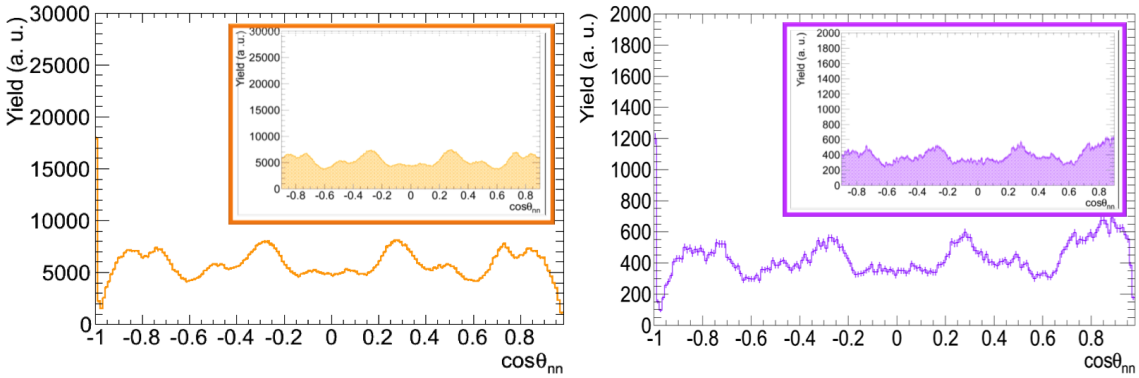

Figure 4.5: Left: detector response determined by an uncorrelated $\cos\theta_{nn}$ distribution between different fission events. Right: detector response to a pure isotropic emission. In the inserts the range of the detector response is restricted to [-0.9,+0.9] to avoid big oscillations of the distribution.

Now we need to determine the detector response distribution $R(\cos\theta_{nn})$. For this purpose two different strategies are followed:

simulated isotropy in the laboratory frame $R_i(\cos\theta_{nn})$: the detector response is simulated as the correlation distribution resulting from a pure isotropic emission in the laboratory system, as is shown in the right side (purple curves) of fig. 4.5. In this case the simulation is performed with the parameter pair A_{nJ}=0 and ω_{sci}=0% without the kinematical focusing effect. Thus to reproduce a perfect isotropy in the laboratory frame the velocity of the fission fragments v_{FF} is set to zero, in order to use the same simulation code.

uncorrelated events: this method consists in building up the $R_u(\cos\theta_{nn})$ distribition by taking the two neutrons randomly from different fission events. The obtained distribution is shown on the left side of fig. 4.5 (orange curves).

4.1.2.1 Simulated isotropy in the laboratory frame $R_i(\cos\theta_{nn})$ strategy

The initial $I_i(\cos\theta_{nn})$ shown in fig. 4.6 is evaluated applying equation 4.5 using as denominator $R_i(\cos\theta_{nn})$ simulated assuming a neutron isotropic emission in the laboratory frame, as mentioned above. The i index refers to isotropy. The left side of fig. 4.6 presents two data sets:

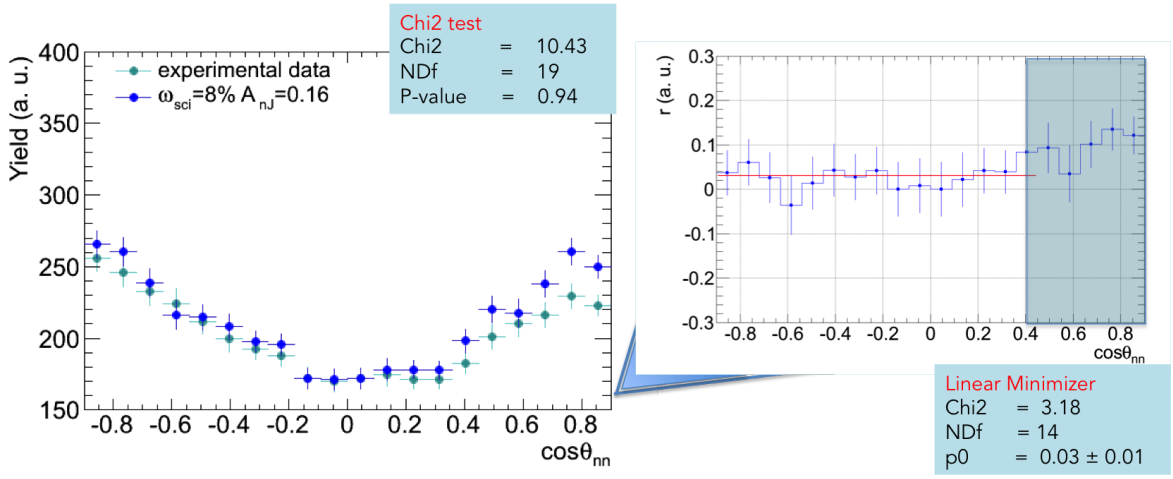

Figure 4.6: Left: $I_{i,exp}(\cos\theta_{nn})$ in cyan and $I_{i,sim}(\cos\theta_{nn})$in blue are compared. A very good agreement between the simulation and the experimental distributions can be observed in the interval $\cos\theta_{nn} \in$ [-0.9, 0.4]. For $\cos\theta_{nn} \geq 0.4$ some discrepancies appear. Also the dispersion $r = \frac{I_{i,sim}(\cos\theta_{nn}) - I_{i,exp}(\cos\theta_{nn})}{I_{i,exp}(\cos\theta_{nn})}$, presented on the right side, shows that the simulation doesn't reproduce very well the experimental points at small angles.

- the blue dots represent the simulation results. $I_{i,sim}(\cos\theta_{nn})$ of formula 4.6 is obtained dividing the smeared filtered distribution $F_{sim}(\cos\theta_{nn})$ extracted by a calculation considering the couple A_{nJ}=0.16 and ω_{sci}=8% by the isotropic response function $R_i(\cos\theta_{nn})$:

$$I_{i,sim}(\cos\theta_{nn}) = \frac{F_{sim}(\cos\theta_{nn})}{R_i(\cos\theta_{nn})} \tag{4.6}$$

- the cyan dots represent the initial experimental distribution $I_{i,exp}(\cos\theta_{nn})$ estimated by formula 4.7:

$$I_{i,exp}(\cos\theta_{nn}) = \frac{F_{exp}(\cos\theta_{nn})}{R_i(\cos\theta_{nn})} \tag{4.7}$$

Now we can apply the χ^2 test to confront $I_{i,sim}(\cos\theta_{nn})$ and $I_{i,exp}(\cos\theta_{nn})$. In chapter 3 we saw that, due to the DEMON angular spacings, 20 bins were a good choice; this value fulfils also the "minimum 5-counts" criterion. This leads to d=19 degrees of freedom. The parameter couple A_{nJ}=0.16 and ω_{sci}=8% was used. The resulting χ^2 is $\chi^2_o = 10.43$, as shown in the left part of fig. 4.6, leading to $\tilde{\chi}^2_o \approx 0.6$. This latter value is less than one, so we can conclude that the agreement "simulation with A_{nJ}=0.16 and ω_{sci}=8% - experiment" is satisfactory. However, this value doesn't give stronger confidence than a value $\tilde{\chi}^2_o = 1$ would give. It means only that

$\tilde{\chi}^2_o$ is just the result of a large chance fluctuation away from the expected value $\bar{\chi}^2_o$ [91]. In no way it gives extra weight to conclude that our simulation follows the experiment.

To get a more quantitative estimation of the χ^2 test a p-value is computed by ROOT and leads to $P(\tilde{\chi}^2 \geq 0.6) = 0.94$. This means that, supposing that the simulation is governed by the experimental distribution, the probability to obtain a value $\tilde{\chi}^2_o$ larger than ours is of about 94%. Setting the confidence $\alpha-$level to 5% as boundary, our $P(\tilde{\chi}^2 \geq 0.6) = 0.94 > 5\%$. This means that the model chosen to simulate the data set, with A_{nJ}=0.16 and ω_{sci}=8% and taking into account all the approximations discussed before for the χ^2 test, is valid to represent the experimental measurement at 2σ.
The right side of the fig.4.6 shows the dispersion r of the simulated data set in respect with the experimental data. A linear minimisation has been performed in the [-0.9, 0.4] range. In this range the values associated to the linear fit are shown in the inset of fig. 4.6. A constant value $p_0 = 0.03 \pm 0.01$ is obtained. The constant hypothesis seems to work very well but for $\cos\theta_{nn} \geq 0.4$ discrepancies appear. The simulated set presents a significant overestimation compared to the experimental one. As explained in chapter 3 and underlined by Y. Kopach [93] and shown in fig. 4.7, the [0.4; 1] interval is the range of major influence of the cross talk effect on the $\cos\theta_{nn}$ distribution. As explained in chapter 3, in the simulation cross talk has been taken into account in the same way as it happens in experiment. But considering the result of fig. 4.6 it seems that the simulated cross talk has been overestimated. This could be explained by the absence of any DEMON cell container or maybe to the arrangement of the DEMON cells in the vacuum, both considered in simulation. Indeed additional materials will for sure decrease the cross talk probability. To illustrate this assertion, only a percentage of 85% of the simulated cross talk events are taken. As a result, fig. 4.8 shows that the simulation-experiment agreement increases by decreasing randomly the simulated cross talk by 15%.

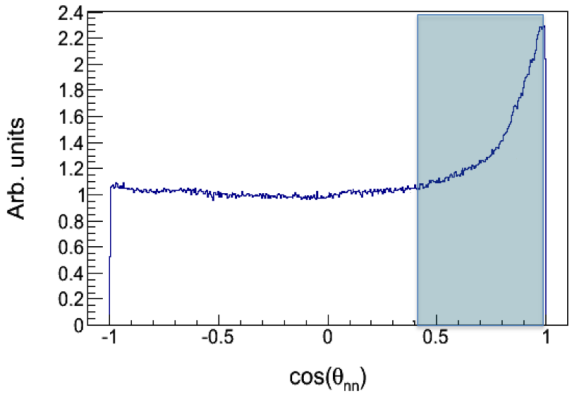

Figure 4.7: Simulated $\cos\theta_{nn}$ distribution which shows the importance of cross talk. From [93].

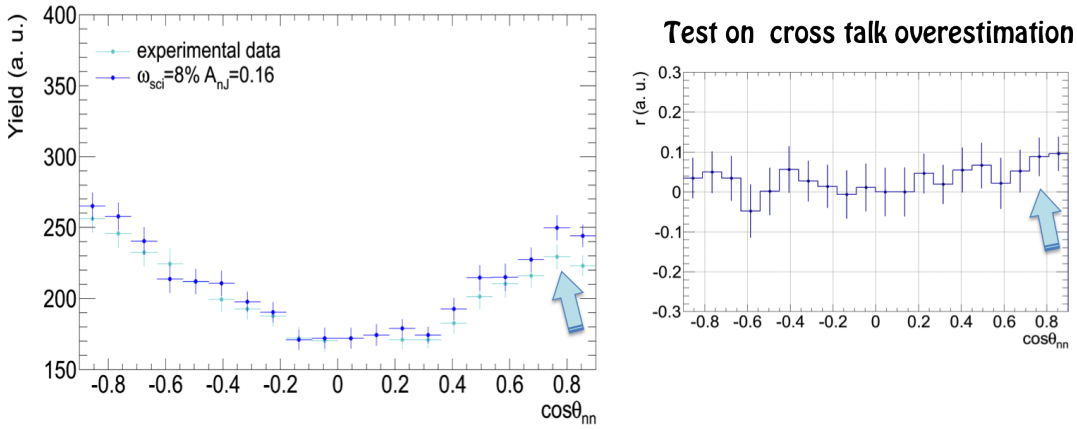

Figure 4.8: Left: $I_{i,exp}(\cos\theta_{nn})$ in cyan and $I_{i,sim}(\cos\theta_{nn})$ in blue are presented taking into account only 85% of the simulated cross talk. Also the dispersion r is shown on the right side in this case. Subtracting 15% of the cross talk events, the agreement between the two data sets increases at small θ_{nn} angles and flatter for $\cos\theta_{nn}$¿0.4 then in the previous case (fig. 4.6).

4.1.2.2 Uncorrelated events strategy

The algorithm to uncorrelate fission neutrons is as follows:

for a given event with ν neutrons

- take 1^{st} neutron from the considered event
- take (ν -1) other neutrons each one randomly among the neutrons from the (n-1) previous events

```
>> example:
        nevt:     n = 3   →   n1  n2  n3          →     N1 = n1

       nevt-1: n = 0  →   -
       nevt-2: n = 1  → n1 → N2 = n
       nevt-3: n = 2  → n1  n2 → N3 = random(n1, n2)


//correlated neutrons:  n1  n2  n3
"uncorrelated neutrons: N1  N2  N3"

problem:  it may happen that 1 or more uncorrelated neutrons are now in the
    same detector
             →  pile up
              These uncorrelated events are suppressed
```

Applying this procedure, the detector responses $R_{u,exp}(\cos\theta_{nn})$ for the uncorrelated experimental data and $R_{u,sim}(\cos\theta_{nn})$ for the uncorrelated simulated ones are obtained. Using the same colour code as before:

– the simulated $I_{u,sim}(\cos\theta_{nn})$, in blue of formula 4.8 is the ratio between the smeared filtered distribution $F_{u,sim}(\cos\theta_{nn})$ with A_{nJ}=0.16 and ω_{sci}=8% and $R_{u,sim}(\cos\theta_{nn})$ is its uncorrelated distribution:

$$I_{u,sim}(\cos\theta_{nn}) = \frac{F_{sim}(\cos\theta_{nn})}{R_{u,sim}(\cos\theta_{nn})} \tag{4.8}$$

– the initial distribution $I_{u,exp}(\cos\theta_{nn})$, in cyan, is computed as formula 4.9, taking into account the experimental uncorrelated distribution $R_{u,exp}(\cos\theta_{nn})$:

$$I_{u,exp}(\cos\theta_{nn}) = \frac{F_{exp}(\cos\theta_{nn})}{R_{u,exp}(\cos\theta_{nn})} \tag{4.9}$$

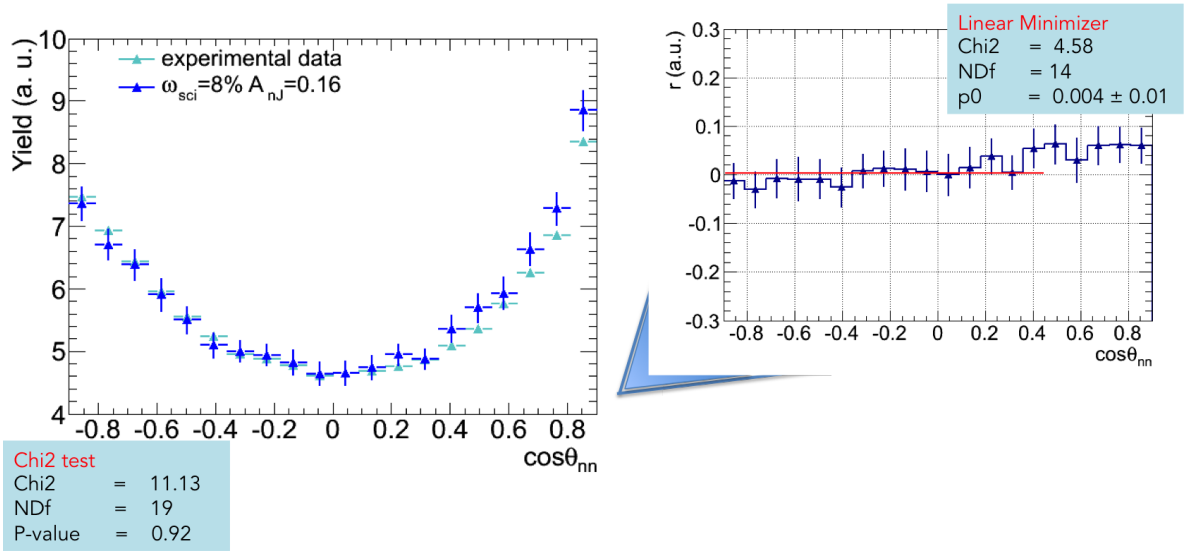

Figure 4.9: Left: $I_{u,exp}(\cos\theta_{nn})$ in cyan and $I_{u,sim}(\cos\theta_{nn})$ in blue are compared. The simulation obtained for the couple A_{nJ}=0.16 and ω_{sci}=8% and $R_{u,sim}(\cos\theta_{nn})$ reproduces very well the experimental points in the interval $\cos\theta_{nn} \in$ [-0.9, 0.4]. Also here for $\cos\theta_{nn} \geq 0.4$ the cross talk overestimation appears. The dispersion r, presented at the right side, seems to be flatter then in the previous case of fig.4.6.

The conclusions, about this strategy, when the χ^2 test is applied, are more or less the same as in the previous case as shown in fig.4.9. The $I_{u,exp}(\cos\theta_{nn})$ and $I_{u,sim}(\cos\theta_{nn})$ distributions seem smoother than before (fig. 4.6). It seams that the uncorrelated detector responses $R_u(\cos\theta_{nn})$ fill the empty areas of the filtered distribution slightly better than the simulated detector response $R_i(\cos\theta_{nn})$. Also the dispersion r presented on the right side of fig.4.9 is flatter than in the previous case and the constant value $p_0 = 0.004 \pm 0.001$ is one order of magnitude smaller. But although it is less important, an overestimation of the cross talk also appears at small angles in this case.

4.1.3 Influence of A_{nJ} and ω_{sci} on $\cos\theta_{nn}$

The $\cos\theta_{nn}$ distributions are simulated with different sets of A_{nJ} and ω_{sci} parameters which quantify the dynamical anisotropy and the contribution of scission emission. It is possible to simulate different cases:

- pure isotropy
- introducing scission and/or anisotropy as predicted by theory [36] as we have seen previously
- unrealistic (A_{nJ}, ω_{sci}) combinations.

In table 4.1 are summarised the different simulations performed and the $\tilde{\chi}^2_o$ obtained.

As mentioned in chapter 1, the two effects appear in the same angular region where they

simulation nº	A_{nJ}	$\omega_{sci}(\%)$	$\tilde{\chi}^2_o$	fig.
1	0	0	7.86	4.10
2	0.16	0	1.51	4.11
3	0	8	0.95	4.12
4	0.16	8	0.60	4.9 and 4.4
5	1	20	2.80	4.13

Table 4.1: Resulting χ^2 obtained by comparing five different sets of parameters with the experiment.

reinforce the kinematical focusing and they act in the opposite way. But the anisotropy increases slightly the focusing whereas the scission neutron emission decreases it in a very significative way in respect with the anisotropy.

The analysis shows that, surprisingly the worse $\tilde{\chi}^2_o$ is obtained for the isotropy rather then for the very unrealistic simulation (case 5). This is due to the opposite effect of the cross talk overestimation and the strong scission neutron presence ω_{sci}. In fact a value of ω_{sci}=20% importantly lowers the curve at small angle where a cross talk overestimation survives. To confirm this argument and to avoid the aberration due to the cross talk overestimation, the $\tilde{\chi}^2_o$ are recomputed in the range $\cos\theta_{nn} \in$ [-0.9, 0.4] and presented in table 4.2.

Now we obtain very realistic results:

- the worse χ^2 is obtained for the most unrealistic set (A_{nJ}=1, $\omega_{sci} = 20\%$) parameter with $\chi^2 = 3.24$. This combination has to be excluded. The other four cases give all χ^2 values $\chi^2 < 1$. None of these combinations has to be excluded to reproduce the experiment. Nevertheless the smallest value, $\chi^2 = 0.24$, is obtained for the combination (A_{nJ}=0.16, $\omega_{sci} = 8\%$) which is the one predicted by I. Guseva *at al.* and already used above. Table 4.2 confirms also that the scission emission effect is more important than the anisotropy.

What about the validity of the two methods used? In fact the filtered distribution $R_{i,sim}(\cos\theta_{nn})$ obtained for the simulated isotropy method takes into account all the biases of the filter, included

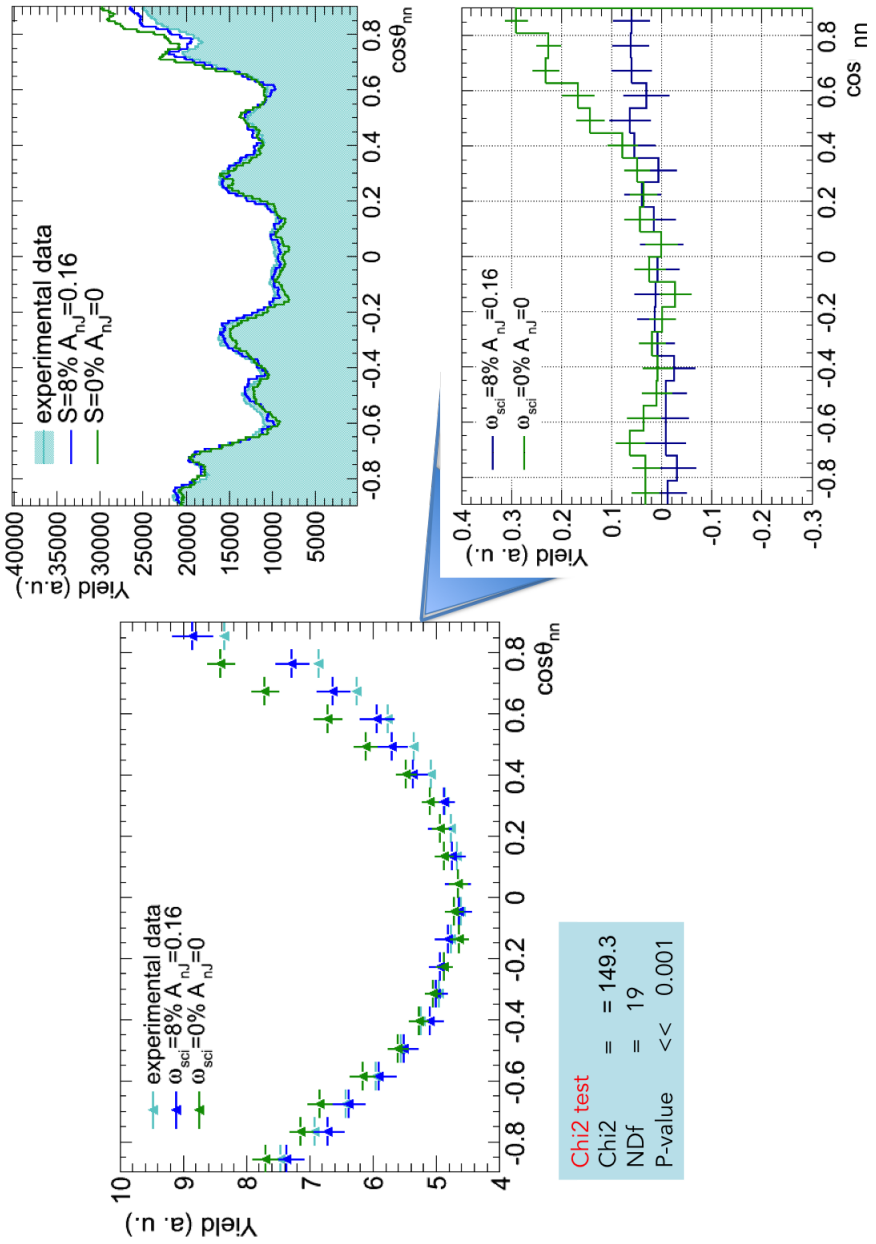

Figure 4.10: Left: Simulated ratio $I_{u,sim}(\cos\theta_{nn})$ (green dots) for A_{nJ}=0 and ω_{sci}=0%
- simulated ratio $I_{u,sim}(\cos\theta_{nn})$ (blue dots) for A_{nJ}=0.16 and ω_{sci}=8%
- experimental ratio $I_{u,exp}(\cos\theta_{nn})$ (cyan dots).
Right: in the upper part $F_{u,sim}(\cos\theta_{nn})$ computed with the same set of parameters mentioned as above and $F_{u,exp}(\cos\theta_{nn})$ the experimental filtered distribution.
In the bottom part the dispersion r is presented.

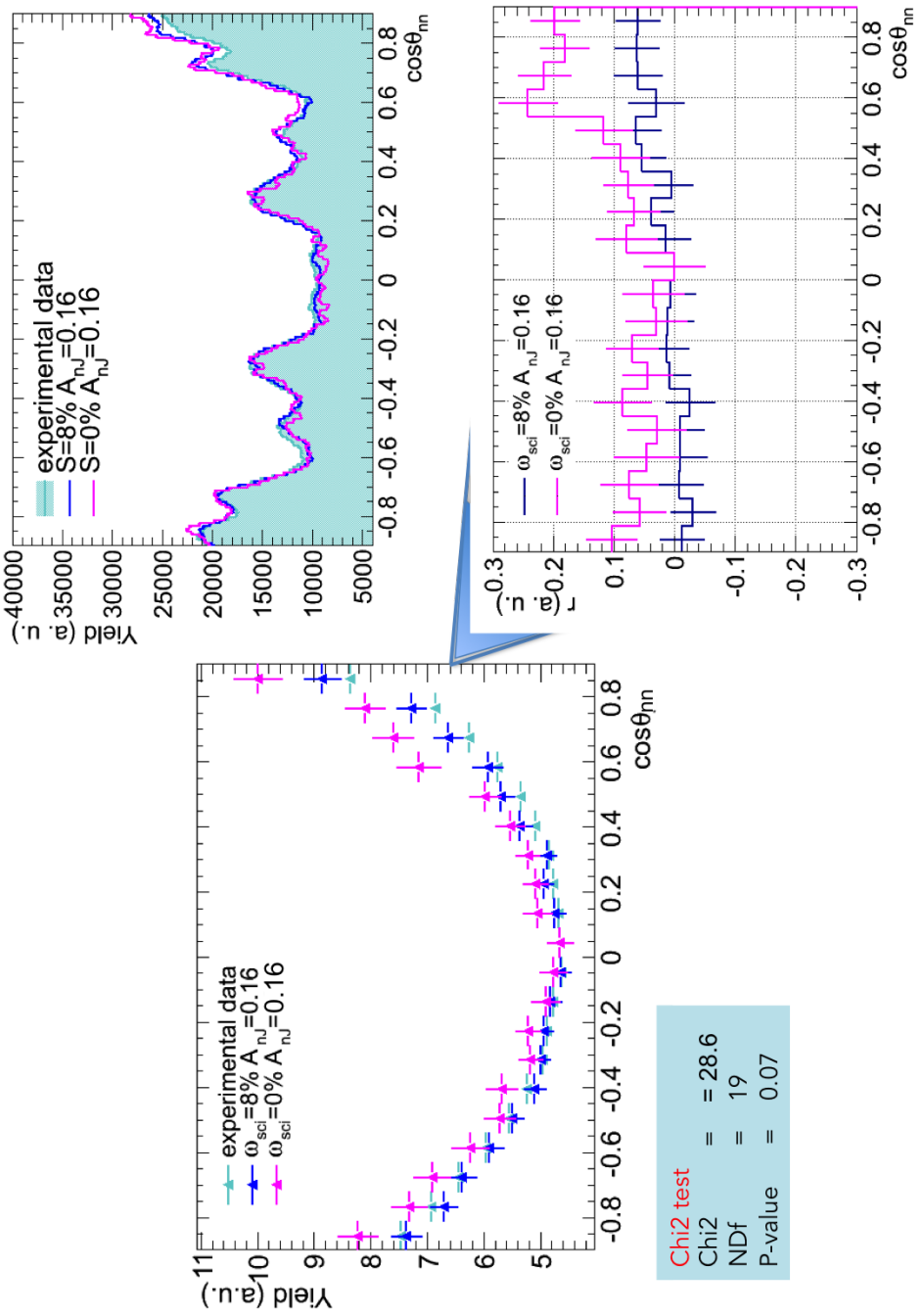

Figure 4.11: Same as fig. 4.10 but with A_{nJ}=0.16 and ω_{sci}=0% for the pink curves.

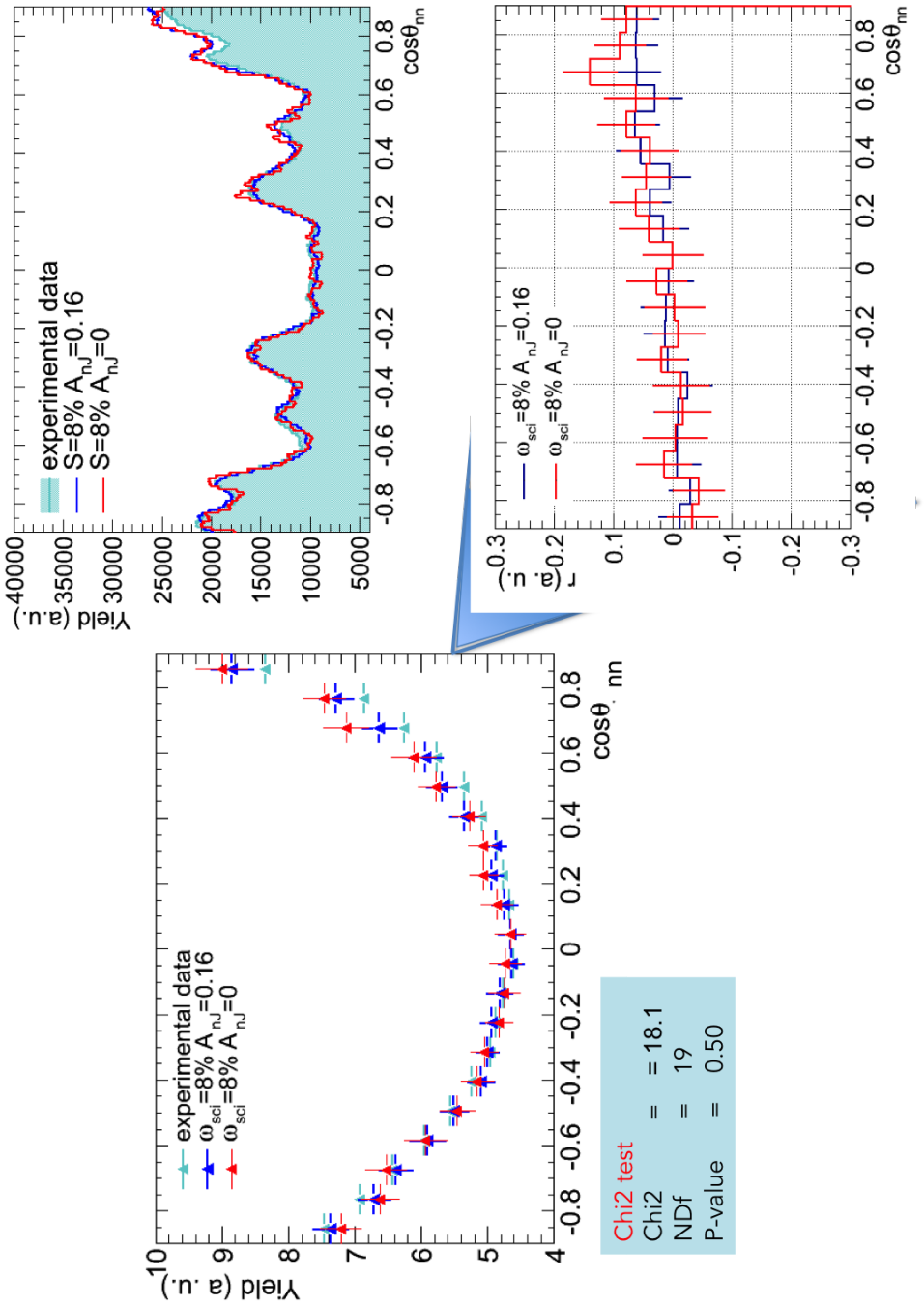

Figure 4.12: Same as fig. 4.10 but with A_{nJ}=0.16 and ω_{sci}=0% for the red curves.

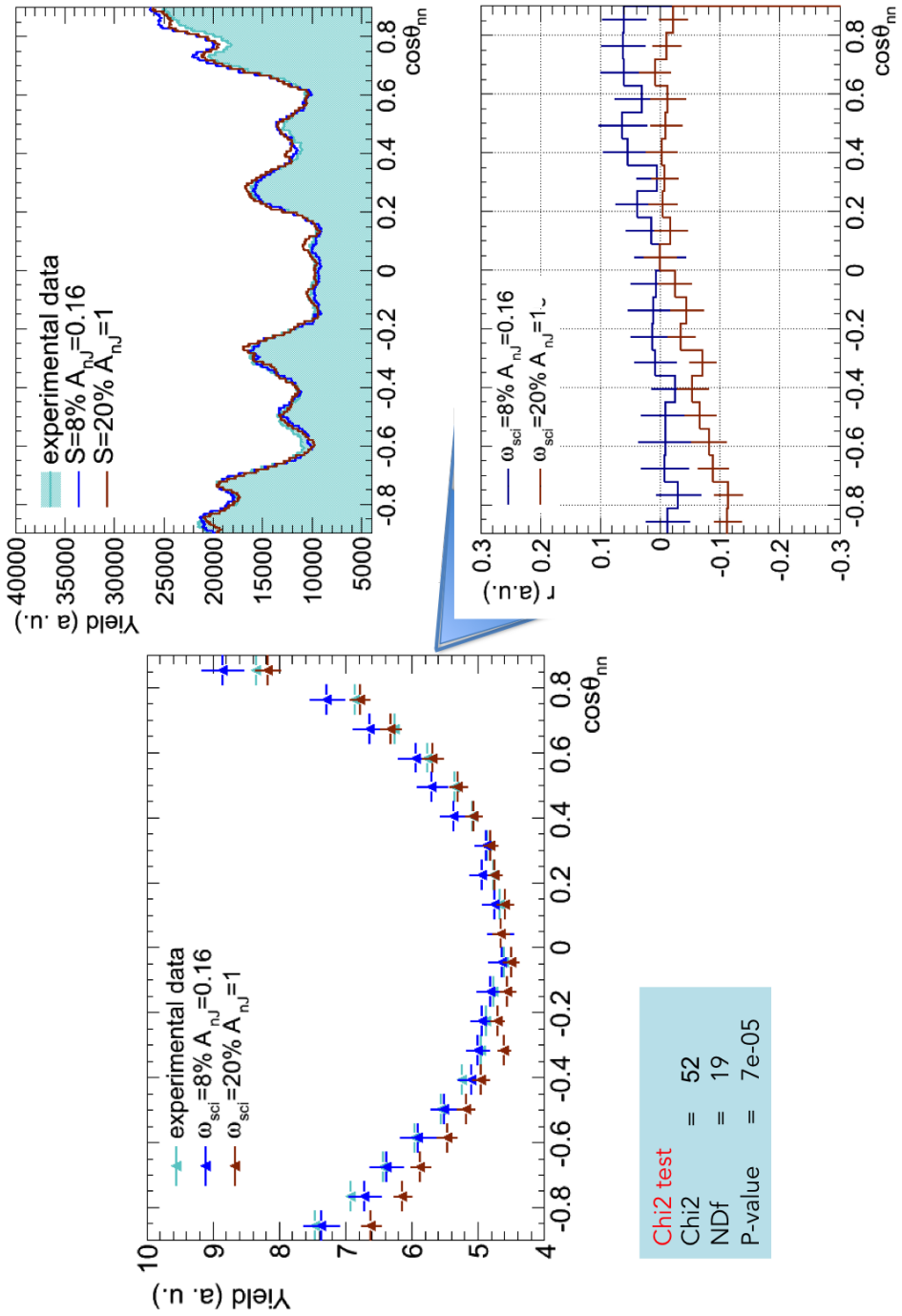

Figure 4.13: Same as fig. 4.10 but with A_{nJ}=1 and ω_{sci}=20% for the brown curves.

Restriction to $\cos\theta_{nn} \in$ [-0.9, 0.4]				
simulation nº	A_{nJ}	$\omega_{sci}(\%)$	$\tilde{\chi}^2_o$	fig.
1	0	0	0.87	4.10
2	0.16	0	0.59	4.11
3	0	8	0.35	4.12
4	0.16	8	0.24	4.9 and 4.4
5	1	20	3.24	4.13

Table 4.2: Resulting χ^2 obtained by comparing the same sets of parameters with the experiment, restricted to $\cos\theta_{nn} \in$ [-0.9, 0.4].

the cross talk. The cross talk overestimation appears also in $F_{sim}(\cos\theta_{nn})$. Does one This effect may disappear by dividing the curves. But it seems, regarding the disagreement at small angles in figs. 4.6 and 4.8, that this overestimation doesnt́ intervene in the same way in the numerator and in the denominator. Moreover the curves of fig.4.6 present some irregularities. This can be due to the fact that the simulated filter $R_{i,sim}(\cos\theta_{nn})$ does not reproduce exactly the real one. The uncorrelated method doesn't present this drawback. As shown in the left part of fig. 4.5, the uncorrelated distribution presents a very symmetric feature in respect with the other method. But the random correlations don't reproduce the bias due to the cross talk. As appears clearly in the left part of fig. 4.9, the yield at small angles is even higher at $\cos\theta \approx$ -1 which is the opposite of the expected behaviour.

4.2 $\cos\theta_{nLF}$ distribution

In the experimental analysis the CODIS potentiality is exploited to infer the FF positions, thus the $\cos\theta_{nLF}$ distribution is obtained. However, as mentioned in chapter 2, a cut on $|\cos\theta_{FF}| > 0.4$ is applied. This procedure induces two discontinuities at $\cos\theta_{nLF} \sim -0.4$ and at $\cos\theta_{nLF} \sim 0.4$ in the experimental data pointed by the arrows in fig. 4.14 a). Since our intent is to analyse the simulated data in the same way as the experimental ones, the same cut is applied, thus the simulated distribution of fig 4.14 b) presents a similar feature. To simulate the data, two smear algorithms are applied:

- one to the DEMON central angles as before;
- to reproduce the experimental CODIS resolution, another one to the FF angles. The FFs smearing code is the following:

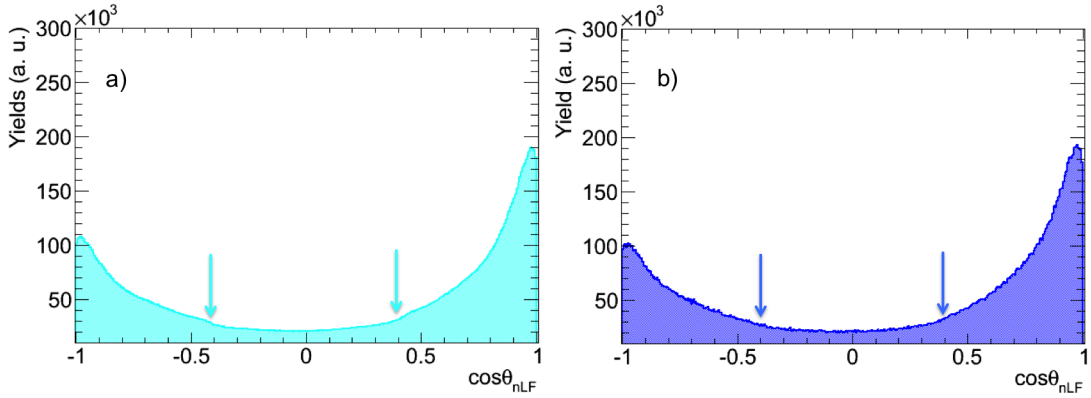

Figure 4.14: (a) experimental filtered distribution $F_{exp}(\cos\theta_{nLF})$ and (b) the simulated $F_s(\cos\theta_{nLF})$ one after the smearing treatment.

```
TVector3 SmearCodis(TVector3 FFvec)
{
        float theta_ff =TMath::Abs(gRandom->Gaus(0,9*TMath::DegToRad()));
        float phi_ff = gRandom->Uniform() * TMath::TwoPi();
        TVector3 uR = FFvec.Orthogonal().Unit();

        TVector3 newFFvec=FFvec;
        newFFvec.Rotate (theta_ff, uR);
        newFFvec.Rotate(phi_ff , FFvec);

        return newFFvec;
}
```

The simulated FF vectors, ***FFvec***, are the input of the function and the smeared fragment vector is ***newFFvec***. θ_{FF}, in the code, is smeared following a gaussian distribution of centroid equal to zero and with a $\sigma = 9°$, corresponding to the mean angular resolution of CODIS.

Fig. 4.15 shows the simulation results obtained for the five pairs of parameters (A_{nJ}, ω_{sci}) chosen before. These simulations are compared to the experimental data presented by the cyan dot curve.

As observed the simulations with the same scission neutron occurrence ω_{sci} are very close to each other. Likewise the $\cos\theta_{nn}$ distribution, the dynamical anisotropy only slightly affects the $\cos\theta_{nLF}$ distribution, but the difference is enough to estimate the best agreement with the experimental data as we will see in the following lines.

As we can observe, the curves that best reproduce the experimental points are the simulation nº 3 (red points) and nº 4 (blue points). For these curves the dispersion r is computed and shown in fig. 4.16. A linear fit is performed. The results of this fit are presented in table 4.3.

As observed in fig. 4.16, a disagreement appears at small θ_{nLF} angles. This can not be due to the cross talk which is spread over the whole θ_{nLF} distribution. A possible reason for this

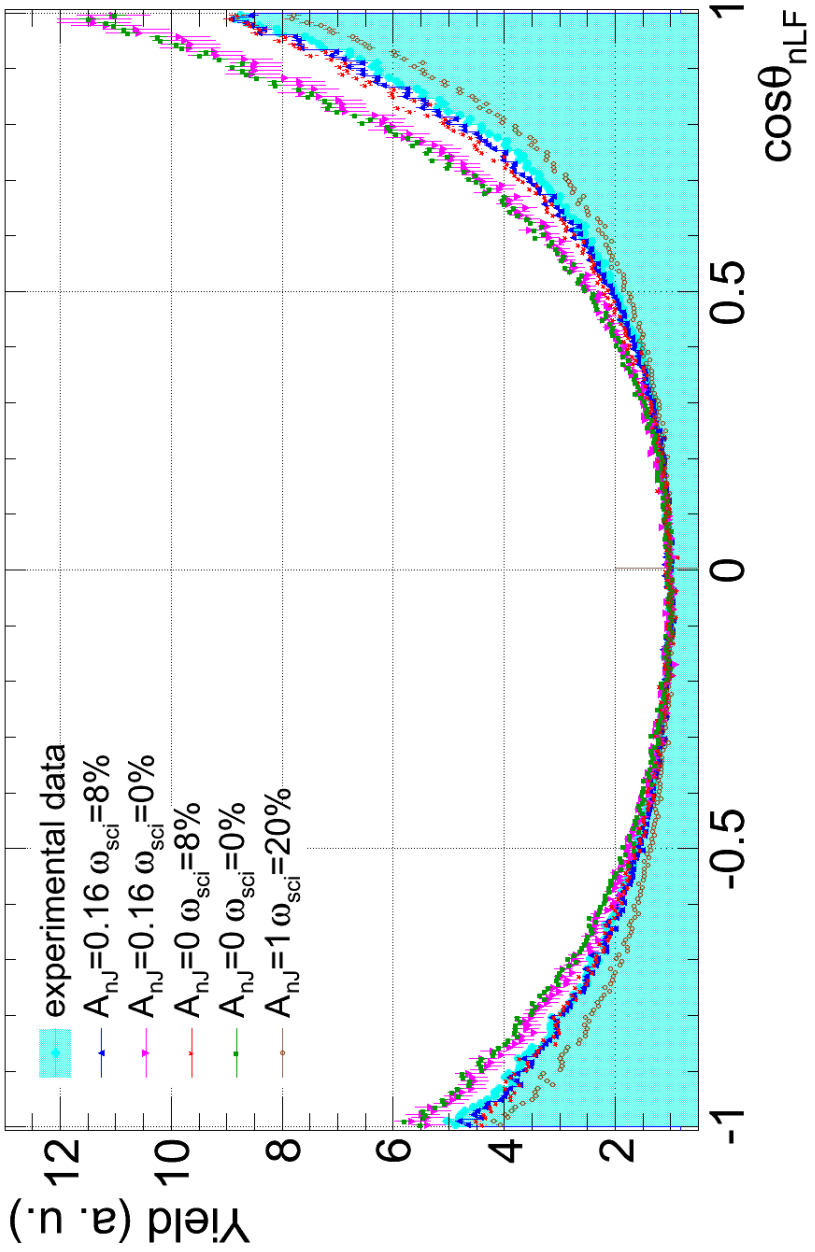

Figure 4.15: Confrontation between the $\cos\theta_{nLF}$ experimental distribution and the simulated ones. The parameters (A_{nJ},ω_{sci}) pairs are the ones of table 4.3.

simulation nº	A_{nJ}	$\omega_{sci}(\%)$	full range		Restricted		
			$\tilde{\chi}^2_o$	d	$\tilde{\chi}^2_o$	d	$P(\tilde{\chi}^2 \geq \tilde{\chi}^2_o)$
3	0 .00	8	5.07	299	1.70	211	<0.00001
4	0.16	8	2.06	299	1.01	211	0.45

Table 4.3: Resulting χ^2-test obtained by a linear minimisation of the dispersion of fig. 4.16.

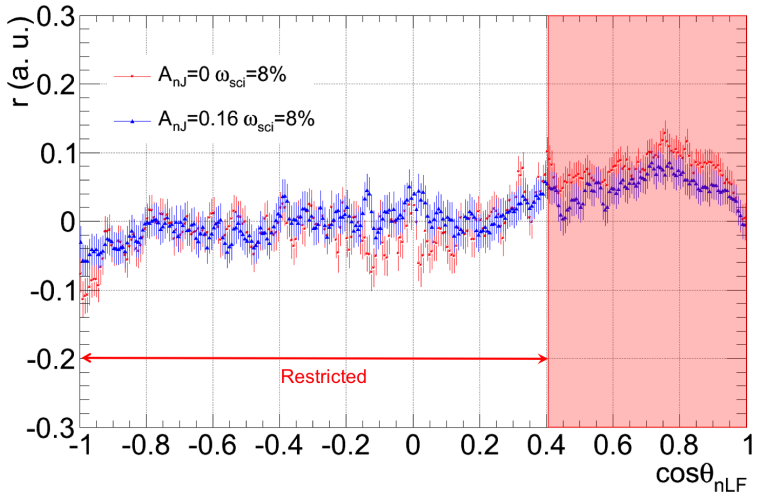

Figure 4.16: Dispersion r computed only for the simulation nº 3 and nº 4 that best reproduce the experimental $\cos\theta_{nLF}$ distribution.

discrepancy could be the fact that in the simulation only mean values of the FF velocities have been used whereas in the experiment the measured ones have ben taken. Another possibility could be related to the neutron energy threshold. Indeed the disagreement is most likely related to energy, either of the fragment or of the neutrons.
The χ^2 results are presented in the right part of table 4.3 when the angular range is restricted to $\cos\theta_{nLF} \in$ [-0.9, 0.4]. In this case, for simulation nº 3, the $\tilde{\chi}^2$ is high enough to reject this couple of parameters even at a boundary level of 1% as the p-value is very small. On the other hand the simulation nº 4 leads to a $\tilde{\chi}^2 \approx 1$ with a p-value $P(\tilde{\chi}^2 \geq \tilde{\chi}^2_o)$=0.45 which allows to accept this parameter configuration at a boundary level of 32% (1σ). Thus the predicted configuration A_{nJ}=0.16 and ω_{sci}=8% gives the best agreement between simulation and experiment.

The analysis of $\cos\theta_{nLF}$ reinforces the results obtained with the $\cos\theta_{nn}$ distribution, although the relative effects between the different set of parameters are less marked.

4.3 $\phi_{nn|_{LF}}$ distribution

Let's finish with the aspect the CORA experiment was designed for: the $\phi_{nn|_{LF}}$ distribution. The method used for this analysis has been presented in detail in chapter 1. The advantage of this method is that it is an independent approach of the anisotropy estimation as we get rid of the kinematic focusing as well as of the scission emission.

Before confronting the simulation results to the experimental ones, the procedures to build the detector responses with the two strategies seen before are tested. The projection of the neutron-neutron angular distribution $\phi_{nn|_{LF}}$ onto the (x, y) plane (see fig.1.14) has to be simulated. As the effect of A_{nJ} on the $\phi_{nn|_{LF}}$ distribution is expected to be very weak it will be tricky to extract. Thus in a first step, to check the different ingredients, an unrealistic anisotropy coefficient A_{nJ}=1, which is about a factor 10 larger than expected the model [36], will be used. Our attention will focus on each step of the experimental filter (the DEMON geometrical acceptance, the pileup treatment, the threshold energy, the intrinsic efficiency, the cross talk and the DEMON central angles), because it may distort the resulting distribution.
The cross talk will have to be taken carefully into account. In this purpose we apply the condition $\cos\theta_{nn} > 0.4$ which was determined previously to minimize its effect.

In the same way as for the $\cos\theta_{nn}$ distribution, two methods to take into account the detector response will have be considered. In the uncorrelated method, neutrons from different fission events have to be coherent: the corresponding uncorrelated emitting fragment vector has to be the same or at least very close to the correlated one. For this reason in a first step we select only those events, for which the fission fragments are emitted along the chamber axis, the z-axis. In a further step the procedure can be extended to the full angular range of CODIS.

4.3.1 A_{nJ}=1

In chapter 1 the angular distribution of the neutrons emitted by the FF CMs was described as

$$W(\theta_{nJ}) \propto (1+A_{nJ}\, sin^2\theta_{nJ}) \tag{1.9}$$

This formula leads to the $\phi_{nn|_{LF}}$ distribution [36] expressed as

$$W(\phi_{nn|_{LF}}) = p_0(1 + a_2 \cos^2\phi_{nn|_{LF}}) \tag{4.10}$$

The projection of the relative angular distribution of two emitted neutrons onto the plane perpendicular to the fission axis in the CM system for A_{nJ}=1 is shown in fig. 4.17. This distribution is identical in the laboratory and in the CM systems. As expected a huge effect for neutron anisotropy appears. The anisotropy parameter $A_{nJ} = 1$ leads to a_2=0.04 in agreement with the calculation of I. Guseva [45] and shown in fig. 4.18.

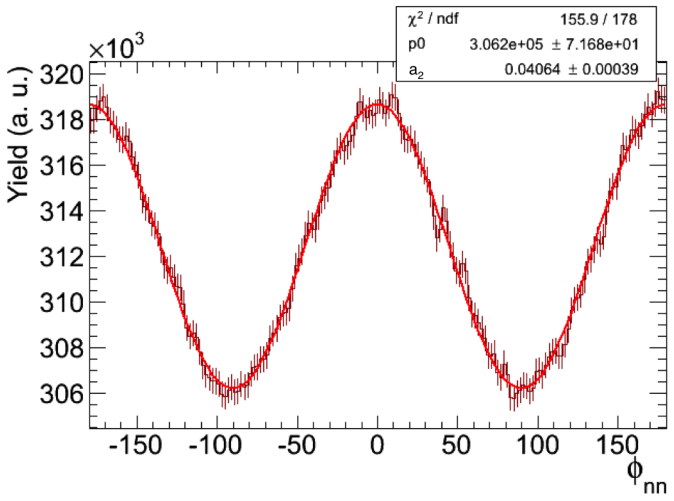

Figure 4.17: Simulated $\phi_{nn|_{LF}}$ distribution for A_{nJ}=1. Regular sinusoidal structures appear. The curve is fitted by formula 4.10. The fit parameters are presented in the insert.

Applying then the experimental filter to the distribution of relative $\phi_{nn|_{LF}}$, the regular sinusoidal structures of fig. 4.17 disappear and many irregular structures appear as shown by the pink curve of the left part of fig. 4.19.

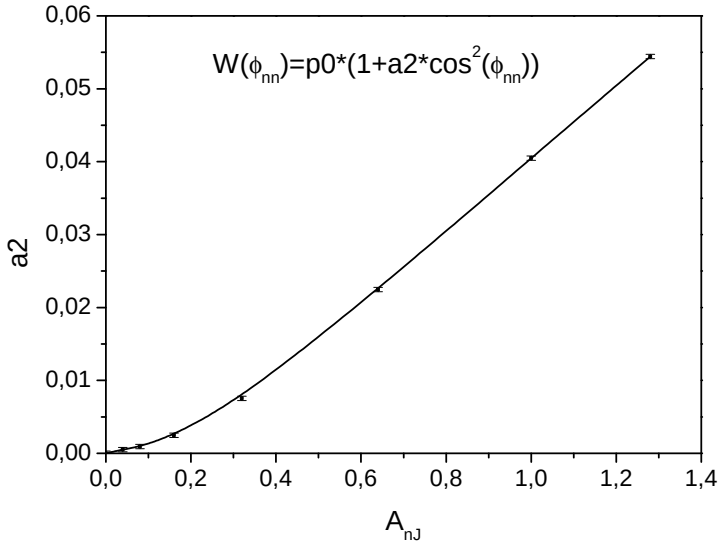

Figure 4.18: The a_2 coefficient as a function of the anisotropy parameter A_{nJ}. From [44].

As explained in section 4.1.2 concerning the cosθ_{nn} distribution, in order to get rid of the DEMON filter effects, one can normalise this distribution $F(\phi_{nn|_{LF}})$ using the adapted detector response distribution $R(\phi_{nn|_{LF}})$. To simulate such a distribution one can use either an isotropic emission in the FF CMs which gives $R_{i,sim}(\phi_{nn|_{LF}})$ or the uncorrelated coincidences leading to $R_u(\phi_{nn|_{LF}})$, as mentioned before.

As this latter method seems to reproduce in a more appropriate way the detector response concerning the cosθ_{nn} distribution, we will go across the different steps of the experimental filter for this case whereas, for the first methodology, we directly show the final obtained results.

4.3.1.1 Simulated isotropy in the laboratory frame $R_{i,sim}(\phi_{nn|_{LF}})$ strategy

The initial $I_{i,sim}(\phi_{nn|_{LF}})$ is evaluated applying equation 4.11 using as denominator $R_{i,sim}(\phi_{nn|_{LF}})$ simulated assuming an isotropic neutron emission in the FF CMs frame this time:

$$I_{i,sim}(\phi_{nn|_{LF}}) = \frac{F_{sim}(\phi_{nn|_{LF}})}{R_{i,sim}(\phi_{nn|_{LF}})} \tag{4.11}$$

As a result of this first method, fig. 4.19 presents on the left the filtered $F_{sim}(\phi_{nn|_{LF}})$ distribution

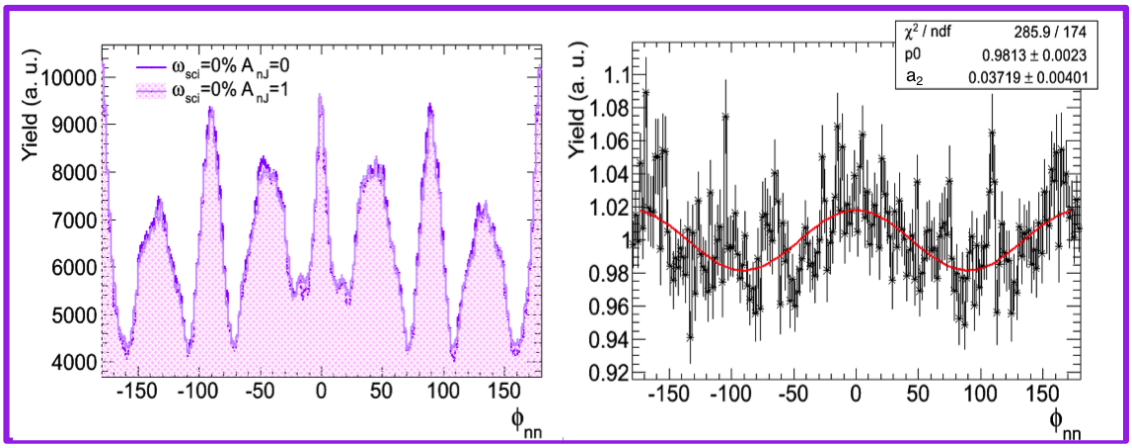

Figure 4.19: $\phi_{nn|_{LF}}$ simulated distribution for A_{nJ}=1. When the experimental filter intervenes more structures appear. The left part of the figure shows the filtered distribution $F_{sim}(\phi_{nn|_{LF}})$ (pink filled curve) and the isotropic detector response $R_{i,sim}(\phi_{nn|_{LF}})$ (purple curve). The ratio $I_{i,sim}(\phi_{nn|_{LF}})$ is presented on the right side together with the fit. With this method some structures appear in the ratio distribution even if the fit result is not far from the predicted one.

(filled pink curve) and the detector response to the isotropic emission $R_{i,sim}(\phi_{nn|_{LF}})$ (purple curve). On the right side, the resulting initial distribution $I_{i,sim}(\phi_{nn|_{LF}})$, which takes into account all the experimental biases is shown. In red is drawn the fit following eq. 4.10 and in the insert are given the fit parameters. The resulting coefficient $a_2 = 0.037 \pm 0.004$ is not far from the predicted one $a_2 = 0.04$ of fig. 4.17. The red curve agrees quite well with the $I_{i,sim}(\phi_{nn|_{LF}})$ distribution although some unexpected structures appear. As already mentioned the $R_{i,sim}(\phi_{nn|_{LF}})$ response function may be not well adapted.

4.3.1.2 Uncorrelated events strategy

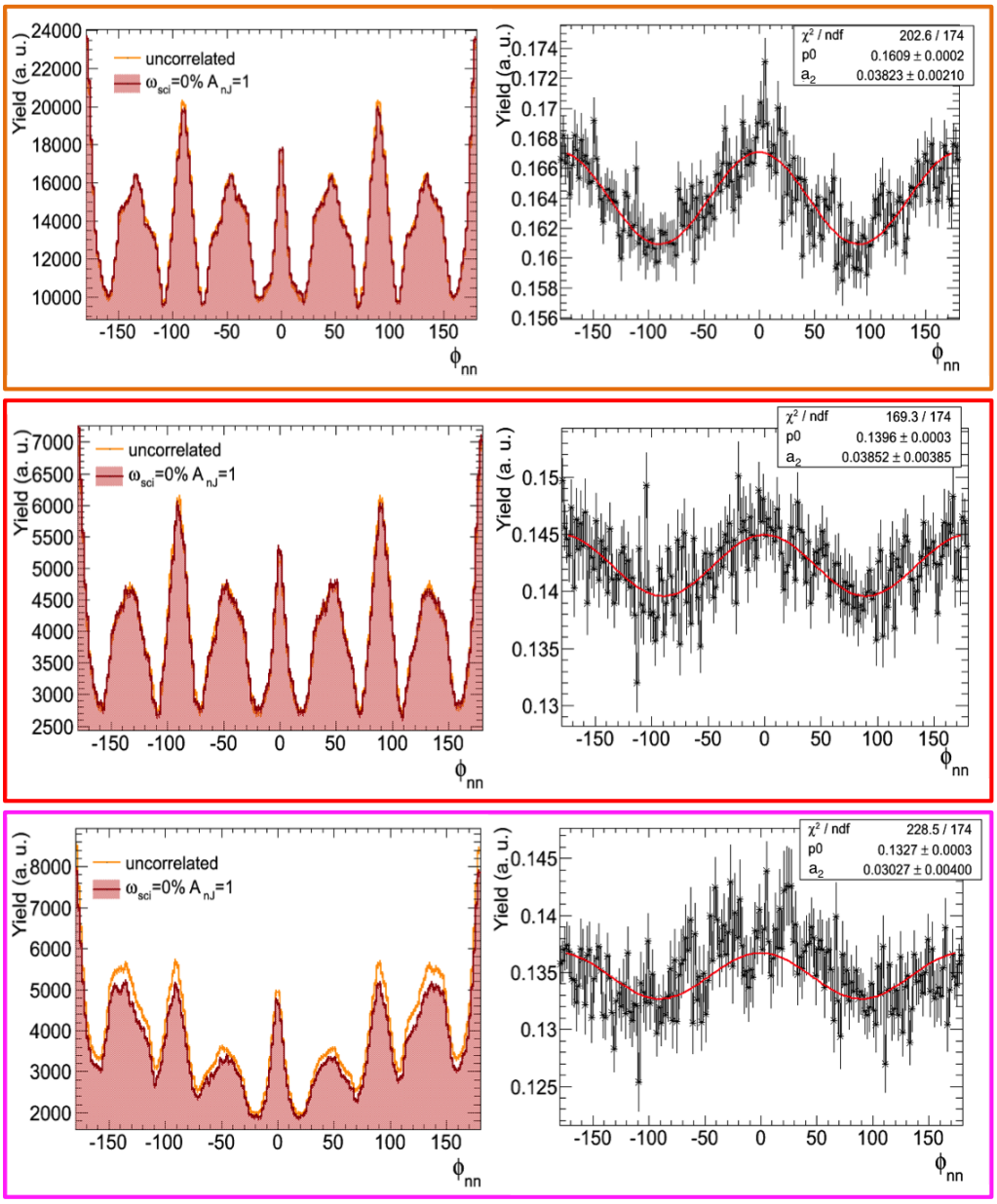

Figure 4.20: The $F_{sim}(\phi_{nn|_{LF}})$, $R_{u,sim}(\phi_{nn|_{LF}})$ and $I_{u,sim}(\phi_{nn|_{LF}})$ simulated distributions for A_{nJ}=1 are shown for the different steps of the geometrical filter. Together with the initial $I_{u,sim}(\phi_{nn|_{LF}})$ distributions the fits are presented. Even if the filter distorts the fit parameter a_2 the results are yet in good agreement with the theoretical prediction.

The uncorrelated algorithm is developed by taking neutrons from different events. The $R_{u,sim}(\phi_{nn|_{LF}})$ distribution should simulate the isotropic neutron distribution with respect to

the fission fragment spin. Since the spins of two different fragments are not correlated, the two neutrons shouldn't exhibit any correlation in the (x, y) plane perpendicular to the fission axis. The $R_{u,sim}(\phi_{nn|_{LF}})$ distribution should be almost flat which is not the case as shown by the orange curve of fig. 4.20. The very marked observed structures are due to the fact that we choose the fission fragments only along the z-axis. Thus the effect of the experimental filter is enhanced.

$$I_{u,sim}(\phi_{nn|_{LF}}) = \frac{F_{sim}(\phi_{nn|_{LF}})}{R_u(\phi_{nn|_{LF}})} \tag{4.12}$$

Fig. 4.20 presents the different distributions at the different steps of the experimental filter applied. More specifically:

- in the orange box, the figure shows at the left the filtered distribution $F_{sim}(\phi_{nn|_{LF}})$ (brown filled curve) and its uncorrelated distribution $R_u(\phi_{nn|_{LF}})$ (orange curve) after the DEMON geometrical acceptance and the pileup treatment. On the right their ratio is plotted together with the best fit. The insert presents the fit parameters.
- in the red box the incoming neutron energy cut and the intrinsic DEMON efficiency is applied.
- the pink box is addressed to the cross talk effect. As mentioned before, when the cross talk neutrons are considered in addition a selection on the relative angles between two neutrons larger than 66° ($\cos\theta_{nn} < 0.4$) is applied on the $F_{sim}(\phi_{nn|_{LF}})$ and $R_u(\phi_{nn|_{LF}})$ distributions in order to get rid of them. This cut is necessary because the uncorrelated procedure doesn't retrace the cross talk.

One can see that the structures due to the experimental filter have disappeared, the anisotropy is clearly visible, although the a_2 coefficient in the fit is somehow smaller than in the original distribution of fig. 4.17. Thus, one can conclude that the method works in a sense that it allows to observe the deviation of the distribution from the isotropic one, which is completely flat. Armed with this method we can try to simulate now the realistic case with A_{nJ}=0.16 and ω_{sci}=8%.

4.3.2 A_{nJ}=0.16

Applying the uncorrelated method tested before to the realistic case A_{nJ}=0.16 and ω_{sci}=8%, a coefficient $a_2 = 0.0044$ is obtained which has to be compared with the expected value $a_2 = 0.005$ shown in fig. 4.18. Except some fluctuations the distribution $I_{u,sim}(\phi_{nn|_{LF}})$ shown in fig. 4.21 is rather in good agreement with the fit prediction (red curve).
Undesired structures may have different origins:

- low statistics: among the 60 million fission events generated, 600000 entries remain in the spectrum of fig. 4.21. Given the weak value of a_2, a higher statistics is required.
- the condition to reject the cross talk, $\cos\theta_{nn} < 0.4$, may be too rough and still overestimated.

– the DEMON configuration, although it has been optimised in CORA3, may still not be completely appropriate to reach the high accuracy necessary to estimate this very low anisotropy parameter.

Nevertheless in spite of these structures, the general trend follows eq. 4.10.
The $a_2 = 0.0044$ value corresponding to $A_{nJ} \approx 0.16$ justifies the use of this value for the previous simulations of $\cos\theta_{nn}$ and $\cos\theta_{nLF}$.

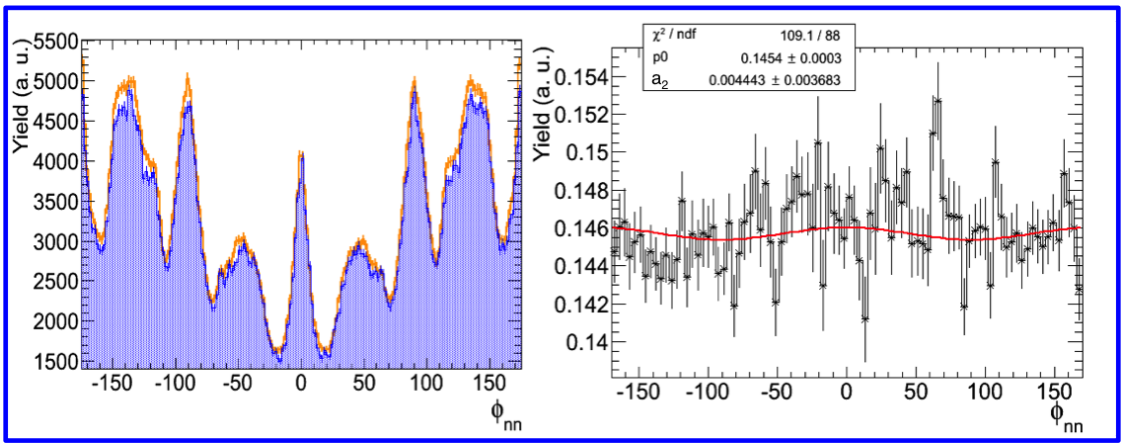

Figure 4.21: Left side: $F_{sim}(\phi_{nn|_{LF}})$ (blue) and uncorrelated $R_{u,sim}(\phi_{nn|_{LF}})$ (orange) distributions. Right side: $I_{u,sim}(\phi_{nn|_{LF}})$ distribution and the best fit (red curve) obtained for A_{nJ}=0.16.

4.3.3 Experimental Results

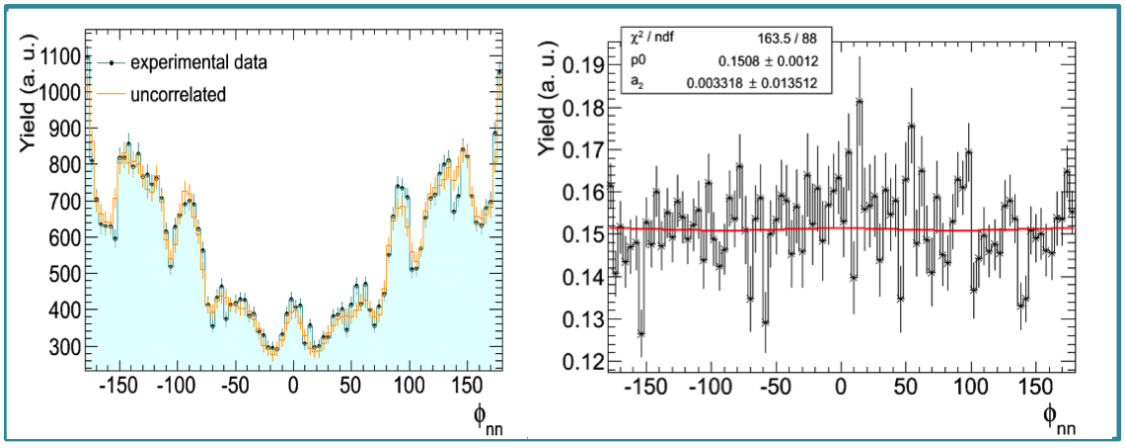

Figure 4.22: The uncorrelated $R_{u,exp}(\phi_{nn|_{LF}})$ distribution is presented in orange, the $F_{exp}(\phi_{nn|_{LF}})$ one in cyan.

The experimental distribution $F_{exp}(\phi_{nn|_{LF}})$ is shown as the cyan curve in fig. 4.22. Also

its uncorrelated $R_{u,exp}(\phi_{nn|_{LF}})$ distribution is plotted as the orange curve. On the right side the ratio distribution $I_{u,exp}(\phi_{nn|_{LF}})$ is shown together with a fit by the formula $W(\phi_{nn|_{LF}}) = p_0(1 + a_2, \cos^2(\phi_{nn|_{LF}}))$. The obtained parameter $a_2 = 3.3\,10^{-3}$ corresponds approximately to the parameter $A_{nJ} = 0.16$. The results of fig. 4.22 have been obtained with only about the fifth of the available experimental statistics. By increasing the experimental statistics, one can note, as shown in fig.4.23, that the a_2 value becomes closer to the predicted one, $a_2^{theo} = 0.005$ and that its uncertainty decreases. Because of lack of time the complete statistics couldn't be extracted.

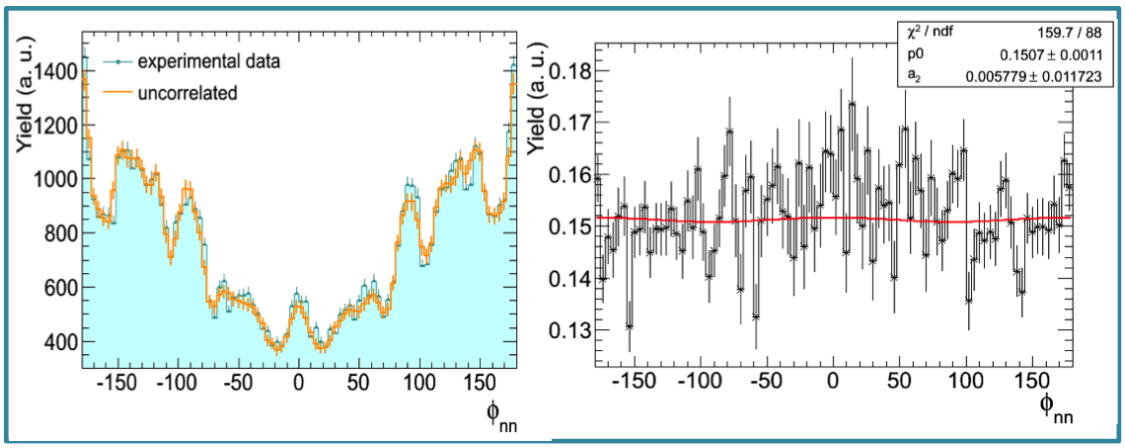

Figure 4.23: Same as fig. 4.22. The results presented have been obtained with a higher statistics although only about the half part of the available experimental statistics has been analysed.

4.4 Conclusions

In this work different approaches and strategies have been developed to determine the CM anisotropy and the scission neutron emission. For each distribution $\cos\theta_{nn}$, $\cos\theta_{nLF}$ and $\phi_{nn|_{LF}}$ an *ad hoc* technique has been provided to characterise these two effects. The analysis of an experiment such as CORA3 required not to leave out of consideration:

- the study of the experimental filter and on how it affects the distributions, hiding the physical phenomenons
- quite imaginative efforts had to be done to retrace the best detector response.
- a statistical approach through a detailed χ^2 analysis was mandatory to accede to quantitative results.
- a good knowledge of various ingredients of the theoretical model implanted in the simulation had to be acquired.

The analysis of the data as well as the Monte Carlo simulations indicate that the two searched effects should exist and that their magnitude is not far from the ones predicted by the calculations

of I. Guseva and those of other authors. Further improvement of the simulations and the analysis, by taking into account fission events with all emission angles and by dealing in a more appropriate way the cross talk may bring a better validation of both the dynamical anisotropy and the scission emission. Up to now the CORA experiment is the only one which gives access simultaneously and independently to the scission neutrons and to the CM dynamical anisotropy in the ^{252}Cf fission process.

Conclusion

The possible existence of both a neutron anisotropy emission in the centre of mass of the fission fragments and scission neutron emission is a puzzling problem since the pioneering work of H.R. Bowman in 1962. Many works, theoretical as well as experimental, have been dedicated to this question since then and led to contradictory results. All the performed experiments have been addressed either to the dynamical anisotropy or to the scission neutron emission. Nobody realised any experiment allowing the measurement of the two processes in the same time. The CORA experiment was initially conceived by F. Gönnenwein to explore the dynamical anisotropy in a novel way which allowed to avoid the influence of the kinematic focusing and of scission neutrons which, in the usual approaches, hide the tiny effect of the dynamical anisotropy. The CORA configuration was optimised up to that of CORA3 experiment which gave the opportunity to measure simultaneously, for the first time, both processes. The θ_{nn}, θ_{nLF} and ϕ_{nn} distributions, usually studied by different authors, could thus be extracted, for the first time, from a simultaneous measurement.
A detailed simulation has been undertaken in parallel with the experimental data analysis in order to get a good control on the many experimental biases. These simulations showed also that a quantitative characterization of the two processes was accessible with the CORA3 experiment. A value of A_{nJ}=0.16 for the dynamical anisotropy together with a scission neutron emission ω_{sci}=8% could be deduced from our work. These quantities are completely coherent with the predictions of I. Guseva. The θ_{nn} and θ_{nLF} distributions show clearly the existence of a scission emission. Unfortunately the anisotropy effect in the ϕ_{nn} distribution has a very weak amplitude and is thus very tricky to extract.

Some improvements of the present results may be obtained within the CORA3 data. Indeed, as has been shown on fig. 4.22 in chapter 4, an increase of the statistics does not change significantly the value of the anisotropy parameter but it decreases its error bar an the error on the fit. In the last figure only half of the available experimental statistics has been used, because of lack of time. The CORA3 experiment has been run for about five months and allowed to collect 10^9 triple coincidences (FF-2n). A new experiment with even more statistics may lead to an error bar low enough to strengthen the anisotropy value we obtained. Complementary simulations with a systematic scan of the (A_{nJ}, ω_{sci}) couples could also be performed to quantify the uncer-

tainty of these quantities but they require a huge computing time. Concerning the experimental biases, a specific experiment dedicated to the cross talk determination has been performed after the CORA3 experiment, using the same DEMON configuration but triggered with a BaF_2 scintillator and using an AmBe source. This source emits in coincidence one neutron and a γ-ray. Selecting the events triggered by the γs, the cross talk rate will be given by the ratio between two or more detected neutrons and one detected neutron. A lack of time didn't allow to finalise the analysis of this experiment. Also the DEMON configuration of the CORA2 experiment was adapted to be able to reject the cross talk events: mounting two adjacent detectors at different distances as shown on fig. 1.15 allows, by kinematic considerations, to reject in a clean way all the cross talk events of course with the compromise of loosing a consequent part of the statistics. For the ϕ_{nn} distribution, only the fragments around 0° have been considered. This angular range can be enlarged to a wider range of CODIS, although at large polar angles θ_{FF}, the resolution and the azimuthal angle φ_{FF} of the fragments are getting worse. As already mentioned a future CORA4 experiment could be considered with higher statistics. In this case DEMON should be mounted at bigger distances to decrease the pile up. A special care should be dedicated also to the cross talk effect including the multi layer configuration used in the CORA2 experiment. To keep a reasonable counting rate, a greater amount of DEMON detectors should in this case be used.

The evolution with the neutron energy will also be investigated as I. Guseva's calculations predict a dependence of the two effects on energy. This procedure requires of course a statistics as high as possible.

Taking into account all these considerations, we can consider that the CORA3 experiment has provided convincing arguments in favour of the existence of a scission neutron emission together with a dynamical anisotropy. Moreover a high confidence level can be attributed to the proportions of the two processes deduced from this work.

Appendix A

R&D: development of a new material for the neutron detection

A R&D project, NEUTROMANIA, has been initiated by the Strasbourg group in 2005. Its initial goal was to develop a new material, which had to be solid, for the detection and the identification of fast neutrons ($E > 100$ keV). Indeed, no development had been undertaken in this field since about 50 years. The development of a solid detector allowing a good neutron-γ discrimination turned out to be necessary in order to replace the scintillating organic liquids which present all major drawbacks: they are toxic, corrosive, flammable, explosive, carcinogenic and dangerous for the environment and of course cannot be operated under vacuum due to high partial vapour pressure. They are thus more and more difficult to operate at nuclear facilities where the security rules become more and more drastic. Solid detectors exist but they are either very expensive in the case of crystals as anthracene or stilbene which present also some hazard or they don't allow any neutron-γ discrimination in the case of the cheap polymer detectors.

The detection of particles by scintillators involves two steps:

- transfer of the incident particle energy to charged particles of the medium
- conversion of these products into scintillation light which is collected by a photodetector and converted into an electrical signal.

The pulse shape difference between neutron and γ ray interactions in a medium is interpreted as follows: charged particles passing through the scintillator (electrons, protons, α particles, etc. produced either outside or inside the scintillator by the interaction of the incoming γ rays and neutrons) transfer their energy to the π electrons of the scintillator. These electrons will either populate singlet states or ionise the molecules of the material and populate triplet states. The deexcitation of the singlet states leads to the fast fluorescence (fast component of the signal). Under certain conditions of high ionisation densities, the annihilation of two triplet states leads to a delayed fluorescence (slow component). These processes are illustrated in the Jablonski diagram shown in fig.A.1 [1]. Neutron-γ ray discrimination is then obtained by a pulse shape

1. F. Borne, PhD thesis, Université de Bordeaux I, 1998, n°1899

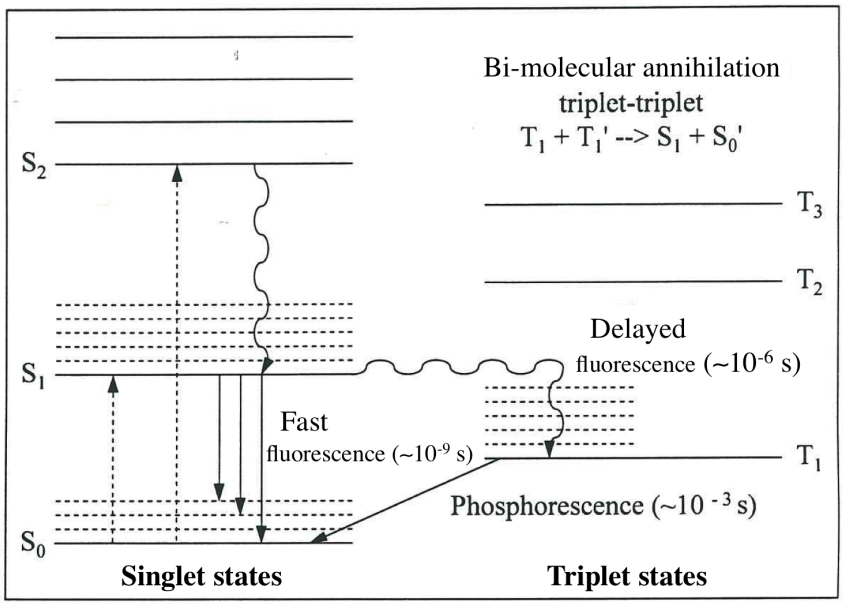

Figure A.1: Jablonski energy diagram illustrating the different processes intervening in the fluorescence mechanism[1].

analysis of the outcoming signal as the behaviour of the slow component depends on the nature of the particle. The γ rays produce a very weak slow component compared to that of neutrons or charged particles. Thus one can integrate the outcoming signal over two different gates as presented on the left part of fig.A.2 already shown in chapter 2: the total gate which covers the entire area of the signal and a slow gate with some delay during which the slow component is integrated. The correlation of these two areas, total vs slow charges, indicated on the right part of fig. A.2 and presenting two well separated branches, shows then the neutron-γ discrimination which is obtained.

The NEUTROMANIA development is based on a strong collaboration between physicists and chemists. The IPHC group collaborates since 2005 with L. Douce *et al.* from IPCMS Strasbourg. They are specialised in the synthesis of organic ionic compounds. These materials present major advantages as shown on fig. A.3:

- they offer an excellent thermal and chemical stability up to about 100°C
- they are non flammable, non volatile; they are thus useable under vacuum
- it is possible to act on the properties of the ionic compound by changing either the anion or/and the length of the alkyl chain. This latter characteristic allows to increase the hydrogen density.

This new approach allowed to obtain very quickly components which discriminate neutrons from γs as shown in fig. A.4 which led to the deposit of a first patent. But it was not possible to synthesize transparent materials: the compounds were either transparent but didn't discriminate

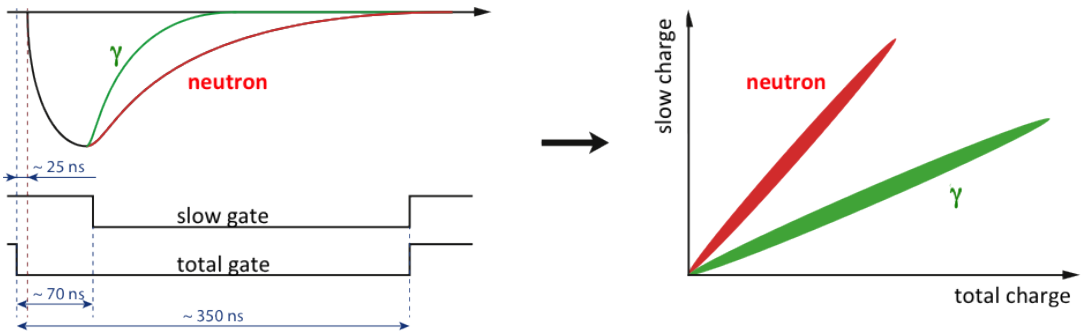

Figure A.2: Diagram of the outcoming signals of a discriminating scintillator which indicates the different slow components of a γ ray and a neutron together with integration gates of the signals (left part) and the resulting correlation between the two integrated charges, slow vs total, which exhibits the neutron-γ discrimination (right part).

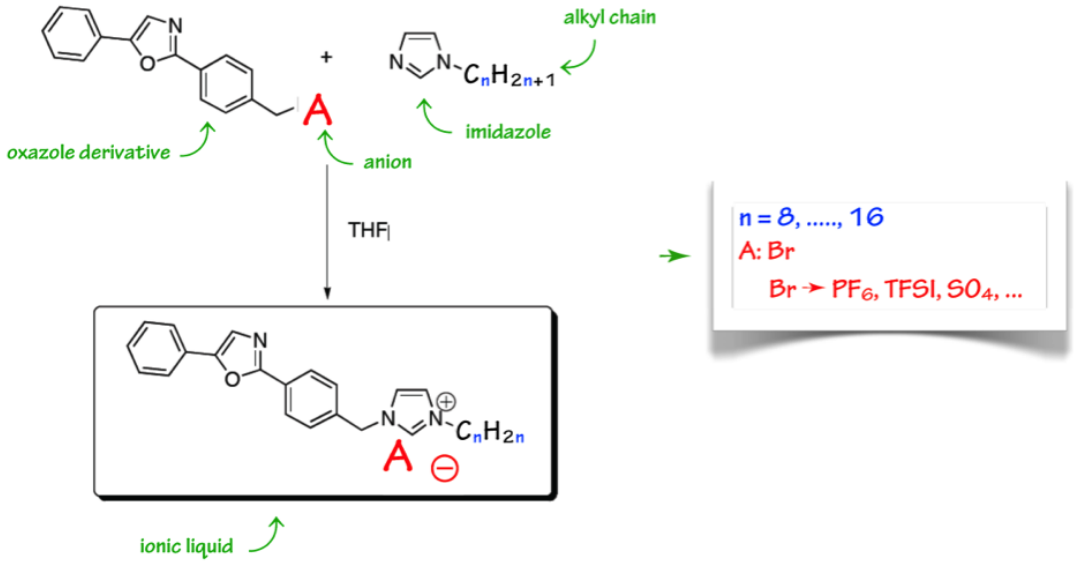

Figure A.3: Example of an ionic material able to discriminate neutron and γ radiations containing three species: 1) luminescent oxazole for blue emission, 2) alkyl tails for a maximum interaction with neutrons and 3) imidazolium/anion to drive unusual properties as thermal stability, non-flammability...

or they discriminated but were not transparent. This limited drastically the size, in particular the thickness, of the synthesized samples and thus the characterization of the physical properties was not easy. This limitation would also compromise the interest of this new component. Indeed, the detection efficiency on a wide neutron energy range depends on the thickness of the scintillator which has to be transparent to its own light. Different crystallisation techniques have been applied to overcome this lock without success.

One has to point out that the origin of the discrimination of a material, the fluorescence, is

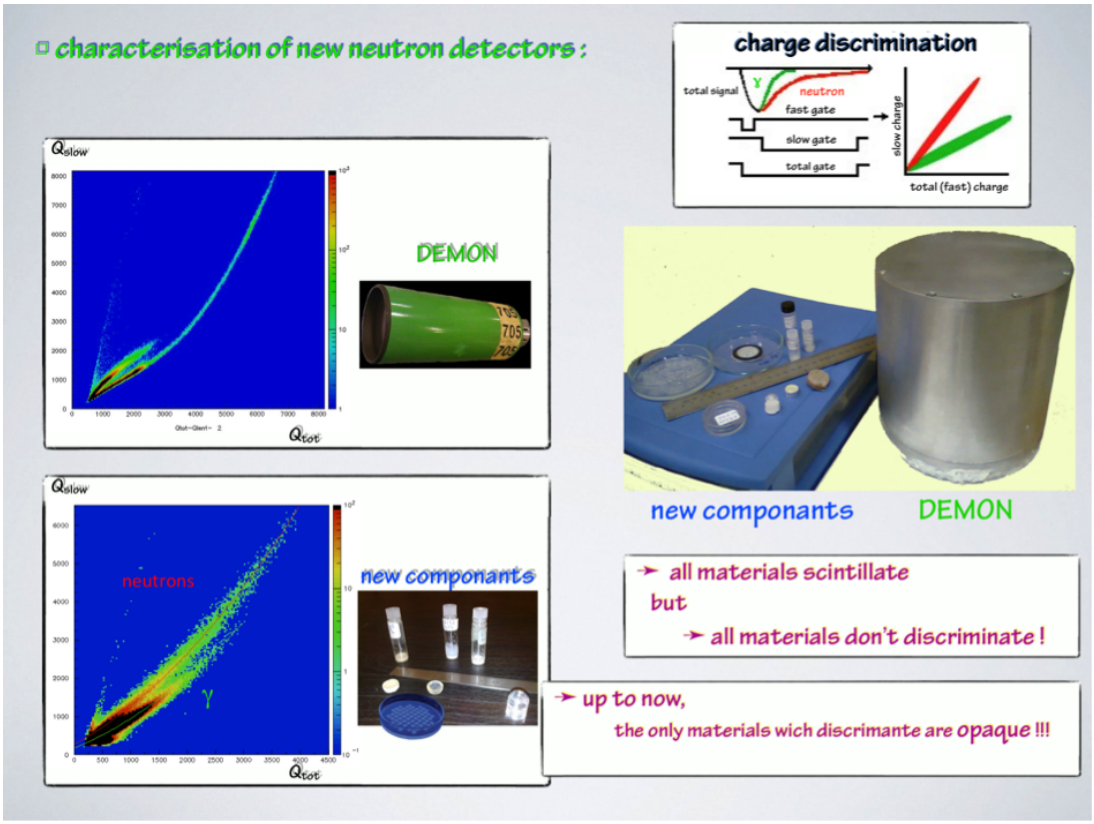

Figure A.4: - left: comparison of the neutron-γ discrimination obtained with a DEMON detector (top) and a sample belonging to the first series of ionic components (first patent)
- right: size comparison between a DEMON cell (L = 20 cm, ϕ = 16 cm) and new components.

not clearly understood and very little theoretical support is available. Moreover, many materials scintillate but very few present a discriminating luminescence property. Thus countless open possibilities exist.

Nevertheless coincidence measurements with a BaF_2 or a DEMON detector irradiated by an AmBe source which emits simultaneously a γ and a neutron were possible as presented on fig. A.5. The measurement of the time of flight associated to the charge discrimination allowed to confirm the discriminating power of these new components and a first indication of their efficiency as a function of the neutron energy could be extracted. These measurements show that with a material transparent only on 500 μm it is possible to detect neutron energies up to about 5 MeV as shown on fig.A.5. The progress achieved by the technique and filed in a second patent appears clearly in fig. A.6 which presents the $Q_{tot} - Q_{slow}$ correlations obtained in the same conditions for components of the two patents. The luminescence is much higher in the right figure. This appears clearly on the bottom figure which compares the two total charges. The new components have gained also in transparency although a complete and satisfactory transparency

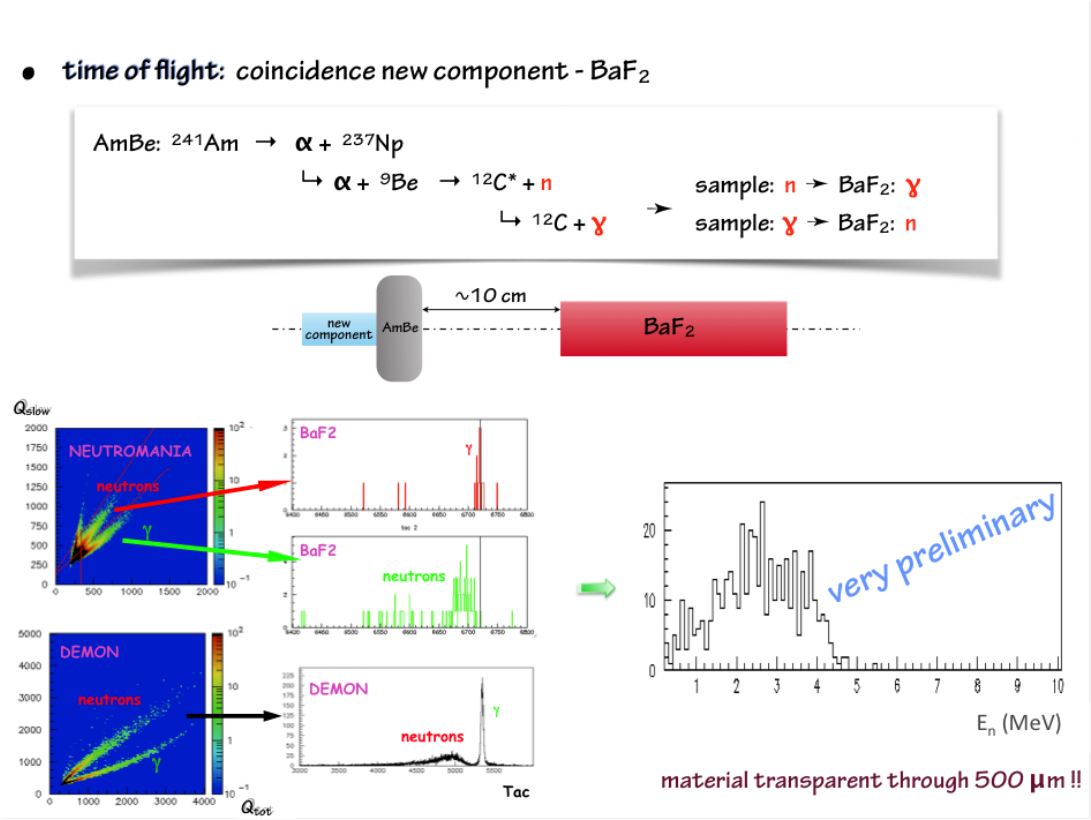

Figure A.5: Coincidence measurement between a BaF_2 scintillator and a new component irradiated by an AmBe source which emits simultaneously a γ and a neutron. This allows to access to the time of flight of the γs and the neutrons and thus deduce the energy of the neutrons (right). The spectra obtained with this new component are compared to those obtained with a DEMON scintillator (bottom left).

has not yet been obtained.

Fig. A.7 shows the spectra of the same ionic liquid based component irradiated by an AmBe source at two different dates. One can notice that no ageing can be observed after one year. An attempt has been performed to determine the figure of merit (FOM) of the new components in order to compare it to existing materials. This is not easy as this parameter is usually given as a function of the light deposited in the scintillator. But this quantity is calibrated with the photopeak or the Compton edge of different γ sources as ^{22}Na, ^{137}Cs and ^{60}Co. Due to the very weak thickness of our components, these quantities are not accessible. Indeed to detect a γ, a reasonable quantity of matter with a high Z value is required, which is not our case. Fig. A.8 shows the discrimination power of a new component irradiated with an AmBe source. The left part shows a two dimensional spectrum of the ratio of the slow over the total charge, $R = \frac{Q_{tot}}{Q_{tot}}$ as a function of the total charge. Four slices, indicated on left-top of fig. A.8,

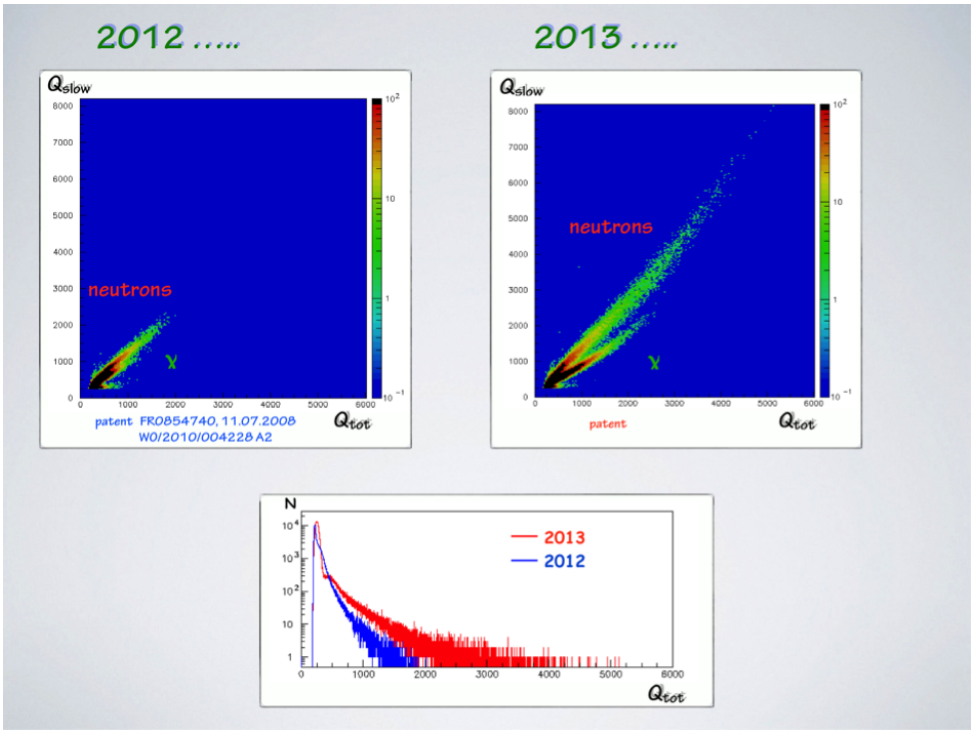

Figure A.6: Total versus slow charges of the neutron-γ signals for two new ionic liquid based components developed in the first (left) and in the second (right) patents, irradiated by an AmBe source. The bottom figure shows the total charge for the two components. One can note the progress achieved in luminescence.

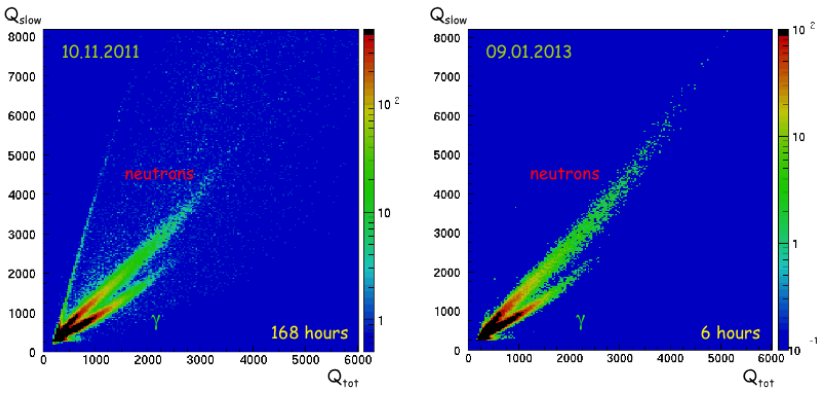

Figure A.7: Total versus slow charges of the neutron-γ signals for a new ionic liquid based component irradiated by an AmBe source at one year interval. The background of the left figure is due to a high statistics and may be to a closer source-detector distance which could explain the pile-up line on the left.

were selected for the projections of R which are shown on the right part of the figure. The left-bottom figure shows the evolution of the FOM which defines the quality of the separation between the γ and the neutron peaks, with increasing deposited energy. The obtained values are comparable with those obtained with the plastic scintillator developed by W. Zaitseva *et al.* [2] and commercialised by ELJEN/SCIONIX (EJ299). The FOM has to be greater than 1 to get an acceptable discrimination. Our FOM which is presently of about 1.1 will probably significantly improve once we get a fully transparent material. A major breakthrough has been achieved

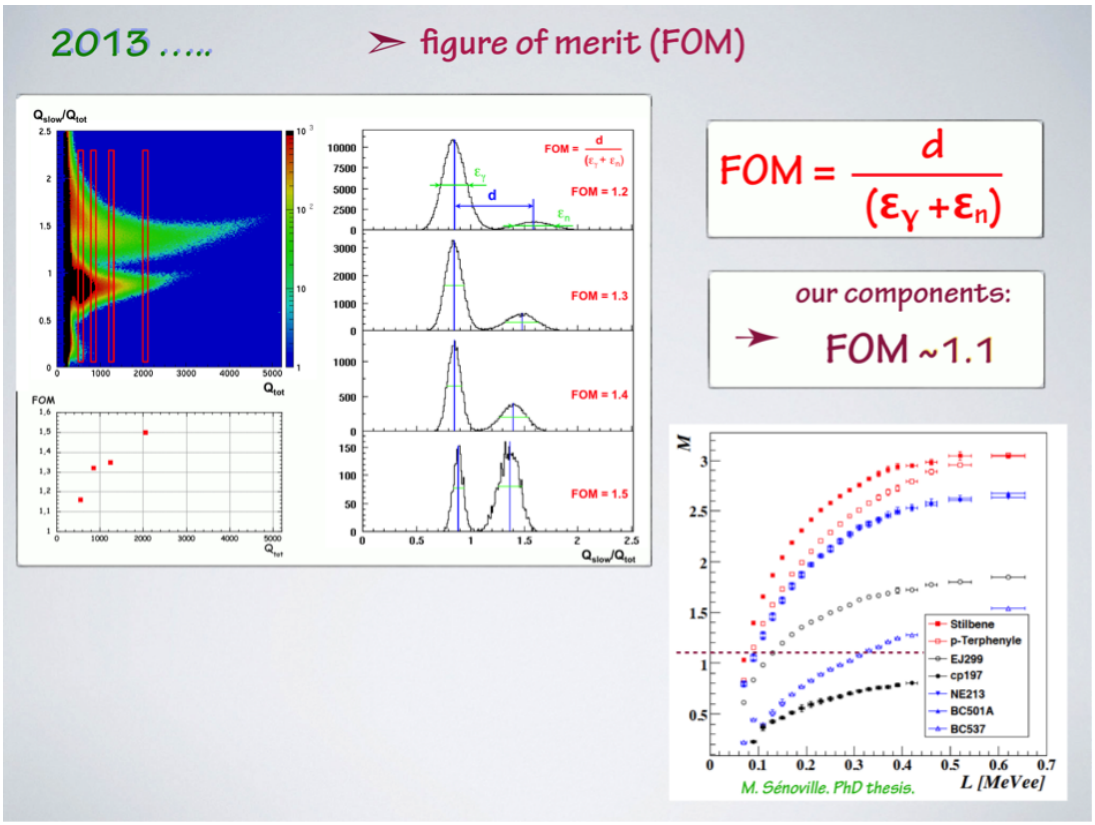

Figure A.8: Figure of merit:
- top figure: Total charge versus the ratio R of the slow charge over the total one (left-top) and projections on the R axis for four selections of the total charge indicated on the left-top figure (right). The evolution of the FOM with Q_{tot} is on the left-bottom figure.
- bottom figure: comparison with FOM of various commercial scintillators.

recently: for the first time, a transparent material which discriminates could be synthesized as shown on fig. A.9 which compares previous opaque materials and the new transparent ones. Also a $Q_{tot} - Q_{slow}$ correlation is shown for these new components which show a very nice neutron-γ discrimination. An important work has to be addressed now to obtain thicknesses of the order of the centimetre in order to cover a reasonable neutron energy range. One has to point out that

2. N. Zaitseva *et al.*, Nucl. Instr. and Meth. A668 (2012) 88-93

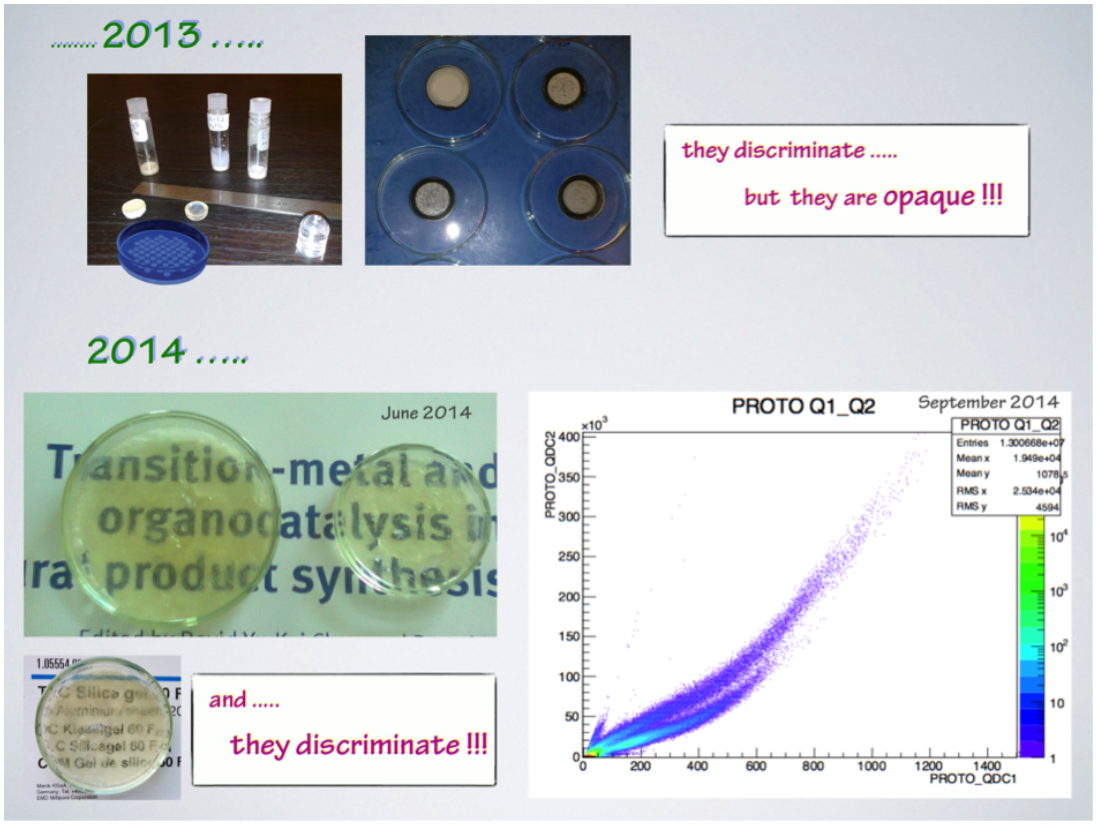

Figure A.9: Progress achieved during the last year:
- top: up to now the discriminating samples were opaque (first generation compounds)
- bottom: recently, we achieved to produce transparent samples which discrimininate.

our components are a 100% active compared to the NE213 material for example which contains only a few percentages of chromophore. This may allow a miniaturisation of the future detectors. A further optimisation of the crystallisation is necessary which implies a systematic investigation of the different parameters intervening. On the physics side, a detailed study of the outcoming signals, possible with the FASTER digitised electronics presented in Appendix B, will allow to optimise the discrimination between neutrons and γs.

An important point has to be studied also: the possibility to detect slow neutrons with these new components. Indeed the possibility to change the anion in our materials allows to introduce boron for example which is one of the materials used presently in the slow neutron detection together with ^{3}He and ^{6}Li as indicated in fig. A.10. This additional property would constitute another breakthrough as up to now the detection principles of slow neutrons is different and detectors of different nature are used for their detection. Moreover the shortage of ^{3}He which is a byproduct of the decay of tritium drives the industrials to find an alternative detection technology, which has to be operative within the next five years. Thus our components could be

$n + {}^3He \rightarrow {}^3H + {}^1H$	Q= 0.764 MeV →	E_{3H} = 0.191 MeV E_p = 0.573 MeV	**$\sigma(n_{th.})$ = 5330 barns**	gas
$n + {}^6Li \rightarrow {}^3H + {}^4He$	**Q= 4.78 MeV →**	**E_{3H} = 2.73 MeV** **E_α = 2.05 MeV**	$\sigma(n_{th.})$ = 940 barns	solid
$n + {}^{10}B \rightarrow {}^7Li + {}^4He$ (6%) $\quad {}^7Li^* + {}^4He$ (94%) $\quad \hookrightarrow {}^7Li + \gamma$	Q= 2.792MeV Q= 2.310MeV →	E_{Li} = 0.84 MeV E_α = 1.47 MeV	$\sigma(n_{th.})$ = 3840 barns	gas

Figure A.10: Characteristics of the reactions induced by slow neutrons and used for their detection. The advantages of each reaction is stressed by bold characters: ^{3}He leads to a high reaction cross section whereas ^{6}Li produces energetic outcoming particles. ^{10}B offers a compromise between these two characteristics.

good candidates to replace the existing ^{3}He gas detectors, mainly used.

This project could start in 2005 thanks to an ANR (Agence Nationale de la Recherche) support in the frame of a program lasting 24 months in collaboration with two other french laboratories, ENSICAEN and CEA-Saclay. Since then different supports (own funds of IPHC, CNRS-Région, 2 contracts with Saint Gobain Recherche, etc..) allowed to continue this research. After two prematuration contracts of a few months supplied by the SATT (Société d'Accélération du Transfert de Technologie) Conectus Alsace, they attributed us a maturing fund of 306.5 k€ during 18 months. This support should allow to finalise the development in order to obtain a marketable product within the next year and a half. Two patents have been filed. The second one may lead either to a valorisation or to the creation of a start up.

Appendix B

FASTER digital electronics

FASTER is a modular digital acquisition system, developed at LPC at Caen [1] and designed to handle from one to some hundred detectors and to treat a huge flux of data, up to 700000 events per second.
All the data are timestamped, allowing nodes to perform online correlations between measurements over a user-defined time window.
FASTER is built to use standard hardware and software components easy to customize. It is based on FPGA circuit boards that users can exploit to program their own signal treatment algorithm and build an acquisition system especially studied for their needs. FASTER is composed, as shown in fig. B.1, of mother boards called SYROCO, connected to daughter cards split in three modules. The main ones are:

- the QDC-TDC module which is a signal processing module designed for the charge and time measurements. The signals are digitized by a 12-BIT sampling using a CARAS board. This board is characterised by a 500 MHz analogic-to-digital converter. This means that the module receives a 12 BIT-sample every 2 ns and is able to timestamp its output data with an accuracy of 2 ns. The event date in nanoseconds is obtained multiplying by 2 ns each event timestamp.
- the ADC module is a signal processing module able to perform the signal pulse shape and to compute its amplitude. It has been designed for signals digitalized by a 14-BIT sampling, 125 MHz analogic-to-digital converter. This means that the module receives a 14-BIT-sample every 8 ns and is able to timestamp its output data with an accuracy of 8 ns.

The data flux got from the different FASTER modules are connected on a tree model architecture where main decision levels are set.

FASTER allows to optimise the neutron-γ discrimination based on the charge comparison computed on different integration windows. This is due to the fact that the on-line FASTER

1. http://faster.in2p3.fr/index.php/introduction

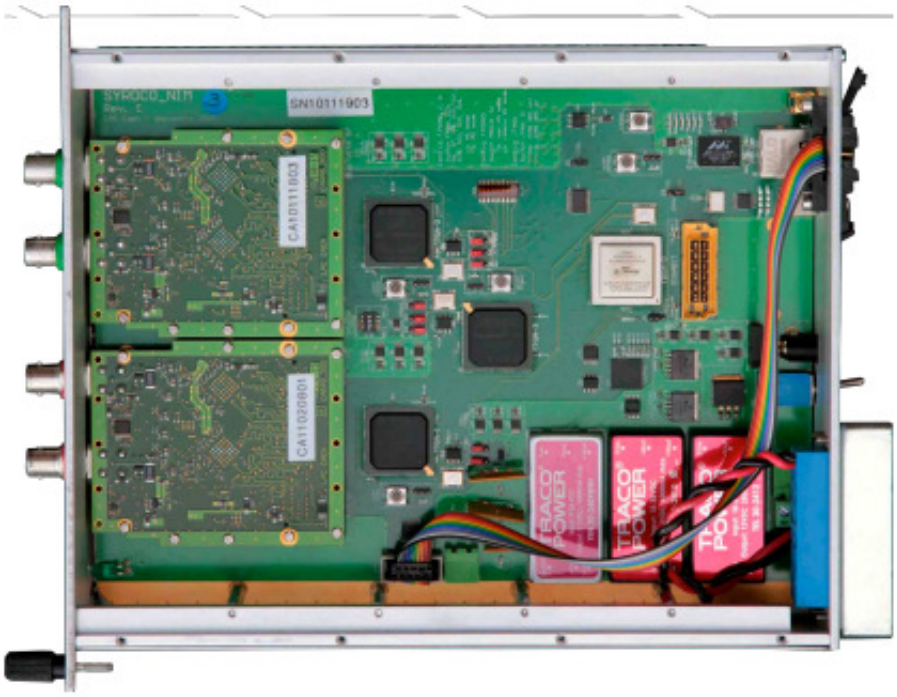

Figure B.1: Overview of a FASTER module with 4 standard NIM channels. This case contains a mother board on which two secondary cards are connected. We distinguish 3 FGPA circuits connected with the mother card.

digital electronics allows to refine the row signals. For example, if a time-fluctuating base line is added to the physical signal, the charge computed after the signal integration will also contain this contribution. FASTER allows to follow the base line and to subtract it from the physical signal. The base line is measured instantaneously when a given threshold is reached. Moreover, thanks to some tools associated to the FASTER software and developed by LPC-Caen, a better neutron-γ discrimination in comparison with that produced with an analogical electronics as the VME type is reached. With these tools we can, in an off-line analysis, exactly individuate where the contribution of each signal is located in a $[Q_{tot}, Q_{slow}]$ matrix.
Moreover for the on-line data visualisation a software based on ROOT is employed to visualise directly the signals in the oscilloscope mode, the integrated charges histograms and the $[Q_{tot}, Q_{slow}]$ matrix.

Thanks to these feature, FASTER represents a perfect tool for the R&D that we are undertaking.

Bibliography

[1] K. Becker, J.R. Parker. The Guide to Computer Simulations and Games.

[2] A. Chietera, L. Stuttgé, F. Gönnenwein, Yu. Kopatch *et al.* *Proc.Interactions of Neutrons with Nuclei ISINN-22, Dubna Russia*, 2014.

[3] A. Chietera, L. Stuttgé, F.Gönnenwein, Yu. Kopatch *et al.* *Acta physica polonica B*, 46-3:569–574, 2014.

[4] O.Hahn and F.Strassmann. *Naturwissenschaften*, 27:11, (1939).

[5] J. Chadwich. *Proc. R. Soc. Lond. A*, 1932.

[6] N. Bohr and F. Kaickar. On the transmutation of atomic nuclei by impact of material particles. *Det. Kgl. Danske Videns. Selsk. Mat-Medded*, 14, No. 10:1–40, 1937.

[7] O.R. Frisch. The interest is focussing on the atomic nucleus. *Niels Bohr, his life and work as seen by his friends and collegues*, edited by S. Rozental, 1967.

[8] E. Amaldi. From the discovery of neutron to the discovery of nuclear fission. *Phys. Rev.*, 111:1, 1984.

[9] N.Bohr and J.Wheeler. The mechanism of nuclear fission. *Phys. Rev.*, 56:426, (1939).

[10] C. F. von Weizsäcker. *Z. Phys.*, 96:431, 1935.

[11] K.H. Schmidt. *École Joliot-Curie*, 1996.

[12] P. Reuss. Précis de neutronique. *EDP SCIENCES*, 2003.

[13] J.F. Berger. LA FISSION : DE LA PHÉNOMÉNOLOGIE Á LA THÉORIE. *École Joliot-Curie*, 23c:4–8, 2006.

[14] R. Vandenbosch and R. Huizenga. Nuclear fission. *Academic Press*, 1973.

[15] C. Wagemans *et al.* The nuclear fission process. *CRC Press*, 1991.

[16] W. D. Myers and W. J. Swiatecki. *Ann Phys. (N.Y.)*, 55:395, 1969.

[17] K. Pomorski and J. Dudek. *Phys. Rev. C*, 67:044316, 2003.

[18] J. R. Nix H. J. Krappe and A. J. Sierk. *Phys. Rev. C*, 20:044316, 1979.

[19] P. Möller, J. R. Nix, W. D. Myers, and W. J. Swiatecki. Atomic data nucl. data tables. *Phys. Rev. C*, 59:185, 1995.

[20] J.F. Berger, M. Girod and D. Gogny. *Nucl. Phys. A*, 23c:428, 1984.

[21] S. G. Nilsson. *Dan. Mat. Fys. Medd.*, 29:16, 1955.

[22] V. M. Strutinsky. Shells. *Nucl. Phys.*, 1:A122, 1968.

[23] P. Möller, J. R. Nix *et al. Phys. Rev. C*, 79:064304, 2009.

[24] S. Frankel and N. Metropolis. *Phys. Rev.*, 72:914, 1947.

[25] W. J. Swiatecki. *Phys. Rev.*, 100:937, 1955.

[26] P. Möller, J. R. Nix *et al. Proceedings of the Third IAEA Symposium on the Physics and Chemistry of Fission, Rochester, NY, (IAEA, Vienna, 1974)*, I:103, 1973-1974.

[27] V. F. Weisskopf. Statistics and n*et al*uclear reaction. *Phys. Rev.*, 52:295–303, 1937.

[28] H. R. Bowman et al. *Phys. Rev.*, 126:2120, 1962.

[29] C.B. Franklyn *et al.* . *Phys. Lett. B*, page 564, 1978.

[30] A. S. Vorobyev *et al. Proc.Interactions of Neutrons with Nuclei ISINN-17, Dubna Russia*, page 60, 2009.

[31] F. Märten, *et al. IAEA Consult. Meeting. Vienna, INDS (NDS)*, 220:245, 1989.

[32] C. Budtz-Jørgensen and H.H. Knitter. *Nucl. Phys. A*, 490:307, 1988.

[33] N. V. Kornilov *et al.* New evidence of an intense scission neutron source in the ^{252}Cf(sf). *Nucl. Phys. A*, 490:307, 1988.

[34] A. M. Gagarski *et al. Proc.Interactions of Neutrons with Nuclei ISINN-20, Dubna Russia*, 2012.

[35] S. DeBenedetti *et al.* Angular dependence of coincidences between fission neutrons. *Phys. Rev. E*, 4:1645, 1948.

[36] V. Bunakov *et al. Proc. Interactions of Neutrons with Nuclei ISINN-13, Dubna Russia*, page 175, 2005.

[37] I. Halpern. *Proc. Physics and Chemistry of Fission IAEA*, 2:369, 1965.

[38] N. Carjan *et al.* Emission of scission neutrons in the sudden approximation. *Nucl. Phys. A*, 792:102–121, 2007.

[39] R.W. Fuller. *Phys. Rev.*, 126:648, 1962.

[40] N. Carjan *et al.* Scission neutrons and other scission properties as function of mass asymmetry in ^{235}U(n_{th}, f). *Phys. Rev. C*, 82:014617, 2010.

[41] N. Carjan *et al.* Partition between the fission fragments of the excitation energy and of the neutron multiplicity at scission in low-energy fission. *Phys. Rev. C*, 85:044601, 2012.

[42] N. Carjan *et al.* Nonadiabatic transition of the fissioning nucleus at scission: the time scale. *Int J Mod Phys E*, 21:1250031, 2012.

[43] A. Gavron. *Phys. Rev. C*, 13:2562–2563, 1976.

[44] I. Guseva *et al. Proc.Interactions of Neutrons with Nuclei ISINN-23, Dubna Russia*, 2015.

[45] I. Guseva. *Proc.Interactions of Neutrons with Nuclei ISINN-21, Dubna Russia*, page 91, 2013.

[46] F. Gönnenwein *et al. Seminar on Fission 6*, 1 (World Scientific), 2007.

[47] F. Gönnenwein *et al. Lecture Notes Neutrons from Fission" 6*, unpublished, 2007.

[48] L. Stuttgé *et al.* Anisotropic neutron evaporation from spinning fission fragments. *Proc. Seminar on Fission VII Het Pand, Belgium*, page 181, 2010.

[49] Yu. N. Kopatch,P. Singer, M. Mutterer *et al. Phys. Rev. Lett.*, 85 2:303–306, 1999.

[50] I. Guseva. Private comunication.

[51] T.E. Cranshaw O. Buneman and J.A. Harvey. *Can. J. of Research*, 27:191, 1949.

[52] F. Gönnenwein. Lecture notes on fission. *unpublished.*

[53] G.F. Knoll. Radiation detection and measurement. *John Wiley and Sons, Inc.*, Third Edition:227, 564, 2000.

[54] R.L. Platzman. *Int. J. App. Rad and Isotopes*, 10:116, 1961.

[55] A. Göök, M. Chernykh, J. Enders *et al. Nucl. Instr. and Meth. A*, 621:401, 2010.

[56] A. Göök, F.-J. Hambsch, S. Oberstedt *et al. Phys. Procedia*, 64:190, 2015.

[57] Fitzgerald J.B.*et al. Z. Phys*, A 355:401, 1996.

[58] A. Hotzel, P. Thirolf, Ch. Enders *et al. Zeitschr. f. Phys A*, 356:299–308, 1996.

[59] Yu. N. Kopatch, M. Mutterer, D. Schwalm *et al. Phys. Rev. C*, 65:044614, 2002.

[60] J. Va'vra, P. Coyle, J. Kadyk *et al. Nucl. Instr. and Meth. A*, 324:113, 1993.

[61] H. Henschel. Absolute Measurement of Velocities, Masses, and Energies of Fission Fragments from ^{252}Cf (SF). *Nucl. Instr. and Meth. in Physics Research.*, 190:125–134, 1981.

[62] Hans G. Börner, F. Gönnenwein. A tool and an object in nuclear and particle physics. 2012.

[63] J. Pluta *et al. Nukleonika*, 43:321–335, 1998.

[64] Y. EL Masri. *École Joliot-Curie*, 1994.

[65] M. Senoville. *PhD thesis, Université de Caen*, 2014.

[66] O. Dorvaux. *PhD thesis, Université de Strasbourg*, 1997.

[67] Erik Meijering. A chronology of interpolation: from ancient astronomy to modern signal and image processing. *Proceedings of the IEEE*, 90 (3):319–342, 2002.

[68] P. Désesquelles *et al. Nucl. Instrum. Methods A*, 307:366, 1991.

[69] P. Désesquelles, J.P. Bondorf, A. Botvina, I. Mishustin. *Nucl. Phys. A*, 604:183, 1996.

[70] P. Désesquelles. *Annales de Physique*, 20:1–45, 1995.

[71] A. Chietera, P. Désesquelles, L. Stuttgé. Improved method for the determination of neutron energies from their times-of-flight. *Nuclear Inst. and Methods in Physics Research, A*, pages NIMA–D–15–00472R1, 2015.

[72] J. Allison *et al.* Anisotropic neutron evaporation from spinning fission fragments. *EEE Transactions on Nuclear Science*, 53,1:270–278, 2006.

[73] S. Agostinelli *et al.* Anisotropic neutron evaporation from spinning fission fragments. *Nucl. Instrum. Methods A*, 506, 3:250–303, 2003.

[74] R. Brun. *Nucl. Instrum. Methods A*, 389:81–6, 1997.

[75] B. Roeder. *EURISOL Design Study*, pages 38–44, 2008.

[76] J. Terrell. Distributions of fission neutron numbers. *Phys. Rev.*, 108, 3:783–789, 1957.

[77] A. S. Vorobyev *et al.* Correlation between fission neutron multiplicity, mass and kinetic energy of fission fragments for spontaneous fission of ^{252}Cf, ^{244}Cm and ^{248}Cm. *Interactions of Neutrons with Nuclei, Dubna*, pages 276–287, 2001.

[78] A. S. Vorobyev *et al.* Prompt Neutron Emission from Fragments in Spontaneous Fission ^{252}Cf, ^{244}Cm and ^{248}Cm. *AIP Conference Proceedings*, 798 (1):255–262, May 2005.

[79] W. J. Swiatecki J. R. Nix. *Nucl. Phys. Rev.*, V:71, 1965.

[80] B. Jansson. Generation of random bivariate normal deviates and computation of related integrals. *j-NORDISK-TIDSKR-INFORM-BEHAND*, IV, 4:205–212, Dec, 1964.

[81] W. Mannhart. *IAEA TECDOC.*, 410:158, 1957.

[82] K.J. Le Couteur and Lang. *Nucl. Phys.*, 13:32, 1959.

[83] W. E. Stein. *Phys. Rev.*, 108:94, 1957.

[84] J. Terrell. Neutron yields from individual fission fragments. *Phys. Rev.*, 127, 3:880–904, 1962.

[85] A. M. Gagarski, I. Guseva *et al.* Neutron–Neutron Angular Correlations in Spontaneous Fission of ^{252}Cf. *Bulletin of the Russian Academy of Sciences: Physics*, 72 (6):773–777, 2008.

[86] N.V. Kornilov *et al. IAEA 2*, 61, 2001.

[87] K. H. Schmidt and B. Jurado. Final excitation energy of fission fragments.

[88] J. S. Pringle and F. D. Brooks. Angular Correlation of Neutrons from Spontaneous Fission of ^{252}Cf. *Phys. Rev. Lett.*, 35 (23):1563, 1975.

[89] Robley D. Evans. The atomic nucleus. page Chapter 27, 1969.

[90] F. Camera. Statistica. *http://www.mi.infn.it/ camera/lab-fisica/dispense/7-Statistica-2013.pdf*, 2013.

[91] J. Taylor. An introduction to error analysis the study of uncertainties in physical measurements. second edition:261–277, 1997.

[92] N.Gagunashvili. Comparison weighted and unweighted histograms. *Proceedings of PHYSTAT05*, 2005.

[93] Y. Kopach. ANGULAR CORRELATIONS BETWEEN FRAGMENT SPINS AND PROMPT NEUTRONS IN SPONTANEOUS FISSION OF 252Cf. *Proc.Interactions of Neutrons with Nuclei ISINN-20, Dubna Russia*, 2012.

Andreina Chietera

Corrélations angulaires entre les fragments et les neutrons dans la fission spontanée du ^{252}Cf

Mots-clefs: Réactions de fission, fission spontanée, émission des neutrons, anisotropie dynamique, neutrons de scission, détection des neutrons.

L'objectif de cette thèse est d'explorer les mécanismes d'émission des neutrons émis lors du processus de fission. En particulier, la question ouverte de l'existence d'une anisotropie dynamique dans le centre de masse des fragments de fission et/ou de la possibilité d'une émission de neutrons de scission est explorée. Dans ce but, une analyse originale a été conçue dans le cadre de la collaboration CORA; elle est basée sur une nouvelle stratégie visant à déconvoluer ces phénomènes physiques des autres effets parasites.
La thèse débute par une introduction aux concepts théoriques permettant de décrire les processus de fission et les mécanismes d'émission de neutrons. La nécessité de concevoir une méthode d'analyse appropriée permettant de caractériser des mécanismes très subtiles est ensuite discutée, en insistant notamment sur l'importance de maîtriser les diverses approximations ou/et les biais expérimentaux pouvant cacher les phénomènes physiques étudiés.
Le travail effectué dans le cadre de cette thèse a exigé un effort important de simulation, à travers le développement d'une procédure Monte Carlo basée sur un modèle cohérent de fission spontanée du ^{252}Cf, ainsi qu'une modélisation précise du dispositif expérimental de l'expérience CORA3.
Dans ce travail nous proposons pour la première fois une approche simultanée et indépendante des deux mécanismes, émission de scission et anisotropie dynamique, ainsi que des valeurs quantitatives d'anisotropie et d'émission de scission mesurées expérimentalement.

Angular correlations between fragments and neutrons in the spontaneous fission of ^{252}Cf

Keywords : Fission reactions, spontaneous fission, neutron emission, dynamic anisotropy, scission neutrons, neutron detection.

The subject of this thesis is to explore the neutron emission mechanisms in the fission process. In particular a long standing open question, the existence of a dynamical anisotropy in the centre of mass of the fission fragments and/or a possible scission neutron emission is explored. For this purpose a very original analysis based on a new strategy designed by the CORA collaboration to disentangle these two physical phenomena from other effects has been developed.
The thesis starts with an overview of the theoretical concepts on the fission process and on the neutron emission mechanisms. Also the necessity to conceive an appropriate analysis method is stressed when a very subtle mechanism is studied as various approximations and/or experimental biases not completely handled can hide the physical phenomena. In the presented work a huge effort was required to write a Monte Carlo procedure based on a coherent model for the spontaneous fission of ^{252}Cf and to couple it with the devices exploited in the CORA3 experiment.
In this work we propose for the first time a simultaneous approach of the two processes, dynamical anisotropy and scission neutron emission, as well as quantitative values of the neutron anisotropy and scission emission measured experimentally.